UNIVERSITY OF LJUBLJANA
FACULTY OF MATHEMATICS AND PHYSICS
DEPARTMENT OF PHYSICS

Gašper Razdevšek

Image quality in Cherenkov positron emission tomography

Doctoral thesis

ADVISER: doc. dr. Rok Dolenec

Ljubljana, 2023

UNIVERZA V LJUBLJANI
FAKULTETA ZA MATEMATIKO IN FIZIKO
ODDELEK ZA FIZIKO

Gašper Razdevšek

Kakovost slike pri Čerenkovi pozitronski emisijski tomografiji

Doktorska disertacija

MENTOR: doc. dr. Rok Dolenec

Ljubljana, 2023

Acknowledgements

I would like to express my sincere gratitude to my supervisor Dr. Rok Dolenec for his guidance and support throughout my thesis. His expertise, knowledge, and encouragement played a vital role in helping me overcome the challenges of this work. I would also like to extend my heartfelt thanks to my friends and colleagues from the F9 experimental particle physics department of the Jožef Stefan Institute and the Medical Physics Group from the Faculty of Mathematics and Physics. The valuable discussions and their insights were instrumental in guiding me and improving my work. I am thankful for having the opportunity to work alongside such a skilled and committed group of individuals. I am also grateful to my family and friends for their love and support throughout this journey.

Image quality in Cherenkov positron emission tomography

Abstract

Positron emission tomography (PET) is an important medical imaging modality, and although the technology is well established, there are still opportunities as well as a demand for better PET systems. The detection of annihilation photons in PET is based on scintillation light detection, but an interesting alternative is detection based on Cherenkov photons. Dense Cherenkov radiators provide an opportunity for high gamma detection efficiency - due to their high stopping power and photofraction - and excellent coincidence time resolution (CTR). However, because only a few tens of Cherenkov photons follow a gamma interaction in the radiator, the detection efficiency and the energy resolution of a pure Cherenkov detector are an issue. This work explores the performance of PET scanners based on Cherenkov detectors through Monte Carlo simulations and aims to determine whether such scanners are clinically feasible. First, single PbF_2 crystal based detectors with different surface treatments and photo-detectors covering one or multiple crystal faces were studied. Then, the potential performance of a full-size Cherenkov PET scanner was investigated using the NEMA NU 2-2018 standard and compared with a reference scanner - Siemens Biograph Vision PET scanner. The simulations were performed on a super-computing network using GATE software, and CASToR software was used for (TOF-OSEM) image reconstruction. Cherenkov scanner with single-sided readout performed similarly, while multi-sided readout detector designs performed better than the reference scanner, thanks to their improved coincidence detection efficiency and CTR. This work demonstrates that even though pure Cherenkov scanners have basically no energy resolution, the scatter fraction of around 50% is not prohibitively large, and images comparable to the state-of-the-art clinical PET scanner can be achieved. Cherenkov detectors are expected to perform even better in low-scatter environments - brain, breast, or preclinical imaging studies - and their potential for low cost could make them very interesting for total-body scanners.

Keywords: TOF PET, Cherenkov radiation, multi-sided crystal readout, PbF_2, Geant4/GATE Monte Carlo simulation, CASToR, NEMA NU 2-2018

Kakovost slike pri Čerenkovi pozitronski emisijski tomografiji

Izvleček

Pozitronska emisijska tomografija (PET) je pomemben način medicinskega slikanja. Čeprav je metoda široko uveljavljena, še vedno obstajajo priložnosti za njeno izboljšavo, prav tako pa obstaja potreba po boljših sistemih PET. Zaznavanje anihilacijskih fotonov v PET temelji na detekciji scintilacijske svetlobe, zanimiva alternativa pa je detekcija na podlagi fotonov Čerenkova. Čerenkovi sevalci z veliko gostoto ponujajo priložnost za visoko učinkovitost detekcije žarkov gama - zaradi visokega atenuacijskega koeficienta in visokega deleža fotoefekta - in odlično časovno ločljivost koincidenc (CTR). Pri interakciji žarka gama v sevalcu nastane le nekaj deset fotonov Čerenkova, kar vpliva na učinkovitost detekcije in energijsko ločljivost ter predstavljata potencialni problem te metode. To delo raziskuje delovanje skenerjev PET na osnovi Čerenkovih detektorjev z uporabo simulacij z metodo Monte Carlo in se osredotoča na raziskavo, ali so taki skenerji klinično sprejemljivi oz. uporabni. Najprej so bile raziskane različne konfiguracije detektorjev na osnovi svinčevega fluorida (PbF_2) z različnimi površinami kristalna in fotodetektorji, ki prekrivajo eno ali več ploskev kristala. Nato je bila preučena potencialna zmogljivost Čerenkovega PET skenerja z uporabo NEMA NU 2-2018 standarda. Zmogljivost je bila primerjana tudi z referenčnim skenerjem - Siemens Biograph Vision PET skenerjem. Simulacije so bile izvedene na superračunalniški mreži z uporabo GATE programske opreme, program CASToR pa je bil uporabljen za rekonstrukcijo slike. Čerenkov skener z enostranskim branjem detektorjev je deloval podobno kot referenčni skener, medtem ko so skenerji z večstranskim branjem delovali bolje, zahvaljujoč izboljšani učinkovitosti detekcije koincidenc in CTR. Delo dokazuje, da lahko s čistimi Čerenkovimi skenerji, kljub odsotnosti energijske ločljivosti, dobimo primerljive, v določenih detektorskih konfiguracijah pa tudi boljše slike, v primerjavi s sodobnimi skenerji. Znatno boljše slike, pa lahko čisti Čerenkovi skenerji dosežejo v okoljih z nizkim sipanjem, pri pregledih možganov, prsi ali predkliničnih raziskavah. Zaradi potencialne cenovne dostopnosti lahko postanejo Čerenkovi detektorji tudi zelo zanimivi za skenerje celotnega telesa.

Ključne besede: TOF PET, svetloba Čerenkova, večstransko branje kristala, PbF_2, Geant4/GATE Monte Carlo simulacije, CASToR, NEMA NU 2-2018

Contents

List of abbreviations and acronyms

CASToR Customizable and Advanced Software for Tomographic Reconstruction

CTR Coincidence time resolution

DOI Depth-of-interaction

EC Electron capture

FDG ^{18}F-fluorodeoxyglucose

FOM Figure of merit

FOV Field-of-view

FWHM Full width at half maximum

FWTM Full width at tenth maximum

GATE Geant4 Application For Tomographic Emission

LAFOV Long axial field of view

LOR Line of response

LSO Lutetium oxyorthosilicate

LTE Light transfer efficiency

LYSO Lutetium–yttrium oxyorthosilicate

ML-EM Maximum likelihood expectation–maximization

MPPC Multi pixel photon counter

MRD Maximum ring difference

MRI Magnetic resonance imaging

MSSIM Mean structural similarity index

NECR Noise equivalent count rate

NEMA National Electrical Manufacturers Association

PDE Photon detection efficiency

PET Positron Emission Tomograph

PSF Point-spread function

ROI Region of interest

SiPM Silicon photomultiplier

SLING Slovenian national super-computing network

SNR Signal-to-noise ratio

SPAD Single-photon avalanche diode

SPECT Single-photon Emission Computerized Tomography

SPTR Single photon timing resolution

SSPM Solid-state photomultiplier

TOF Time-of-flight

XCAT eXtended CArdiac-Torso

1. Introduction

In vivo structural imaging provides valuable data in clinical and preclinical studies, but to reveal the true structures of the physiological time-varying processes that explain disease phenomena, it is necessary to combine morphological information with in vivo molecular imaging. Of all the tomographic molecular imaging modalities available for noninvasively studying physiology, metabolism, and molecular pathways in humans, positron emission tomography (PET) is widely considered the most sensitive and specific [1]. PET is based on detecting two time-coincident high-energy (511 keV) photons that follow positron annihilation. The PET scanners create an image of the distribution of the positron-emitting radioisotope in the body. The physics of the emission, and the detection of the coincident photons, give PET imaging unique capabilities for both very high sensitivity and accurate estimation of the in vivo concentration of the injected radioactive compound (radiotracer). PET imaging has been widely adopted as an important clinical modality for oncological, cardiovascular, and neurological applications [2].

Despite decades of development, significant opportunities still exist to make major improvements in the performance of PET systems for a variety of clinical and research tasks [3]. All nuclear medicine studies in humans are limited by the tradeoffs between the number of detected decay events, imaging time, and absorbed dose. Signal-to-noise ratio (SNR) is a critical measure of image quality, and in PET imaging, it is determined, to first order, by the number of detected events. Low SNR is arguably the biggest technical limitation in PET imaging today, as it also plays a central role in some other limitations of PET imaging, like low spatial resolution, long scan time, and relatively high radiation burden [4].

The detectors have a primary role in determining the performance of the PET scanner. Therefore it is not surprising that many of the innovations in PET instrumentation focus on developing better or new detector technology. This work explores the possibility of improving PET scanners' performance by using detectors based on the detection of Cherenkov light instead of scintillation light. Two important aspects of the detector that directly impact the SNR of the scanner are gamma detection efficiency and time resolution. In this work, PbF_2 is studied as a potentially excellent material for stopping and detecting gammas due to its high density and high effective atomic number resulting in photofraction and attenuation coefficient higher than that of L(Y)SO - the most widely used scintillator in PET. Furthermore, Cherenkov photons are produced promptly - radiated at the timescale of several picoseconds - as opposed to scintillation light, which is produced on the time scale of nanoseconds to microseconds [5]. This makes Cherenkov radiation a very attractive mechanism to be exploited for fast-timing applications, as there is a negligible contribution of the emission process to the overall time resolution of the detector.

However, because the number of produced Cherenkov photons is relatively small - a few tens as opposed to thousands of scintillation photons in the scintillators - this creates a challenge in terms of photon detection efficiency and the energy resolution of a pure Cherenkov detector. It is accepted that in order for the detector to discriminate scattered photons from primary photons efficiently, the detector's energy resolution should be as high as possible. Also, high detection efficiency of the photo-detector is essential for a pure Cherenkov PET detector since if none of the few produced Cherenkov photons is detected, the event is lost, resulting in reduced detector sensitivity. Silicon photomultipliers (SiPMs) have become the photo-detectors of choice for the clinical/scintillation PET detectors and are also very promising photo-detectors to be used with pure Cherenkov radiators. Using novel SiPMs with good photon detection efficiency (also in the UV regime) Kratochwil *et al* 2021 [6] estimated from measurements a very promising 74% probability of detecting a coincidence event using 20 mm long PbF_2 crystals.

This work explores the performance and image quality obtained with Cherenkov time-of-flight (TOF) PET scanners through Monte Carlo simulations using GATE software. The simulations were performed on the Slovenian national super-computing network (SLING). The main research question this work tries to answer is: Can a scanner based on PbF_2 - a pure Cherenkov radiator that has basically no energy resolution - provide competitive image quality compared to the current state-of-the-art PET scanners? Keeping in mind that the negative impact of collecting more scattered events on the image quality can be compensated by collecting more true events, different Cherenkov detector designs with a potential for higher detection efficiency were also studied.

Pure Cherenkov PET detectors possess not only the capability for high performance, but also the potential for low cost, as a result of the relatively low material cost associated with PbF_2. The use of Cherenkov detectors in the high sensitivity but currently very expensive total-body scanners could make these scanners more affordable and more widely available.

The dissertation is structured as follows: Chapter 2 gives theoretical background and reviews the basic science of PET imaging. The theory behind Cherenkov detectors and the rationale for focusing on PbF_2 in this study is given in Chapter 3. The methodology of simulating and evaluating Cherenkov detectors and scanners is presented in Chapter 4. Results are shown in Chapter 5, followed by a discussion in Chapter 6, where the significance of results is considered along with the limitations of the study. Finally, Chapter 7 summarizes the work, its implications, and gives prospects for future research.

2. Positron Emission Tomography

2.1 Basic principle

Positron emission tomography (PET) is a functional imaging technique that images biomarkers radiolabeled with isotopes that decay through positron emission (β^+ decay). The positrons emitted by the radionuclides almost immediately annihilate with electrons in the human body, resulting in the back-to-back emission of pairs of 511 keV annihilation photons, as illustrated in Figure 2.1.

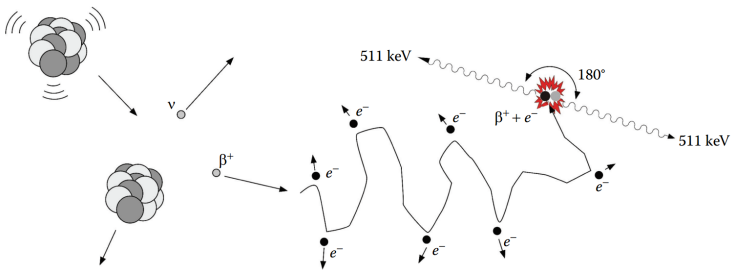

Figure 2.1: Illustration of the basic principle of PET: the decay of the radionuclide, positron (β^+) emission, multiple electromagnetic interactions (scattering) of the positron with the electrons in tissue, annihilation with an electron, and production of two back-to-back 511 keV annihilation photon (from [7]).

The fact that the two simultaneously emitted photons have an energy of 511 keV and these two photons are emitted almost exactly 180° apart is what is utilized in PET to localize the radionuclide in a PET scanner. A PET scanner essentially consists of a ring of detectors arranged around the object to be imaged. Its main components are schematically shown in Figure 2.2.

If the two 511 keV annihilation photons are registered by a pair of detectors within a narrow time window of a few nanoseconds, then it is assumed that somewhere along the line connecting the two detectors, an annihilation occurred, which is also assumed to be the approximate location of the radioactive decay. This detection technique is commonly referred to as coincidence detection, and the line connecting a pair of detectors in a PET system is usually referred to as the line of response (LOR). Since the two photons are detected in coincidence along the straight line in the absence of an absorptive collimator like in single-photon emission computerized tomography (SPECT), this technique is called electronic collimation. After collecting a large number of LORs, one can reconstruct a tomographic image of the biomarker distribution within the subject.

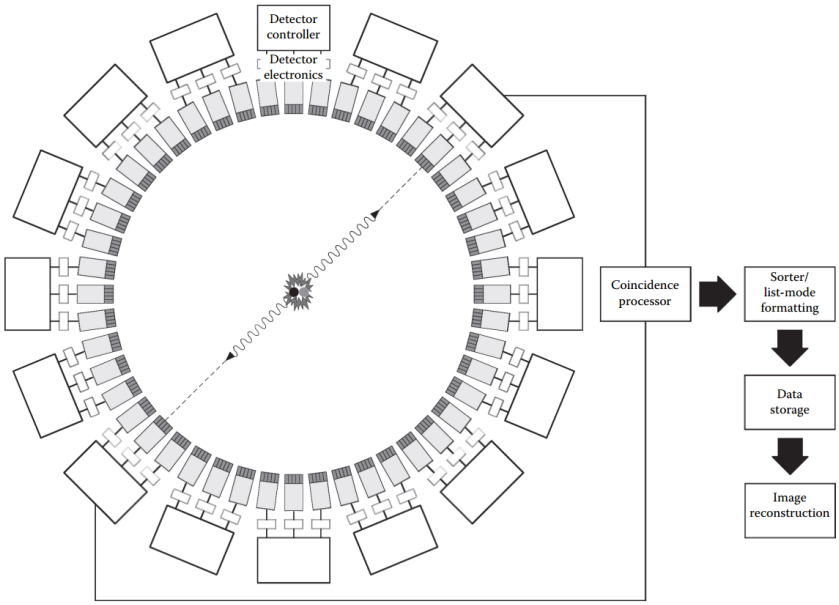

Figure 2.2: Block diagram of the main components of a PET scanner. A large number of detectors are arranged around the object to be imaged. Each detector module is connected to its own electronics. When a detector is struck by a photon, the signal is processed by the detector's electronics. If the signal is a valid event (e.g., the energy falls within the energy window), it is passed on to the detector electronics, which will take the signals from a group of detectors and pass the position and timing information to the coincidence processor. The coincidence processor will determine if two detector modules registered two events within the predefined time window. If this is the case, the event will be saved and passed to the sorter system, where the event is saved in a sinogram or formatted for list-mode storage. The event is finally stored on disk. When the acquisition is finished, the data is reconstructed (from [7]).

2.2 Radiopharmaceuticals

The science and clinical practice of nuclear medicine involves injecting a compound, which is labeled with a gamma-ray-emitting or positron-emitting radionuclide, into the subject. Most of the radionuclides used in modern nuclear medicine are manufactured by bombarding nuclei of stable atoms with subnuclear particles (such as neutrons and protons) so as to cause nuclear reactions that convert a stable nucleus into an unstable (radioactive) one. The most common radionuclides for PET radiopharmaceuticals, together with some of their properties, are listed in Table 2.1.

In elemental form, radionuclides themselves generally have a relatively small range of biologically interesting properties. Therefore, most studies in nuclear medicine employ radiopharmaceuticals, in which the radionuclide is attached as a label to a compound that has useful biomedical properties. Radiopharmaceuticals are often also called radiotracers. Table 2.2 lists the most commonly used radiopharmaceuticals and their uses, illustrating the wide range of diagnostic uses of PET and biological processes, which can be studied with it. ^{18}F-fluorodeoxyglucose (FDG) is currently by far the most commonly used radiotracer for clinical studies. FDG is an analog of glucose, and its uptake reflects glucose metabolism in tissues.

Radionuclide	Half-life	$E_{\beta^+,max}$ (MeV)	$\overline{E}_{\beta^+}$ (MeV)	β^+ max range (mm)	β^+ mean range (mm)	Production method
C-11	20.4 min	0.96	0.39	4.1	1.1	Cyclotron
N-13	10 min	1.19	0.49	5.1	1.5	Cyclotron
O-15	123 s	1.72	0.73	7.3	2.5	Cyclotron
F-18	110 min	0.635	0.24	2.4	0.6	Cyclotron
Ga-68	68.3 min	1.9	0.84	8.2	2.9	Generator (from Ge-68)
Rb-82	78 s	3.35	1.52	14.1	5.9	Generator (from Sr-82)

Table 2.1: The commonly used positron emitters in PET imaging and their physical properties; half-life, maximum, and mean kinetic energy of the positron ($E_{\beta^+,max}$ and $\overline{E}_{\beta^+}$), maximal and mean positron ranges in water, and production method (adapted from [8]).

Probe	Target	Process	Application
^{18}F-fluorodeoxyglucose	GLUT1, GLUT3, hexokinase	Glycolysis	Cancer, cerebral cortical function, myocardial viability, inflammation/ infection
^{18}F-tyrosine, ^{11}C-methionine	LAT	Amino acid transport	Cancer
^{18}F-DOPA	LAT	Amino acid transport	Cancer
	DOPA decarboxylase	Presynaptic dopaminergic function	NET
			Movement disorders
^{68}Ga-DOTATATE/TOC	SSR2	SSR expression	NET
^{13}N-ammonia	Glutamine synthase	Myocardial blood flow	Coronary artery disease
^{82}Rb	Na/K pump	Myocardial blood flow	Coronary artery disease
^{18}F-florbetapir	Beta-amyloid	Amyloid accumulation	Progressive neurodegenerative diseases
^{18}F-sodium fluoride	Hydroxyapatite	Bone metabolism	Cancer, degenerative bone disease, trauma

Note: GLUT, glucose transporter; LAT, L-amino acid transporter; SSR2, somatostatin receptor 2; NET, neuroendocrine tumor.

Table 2.2: Clinical applications and mechanisms of action of frequently used PET radiopharmaceuticals/probes (from [7]).

2.3 Basic PET Physics

2.3.1 Positron (β^+) decay and electron capture

Proton-rich radio nuclei achieve their stability by a nuclear change which requires either a positively charged antielectron emission (positron decay) or a capture of orbital electron (electron capture). Positron decay is the conversion of a proton into a neutron by the emission of a positron (the antiparticle of the electron) and a neutrino. The expression representing β^+ decay is

$$ {}^{A}_{Z}P \rightarrow {}^{A}_{Z-1}D + e^{+} + \nu \tag{2.1} $$

The β^+ decay is possible if the mass of the parent nucleus (P) is at least two electron rest masses ($2m_0c^2 = 1.022$ MeV) larger than the mass of the daughter nucleus (D). The positron decay of ${}^{18}_{9}$F, the most commonly employed radionuclide for PET, is shown in Figure 2.3. The excess transition energy above 1.022 MeV is shared between the positron (kinetic energy) and the neutrino. The energy spectrum of e^+ particles is continuous; some examples are shown in Figure 2.4. With some radionuclides, β^+ decay may leave the daughter nucleus in an excited state, and thus additional γ rays may also be emitted.

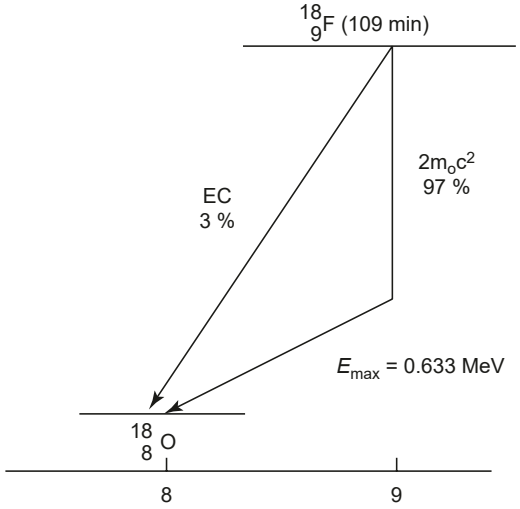

Figure 2.3: Energy level diagram for the decay of ^{18}F (from [8]).

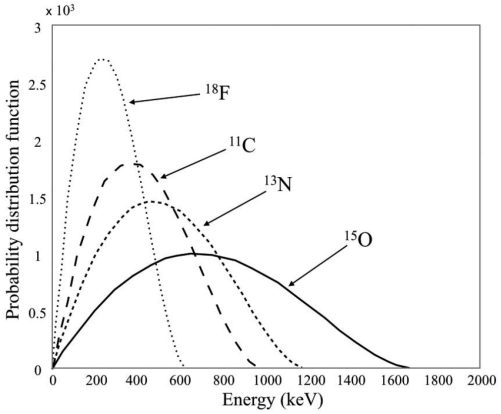

Figure 2.4: Positron energy spectrum of the most used radioisotopes in PET as a function of the positron kinetic energy (from [9]).

An alternative or competing decay path to positron decay is electron capture (EC). An orbital electron is "captured" by the nucleus and combines with a proton to form a neutron, plus a neutrino is emitted. The equation for EC is

$$ {}^{A}_{Z}P - e^{-} \rightarrow {}^{A}_{Z-1}D + \nu \tag{2.2} $$

EC can occur so long as the mass of the parent is larger than that of the daughter nuclide. Since there is no need for the margin of 1.022 MeV as required for positron decay, EC can occur for transitions not energetically possible for positron decay. Among the radioactive nuclides, one finds that β^+ decay occurs more frequently among lighter elements, whereas EC is more frequent among heavier elements, because in heavy elements, orbital electrons tend to be closer to the nucleus and are more easily captured.

2.3.2 Interactions of charged particles with matter

Charged particles traveling through matter lose energy in the following ways:

1. In Coulomb interactions with electrons and nuclei
2. By emission of electromagnetic radiation (bremsstrahlung)
3. In nuclear interactions
4. By emission of Cherenkov radiation

The energetic charged particles, while passing through matter, lose their energy primarily by interacting with orbital electrons of atoms in matter. As a result of these interactions, which cause ionizations and excitations, the charged particles lose their energy continuously, and finally, they stop after traversing a finite distance. The lighter charged particles (e.g., β particles) move in a zig-zag path in the matter (Figure 2.5). In contrast, the heavier particles (e.g., α particles) move (mostly) in an almost straight line due to their larger masses compared to electrons and because they, on average, lose smaller amounts of energy per collision. The range of a charged particle is the distance it travels through a particular material before it comes to rest (thermalises). The range depends on the type and energy of the particle and the material through which the particle moves.

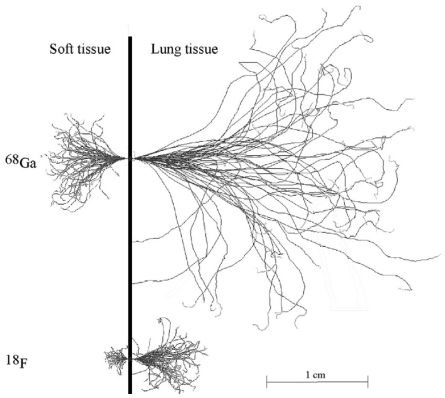

Figure 2.5: Monte Carlo simulation of different positron tracks from the decay of Gallium-68 and Fluorine-18 in human lung and soft tissues (from [10]).

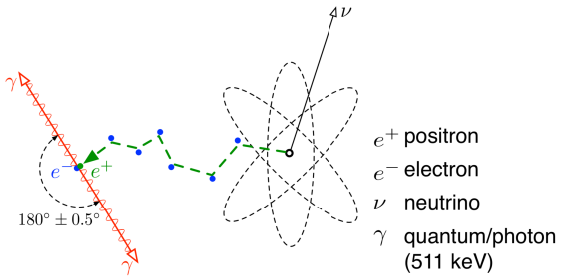

Figure 2.6: Illustration of electron-positron annihilation following a beta plus decay.

A unique situation is the passage of a positron through matter as it will eventually combine with an electron in an annihilation reaction (Figure 2.6). A short-lived hydrogen-like state known as positronium may be formed before the annihilation process with a mean lifetime on the order of 10^{-10} s. Positronium formation occurs with a high probability in gases and metals, but only in about one-third of cases in water or human tissue where direct annihilation of the electron and the positron is more favorable [11].

When the positron and electron eventually combine and annihilate, electromagnetic radiation is given off. The most probable form that this radiation takes is of two photons of 0.511 MeV (the rest-mass equivalent of each particle). However, three photons can also be emitted (<1% probability). The two photons are emitted in opposite directions to conserve momentum, which is close to zero before the annihilation. Many photon pairs are not emitted strictly at 180° but at directions slightly off from the ideal back-to-back emission by perhaps a few tenths of a degree due to non-zero momentum when the positron and electron annihilate.

Charged particles traveling through matter can also lose energy by emitting Cherenkov radiation. Although Cherenkov radiation constitutes a very small fraction of the energy loss (about 0.5% of that due to ionization, for a minimum ionizing particle [12]), it is essential in the operation of Cherenkov detectors.

2.3.3 Interaction of high-energy photons with matter

There are five mechanisms by which high-energy photons (γ rays, x-rays, annihilation radiation, and bremsstrahlung) interact with matter:

1. Coherent (Rayleigh) Scattering → type of scattering interaction that occurs between a photon and an atom as a whole. As a result of the interaction, the photon undergoes a change in direction with negligible energy loss to the atom. Coherent scattering is important only at relatively low energies ($\ll$ 50 keV) and is of little practical importance in PET
2. **Photoelectric effect** → of major importance in PET and discussed in more detail bellow
3. **Compton Scattering** → of major importance in PET and discussed in more detail bellow
4. Pair Production → photon interacting primarily with the nucleus can be converted into a pair of particles. In order for this interaction to occur, the photon must have sufficient energy to create these two particles, with a minimum of 1.022 MeV (creation of electron-positron pair), thus pair production is an interaction that is not observed in PET.
5. Photodisintegration → photons interact with nucleons inside of the nucleus and results in the ejection of one or more nucleons. Since nuclear binding energies are much larger than the energy of annihilation gammas, this interaction is not observed in PET imaging.

The *photoelectric effect* is schematically depicted in Figure 2.7. In this interaction, a photon is absorbed by a bound electron providing it with all of its incident energy (E_i). This energy is used to overcome the electron's binding energy (E_b), and the remainder (E_e) is carried away as kinetic energy by the electron, which is called a photoelectron.

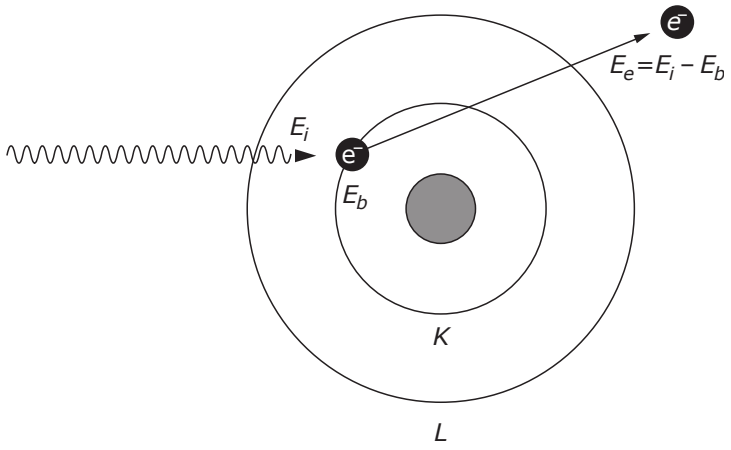

Figure 2.7: Depiction of photoelectric interaction. A photon is absorbed by a K-shell electron in this example, and provides enough energy to free the electron from the atom (from [7]).

For this interaction to occur, the incident photon energy must be greater than the binding energy of the electron, i.e., $E_i > E_b$. If sufficient photon energy is available, the photoelectron will most likely be ejected from the innermost possible shell. For example, the ejection of a K-shell electron is four to seven times more likely than the ejection of an L-shell electron when the energy requirement of the K shell is met, depending on the absorber element [13]. The photoelectric effect creates a vacancy in an orbital electron shell, which in turn leads to the emission of characteristic x-rays (or Auger electrons).

The second important interaction mode in PET is *Compton scattering*, schematically depicted in Figure 2.8. Compton scattering is an interaction between a gamma ray and valence electron of an atom whose binding energy is much lower than gamma ray energy (considered as a collision with a free electron). This effect dominates in human tissue at energies above approximately 100 keV and less than ~ 2 MeV.

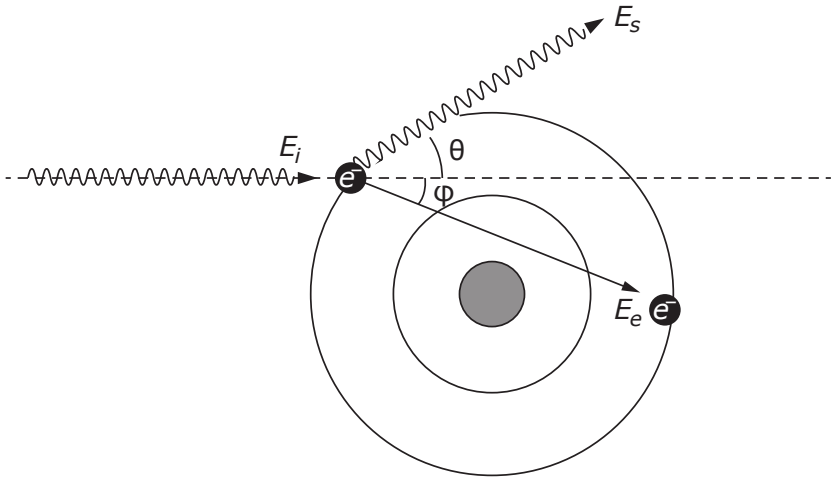

Figure 2.8: Depiction of Compton scattering. A photon comes in from the left; interacts with a loosely bound electron, freeing it from the atom; and is scattered at a lower energy to travel in a different direction (from [7]).

The photon does not disappear in Compton scattering. Instead, it is deflected through a scattering angle θ. Part of its energy is transferred to the recoil electron; thus the photon loses energy in the process. The energy of the scattered photon (E_s) is related to the scattering angle θ by considerations of energy and momentum conservation according to the equation

$$E_s = \frac{E_i}{1 + \frac{E_i}{m_0 c^2}(1 - \cos\theta)} \tag{2.3}$$

where E_i is the energy of the incident photon and $m_0c^2 = 511$ keV is the rest mass energy of the electron. The energy transferred to the electron $E_e = E_i - E_s$ does not depend on the density, atomic number, or any other property of the absorbing material. Compton scattering is strictly a photon-electron interaction. From consideration of the Compton equation 2.3, it can be seen that the maximum energy loss occurs when the scattering angle is 180° ($\cos(180°) = -1$), i.e., the photon is back-scattered. A 180° back-scattered annihilation photon will have an energy of 170 keV (Figure 2.9)

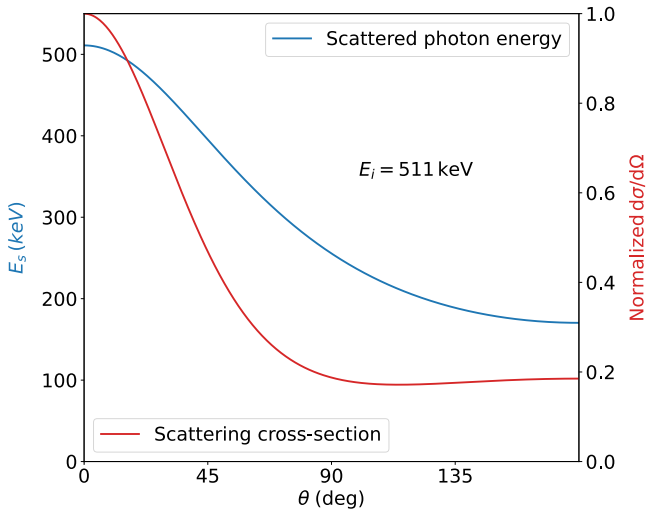

Figure 2.9: The angular probability distribution (differential scattering cross-section) and resultant energy for Compton-scattered annihilation (511 keV) photons.

Compton scattering is not equally probable at all energies or scattering angles. The probability of photon scattering from a single free electron, is given by the Klein-Nishina equation

$$\frac{d\sigma}{d\Omega} = r_0^2 \left(\frac{1}{1+\alpha(1-\cos\theta)} \right)^2 \left(\frac{1+\cos^2\theta}{2} \right) \left(1 + \frac{\alpha^2(1-\cos\theta)^2}{(1+\cos^2\theta)(1+\alpha(1-\cos\theta))} \right) \quad (2.4)$$

where $d\sigma/d\Omega$ is the differential scattering cross-section, $r_0 = \frac{1}{4\pi\epsilon_0}\frac{e^2}{m_0c^2} \approx 2.82 \times 10^{-15}$ m is the classical electron radius, and $\alpha = E_i/m_0c^2$. Figure 2.9 shows the form that this function takes for the annihilation photons ($\alpha = 1$). The total cross section (integrated differential cross section) and expected deflection angle decrease with increasing photon energy (Figure 2.10).

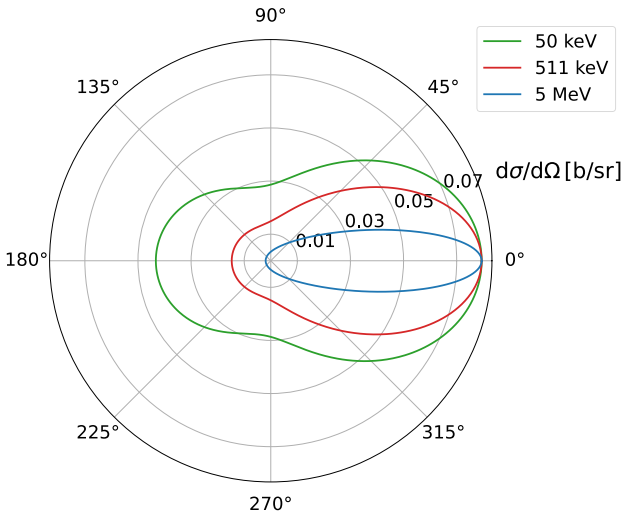

Figure 2.10: Klein-Nishina differential cross-sections (in barns per steradian) as a function of the scattering angle and three different incoming photon energies.

Which gamma interaction with matter will be dominant depends on the atomic number of absorbing material Z and gamma energy E_γ (Figure 2.11).

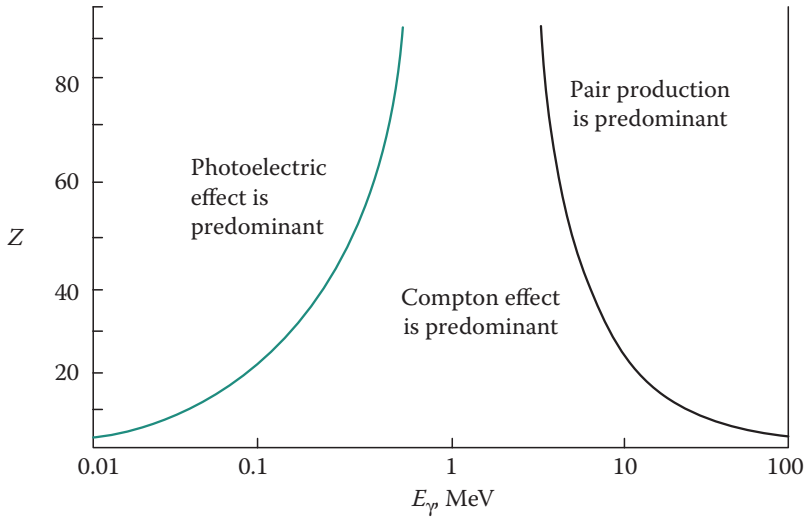

Figure 2.11: The relative importance of the three major gamma interactions in the range from 10 keV to 100 MeV. Solid lines represent the borders, where the probabilities for the two neighboring modes of interaction are equal (from [14]).

2.3.4 Attenuation of high-energy photons

When a beam of photons traverses a material, some of the photons can pass through the material without interacting. These transmitted photons are unaltered in energy or direction. Other photons will undergo one of the modes of interaction discussed in the preceding section, resulting in attenuation or a reduction in the intensity of the beam. Calculations of photon interactions are given in terms of atomic cross sections (σ) with units of cm^2/atom. The total atomic cross section is given by the sum of the cross sections for all of the individual processes

$$\sigma_{tot} = \sigma_{coh} + \sigma_{pe} + \sigma_{incoh} + \sigma_{pair} + \sigma_{nph} \tag{2.5}$$

where the cross sections are for coherent (Rayleigh) scattering (*coh*), photoelectric effect (*pe*), incoherent Compton scattering (*incoh*), pair production (*pair*), and nuclear photoabsorption (*nph*). As an example, Figure 2.12 shows, in a wide range, the energy dependence of the absorption cross section of photons in tungsten.

By multiplying σ_{tot}, with the number density of atoms (N) we obtain the linear attenuation coefficient (μ)

$$\mu = N\sigma_{tot} = \sigma_{tot}(\rho N_A/A) \tag{2.6}$$

where N_A is the Avogadro's number, ρ is the the density of the material, and A is molecular weight. The linear attenuation coefficient gives us the probability for interaction (attenuation) per unit of length (units: cm^{-1}), and is a function of the density (ρ) and atomic number of the material (Z), and energy (E) of the photons; $\mu = \mu(\rho, Z, E)$.

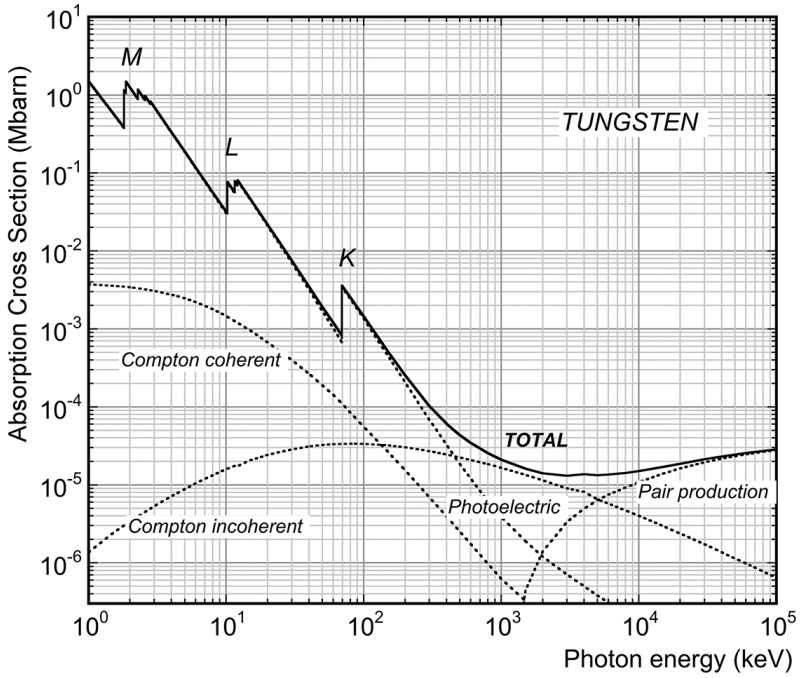

Figure 2.12: Photon absorption cross section for tungsten (from [15]).

If the original intensity of the beam of photons is I_0, then the intensity I of the beam of photons after passing through a thickness x of some material is given as

$$I(x) = I_0 e^{-\mu x} \tag{2.7}$$

Equation 2.7 is only accurate under the good-geometry attenuation or narrow-beam condition that as soon as a photon undergoes any interaction, it is no longer counted as a member of the beam.

2.4 PET scanners

The goal of a PET imaging system is to detect the 511 keV photons created in the positron annihilation process with a high efficiency and accurate measurement of detection position, photon energy, and arrival time in order to allow reliable identification of coincidence photon pairs (Figure 2.13). Positron emission detection systems have greatly developed since their first use in the 1950s, and over the years, different design trends have emerged, with PET scanners now available with a broad spectrum of features, from those available commercially for clinical applications to others designed primarily in research laboratories specifically for very high-resolution research applications. The latter category includes organ-specific (brain, breast, prostate) and small-animal imaging systems (Figure 2.14). Commercial clinical scanners have converged on a fairly consistent design, using scintillation detectors arranged in 80- to 90-cm diameter rings around the subject, while covering an axial extent along the body of 15-30 cm. Since 2001, essentially all PET scanners are physically combined with an anatomical imaging device, most commonly with computed tomography (CT) or, from 2010, a magnetic resonance imaging (MRI) scanner. The second modality not only provides a high spatial resolution anatomical framework that is accurately coregistered with the functional PET image, but also can be used to improve the quality of the PET image.

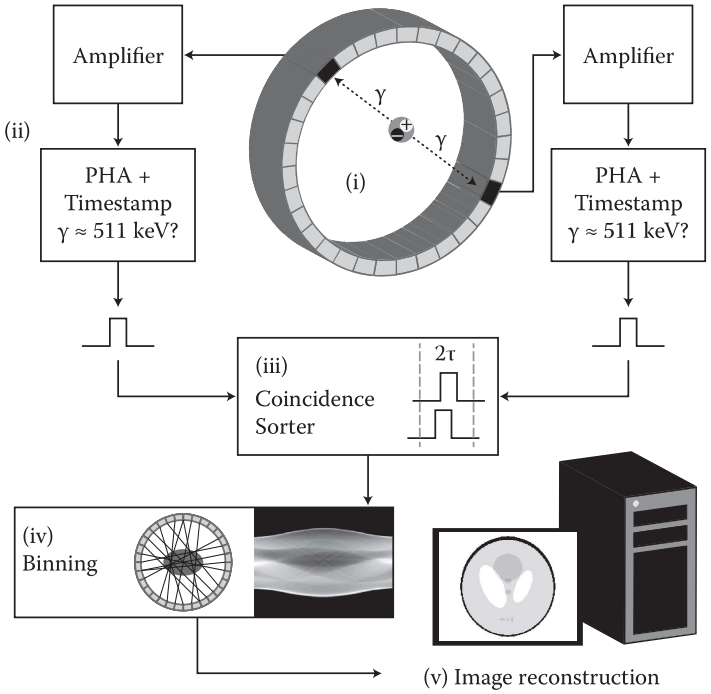

Figure 2.13: A typical PET system consists of (i) a detector ring for detecting 511 keV photons; (ii) a data acquisition system, which can perform pulse height analysis (PHA) to identify likely 511 keV photons and provide a time stamp for each event; (iii) a coincidence sorter to identify pairs of 511 keV photon detection events; (iv) a method of binning the data; and (v) a method of reconstructing the data into images (from [7]).

(a) (b) (c)

Figure 2.14: (a) Siemens Biograph Vision PET/CT (siemens-healthineers.com): example of a clinical (whole-body) scanner, (b) CareMiBrain PET system (caremibrain.com): example of a brain-dedicated scanner, (c) Mediso nanoScan PET/MRI (mediso.com): example of a preclinical PET system.

2.4.1 Scintillation detectors

The interactions of ionising radiation with matter form the basis upon which radiation detectors are developed. Scintillation detectors are the most common method for the detection of 511 keV photons in PET imaging due to their good stopping efficiency and energy resolution. These PET detectors consist of an inorganic scintillation crystal (scintillator) coupled to a photo-detector (Figure 2.15).

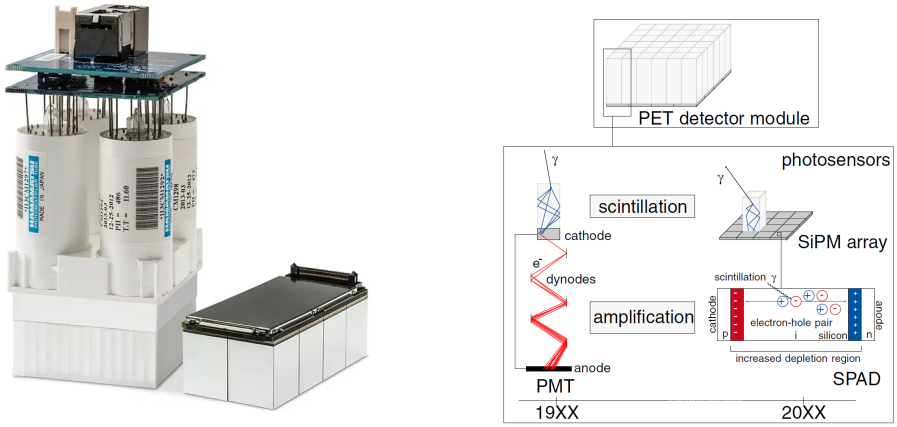

(a) (b)

Figure 2.15: (a) PET detectors where the scintillator crystals (LSO) are coupled to a photomultiplier (left) and SiPMs (right). Pictures courtesy of Siemens Healthineers. (b) Illustration of the PMT and SiPM optical photon sensing techniques (from [16]).

A scintillator is a material that can absorb ionizing radiation, such as x-rays or gamma rays, and convert a fraction of the absorbed energy into visible or ultraviolet (UV) photons. This light pulse is sensed by a photo-detector and converted into an electrical signal. This detection principle, where the high-energy photon is first converted to lower-energy photons and then subsequently converted to electrons (signal), is commonly referred to as indirect conversion. The mechanism of scintillation can be characterized as a sequence of three major steps:

1. Creation of primary electrons and holes via ionization of the matrix material, the subsequent creation of numerous secondary excitations (1-100 fs), and thermalization (1-10 ps) to create unbound e-h pairs and bound pairs (excitons)
2. Migration of e–h pairs to luminescence (activation) centers (times as long as 1-10 ns are not uncommon.)
3. Emission of the luminescent center itself (characteristic time constant ranges from $<$1 ns to $>$1 ms and is 20-70 ns in many common PET scintillators)

From the timescales noted above, it is apparent that the observed emission time of a scintillator is dominated by the migration time of excitons and e–h pairs and the excited state lifetime of the luminescence center, which are intrinsic properties of the scintillator material.

An important property of the scintillator is its ability to respond proportionally to the energy deposited by the 511 keV photon, i.e., the number of scintillation photons produced is directly proportional to the energy deposited by the 511 keV photon. An ideal PET scintillator should have the following:

1. High density and large atomic number to efficiently stop 511 keV photons with the least amount of scintillator material
2. The scintillation light pulse should have a fast response to provide high count rate capability and good timing resolution
3. High light output and good energy resolution

In addition, the scintillation material should be optically transparent, mechanically rugged, non-hygroscopic, affordable, and easy to produce. Among all the known scintillators, lutetium-based scintillators such as LSO and LYSO are the most widely used as they offer the best combination of properties for PET. Their high density (7.4 g/cm^3), high light output (32,000 photons/MeV), and fast response time (decay time = 41 ns) make them appropriate for use in PET [8].

2.4.2 Photo-detectors

Historically, fast photomultiplier tubes (PMTs) were used in PET detectors owing to their relatively low noise, fast response, and high sensitivity compared with other technologies. However, following 10-15 years of development, **silicon photomultipliers (SiPMs)** are now the photo-detector of choice for modern PET detectors, mainly thanks to their compact size, high photon detection efficiency (PDE), and low timing jitter. They have essentially replaced PMTs in both clinical and preclinical systems [3]. SiPMs also provide improved detector performance due to reduced or no signal multiplexing (average number of scintillation detectors per SiPM channel), and are generally not affected by magnetic fields, making them compatible with hybrid PET/MRI systems.

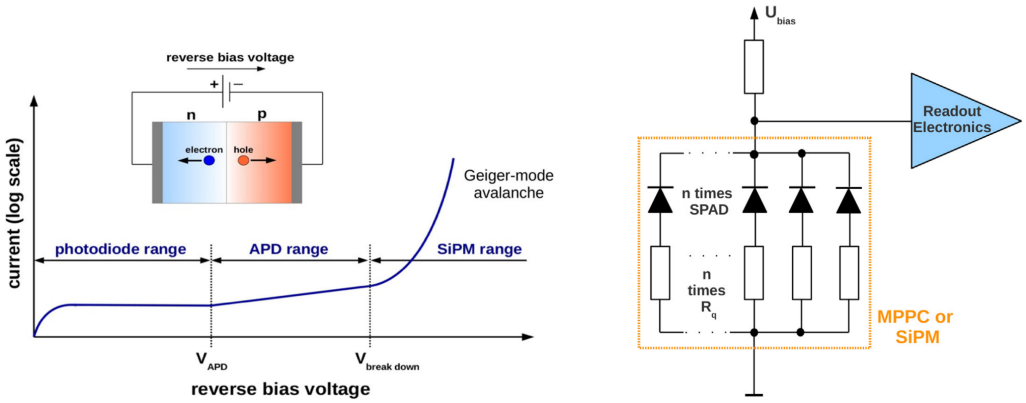

(a) (b)

Figure 2.16: (a) Operation regimes of solid state p-n junction, i.e., photodiode, avalanche photodiode (APD), and SPAD or SiPM range (from [17]). (b) In the analog SiPM, the SPADs are connected in parallel, and their signals are summed up (from [18]).

The SiPM (also solid-state photomultiplier, SSPM, or multi pixel photon counter, MPPC) is a solid state photo-detector made of an array of hundreds or thousands of integrated single-photon avalanche diodes (SPADs), called micro-cells or pixels (square with an edge length between 10-100 μm). Each micro-cell operates in parallel with the other micro-cells, and when scintillation photons reach the SiPM, they initiate a Geiger avalanche in several micro-cells, leading to a current signal that is proportional to the number of micro-cells firing at any given time (Figure 2.16). As long as the number of incident scintillation photons is less than the number of micro-cells (otherwise, the SiPM saturates), the energy of the event will be proportional to the number of micro-cells that fire, which is equivalent to integrating the analog signal.

Recent SiPMs achieve PDEs as high as 50–60% at 420 nm and single photon timing resolution (SPTR) of <70 ps [19]. The SiPM is an established photo-detector, having entered many fields, from basic scientific research to social and medical applications; however, it is still a device with plenty of room for further development [17].

2.5 PET geometry

The core of a PET system is the set of detectors that are positioned around the object under study to detect pairs of annihilation γ-rays. Figure 2.17 shows an example of how a modern detector in PET is composed. There are several detector arrangements that are able to properly sample the LORs. The most common geometry is a circular arrangement of the detectors (ring geometry), but other geometries exist, such as square, hexagon, and octagon. Ring geometry allows many different LORs to be sampled simultaneously without any detector movement. Each detector can acquire data when in coincidence with any detector belonging to an opposite arc of detectors, thus defining a sort of wedge (fan-beam) acquisition. The intersection of all the similarly defined wedges is the field-of-view (FOV) of the PET system (Figure 2.18a). More formally, the FOV is the region of space that is sampled adequately to provide a full set of LORs for the tomographic reconstruction. In ring geometry, it is a circle centered on the scanner axis. Thus, a single-ring PET provides images of slices of the object with an axial extension equal to the detector size along the ring axis. In order to increase the FOV size along the axial direction, PET systems are composed of multiple rings of detectors, and all modern clinical PET systems feature a multi-ring geometry.

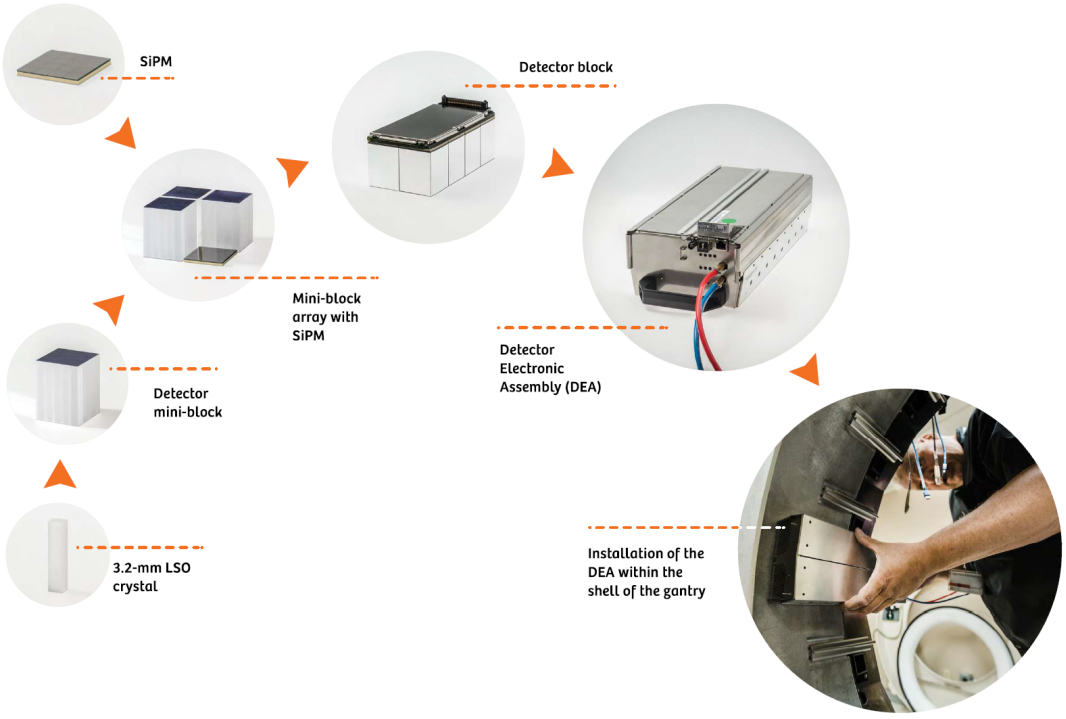

Figure 2.17: Illustration of how the Detector Electronic Assembly (DEA) is composed and installed in Siemens Biograph Vision PET/CT. Pictures courtesy of Siemens Healthineers.

Originally, most PET scanners were designed with axial collimators or septa between each ring of detectors, and they acquired data in so called 2D mode. In 2D PET, coincidences among detectors belonging to two different rings are not allowed; thus, a single ring records data from a single slice of the object/patient. This simplification makes the image reconstruction process easier. In 3D acquisition mode, the interplane septa are removed from the PET scanner, and data are obtained for all possible lines of response, as shown in Figure 2.18b. This step was made possible with the advent of more advanced reconstruction algorithms and more powerful hardware resources to manage this 3D data. The 3D modality is a big step forward in terms of system sensitivity and is now the clinical standard.

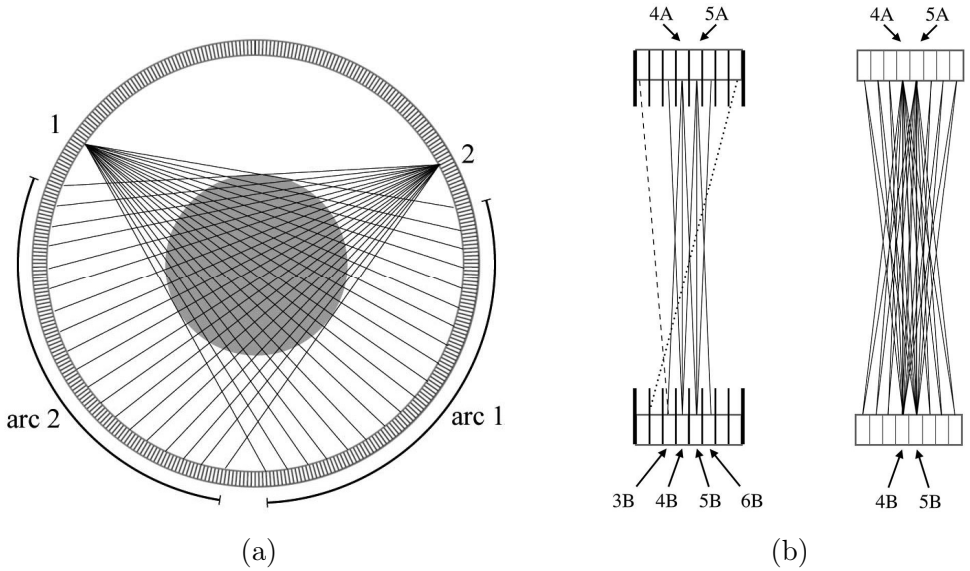

Figure 2.18: (a) Pictorial view of the detectors in coincidence with a single block, e.g., detector 1 (2) in coincidence with all detectors in the arc 1 (2). The subtended arc defines the borders of the field-of-view. The full FOV is given by the intersections of all arcs. (b) Axial section of a 2D (left) and 3D (right) PET showing the limited angular acceptance for LORs inclined along the scanner axis in 2D PET (from [20]).

2.6 Data Acquisition

The outputs from the detector modules are fed into a processing unit or detector controller that determines which detector element within the module was hit by a 511 keV photon, how much energy was deposited, and timing information when the interaction occurred. This information is then fed into a coincidence processor, which receives data from all detectors in the system. An event is regarded as valid if:

1. two photons are detected within a predefined electronic time window known as the coincidence window,
2. the subsequent line-of-response formed between them is within a valid acceptance angle of the tomograph, and,
3. the energy deposited in the crystal by both photons is within the selected energy window.

Such coincident events are often referred to as prompt events (or "prompts"). However, a number of events registered as having met the above criteria are, in fact, unwanted events as one or both of the photons have been scattered, or the coincidence is the result of the "accidental" detection of two photons from unrelated positron annihilations (Figure 2.19).

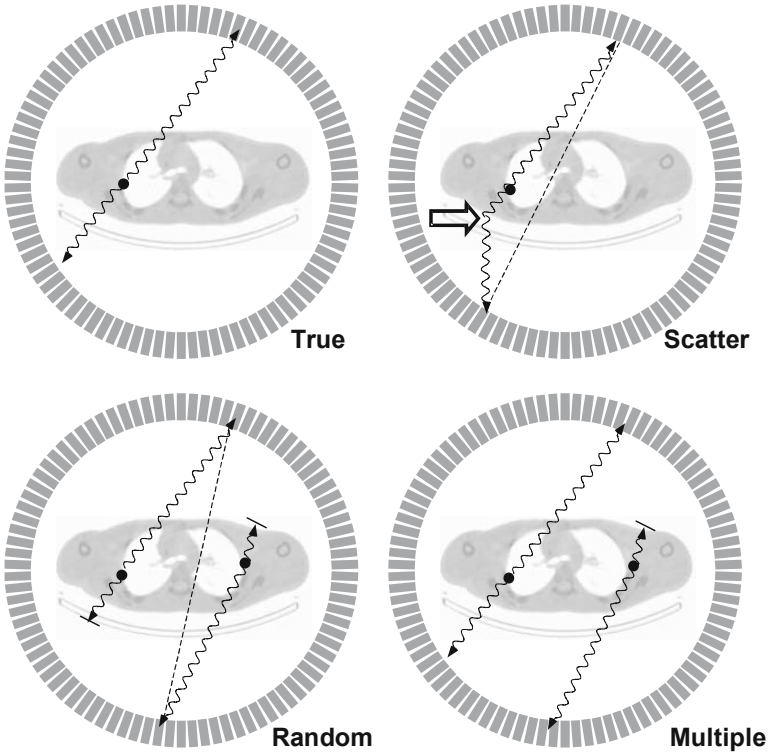

Figure 2.19: The various coincidence events that can be recorded in PET are shown schematically for a full-ring PET system. The black circle indicates the site of positron annihilation. From top left clockwise, the events shown are: a true coincidence, a scattered event where one or both of the photons undergo a Compton interaction (indicated by the open arrow), a multiple coincidence arising from two positron annihilations in which three events are counted, and a random or accidental coincidence arising from two positrons in which one of the photons from each positron annihilation is counted. In the case of the scattered event and the random event, the misassigned line of response is indicated by the dashed line (from [11]).

The terminology commonly used to describe the various events in PET detection are:

(i) A **single** event is, as the name suggests, a single photon counted by a detector. A PET scanner typically converts between 1% and 10% of single events into paired coincidence events;

(ii) A **true coincidence** is an event that derives from a single positron-electron annihilation. The two annihilation photons both reach detectors on opposing sides of the tomograph without interacting significantly with the materials in the way and are recorded within the coincidence timing window. In an ideal situation, only these types of events would be recorded by the detection system;

(iii) A **random** (or accidental) **coincidence** occurs when two nuclei decay at approximately the same time. After the annihilation of both positrons, four photons are emitted. Two of these photons from different annihilations are counted within the timing window and are considered to have come from the same positron, while the other two are lost. Since the coincidence is produced by two unrelated annihilations, these types of events do not provide any useful information about the activity distribution and should therefore be rejected. The random coincidences are unfortunately indistinguishable from the true coincidences, and the recorded coincidences are therefore a mix of the two event types. The random events tend to add a fairly uniform background to the true events, and if not corrected for, this background will reduce image contrast and compromise quantification. The rate of detected random events between a pair of detectors is given by

$$R_{\text{random}} = 2\tau R_1 R_2 \tag{2.8}$$

where 2τ is the coincidence time window, and R_1 and R_2 are the individual or singles count rates in detectors 1 and 2, respectively. Since the singles rates R_1 and R_2 are directly proportional to the activity in the FOV, the random rate is then proportional to the square of the activity in the FOV. The random rate is also directly proportional to the width of the coincidence window and can therefore be reduced by narrowing the time window. However, the time window needs to be set to a finite width (typically a few ns) to ensure that most of the true coincidences are recorded.

(iv) **Multiple events** are coincidences between three or more detected photons. These events may contain a true coincidence and a single unrelated photon, or be triggered by three unrelated photons. Because of the ambiguity of how to assign these events to a specific LOR, these events are often rejected, but also other coincidence sorting policies can be used, e.g., taking all good pairs. Again, the multiple event detection rate is a function of the count rate.

(v) **Scattered events** arise when one or both of the photons from a single positron annihilation detected within the coincidence timing window have undergone a Compton interaction. Compton scattering causes a loss in the photon's energy and a change in the direction of the photon. Due to the relatively poor energy resolution of most PET detectors, many photons scattered within the emitting volume cannot be discriminated against on the basis of their loss in energy. The consequence of counting a scattered event is that the LOR assigned to the event is uncorrelated with the origin of the annihilation event. This causes inconsistencies in the projection data and leads to decreased contrast and inaccurate quantification in the final image if not corrected for. This discussion refers primarily to photons scattered within the object containing the radiotracer. However, scattering also arises from the radiotracer in the subject but outside the coincidence FOV of the detector, as well as scattering off other objects such as the gantry of the tomograph, the lead shields in place at either end of the camera to shield the detectors from the rest of the body, the floor and walls in the room, the septa, and also within the detector. The fraction of scattered events is not a function of the count rate but is constant for a particular object and radioactivity distribution.

2.6.1 Data Organization

Coincidence data generated by a PET system contains information about the two locations of the interaction of the pair of single events. For a system with discrete crystal elements, this information is represented by a pair of crystal identification (ID) numbers. In contrast, for a system with continuous detectors, the location may be either a Cartesian coordinate (x, y, z) or a detector pixel number. In addition, coincidence data commonly includes time information (timestamp), and bed position information, while it can also contain other information, e.g., physiological gating information.

The acquired coincidences can be stored as a long list of events - list mode data storage - or they are sorted into arrays in order to save storage space and have more efficient image reconstruction. The most common approach used to histogram PET data is the sinogram. The sinogram can be thought of as a Radon transform, or line integral, of the emission data in which the data along a particular radial offset s and angle ϕ is mapped into a (row, column) position, as shown in Figure 2.20. For a source distribution that contains a point source, the pattern traced out by the source in the sinogram resembles a sine wave curve.

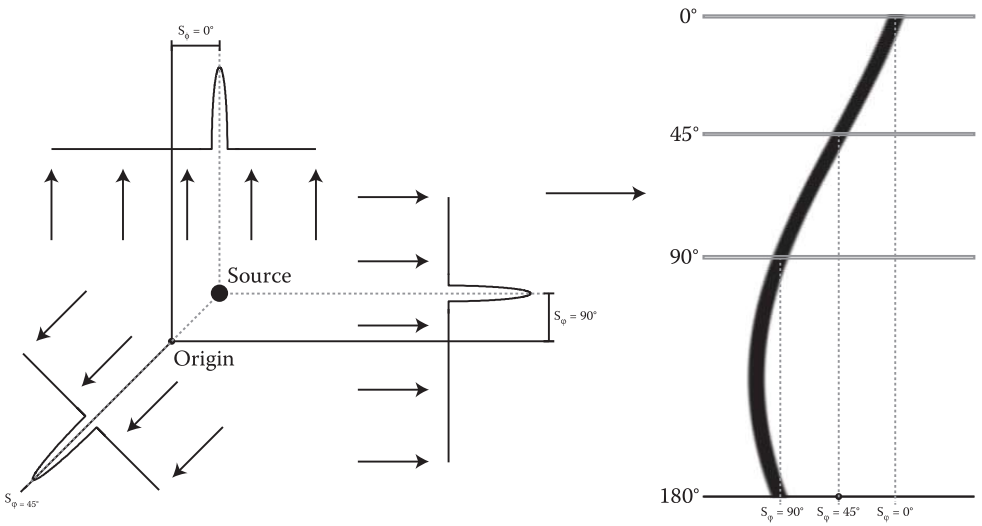

Figure 2.20: *Left:* Relationship between radial offset s and angle of projection ϕ for a point source of emission. *Right:* Sinogram of point source (from [7]).

The sinogram construction is straightforward in a single ring or 2D acquisition mode, but is not so obvious in the 3D data acquisition mode with multi-ring scanners, which are now the commercial standard. An initial approach one can consider is to simply create a unique 2D sinogram for each possible crystal ring combination, resulting in M^2 2D sinograms for a system with M rings. Since the number of three-dimensional (3D) sinograms scales as the square of the number of rings, the size of the sinogram data can quickly become very large for large axial FOV systems. A practical method used to reduce the number of sinograms in the 3D data set to manageable amounts is to employ axial binning, commonly referred to as axial mashing, but this inevitably leads to some loss in spatial resolution. TOF PET adds complexity to data organization and computation time to the reconstruction algorithm. If the reconstruction is sinogram-based, TOF information adds a 4th dimension to the 3D sinogram representation changing data storage and dynamic

memory requirements. There is also a sligh degradation of TOF resolution due to the finite size of a TOF bin in the sinogram.

List mode preserves the full spatial and temporal resolution of the measurements. Thus images reconstructed using list-mode reconstruction can be sharper with better contrast [21]. Thanks to the increasing storage and computational power, list mode is being increasingly used, especially for TOF and dynamic PET [1]. For the latter application, it also allows for retrospective gating of the data into different breathing and cardiac phases.

2.7 Data Corrections

One goal of PET imaging is obtaining an accurate and quantitative image, meaning that the the intensity of the reconstructed image should be proportional to the amount or concentration of activity at the corresponding location in the object. This is desirable for accurate comparisons of activity levels in different organs or in diseased versus normal tissues. A number of corrections are required to achieve this goal, namely normalization, attenuation, scatter, random, and dead-time correction. The accuracy of these corrections strongly affects the quality of the PET image [22].

2.7.1 Normalization

Data normalization in PET refers to corrections for various nonuniformities in the data collection process that lead to a varying LOR sensitivity. The sources of these LOR nonuniformities can be separated into two distinct categories: (1) variations in crystal efficiency and (2) geometric effects. Variations in crystal efficiency can arise due to random variations in the intrinsic efficiency of individual crystals, as well as systematic variations in collected light and timing for each crystal, which can be reduced with accurate energy and timing calibrations. The geometric factors affecting LOR uniformity arise from effects related to the change in the detector solid angle and the angle of incidence of annihilation photons at the detector surface for increasing LOR radial position. Failure to account for variations in LOR sensitivity leads to bias and high-frequency artefacts in the reconstructed images.

The simplest way to implement this normalization process is to illuminate all LORs with a uniform source (rotating point or line source of ^{68}Ga, a planar sheet source, or a uniform cylinder). The required normalization coefficients (NCs) are then proportional to the reciprocal of the number of counts obtained in each LOR. This process is known as direct normalization (direct inversion technique). The disadvantage of this technique is the need for a very high number of counts to achieve reasonable count statistics per LOR for direct inversion, leading to long scan times with a low-activity source. In addition, scatter in the uniform cylinder can be confounding, since accurate scatter correction is needed for an estimate of the normalization factors.

In order to overcome these disadvantages, component-based normalization methods [23] that make use of variance reduction techniques to reduce scan time and improve the statistical accuracy of the data are more routinely used nowadays. In this methods, NCs are expressed as a product of factors representing the variations in the intrinsic efficiency of each detector element and variations in the efficiency of each LOR due to, for example, changes in the angle between the LOR and the relevant detector faces. Details of these methods can be found in [24].

2.7.2 Correction for Random Coincidences

In order to detect coincident events in a PET scanner, whenever a photon is detected in one of the PET detectors, i, coincidence electronics search for another photon detected in one of the other detectors, j, within a time τ (coincidence timing window) of the first photon. For a typical scanner with a transverse FOV of 60 cm in diameter, the TOF difference between two coincident photons emitted at the edge of the FOV will be 2 ns. Hence, the coincidence timing window τ has to be at least 2 ns in order to collect all true coincidence events generated within the imaging FOV. Additionally, the nonzero timing resolution of a PET detector leads to a convolution of the 2 ns TOF difference with a Gaussian function with full width at half maximum (FWHM) equal to the scanner timing resolution. In practice, the coincidence timing windows are typically 3-5 ns in the current generation of TOF PET scanners. Due to the finite size of the coincidence timing window, uncorrelated single photons from two different annihilation events will have a nonzero probability of being detected within this coincidence timing window as well, with the probability increasing as the singles rate in the scanner increases. Figure 2.21 shows a schematic describing the detection of a true coincident event as well as a random coincident event.

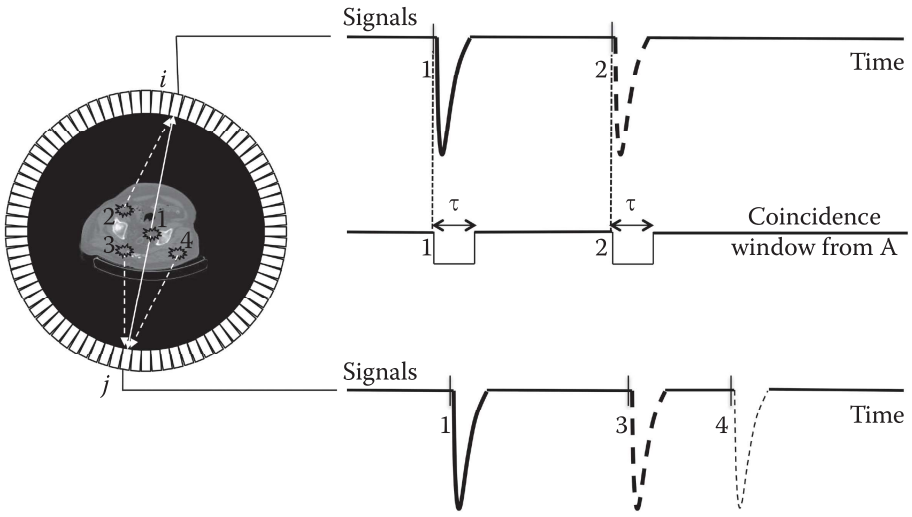

Figure 2.21: Schematic showing collection of coincident events in detectors i and j in a PET scanner. Solid lines are signals from true coincident events, dashed lines are from single events, and thick lines in the two detector signal chains show a detected coincident event. Event 1 represents a positron annihilation where the two coincident 511 keV photons are detected in detectors i and j (true coincidence). Events 2–4 are positron annihilations that occur close to event 1 temporally, but where only one of the two photons is detected in either detector i or j (single events). The coincidence logic determines photons from event 1 as a valid coincident event. In addition, event 2 in detector i and event 3 in detector j are also in coincidence, and hence an incorrect, or random, coincident event is detected (from [7]).

Since the photons that form a random coincidence are generated from two unrelated annihilation events, they add a bias in the image that will affect image contrast, as well as the measured activity uptake. Hence, correction techniques are needed to produce accurate PET images.

Randoms correction can be performed based on the single-photon count-rate information (Eq. 2.8) along each LOR. This method is called the "singles-based" and in order to obtain an accurate estimate, a proper modeling of detector dead time in the individual detectors, as well as variability in timing between detector pairs, needs to be performed.

The most common technique for randoms estimation is the delayed window technique that is routinely used in most commercial PET scanners. This technique makes use of the fact that the two photons forming a random coincident event are not related to each other spatially or temporally. Hence, by using an additional coincidence timing window that is delayed by a time τ_d relative to the detection of the first photon, one can get an accurate estimate of the random coincidences without any true coincidences being collected in this data acquisition channel. The data collected in the delayed window sinogram can be subtracted from the emission sinogram to obtain an accurate measure of true and scattered coincidences. Relative to the singles-based randoms estimation technique, the delayed coincidence window technique is very accurate since it acquires data at the same rate as the true coincidence data, and hence suffers from the same dead-time effects. However, the collected counts in each LOR can be very small, so the noise propagated into the randoms-corrected emission sinogram may be high. Noise propagation due to randoms correction can be reduced if the delayed window data are collected separately and variance reduction techniques utilized before their subtraction from the prompt events [25].

2.7.3 Scatter Correction

The primary interaction of 511 keV photons inside a patient is elastic scattering off an electron through Compton scatter. While undergoing this process, the 511 keV photon loses some energy and also changes its direction (as described by Equation 2.3). One or both of the coincident 511 keV photons can undergo single or multiple scattering. Because the assigned LOR of a scatter coincidence does not pass through the annihilation or emission point, this leads to a bias in the collected data, and consequently in the image, if it is not corrected. This bias leads to a reduced contrast in the image and an incorrect estimate of activity.

The proportion of accepted coincidences that have undergone Compton scattering is referred to as the scatter fraction and its magnitude depends on several factors, including the size and density of the scattering medium, the geometry of the PET scanner and the width of the energy acceptance window (which is mainly determined by the energy resolution of the detectors). The impact of the size of the scattering medium and the energy resolution of a whole-body PET scanner on the number of detected true, single scatter, and multiple scatter 511 keV photons is illustrated in Figure 2.22. In general, the fraction of scattered events in PET can be very high, especially in 3D imaging of the abdomen, where it may be as high as 60% to 70%.

Several scatter correction techniques have been developed over the years, and they can be classified according to the way the scatter count distributions are estimated. These include analytical methods [26, 27], Monte Carlo simulation techniques [28], multiple (e.g., dual [29] or triple [30]) energy window methods and model-based scatter correction algorithms [31, 32].

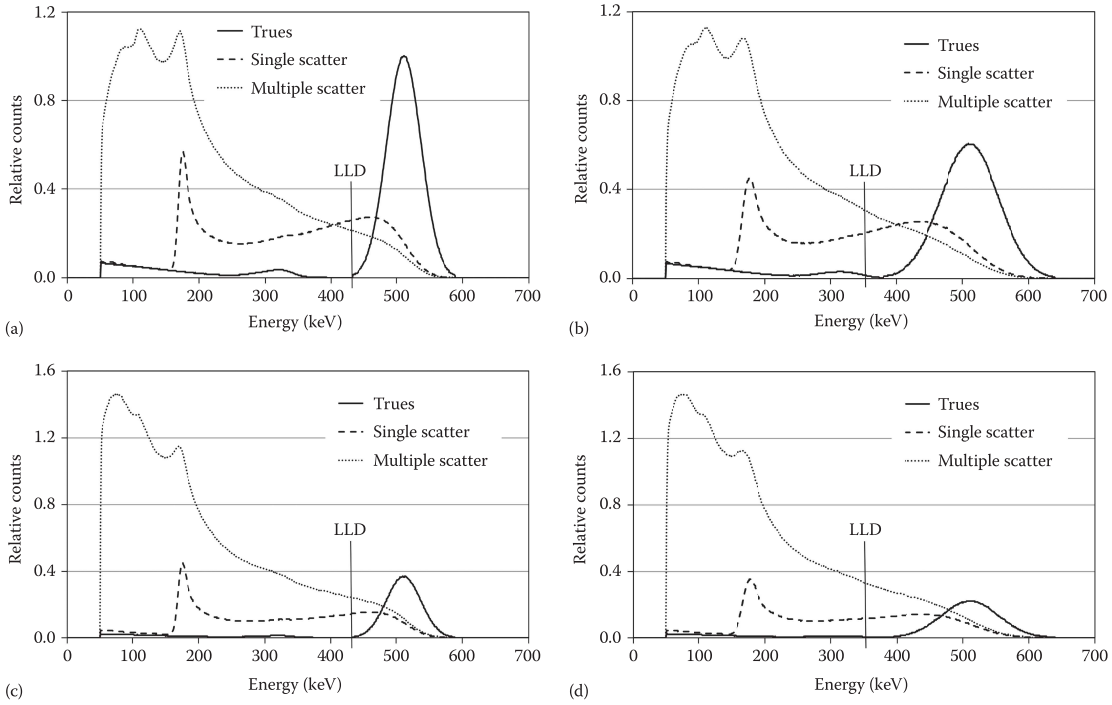

Figure 2.22: (a) Simulated energy spectra for true, single scatter, and multiple scatter 511 keV photons detected in a PET scanner with 12% energy resolution for a 20 cm diameter by 40 cm long cylinder. The LLD value sets the lower energy gate for collected events in the scanner. (b) 20% energy resolution, 20 cm diameter by 40 cm long cylinder. (c) 12% energy resolution, 35 cm diameter by 40 cm long cylinder. (d) 20% energy resolution, 35 cm diameter by 40 cm long cylinder (from [7]).

In recent years, the most popular and clinically used technique for scatter correction in PET has been the model-based single scatter simulation (SSS) [33], which is based upon the observation that in PET scanners with good energy resolution (and hence a higher energy threshold), the dominant form of scattered events is single scatter events (Figure 2.22). The SSS technique starts with an initial estimate of the emission image without any scatter correction, while the attenuation image is used to distribute scatter points within the patient. The Klein–Nishina equation (Eq. 2.4) is then used to obtain an estimate of the number of counts contributed to each LOR by every scatter point within the patient based on the emission activity distribution. In this manner, an estimate of the total scatter distribution is obtained for all possible LORs. While the SSS method provides an estimate of the scatter distribution, it does not provide an absolute measure of the number of scattered events in every LOR. In order to scale the scatter distribution obtained from SSS to an absolute measure, the tails of the scatter estimate are scaled to the number of counts present beyond the object boundary in the sinogram for an absolute estimate of the scattered events. Since this scatter calculation (first iteration) is based on an initial emission image without any scatter correction, the SSS algorithm needs to be repeated for a few (typically three or four) iterations using the scatter estimate from the previous iteration for a more accurate initial emission image.

With the advent of TOF PET, the SSS technique was easily extended in the TOF dimension [34], since, for each scatter event, there is a precise measure of the

distance traveled by each photon, and hence the TOF for each scattered event (after convolving it with the scanner timing resolution) is naturally available. A primary limitation of the SSS technique is the assumption that all scattered events are single scatter, which breaks down for scanners with poor energy resolution, especially those operating in a fully 3D mode. Current and previous generations of PET scanners with an energy resolution of 15% or less and operating in the fully 3D mode have generally performed well when using the SSS technique for scatter estimation.

A very precise estimation of scattered coincidences in a data set can be achieved through the use of a full Monte Carlo simulation [35, 36]. This will include an accurate modeling of the scanner geometry and shielding, as well as the detector parameters, which will have an impact on the collected events; an a priori knowledge of the patient activity distribution inside and outside the FOV; and the attenuation map. All these patient and scanner-specific requirements make the full Monte Carlo techniques computationally exorbitant and slow, and are currently difficult to implement in a clinical environment. However, it is an important option to consider when multiple scatter contributions to the images cannot be ignored.

2.7.4 Attenuation Correction

The linear attenuation coefficient of tissue at 511 keV is approximately 0.096 cm^{-1} for soft tissue while for bone it is 0.12 to 0.14 cm^{-1}. Hence, there is a relatively high probability for an annihilation photon to interact in patient tissues before reaching the surrounding PET detectors, mainly via Compton scattering or photoelectric absorption. The consequence of the interaction is that the intensity of true coincidences along a specific LOR is reduced or attenuated. The main challenge of attenuation correction (AC) lies in finding reliable attenuation-correction factors (ACFs) compensating for this loss before or during image reconstruction. If the loss of events along a LOR is not corrected for, the resulting image will have a distortion of the activity distribution, where the activity concentration in the center of the object will be underestimated. AC is by far the largest single correction in PET, and its importance is illustrated in Figure 2.23.

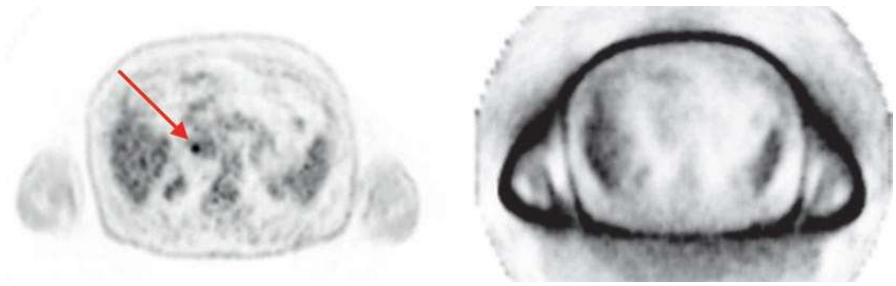

Figure 2.23: Importance of attenuation correction in PET: Shown are transverse images from a whole-body ^{18} FDG PET scan, with attenuation correction (left) and without attenuation correction (right). If uncorrected for, attenuation effects can impair lesion detectability, as highlighted by the red arrow (from [8]).

The amount of attenuation along a specific LOR depends on the total attenuation along the LOR. Consider a source located at a depth x inside an object of thickness D, which has a uniform attenuation coefficient, as shown in Figure 2.24. Both of the photons from an annihilation event in the source must be detected to record a valid

event. Assuming that they are emitted in the appropriate directions, the probability that both photons will reach the detector is given by the product of their individual probabilities

$$p_1 p_2 = e^{-\mu x} e^{-\mu(D-x)} = e^{-\mu D} \tag{2.9}$$

Thus, the amount of attenuation is independent of the location along the LOR of the source, and the amount of attenuation is only dependent on the total attenuation along the LOR. It can be shown that this is also true for a distributed source. If the attenuation is not uniform, the attenuation factor (μD) is replaced with a line integral of the attenuation coefficients along the LOR ($\int \mu(x)dx$).

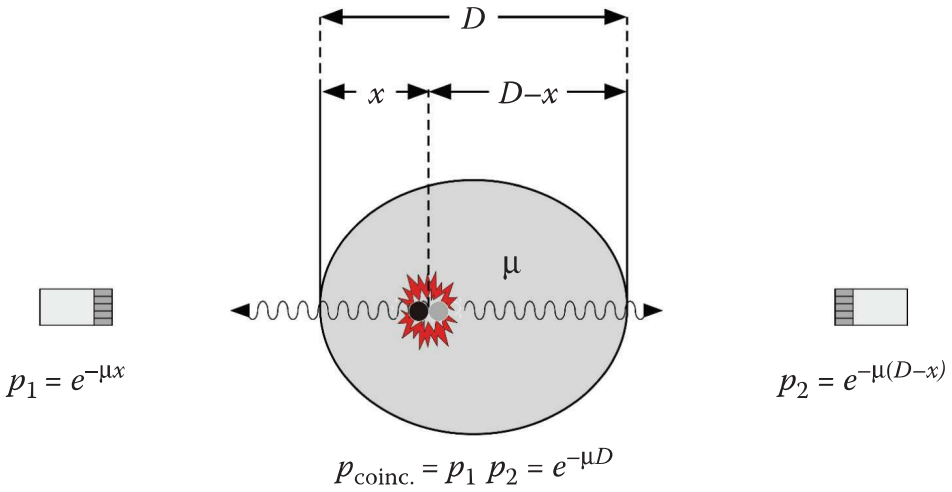

Figure 2.24: Illustration of attenuation in PET (from [7]).

ACFs are usually calculated from an attenuation map (μ-map) which represents the spatial distribution of linear attenuation coefficients of objects in the PET imaging FOV; hence, of the patient and equipment supporting or surrounding the patient. In many applications, accurate μ-maps (and hence, ACFs) can be challenging to obtain. Transmission measurements have been used to this end for a long time, using PET detectors in both coincidence mode (with positron-emitting sources such as ^{68}Ge/^{68}Ga [37]) and singles mode (with ^{64}Cu, ^{68}Ge/^{68}Ga, or gamma sources such as ^{137}Cs [38]). These approaches benefited particularly from the introduction of PET/CT, which uses an X-ray source and dedicated detectors for transmission measurements and is now considered the gold standard for AC.

However, even CT-based AC has its limitations, such as metal-induced or beam-hardening artifacts, or patient motion between CT and PET acquisitions. Furthermore, conversions from Hounsfield units measured using polychromatic X-radiation to linear attenuation coefficient for monochromatic radiation from radionuclides are mainly approximations [39]. But even accepting these limitations, one may find that CT is undesirable or unavailable mainly in two kinds of applications.

Examples of the first category are pediatric applications, in which radiation dose delivered to the patient is a major concern, and research applications, in particular those with serial PET scans. Here, a CT-based μ-map can in principle be acquired, but the subject would benefit from alternative approaches. Furthermore, motion-aware AC using only CT information is limited due to dose constraints.

PET/MRI is an important example of the second category, where the strong magnetic field prohibits the presence and use of state-of-the-art rotating X-ray tubes, hence rendering transmission-based AC challenging [40]. The situation is similar for low-cost PET scanners, where a CT may not be integrated by design.

If available, such as in PET/MRI, MRI-based AC is often the next best option; however, MRI-based μ-maps may still suffer from artifacts through patient motion, truncation of the MRI FOV, metal implants, and tissue misclassification (in particular, missing bone information) [41]. Hence, PET-AC methods other than CT- or MRI-based ones are still needed and researched [42].

2.7.5 Dead-time Correction

Like all radiation detectors, PET scanners suffer from dead-time effects at high count rates, which manifest themselves in two ways: pulse pileup effects that degrade data quality and can lead to a loss in image quality, and dead-time effects that lead to a loss in collected events. Pulse pileup effects arise when two or more single events occur close to each other both spatially and temporally so that the scintillation pulses overlap, leading to a miscalculation of the energy as well as interaction position. In some situations, the total measured energy will be above the energy window, leading to a rejection (loss) of the event, while in other situations, the image quality will be compromised due to a degraded energy, spatial, or timing resolution.

Since a PET image should provide a quantitative measure of the activity uptake within the patient, an accurate correction for dead-time effects needs to be performed. Pulse pileup effects can be reduced in PET scanners by using a fast scintillator and designing a PET detector with reduced light spread. In addition, dedicated electronics have been developed that make use of the signal shape to reduce the impact of pileup from events that occur close (temporally and spatially) to the event of interest [43]. A fast scintillator and data acquisition architecture with reduced processing times will also help reduce dead-time effects. Despite the hardware solution to reduce loss of counts at high rates, scanner dead-time calibration is required in order to have a linear scanner performance at all activity levels.

A standard technique used for dead-time calibration involves imaging a uniform activity–filled cylinder at a very high activity level (or count rate) and acquiring data as the activity decays. In this way, a lookup table can be derived based on the measured and expected coincidence rate as a function of singles rate in the scanner (similar to the plot shown in Figure 2.25). For a more accurate measure, the dead-time calibration table could also be generated for individual detector modules in the scanner instead of a single value for the whole system.

2.8 Time-of-flight

In theory, it is possible to determine the location of the emission point (x) along a line connecting the detector pair using the time-of-flight (TOF) information - the measured difference in arrival times of the two photons ($t_2 - t_1$) - as

$$x = \frac{c(t_2 - t_1)}{2} \tag{2.10}$$

where c is the speed of light and the origin (i.e., $x = 0$) is at the midpoint between the detector pairs. In conventional PET, the difference in arrival time is used to determine if two detected photons are inside the coincidence time window

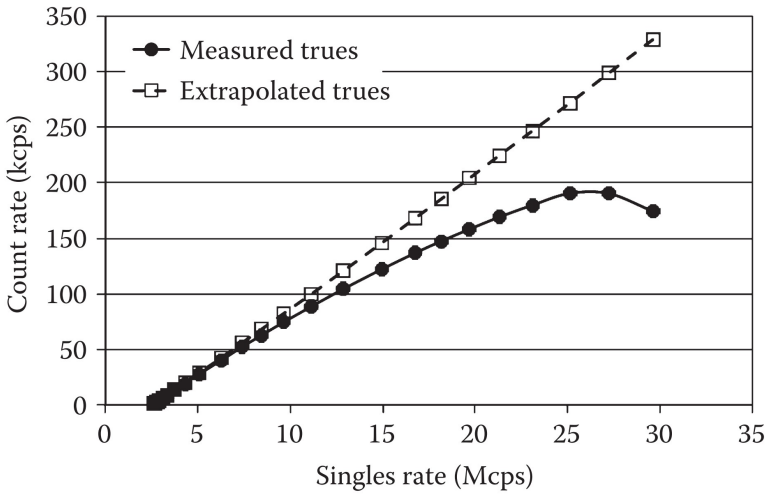

Figure 2.25: The true coincidence rate as a function of singles rate in the Philips Gemini TF PET/CT measured for a 27 cm diameter by 70 cm long line source cylinder. The extrapolated curve shows the rate expected from the sensitivity of the scanner. The measured trues coincidence rate at a high singles rate is lower than the extrapolated rate due to dead-time effects (from [7]).

and therefore belong to the same positron annihilation event, but is not measured precisely enough to localize the emission point along the LOR. TOF PET goes one step further, and uses a more precise time-of-flight difference measurement to better locate the annihilation position of the emitted positron (Figure 2.26).

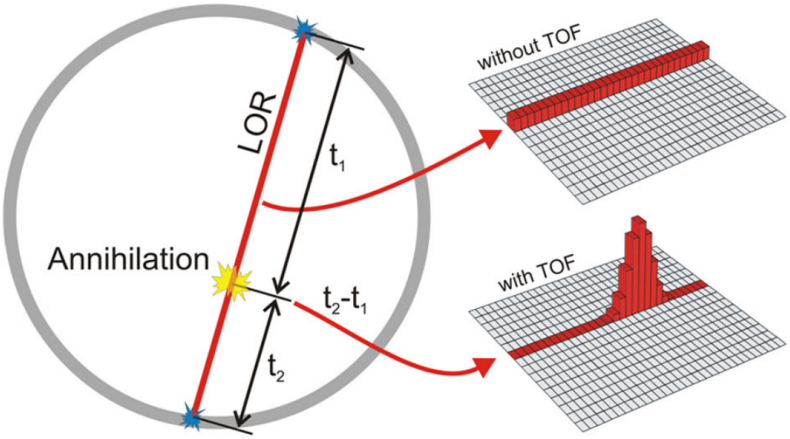

Figure 2.26: Principle of time-of-flight PET (the10ps-challenge.org).

The uncertainty in spatial localization, Δx, along the LOR is determined by the system coincidence timing resolution, Δt, and is given by

$$\Delta x = \frac{c\Delta t}{2} \tag{2.11}$$

If Δx is the same or smaller then the detector spatial resolution (around 3-5 mm for modern PET scanners) then in principle image reconstruction is not needed. To achieve 3 mm resolution along LOR, a time resolution of 20 ps would be required, which is an order of magnitude better than the time resolution achieved by the

current best clinical scanners, and hence image reconstruction is still necessary to produce tomographic images.

However, any spatial localization smaller than the imaged object with diameter D, leads to reduced noise correlations and improved image signal-to-noise ratio (SNR) [44]. TOF reconstruction can be seen as a "sensitivity amplifier", but it is difficult to quantify TOF gain into one factor as the gain depends on the measured distribution, the location within the object, and the count rate [45]. An often used estimate of the signal-to-noise gain [46] introduced by TOF reconstructions is

$$SNR_{TOF} \approx \sqrt{\frac{D}{\Delta x}} = \sqrt{\frac{2D}{c\Delta t}} \tag{2.12}$$

From this equation, it can be observed that the amount of reduction of noise does not depend only on the time resolution but also depends on the size of the imaged object. Large patients benefit more from TOF reconstruction. One of the characteristics of TOF reconstruction is that iterative reconstruction algorithms converge faster and more uniformly (less dependent on surrounding activity) compared to the nonTOF algorithms. Contrast recovery was observed to be better in TOF images [47], and an example of improved lesion detection is shown in Figure 2.27. TOF PET also has improved reproducibility at low count rates, as the uncertainty of the quantification gets considerably smaller with better time resolution [48].

In general, TOF also makes the reconstruction more robust and less prone to inconsistencies between emission data and corrections [22]. This applies to inconsistent normalization, absence of scatter correction, and mismatched attenuation correction (in PET/CT, often present in the case of respiratory motion). Examples of other benefits due to TOF information include the ability for joint estimation of activity and attenuation images up to a scale factor [49] and obtaining images without distortions or artifacts with limited-angle systems [50].

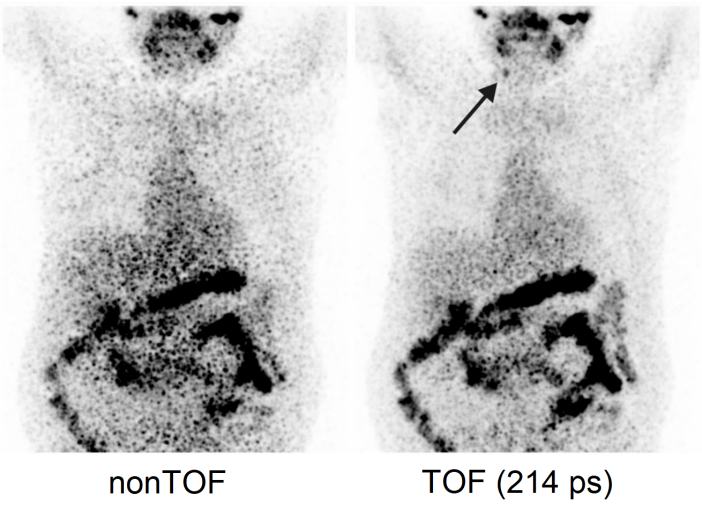

Figure 2.27: The improvement of image quality due to the incorporation of TOF information into the image reconstruction (OSEM). Maximum intensity projection PET images are shown of a patient injected with 37.9 MBq of ^{124}I and the image acquisition (4-min emission time per bed position) took place approximately 1 day after the application. The black arrow indicates an additional cervical lymph node metastasis detected when using TOF reconstruction (from [51]).

2.8.1 TOF PET with scintillation crystals

The first generation of TOF PET scanners developed in the 1980s used CsF or BaF_2 scintillators coupled to photomultiplier tubes and achieved TOF resolution of 400-600 ps [19]. The low stopping power and low light output of these scintillators led to limited system sensitivity as well as poor spatial and energy resolution. The arrival of higher light output and dense lutetium-based (Lu-based) scintillators in the 1990s subsequently led to the development of a second generation of TOF PET scanners in the mid-2000 s with much higher system sensitivity and improved spatial resolution, while achieving TOF resolution in the 450-600 ps range.

In the 2010s, all the major PET scanner manufacturers introducted SiPM based (digital) whole-body TOF PET systems (third generation TOF PET systems). In addition to providing improved intrinsic timing performance relative to the traditional PMTs, SiPMs also provide improved detector performance due to reduced or no signal multiplexing (average number of scintillation detectors per SiPM channel). The best current whole-body PET coincidence time resolution (CTR) is about 200 ps FWHM, achieved by the Siemens Biograph Vision scanner, which uses LSO based scintillation detectors [52].

The intrinsic limitations of scintillator timing are explored in tightly controlled laboratory setups, usually consisting of only two detectors in coincidence, and very small scintillator crystals, minimizing other contributions to the timing. Using a pair of LSO:Ce:Ca crystals coupled to SiPMs and using high-frequency electronics, a CTR of 58 ± 3 ps for $2 \times 2 \times 3$ mm^3 and 98 ± 3 ps for $2 \times 2 \times 20$ mm^3 was recently reported [53]. Note that this, presently the best CTR among the scintillation crystals, cannot be directly transferred into clinical PET systems as it uses unique readout electronics, with impractically high power consumption.

2.9 PET System Characteristics

A major goal of the PET studies is to obtain a good quality and detailed image of an object by the PET scanner, and so it depends on how well the scanner performs in image formation. Several parameters associated with the scanner are critical to good quality image formation, which include spatial resolution, sensitivity, noise, scattered radiation, and contrast. These parameters are interdependent, and if one parameter is improved, one or more of the others are compromised.

2.9.1 Spatial resolution

The spatial resolution of a PET scanner represents its ability to distinguish between two points after image reconstruction and thus determines the smallest structure that can be clearly visualized. It is typically described by the full width at half maximum (FWHM) and full width at tenth maximum (FWTM) values of the point-spread function (PSF) of a point source imaged in the tomograph. In ring geometry systems with scintillator crystal elements aligned along the radial direction, there are different sampling properties in different spatial directions and the resolution in PET is usually specified separately in transaxial (tangential and radial components) and axial directions. The spatial resolution of the PET system is determined by a combination of the physical effects of blurring caused by a combination of the physics of the positron emission and annihilation process, the detector response function, and the image reconstruction algorithm.

Detector response

For detectors with discrete or pixelated detector elements, the coincidence response function (CRF) is determined largely by the solid angle coverage of the pair of detector elements. As shown in Figure 2.28, the response profile at the midway point between the two detectors is a simple triangle function with a FWHM equal to half the detector width d. As the source moves closer to one of the detectors, the response profile changes to become trapezoidal and eventually rectangular.

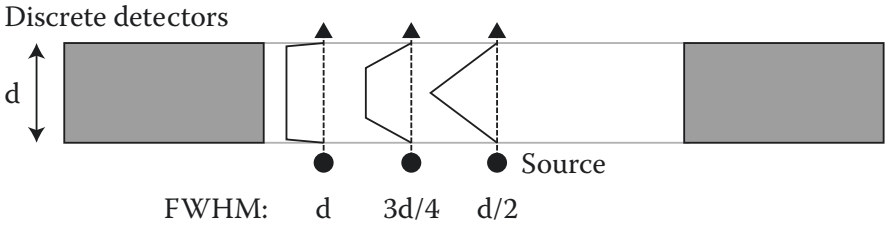

Figure 2.28: Sampling properties of two rectangular detectors for normal incidence photons. As the source moves closer to one of the detectors, the response profile changes from triangular to rectangular (from [7]).

Depth-of-Interaction Effect

A substantial thickness of scintillator material is required to efficiently stop a 511 keV annihilation photon. For photons originating from near the center of the field of view, the photons will be normally incident on the narrow surface of the detector elements, and thus are likely to interact in the detector element that they first pass through. In contrast, as the source of the photons is offset radially, the angle of incidence between the 511 keV photon and the detector surface can be quite large, so that the photon can penetrate through several detector elements before interacting. This process is shown in Figure 2.29, where for radial offsets, there is a marked uncertainty in the location of the positron annihilation event due to the radial elongation of the profile.

This effect is often termed parallax error or the depth-of-interaction (DOI) effect since it originates from the uncertainty in the location of the interaction along the length of the detector element. The DOI effect predominantly degrades the spatial resolution in the radial direction while having minimal impact on the tangential and axial resolutions, as shown in Figure 2.29.

Positron range

The positron emission process results in the positron being emitted from the nucleus with a nonzero kinetic energy, allowing the positron to travel some range prior to annihilating with an electron. The finite range of positron travel has a degrading effect on spatial resolution, because annihilation coincidence detection defines the line along which the annihilation event took place, which is not precisely the location from which the decaying radioactive nucleus emitted the positron. Figure 2.30 shows the positron range distribution for point sources of ^{18}F and ^{15}O which have different positron energy emission spectrum (Figure 2.4).

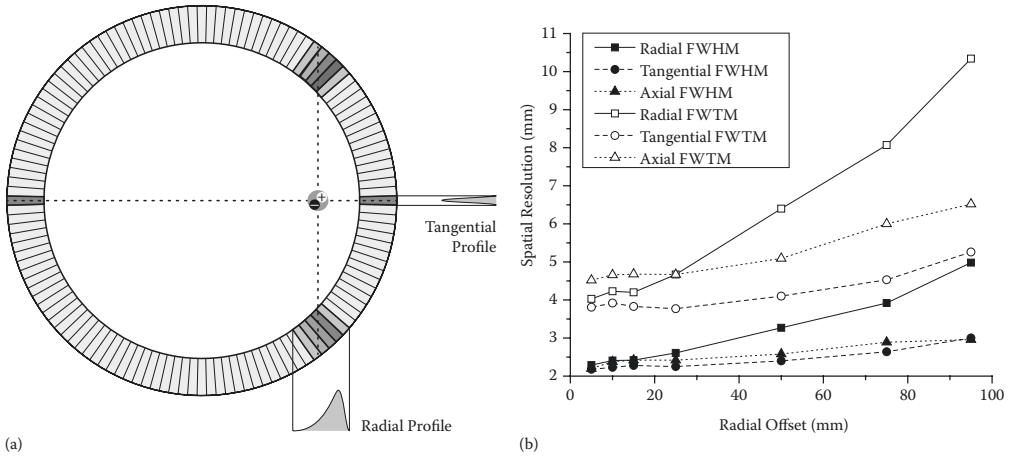

Figure 2.29: Parallax error in a PET scanner: (a) schematic diagram showing the different sampling properties of the PET system in the radial and tangential directions due to the penetration of photons into the detector elements before interacting. This penetration effect results in radial elongation of the response profile, degrading spatial resolution in the radial direction. (b) Dependence of the FWHM and FWTM spatial resolution on radial offset for the radial, tangential, and axial directions of the microPET P4 PET system (from [7]).

Positron range distributions shown have long tails and thus are not well described by Gaussian functions. Therefore the FWHM is not the best indicator of the effect of positron range on the PET system spatial resolution. Instead, the root mean square (RMS) effective range often is used. Figure 2.31 shows the general relationship between RMS effective range and maximum positron energy in water. Note that the positron range is inversely proportional to the density of the absorber, and RMS ranges would be higher in lung tissue (Figre 2.5) and lower in dense tissues such as bone.

Photon noncollinearity

At the time when a positron and electron annihilate, the center of mass of the system is not always at rest. As a result, in order to conserve energy and momentum, the two annihilation photons that are created are not traveling exactly 180° apart. This effect is known as photon noncollinearity, and results in a degradation in spatial resolution due to the uncertainty introduced in the location of the true LOR relative to the location of the LOR identified by the two detected photons (Figure 2.32). It is usually assumed that this noncollinearity of the two photons in PET (i.e., in water) has a FWHM of about 8 mrad or approximately 0.5° (Figure 2.33). Its effect on the PET spatial resolution has been parametrized by the empirical formula [54]

$$R_{180^\circ} = 0.0022D \tag{2.13}$$

where D is the ring diameter of the PET system. For a typical whole-body PET system diameter of 80 cm, the magnitude of this effect will thus be about 1.8 mm, while for a ring diameter of 15 cm, common in small animal PET systems, this effect will be 0.3 mm.

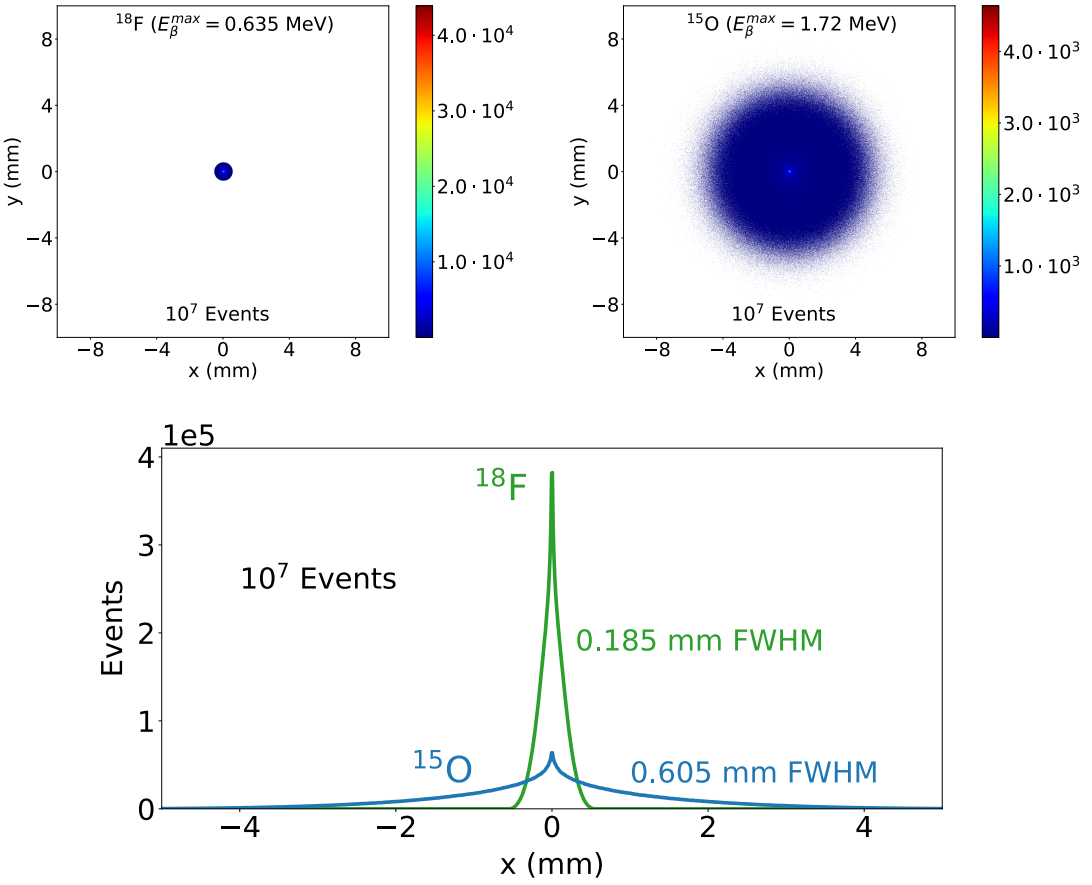

Figure 2.30: Results of Monte Carlo simulations (GATE) showing the distribution of annihilation coordinates for positron-emitting point sources in water for ^{18}F and ^{15}O. The histogram of x coordinates (100 bins/mm) shows a broader distribution for ^{15}O because of its higher average positron energy, which leads to a longer positron range prior to annihilation.

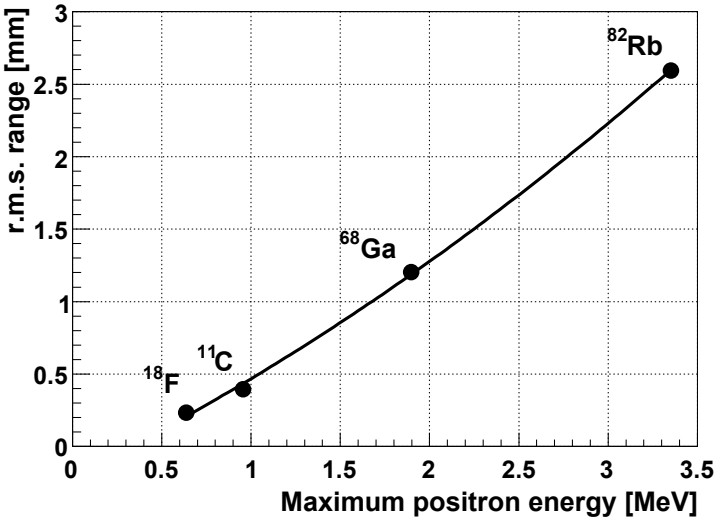

Figure 2.31: Maximum positron energy dependence of RMS effective range for positrons in water (Adapted from [13]).

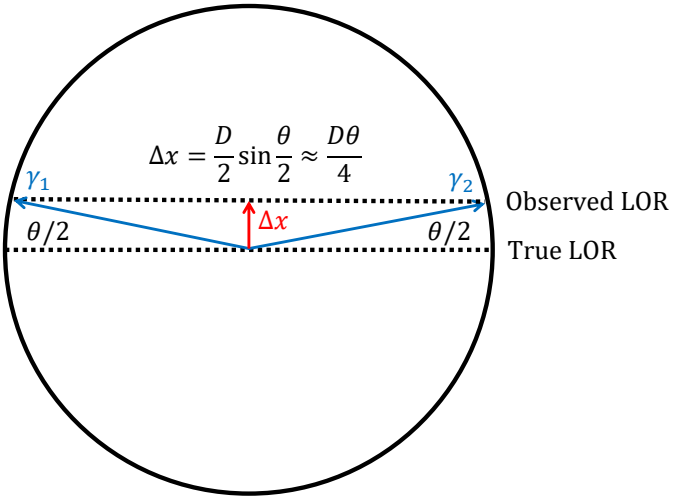

Figure 2.32: The effect of residual momentum of the electron and positron at annihilation resulting in the noncolinearity of annihilation photons. Two detectors in a ring with diameter D detect these photons in a straight line, which is slightly deviated (Δx) from the original annihilation line. Angles are exaggerated in this example for purposes of illustration. Actual range of angles is about $\pm 0.25°$, centered at 180°.

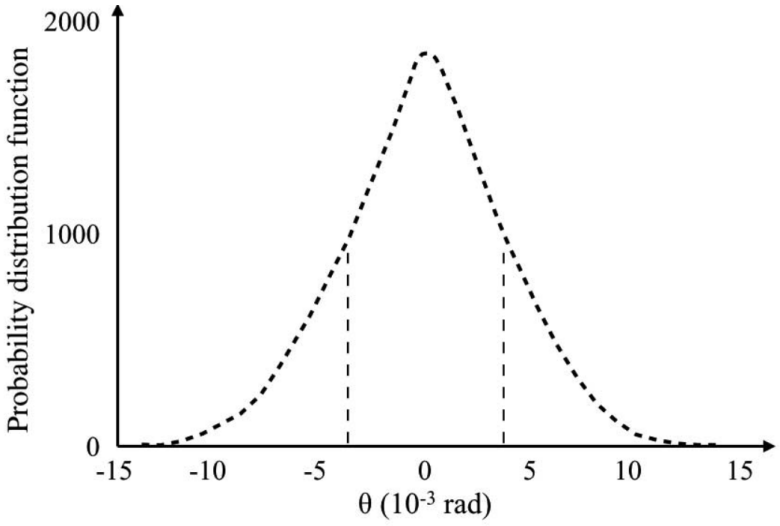

Figure 2.33: Distribution of the deviation of emission angles from 180° for the two gamma rays, following the annihilation in water at 4°C. The FWHM is about 8 mrad or approximately 0.5° [55].

System spatial resolution

The system or total resolution of a PET system is obtained by combining the individual resolution components. For simplicity, it is assumed that all contributions add in quadrature even though not all components are Gaussian in shape. The resulting spatial resolution R_{sys} can be summarized with the following formula

$$R_{sys} = k\sqrt{R_{det}^2 + R_{DOI}^2 + R_{e^+}^2 + R_{180^\circ}^2 + R_b^2} \tag{2.14}$$

where:

- R_{det} is the spatial resolution of the detector system, as determined by the size of the discrete detector elements or the intrinsic resolution of continuous detectors.
- R_{DOI} is radial elongation due to the depth-of-interaction (DOI) effect
- R_{e^+} is the positron range
- R_{180° is blurring caused by noncolinearity
- R_b is the block decoding error or block effect (in detectors that employ multiplexing, in which multiple detector elements are read out by a small number of electronic channels)
- k is a factor describing potential additional blur due to the nonuniform sampling of the LORs in the FOV and the image reconstruction process ($k \approx 1.25$ for reconstruction with filtered backprojection [20]).

Most modern PET systems achieve a reconstructed spatial resolution of 3-5 mm in each direction [3].

2.9.2 Sensitivity

The detection efficiency of a PET scanner, also commonly referred to as the sensitivity, is defined as the fraction of positron annihilation events that are detected in the scanner. Alternatively, it is also often defined as a number of counts per unit time detected by the device for each unit of activity present in a source and expressed in counts per second per microcurie (or megabecquerel) (cps/μCi or cps/MBq). Sensitivity is one of the most important considerations when building a PET system since the number of detected events has a direct impact on the final image quality due to the statistical nature (Poisson distribution) of the data. Signal-to-noise ratio (SNR) in the reconstructed PET image is, to first order, determined by the number of detected events, n:

$$SNR \propto \sqrt{n} \tag{2.15}$$

Low SNR negatively impacts the quantification of radiotracer activity in a region of interest (ROI) and can impair the detectability of small lesions and objects with low contrast.
The sensitivity, S, for a positron-emitting source located in an absorbing medium between a pair of coincidence detectors is given by

$$S = G\varepsilon_D^2 e^{-\mu D} \tag{2.16}$$

where G is the geometric efficiency of the system, ε_D is the intrinsic detector efficiency, μ is the linear attenuation coefficient of the material in which the source is located (e.g., tissue), and D is the thickness of the object. The detection efficiency is proportional to the square of the intrinsic detector efficiency due to the requirement of detecting two photons to form a coincident pair.

Geometric efficiency

Geometric efficiency, G, refers to the solid angle coverage of the PET detector system and is the largest single factor affecting the detection efficiency of the PET system. The geometric efficiency will be at a maximum for a point source located at the center of the PET system. For this special case, the geometric efficiency, G_{max}, is

$$G_{max} = \frac{l}{2\sqrt{R^2 + (l/2)^2}} \tag{2.17}$$

where l is the axial length and R is the ring diameter of the PET system. Geometric efficiency does not change significantly as a function of radial offset of the point source due to the cylindrical geometry of the PET detector ring. On the other hand, it decreases linearly in the axial direction reaching a value of zero at the edge of the axial FOV (Figure 2.34).

The above calculation for G_{max} assumed that all possible detector ring combinations are used in collecting the data. However, in practice the axial acceptance angle can be limited by specifying a maximum ring difference (MRD) between detector rings that can create a coincidence event. Using a MRD that is less than the largest value possible, MRD_{max}, will result in a geometric efficiency that has a trapezoidal shape rather than a triangular shape (Figure 2.34). To a first order, the maximum value of the geometric efficiency in this case, G'_{max}, is

$$G'_{max} = G_{max}\frac{MRD}{MRD_{max}} \tag{2.18}$$

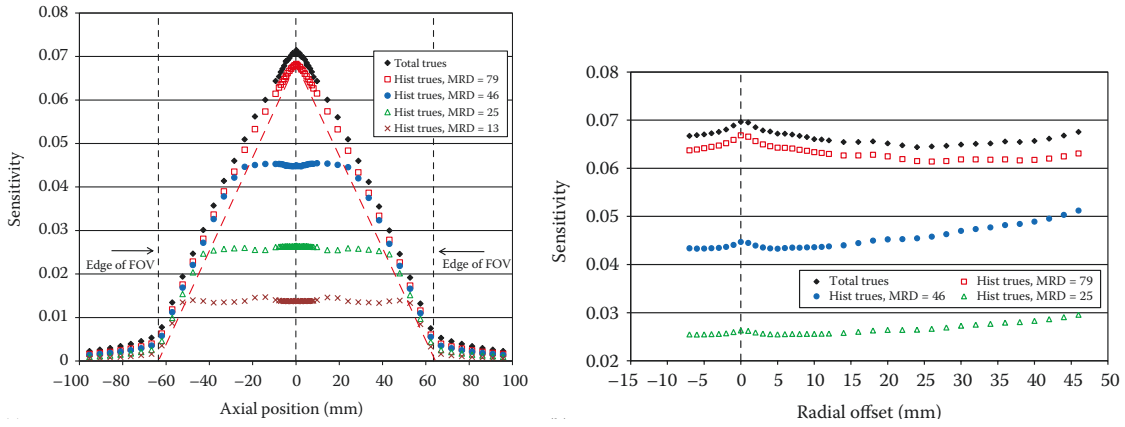

Figure 2.34: Sensitivity images for the Siemens Inveon small-animal PET system. (Left) Axial sensitivity at the radial center for various MRDs. The maximum detection efficiency for this 80-ring PET system is for MRD = 79, and as the MRD is limited, there is a corresponding drop in detection efficiency. (Right) Radial sensitivity profiles for the middle plane with different MRDs.

Detector efficiency

The detector efficiency, ε_D, depends primarily on the stopping power of the detector material and its thickness. The detector efficiency is given by

$$\varepsilon_D = \varepsilon_{int}\varepsilon_{ff}\varepsilon_E \tag{2.19}$$

where:

- ε_{int} is the intrinsic efficiency of a detector - a measure of the probability that a 511 keV photon interacts in the detector - is given by

$$\varepsilon_{int} = 1 - e^{-\mu_d x} \tag{2.20}$$

  where μ_d is the linear attenuation coefficient of the detector material and x is the detector thickness.

- ε_{ff} is the fill factor of the detector, which will be 1 for continuous detector materials and less than 1 for pixelated detectors with dead space between detector elements due to reflector materials.

- ε_E accounts for an energy cutoff or window applied to the detected events. In order to reject scattered events, a common practice in clinical PET is to set an energy window that corresponds to the photopeak region of the energy spectrum. In this case, ε_E can be approximated by the photoelectric fraction of the detector material, PE, given by

$$PE = \frac{\sigma_P}{\sigma_P + \sigma_C} \tag{2.21}$$

  where σ_P is the photoelectric interaction cross section at 511 keV and σ_C is the Compton interaction cross section at 511 keV.

2.9.3 Energy Resolution

Energy resolution refers to the uncertainty or variability in the observed signal from a detector when irradiated with monoenergetic photons. This variability is the result of statistical variations in the production of the signal, and for a given system, there are several contributing factors to this. For instance, in a scintillation detector system, there are statistical variations in the number of produced scintillation photons following a gamma interaction. In addition, there are statistical variations in the number of photoelectrons produced in the photo-detector and variations in the multiplication factor of the photo-detector. Assuming that the formation of each photoelectron is a Poisson process, the energy resolution of a detector is proportional to the square root of the number of produced photoelectrons (N):

$$\frac{\Delta E}{E} \propto \frac{1}{\sqrt{N}} \tag{2.22}$$

In order for the detector to efficiently discriminate scattered photons from primary photons, the energy resolution of the detector should be as high as possible. Current clinical whole-body PET scanners using LSO/LYSO scintillators typically have 10-12 % energy resolution at 511 keV. Due to the finite value of the detector energy resolution, it is not possible to set a fine energy threshold at 511 keV, but a wider energy window must be set (Figure 2.35).

In an ideal detector with perfect energy resolution, photopeak could be separated from the Compton distribution. However, because of the energy resolution, the two interaction distributions blend into each other. By changing the width of the energy window, we can impact the number of detected primary (non-scattered) and scattered annihilation photons. The importance of energy resolution is less significant for small animal PET where object scatter from the animal is small relative to that observed in clinical whole-body imaging.

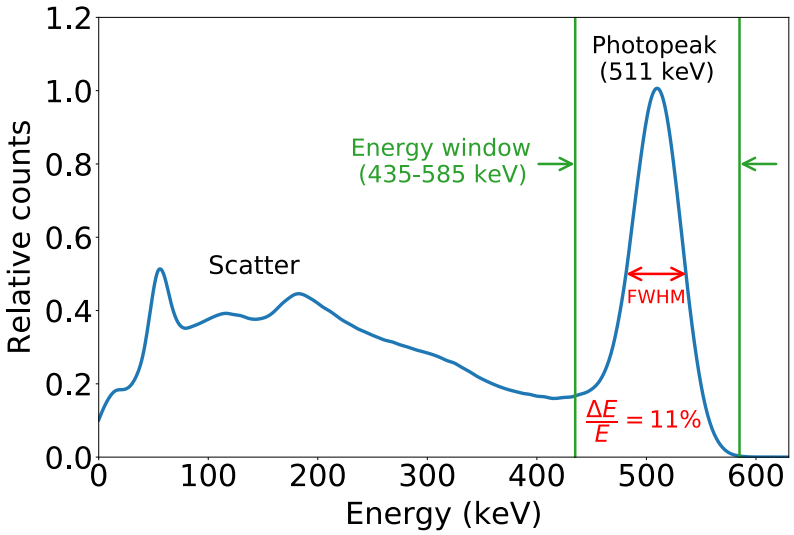

Figure 2.35: Example of a PET scanner energy spectrum.

Scatter fraction

The scatter fraction (SF) is one of the parameters that is often used to compare the performances of different PET scanners, as it indicates the relative weight of the effect of scattered events on the reconstructed image. It is determined from the true (T) and scatter counts (S) as

$$\mathrm{SF} = \frac{S}{T+S} \tag{2.23}$$

The fraction of scattered events is dependent on object size, density, acceptance angle, energy discriminator settings, activity distribution, etc., and is typically in the range 20-50 %.

2.9.4 Noise equivalent count rate (NECR)

The correction of the total or prompt coincidence count rate for random and scattered coincidences adds noise to the net true coincidence count rate. The magnitude of the noise increase depends on several factors including activity in the FOV, count rates, and the scatter environment. In a low scatter situation and at low count rates, where the random count rate is expected to be low, the noise increase should be minimal. On the other hand, if the scatter and the randoms rates are high, then the noise contamination can be substantial.

The noise equivalent count rate (NECR) is a metric used to describe this increase in noise due to the randoms and scatter corrections applied to the total coincidence count rate. The NECR is defined as

$$NECR = \frac{T^2}{T+S+kR} \tag{2.24}$$

where T is the true count rate, S is the scatter count rate, R is the randoms or randoms count rate, and k is either 1 or 2, depending on how the randoms are estimated (i.e., 1 for estimation from singles and 2 from delayed coincidence measurement).

It has been demonstrated that the NECR is roughly proportional to the square of the signal-to-noise ratio of the reconstructed activity values when the object is a cylinder with a uniform activity concentration [56]:

$$NECR \propto SNR^2 \tag{2.25}$$

Thanks to this relation, NECR is a frequent metric used to compare the performance of PET systems as it characterizes the global SNR and acts as a surrogate for system-level image quality. Since both the scatter and random coincidences depend on the source distribution, these comparisons are only meaningful under highly standardized imaging conditions.

Figure 2.36 shows typical NECR curves for a particular PET scanner and phantom. At higher activities, the NECR actually decreases because the rate of random coincidences increases as roughly the square of the activity, and dead-time losses also reduce the observed counting rate. Often the peak NECR rate, and the activity concentration at which it is achieved, is reported. However, the values strongly depend on the size of the object that is imaged, and other factors such as the energy and timing windows, and the activity distribution within the phantom. Nonetheless, assuming the phantom used to acquire the NECR data is a reasonable approximation of the object that is to be imaged in a particular clinical or research task, the NECR provides a helpful guide for estimating the activity concentrations that provide the images with the highest SNR. In some cases, it may not be possible to reach this activity concentration because of radiation dosimetry considerations.

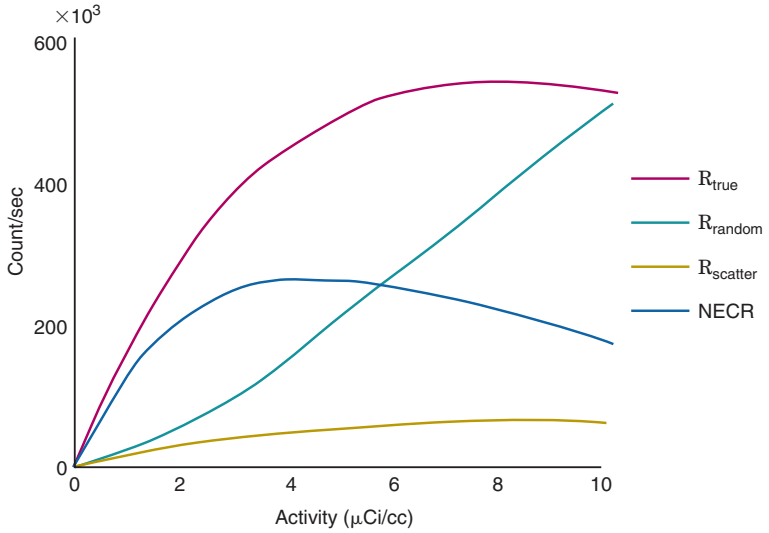

Figure 2.36: Example of various coincidence counting rates and noise equivalent counting rate (NECR) for a clinical whole-body scanner. These data predict that for the phantom used in this study, the best signal-to-noise (corresponding to the peak of the NECR curve) in the reconstructed image would be achieved with an activity concentration of about 4 μCi/cm^3 (from [13]).

The standard NECR calculation does not take into account the TOF information and the resulting sensitivity gain. By combining the equations 2.12 and 2.25 the effective (TOF-modified) noise equivalent count rate ($NECR_{TOF}$) can be expressed as

$$NECR_{TOF} = \frac{D}{\Delta x} NECR = \frac{2D}{c\Delta t} NECR \tag{2.26}$$

In Table 2.3, the estimated TOF NECR gain is reported as a function of the coincidence time resolution, given an object (patient) size equivalent to a 30 cm diameter (D) cylinder. It shows the large potential of TOF measurement as a sensitivity amplifier.

Table 2.3: Coincidence time resolution, spatial uncertainty and estimated TOF NECR gain for a 30 cm diameter uniform cylinder.

CTR (ps)	Δx (cm)	$NECR_{TOF}/NECR$
400	6.0	5
200	3.0	10
100	1.5	20
50	0.75	40

2.10 Image Reconstruction

The goal of PET image reconstruction is to form images of radiotracer distribution in an object, using the coincidence events detected by a scanner. Image reconstruction can be performed either as a series of two-dimensional (2D) reconstructions or in a fully three-dimensional (3D) manner. In 2D image reconstruction, data are first separated into a stack of 2D datasets, each of which corresponds to a single image slice. These 2D datasets are then reconstructed slice by slice to form a set of 2D images that are stacked to form the final 3D image. In 3D image reconstruction, all data are used together to directly form a 3D image.

Image reconstruction algorithms can be classified into two main groups: analytical and statistical or model-based reconstruction. Analytical approaches are based on inverting the mathematical relationships between a function and its line integrals or projections. While analytic reconstruction methods, in particular the most widely used filtered backprojection algorithm, are fast and easy to implement, the reconstruction accuracy is limited by several factors. First, analytic image reconstruction cannot model the degrading factors in a PET scanner, such as intercrystal scatter, positron range and noncollinearity. Second, these methods do not account for the stochastic variability in photon detection.

2.10.1 Model-Based Statistical Reconstruction

Statistical approaches use computational models of the physical and statistical aspects of the data acquisition process, possibly also incorporating prior information about the radiotracer biodistribution, to arrive at an image that best explains the data. As a result of these physical and statistical models, images reconstructed using model-based statistical methods have less noise and higher resolution compared to analytic reconstruction methods. All recent commercial PET scanners have model-based statistical reconstruction packages, and most clinics have switched to them for their routine clinical applications.

Model-based statistical image reconstruction methods consist of the following five elements:

1. **Basis function selection:** The continuous image is represented as a linear combination of basis functions; in most cases the voxel, which represents tracer uptake over a small cubic volume of tissue. This allows for a discrete representation of the image as a vector of basis function coefficients.

2. **System model:** The system model relates the image to the data. The spatial resolution of PET is limited by several factors such as positron range, photon noncollinearity, and penetration and scattering of the photon in the detector. One critical limitation of analytic reconstruction methods is that these factors are neglected in the simple line integral model. With model-based statistical reconstruction, we use a system model to account for these resolution-deteriorating effects. Other factors may also be included in the system model such as the attenuation of the photons in the body, nonuniform efficiencies of the detectors, and random and scattered events. In the absence of noise, the mean measured counts ($\overline{y}_i$) by the detector pairs i in PET can be expressed as a linear function of the image, as represented by the coefficients x_j of the selected basis function:

$$\overline{y}_i = \sum_{j=1}^{N} p_{ij} x_j + \overline{r}_i \tag{2.27}$$

   where p_{ij} are the elements of the system matrix P containing the probabilities that events originating in voxel j (from N possible image voxels) are detected by detectors forming the ith LOR, and $\overline{r}_i$ denotes the sum of the expected number of random and scattered events. This relationship can be expressed in matrix-vector format as $\overline{y} = Px + \overline{r}$. System modeling involves the computation of the matrix P that accurately represents data acquisition by the scanner. One approach to system modeling in PET is the factored system matrix model

$$P = P_{norm} P_{blur} P_{attn} P_{geom} P_{range} \tag{2.28}$$

   where P_{range} models blurring due to positron range in image space; P_{geom} is the geometric probability matrix that depends on the solid angles subtended by each voxel at the detector pairs involved in each LOR; P_{attn} is a diagonal matrix containing the attenuation factors; P_{blur} models the blurring in sinogram space due to photon pair noncollinearity, intercrystal penetration, and scattering; and P_{norm} is a diagonal matrix containing calibration and detector sensitivity normalization factors. These matrices are computed through some combination of geometric calculation, Monte Carlo modeling, and experimental detector response measurement.

3. **Noise model:** PET data is inherently noisy and the noise model describes how measured data deviate from their expected value through the data probability distribution. The number of events detected at a detector within a given

time due to the radioactive decay inside the object can be accurately modeled by the Poisson distribution:

$$P(n|\lambda) = \frac{e^{-\lambda}\lambda^n}{n!} \tag{2.29}$$

where n is the number of decays, and λ is the mean, which is equal to the variance. Most statistical reconstruction methods use this Poisson noise model. For data precorrected for physical effects such as dead time, attenuation, scatter, and randoms, the Poisson nature of the data may be lost, and other noise models may be more appropriate (e.g., Gaussian). The use of an accurate noise model can lead to an improved trade-off between resolution and SNR, as well as more accurate quantitation in reconstructed images.

4. **Objective function:** System and noise models are combined to determine the likelihood of observing measured data for a given image. The objective function to be optimized is then a combination (i.e., weighted sum) of the data likelihood and penalty terms that are designed to penalize structure in the reconstructed images that deviates from our prior knowledge about the tracer distribution, for example, images that have negative intensity, are not piecewise smooth, or differ greatly from corresponding anatomical images. Regularization through the introduction of these penalty terms tends to make the reconstruction problem better conditioned; in other words, the reconstructed images are less sensitive to noise in the data and avoid noise amplification problems that can occur in methods based only on the maximization of the data likelihood.

5. **Numerical optimizer:** The numerical optimizer is a mathematical optimization algorithm that computes the reconstructed image that maximizes the objective function.

Maximum Likelihood - Expectation Maximization

Maximum likelihood (ML) is a widely used statistical estimation method and has been applied to PET image reconstruction. The likelihood function of the data is the probability of observing the data given the image. The log-likelihood function under the Poisson noise model is given by

$$L(x) = \sum_{i=1}^{M} y_i \log \overline{y}_i(x) - \overline{y}_i(x) \tag{2.30}$$

where M denotes the total number of LORs. Maximizing the logarithm of the likelihood is equivalent to maximizing the likelihood because the logarithm is a monotonically increasing, one-to-one function. There are many numerical algorithms that can be used to find the ML estimate of the image, such as coordinate ascent or gradient-based methods. One of the earliest approaches used for ML PET image reconstruction is the expectation–maximization (EM) algorithm [57]. EM is a general framework to compute the ML solution through the use of "complete" but unobservable data and is composed of two steps. The first step, called the E-step, involves the calculation of the conditional expectation of the complete data, and the second step, called the M-step, maximizes this conditional expectation with respect

to the image. In PET, a very common choice for complete data, is the number of events detected by the ith LOR that are emitted from the jth voxel. Shepp and Vardi first applied EM to emission image reconstruction [58]. When the ML-EM algorithm is applied to PET image reconstruction, it leads to the simple iterative equation

$$x_j^{k+1} = \frac{x_j^k}{\sum_{i'} p_{i'j}} \sum_i p_{ij} \frac{y_i}{\sum_{j'} p_{ij'} x_{j'}^k} \tag{2.31}$$

where x_j^{k+1} is next estimate of voxel j based on the current estimate x_j^k. The flow diagram of the ML-EM algorithm is shown in Figure 2.37.

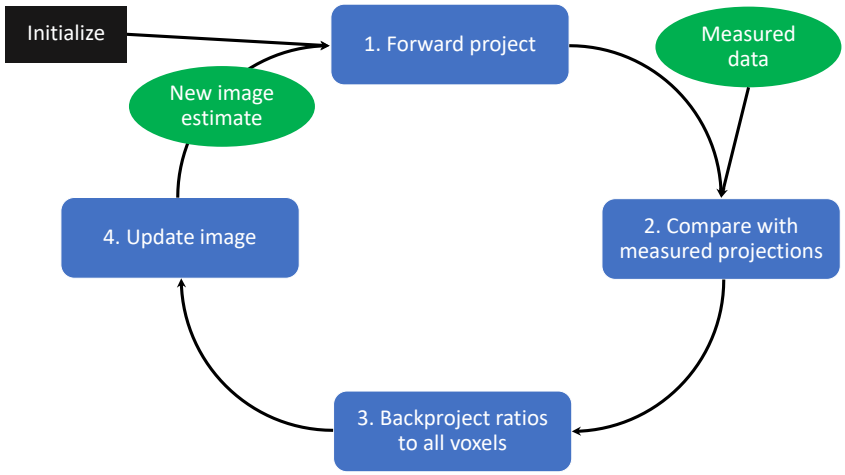

Figure 2.37: Flow diagram of maximum-likelihood expectation-maximization algorithm. Starting from the initialization in the upper left, the algorithm iteratively updates the image estimate and is stopped after reaching a preselected iteration.

The EM algorithm is usually initialized using a uniform image. A new image is then calculated using Eq. 2.31. This process is repeated until an acceptable solution is reached (in the order of 30–100 iterations with typical PET data [59]). The TOF information can be used not only to improve the quality of the reconstructed image but also to speed up the convergence of the ML-EM algorithm (2.38).

To reduce the noise in the reconstructed image, the algorithm is usually stopped early (before convergence) and a smoothing filter is applied afterward. Considering that ML-EM requires one forward projection and one backprojection at each iteration, it is significantly more time consuming than, e.g., the filtered backprojection approach, but usually leads to a more accurate reconstruction.

Ordered Subsets Expectation Maximization

Ordered Subsets Expectation Maximization (OSEM) was introduced in 1994 [60] to reduce the reconstruction time of conventional ML-EM. The OSEM algorithm partitions the projection data into subsets (typically mutually exclusive) and uses only one subset of data for each update. In early iterations, OSEM can speed up the reconstruction by approximately a factor equal to the number of subsets. As a result, OSEM reconstruction times became practical for clinical applications, leading to its rapid adoption for use in clinical PET and SPECT.

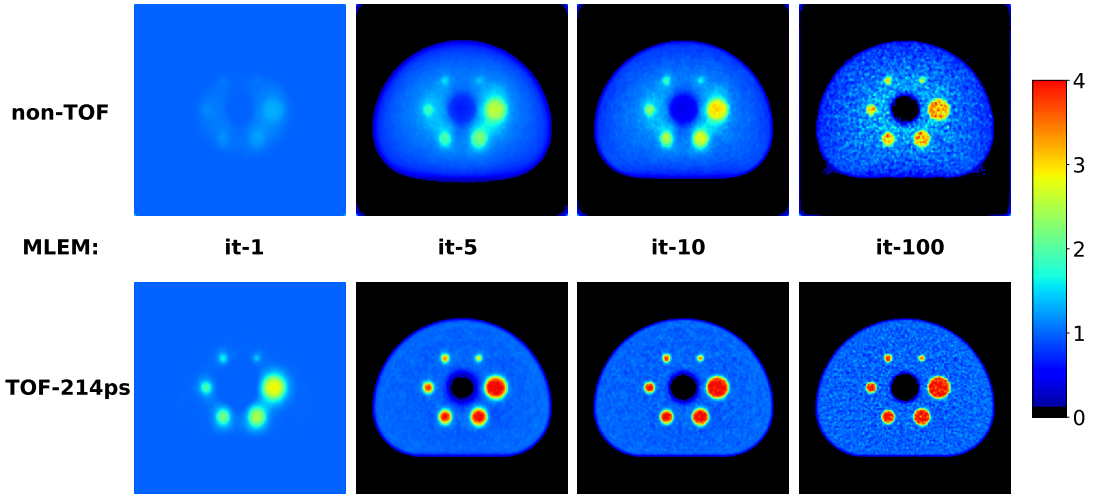

Figure 2.38: Reconstructed images of a phantom using MLEM with and without TOF information for different iteration numbers. A faster convergence and better contrast recovery can be observed in the TOF images.

The speedup of OSEM is due to the fact that far away from the solution, the approximate gradient of the likelihood computed from a subset of the data provides a reasonable search direction for increasing the log-likelihood (the EM algorithm can be recast in terms of the gradient of the log-likelihood with respect to the image). However, as we get closer to the maximum, the error in the gradient due to the use of only subsets of the data can cause the image to enter a limit cycle. This is illustrated in Figure 2.39.

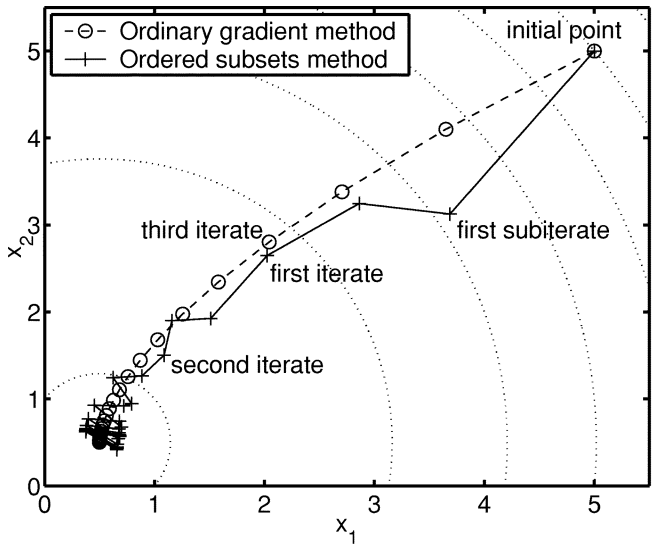

Figure 2.39: Simple 2D example of the ordered subset method showing the trajectory from initialization toward the maximizer of the objective function. Note the fast initial convergence of the ordered subset method, but eventual limit cycle behavior (from [61]).

Original paper [60] recommended "subset balance"; that is, the subsets should be chosen such that the detection probability of each voxel is equal for each subset. In practice, subset balance is difficult to achieve due to differences in sensitivity and attenuation. Typically, the projections in each subset are chosen with maximum angular separation to avoid directional artifacts. With consistent data and under the condition of subset balance, OSEM can be shown to converge to the ML solution [60]. However, in general, data are not consistent due to noise, and OSEM is not convergent [61], as illustrated in Figure 2.39.

One way to ensure OSEM converges is to gradually reduce the number of subsets to one as iterations proceed. Alternatively, one can use OSEM in the early iterations and switch to an alternative convergent algorithm to ensure convergence. Despite convergence issues, the original OSEM algorithm remains the most widely used algorithm for ML reconstruction in clinical PET and SPECT [7].

2.11 State-of-the-art in PET technology

Since the early years, PET systems have been improved steadily with regard to sensitivity and spatial resolution by optimising the detectors and geometry [62]. After the integration of PET with CT, time-of-flight technology has been introduced in clinical PET systems. The trend towards fully 3D acquisitions and longer axial FOV started even before the clinical introduction of PET/CT and TOF. Most recent clinical systems have an axial extent of 15–30 cm, work in fully 3D mode and have a timing resolution in the range of 200–400 ps [19].

Spatial resolution has been improved by using smaller detector pixels and reducing the light spread toward the photodetector. The switch from large conventional photomultiplier tubes to small solid state silicon photomultipliers (SiPMs) has been the latest step in this development [63]. Some of the most recent systems even have one-to-one coupling of scintillator pixels to SiPM pixels.

A system with good spatial resolution is not sufficient; it needs to be combined with sufficient sensitivity. High sensitivity directly impacts the obtained SNR per voxel, which can be increased by a higher number of detected counts. Compared to the first PET systems, the sensitivity of current systems has been increased by 3 major factors:

1. The use of thick detectors (20-30 mm) with higher detection efficiency (first for BGO, but also more recently L(Y)SO)
2. The removal of axial septa: systems have evolved from 2D to 3D with limited acceptance angles and finally to fully 3D systems
3. Increasing the axial length of the system

Besides increasing the number of detected photon pairs, the information content per photon pair has also been improved, and thus the effective sensitivity of the system, by introducing TOF measurements (Section 2.8). The major improvements in PET system design are shown in Figure 2.40.

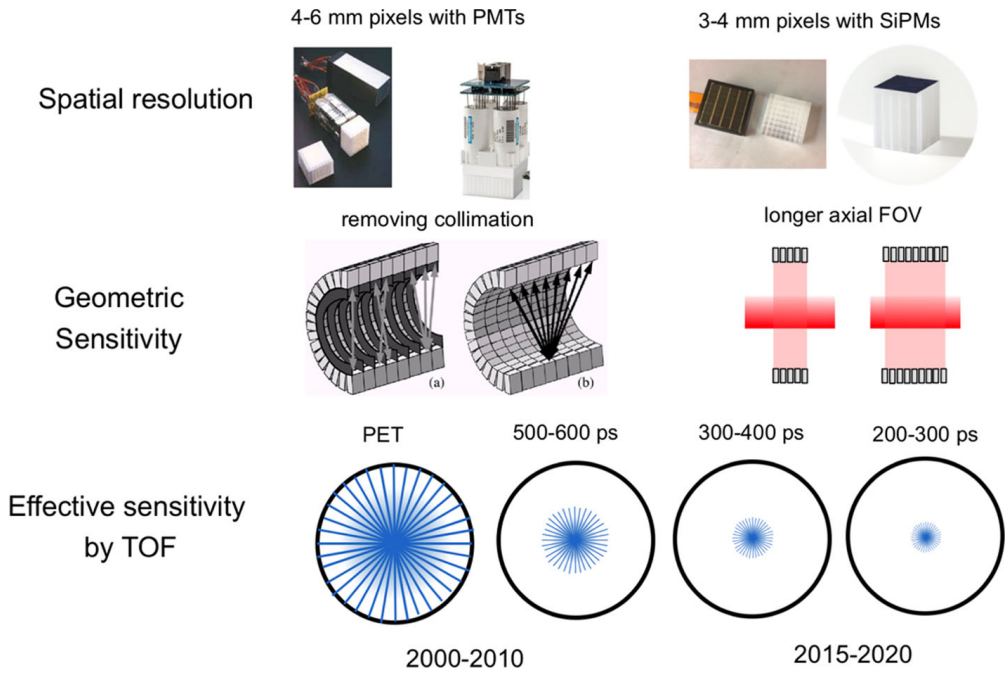

Figure 2.40: The three major improvements in PET technology during the last three decades (from [64]).

Using a conventional PET scanner with an axial FOV of about 20 cm, a whole-body scan is acquired by moving the patient bed through the gantry (Figure 2.41). These scans are obtained by acquiring the data in step-and-shoot mode (with some overlap in the axial direction in order to improve the uniformity of axial sensitivity) or with continuous bed movement. In step-and-shoot mode, one bed position takes about 1–3 min, the data from the different axial positions (or the continuous movement) are stitched together, and body scans are acquired in 10-30 min.

An obvious limitation of the current whole-body PET scanner is that roughly 85%-90% of the body is outside the FOV of the scanner, and no signal from these regions of the body is collected. Second, even for the tissues and organs within the scanner FOV, no more than about 3%-5% of the available signal (photon pairs that escape the body without being attenuated or scattered) can be collected, because the radiation is emitted isotopically, and most does not intercept the detector rings. Both factors are addressed by extending the detector rings, and if the detectors cover the entire body, it is also refered to as total-body PET [4].

2.11.1 Long axial field of view PET scanners

The idea of a very sensitive positron emission tomography (PET) system covering a large portion of the body of a patient already dates back to the early 1990s. In the period 2000–2010, only some prototypes with long axial field of view (LAFOV) have been built, which never resulted in systems used for clinical research. One of the reasons was the limitations in the available detector technology, which did not yet have sufficient energy resolution, timing resolution, or count rate capabilities for fully exploiting the benefits of a LAFOV design. PET was also not yet as widespread as it is today: the growth in oncology, which has become the major application of PET, appeared only after the introduction of PET-CT (early 2000).

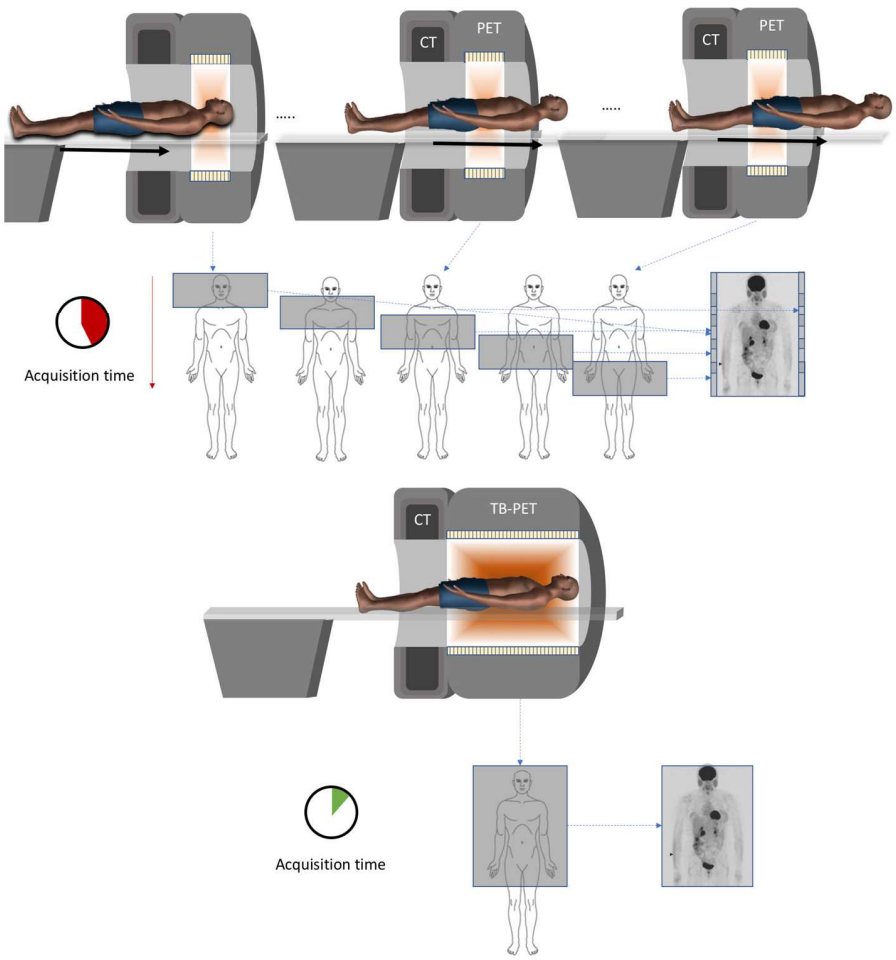

Figure 2.41: The difference between a current PET-CT (top figure) and a total body PET-CT (bottom figure). Different bed positions to complete a body scan are not required anymore (from [64]).

The first total-body PET/CT scanner with a total AFOV length of 194 cm (Figure 2.42), called uEXPLORER [65], was developed through collaboration between UC Davis and United Imaging Healthcare as part of the EXPLORER Consortium. The detector is composed of $2.76 \times 2.76 \times 19.1$ mm^3 LYSO pixels, and the whole system became operational in mid-2018. The direct benefits of long axial FOV systems are mostly related to the higher sensitivity. For single organ imaging, the gain is close to the point source sensitivity, which increases linearly with the axial length until it is limited by solid angle and attenuation of the body. The gains for a single organ (compared to a fully 3D PET 20-cm axial FOV) are limited to a factor $3-4\times$. But for long objects (like body scans), it increases quadratically with scanner length, and factors of $10-40\times$ higher sensitivity are predicted for the long axial FOV scanner. The rationale behind high sensitivity total-body scanners is that they can image better, faster, later after injection, or with lower dose; and that such a device can generate total-body dynamic images with high temporal resolution [4, 66], and the first patient studies show promising results [67, 68].

The major hurdle for spreading this technology in clinical centers is the much higher cost of such scanners. The cost is directly linked to the axial length of the scanner and it was shown, that for body imaging, quite large gains ($9 - 10\times$) can already be obtained using scanners with an axial length of 70 cm, and this length is already optimal for organ-specific imaging like brain scanning [64]. Siemens has recently released a LAFOV scanner with an intermediate length (106 cm long FOV) called Biograph Vision Quadra (Figure 2.42). Total-body and LOFOV imaging is still in its infancy, and many opportunities and challenges still need to be researched. Ultimately, the cost-to-benefit ratio will determine how well this technology will spread to clinical centers and whether its use will be broad or limited.

Figure 2.42: Left: uEXPLORER total-body PET/CT scanner. Right: Siemens Biograph Vision Quadra

3. Cherenkov PET

3.1 Cherenkov radiation

Cherenkov radiation is prompt bluish-white light (Figure 3.1) emitted when a charged particle passes in a dielectric medium with a velocity greater than the phase velocity of light in that medium. As the charged particle moves through the medium, the associated electromagnetic field close to the particle polarizes the medium along its track so that the electrons attached to the atoms follow the pulse waveform as the particle goes by. It is important to note that in this process, the atoms are neither excited nor are the electrons removed from their bound states (ionization). There is indeed additional ionization when the impacts are sufficiently close. Still, the process we are concerned about here arises from only tiny displacements by a vast number of electrons. In the general case, the radiation from these displaced electrons, which return immediately to their normal positions after the particle has passed, is not observed, owing to destructive interference (Figure 3.2). If, however, the velocity of the particle in the medium is faster than the phase velocity of light in the medium, the wavelets from all portions of the track are in phase with one another on a wavefront inclined to the direction of the track, and a coherent radiation is then observed [12]. These photons are referred to as Cherenkov radiation, in honor of the Russian physicist Pavel A. Cherenkov for his basic research and discovery of the properties of this unique radiation [69, 70].

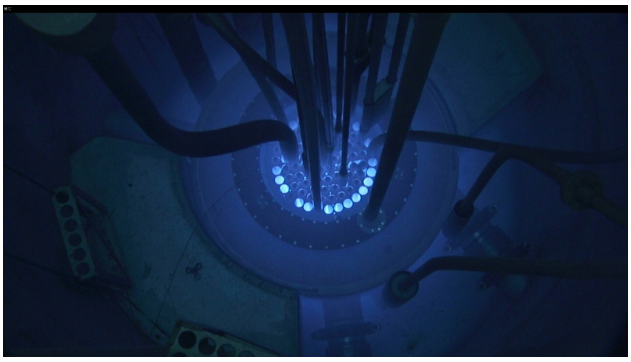

Figure 3.1: Cherenkov radiation (bluish-white glow) produced in the water surrounding the core of a nuclear reactors (https://ric.ijs.si/).

The Cherenkov radiation is emitted on a cone around the charged particle direction (Figure 3.2). The characteristic emission angle θ depends on the velocity of the particle $\beta = v/c$ (with c being the speed of light in vacuum) and the refractive index of the medium n (which depends on the frequency of light ω), through the Cherenkov relation

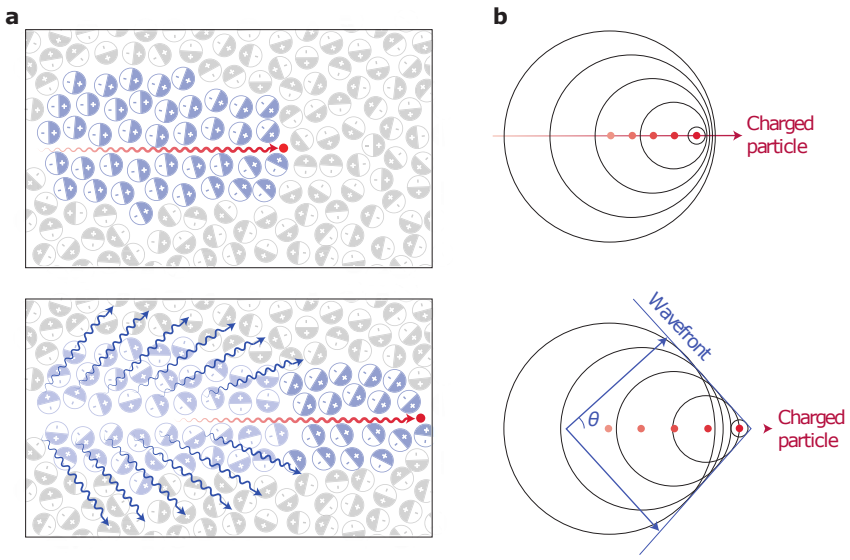

Figure 3.2: Schematic illustration of the Cherenkov radiation production process. **a**, Top: A charged particle (red dot) travelling faster than light in a medium polarizes the medium. Bottom: As the medium returns to the ground state, blue-weighted light (blue wavy lines) is emitted in a forward direction. **b**, Analogous to a sonic boom, coherent waves are produced through the Cherenkov mechanism, leading to a photonic wavefront. As the particle travels forward (lower panel), the photonic wavefront propagates at an angle θ relative to the direction of travel (from [71]).

$$\cos\theta = \frac{1}{\beta n(\omega)} \tag{3.1}$$

The Cherenkov angle is reduced as the particle slows down in the medium (Figure 3.3). Due to the fact that β and $\cos\theta$ are limited to an interval between 0 and 1, the Cherenkov relation (3.1) has three consequences:

1. Maximum emission angle: $\theta_{max}(\beta \to 1) \to \arccos(1/n)$
2. Minimum velocity for emission (Cherenkov threshold): $\beta_{min}(\theta = 0) = 1/n$
3. Minimum n for Cherenkov light to be produced: $n_{min}(\theta = 0) = 1/\beta$

The Cherenkov threshold can be expressed in terms of the kinetic energy (T) of the charged particle with the following equation:

$$T_{min} = mc^2 \left[\frac{1}{(1-\beta_{min}^2)^{1/2}} - 1 \right] = mc^2 \left[\left(1 - \frac{1}{n^2} \right)^{-1/2} - 1 \right] \tag{3.2}$$

where mc^2 is the rest mass of the charged particle. The threshold kinetic energy for the Cherenkov emission by a β particle ($m_0c^2 = 0.511$ MeV) as a function of the refractive index of the medium is shown in Figure 3.4. Due to the dispersion of the refractive index, different wavelengths will have a slightly different Cherenkov threshold. The dispersion, together with the energy loss and the multiple scattering of the charged particle in the medium, causes a spread of the emitted light around the Cherenkov angle and a finite duration of the light flash.

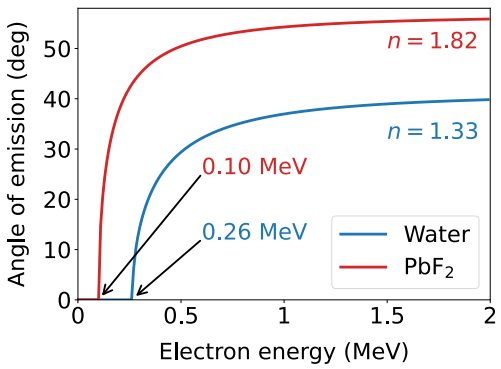

Figure 3.3: Cherenkov photon emission angles (θ) in water and in PbF_2 as a function of electron energy. The threshold energies for the production of Cherenkov photons are also shown.

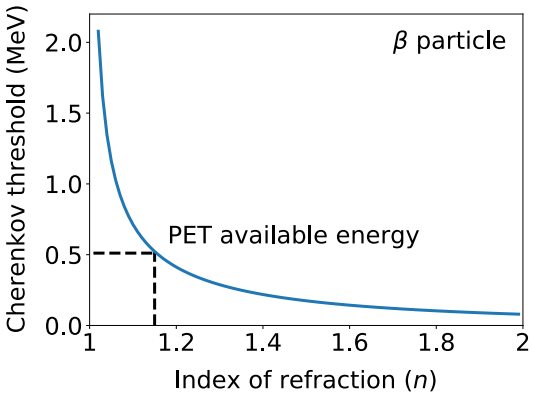

Figure 3.4: Cherenkov threshold as a function of the refractive index of the radiator for a β particle. For the energy available in PET the $n_{min} = 1.15$, for Cherenkov photons to be produced.

The Cherenkov emission is strongest in the ultraviolet-blue region and conforms to the inverse square wavelength dependence as outlined in the Frank and Tamm formula [72]. The number of photons emitted per unit path length and per unit wavelength by a particle with charge e is

$$\frac{d^2N}{dl\,d\lambda} = 2\pi\alpha\left(1 - \frac{1}{\beta^2 n^2(\lambda)}\right)\frac{1}{\lambda^2} \tag{3.3}$$

where $\alpha \approx 1/137$ is the fine structure constant. Due to the non-linear relationship between energy and wavelength ($E = hc/\lambda$), the energy spectrum of the emitted radiation appears flat

$$\frac{d^2N}{dl\,dE} = \frac{\alpha}{\hbar c}\left(1 - \frac{1}{\beta^2 n^2(E)}\right) \tag{3.4}$$

The formula for the Cherenkov spectrum predicts an infinite amount of light production. However, in reality, there are two cut-offs that limit this production. The first cut-off occurs at long wavelengths due to self-absorption within the medium. The second cut-off occurs at short wavelengths in the X-ray region, where the refractive index (n) becomes less than unity, a phenomenon known as anomalous dispersion. The Cherenkov relation (3.1) is no longer satisfied in this region, and light production stops [73].

Cherenkov radiation is emitted in the timescale of several picoseconds [12], which makes it a very attractive mechanism to be exploited for fast-timing applications like Cherenkov TOF PET, where the Cherenkov emission process has a negligible contribution to the overall CTR of the detector. In contrast, the scintillation process typically requires a few 100 ps to reach a maximum light output which then decreases exponentially with a decay time on the order of 10 ns [74, 75].

3.2 PET detectors and the rationale for using Cherenkov radiation

The ideal detector for PET imaging is one that combines the following performance attributes:

1. High efficiency for detecting 511 keV photons
2. High spatial resolution
3. Good timing resolution to allow use of narrow coincidence timing windows and enable TOF imaging acquisitions
4. Good energy resolution to allow rejection of scattered events

In current practice, the scintillation detector best meets these attributes. Still, other types of detectors for PET are constantly being explored, and one such example are detectors based on Cherenkov light detection. Cherenkov photons promise unprecedented time resolution, thanks to their prompt emission, which can significantly improve the performance of TOF PET scanners. Cherenkov photons are therefore seen as a potential way to achieve the 10 ps time resolution; a goal which was launched as a challenge for the PET community by Paul Lecoq 2017 [76]. A CTR of about 10 ps FWHM would ultimately allow to obtain a direct 3D volume representation of the estimated activity distribution of a positron-emitting radiopharmaceutical at the mm level and without the need for tomographic inversion, thus introducing a quantum leap in PET imaging and quantification [77]. Furthermore, dense Cherenkov radiators with gamma stopping powers (attenuation coefficients) higher than the currently used scintillation crystals also provide an opportunity for higher gamma detection efficiencies.

When designing a new detector, the cost of fabrication, operation, and maintenance should be kept within certain limits, and the detector's performance should be stable in time. Other practical requirements include mechanical robustness, scalability, and low power consumption. In addition, if the detectors are integrated with MRI equipment, the detector should be insensitive to magnetic fields and contain no magnetic components. To compare (TOF) PET detectors, one might define a simple figure of merit (FOM):

$$FOM_{det} = \frac{\varepsilon_D^2 G}{\$} \frac{D}{\Delta t} \tag{3.5}$$

where ε_D is the detection efficiency of the detectors for 511 keV photons, G represents the system geometrical efficiency (solid angle subtended by the PET rings), \$ the total cost of the detectors, Δt the coincidence resolving time, and D is the diameter of the imaged subject. FOM_{det} can be seen as a first-order estimate of the effective system sensitivity per unit cost. Note that ε_D is found squared in this equation because of the requirement to detect both annihilation photons to form a LOR.

Equation 3.5 ignores the influence of spatial resolution, energy resolution, dead time, inter-crystal scatter, etc., on the quality of the reconstructed image, but nevertheless, can serve as a good guide when searching for new detector materials or when designing and evaluating the potential of new PET detectors.

3.3 Cherenkov TOF PET radiator candidates

3.3.1 Requirements for a Cherenkov radiator

The first crucial component of any gamma detecting material is high gamma stopping power, which is achieved through the high density and high atomic number (Z) of the material. To obtain Cherenkov photons, the gamma must transfer a sufficient amount of energy to an electron in a suitable radiator material. The energy of the electron must be above the Cherenkov threshold so that Cherenkov photons can be produced. To increase the number of emitted Chrenkov photons, the electrons should have the highest possible energy. Therefore, the photoelectric effect of the 511 keV gammas is preferred over Compton scattering, since more energy is transferred to the electron that way. The cross-section for photoelectric effect has a stronger dependence on the atomic number of the material ($\sigma_{ph} \propto Z^n$, where the exponent n varies between 4 and 5 [78]), than the cross section for Compton scattering ($\sigma_{incoh} \propto Z$). The photofraction, defined here as a ratio between the cross-section of photoelectric effect and total cross-section, increases with Z (Figure 3.5), therefore radiators with high Z are preferred.

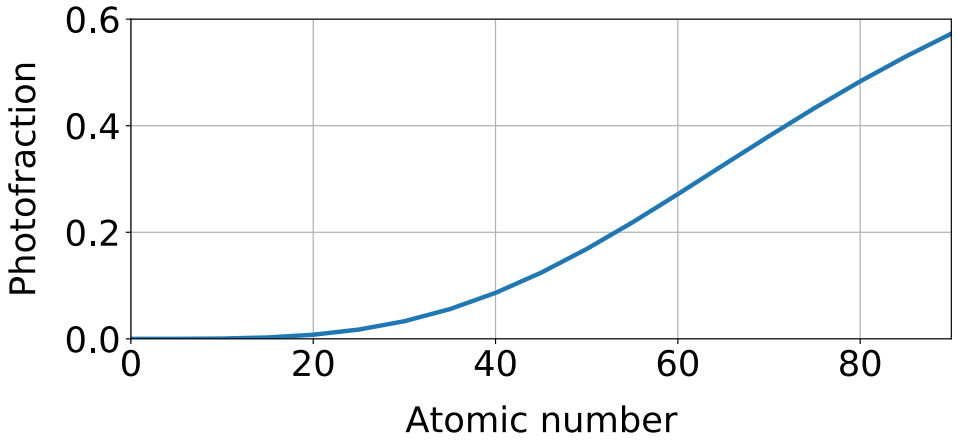

Figure 3.5: Photofraction as a function of atomic number for 511 keV photons (data obtained from NIST [79]).

The second crucial component of a Cherenkov radiator are its optical properties. Its refractive index should be high so that the Cherenkov threshold is low (Eq. 3.1). However, it should not be too high, as this would hamper the photon extraction from the crystal to the photo-detector due to total internal reflection. It also has to have good optical transmission for Cherenkov photons, so that the photons can reach the photo-detector without being absorbed in the radiator.

3.3.2 Pure Cherenkov radiators

The use of Cherenkov light to detect gamma rays in PET was first discussed by Ooba *et al.* 2004 [80], where an improvement in the time resolution was proposed by using Cherenkov light produced in a silica aerogel with a refractive index of 1.2. However, silica aerogel as a radiator would have a very low gamma detection efficiency due to its low density (~ 5 kg/m^3) and low Cherenkov light yield, due to the low refractive index.

Using pure Cherenkov radiators that do not scintillate coupled to microchannel plate photomultiplier (MCP-PMT) as the light sensors, great coincidence time resolutions have been reported. Miyata *et al.* 2006 [81] carried out measurements using lead glass (PbG) and reported a CTR of 170 ps, which was already better, at that time, than the CTR of 350 ps FWHM measured with BaF_2, one of the fastest conventional scintillators.

Lead fluoride (PbF_2) was first experimentally studied by Korpar *et al.* 2011 [82], where 71 ps FWHM and 95 ps FWHM have been achieved with 5 mm and 15 mm thick crystals, respectively. More recently, Ota *et al.* 2019 [83], using 5 mm long PbF_2 crystals, reported a 47 ps FWHM CTR, which corresponds to a position resolution of 7.0 mm along the LOR. The same group also tested a Cherenkov-radiator-integrated micro-channel plate photomultiplier tube (CRI-MCP-PMT), where there were no optical boundaries between the radiator (PbG) and photocathode. They achieved an outstanding CTR of around 30 ps FWHM [84], and direct (reconstruction-free) positron emission imaging was demonstrated, shown in Figure 3.6, using these fast detectors [85]. However, to achieve such a resolution, strong cuts had to be made in timing pick-off threshold and pulse area, meaning only a small fraction of events was used, and the authors acknowledge that these detectors do not satisfy the detection efficiency requirement of clinical PET detectors.

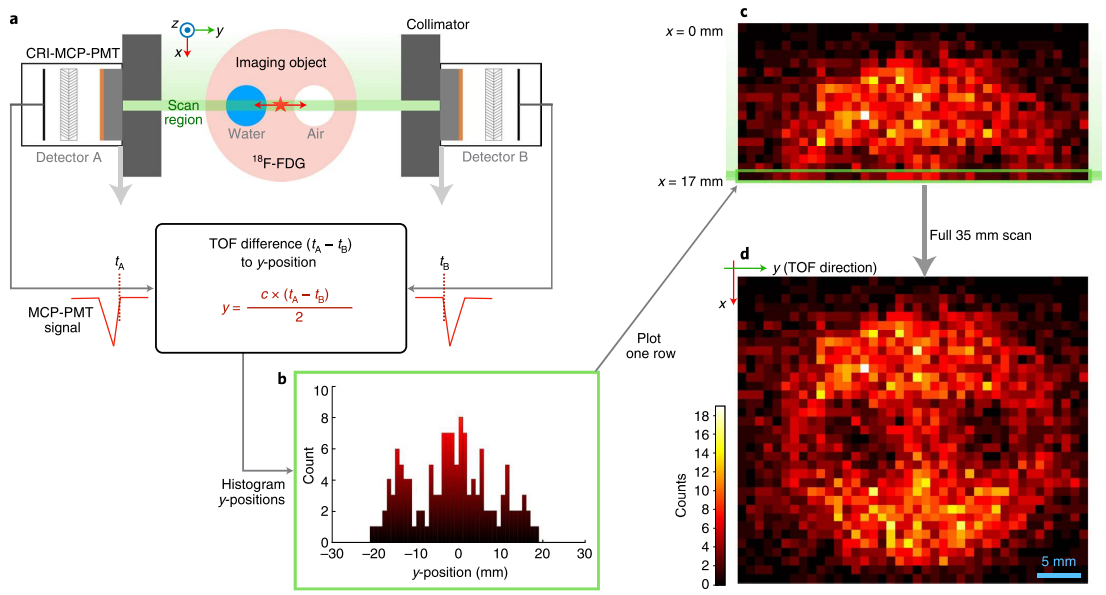

Figure 3.6: Demonstration of reconstruction-free PET. A pair of CRI-MCP-PMT detectors is used to acquire a cross-sectional image. **a**, The x-direction of the image is encoded by the position of the collimated detector pair, whereas the y-direction is encoded by the timing information. **b**, Data are acquired for each x-position of the detector pair, and the timing information is used to determine the distribution of the activity along the line between the two detectors. **c**, The image is built up line by line as the detectors are translated. **d**, The final raw image (from [85]).

Although MCP-PMTs have excellent timing properties, they have several drawbacks like high cost, bulky size, and low photon detection efficiency. High detection efficiency of the photo-detector is crucial for a pure Cherenkov PET detector since if none of the few produced Cherenkov photons is detected, the event (gamma) is not detected.

Silicon photomultipliers are promising photo-detectors to be used with pure Cherenkov radiators. They have a higher photon detection efficiency than MCP-PMTs, are compact, cost-effective, and can sense optical photons with a single photon detection time precision below 100 ps [86]. The use of SiPMs with PbF_2 crystals was studied by Dolenec *et al.* 2016 [87], where the best result obtained for TOF resolution was 297 ps. This value was shown to improve to 197 ps FWHM for 15 mm long crystal when selecting only single micro-cell hits but at the expense of lower efficiency [88]. By using a different detector chain (SiPM+electronics+digitization) a time resolution of 215 ps FWHM (142 ps FWHM) was recently obtained for $2 \times 2 \times 20$ mm^3 ($2 \times 2 \times 3$ mm^3) sized PbF_2 crystals [6]. The above-mentioned Cherenkov detector studies also showed that the surface treatment of the crystals has an important influence on the detector's performance.

Effective noise equivalent count rate and spatial resolution of a whole-body PbF_2 Cherenkov TOF-PET scanner was investigated by Alokhina *et al* 2018 [89] using GATE/Geant4 simulations. Among the studied designs, they obtained the best effective NECR with 10 mm thick crystals with diffuse white coatings, which achieved TOF resolution of 180 ps.

3.3.3 Scintillators exploiting Cherenkov light

Cherenkov photons are also produced in the scintillators, and they can potentially be used to improve the time resolution. There is a renewed interest in BGO as a hybrid scintillator / Cherenkov radiator to be used as a cost-effective solution for TOF PET [90, 91]. Specifically, BGO is approximately one-third the cost of Lu-based scintillators [19].

When measuring with a time-correlated single-photon counting setup and comparing the ratio of prompt light to scintillation light, 17 ± 3 Cherenkov photons are estimated to be produced upon 511 keV interaction in BGO [17]. While BGO was the scintillator of choice for use in whole-body PET scanners starting from the 1980s through the mid-2000s thanks to its high attenuation coefficient and photofraction (higher than L(Y)SO), its low light output and slow scintillation signal were not good enough to perform TOF imaging (the best CTR of about 1.5 ns FWHM was reported for 20 mm long crystals [92]). However, recent work has shown evidence that TOF imaging may be possible with BGO by detecting the prompt Cherenkov photons [93], and a time resolution of about 260 ps was measured with 20 mm long BGO crystals.

3.3.4 Cherenkov light in semiconductors

Semiconductor materials with high transparency to visible light, a high index of refraction, and high gamma stopping power, such as Thallium bromide (TlBr) and Thallium chloride (TlCl), shown in Figure 3.7, were proposed to be used as radiation detectors that can combine excellent energy resolution from charge readout with timing measurement obtained by detecting Cherenkov light [94].

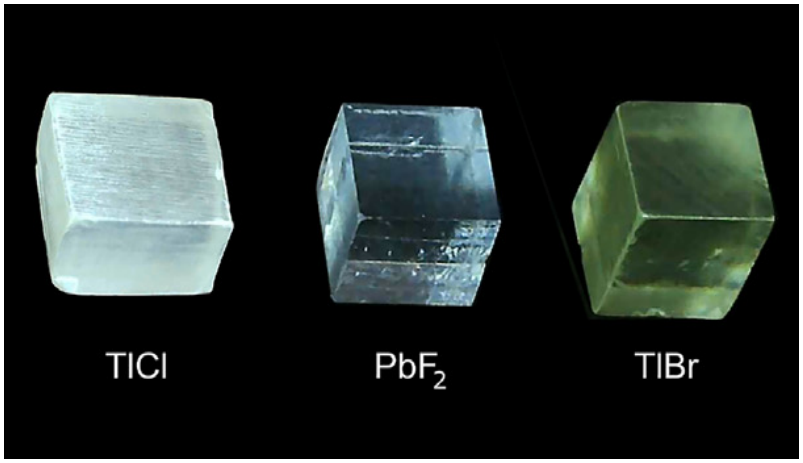

Figure 3.7: TlCl, PbF_2, and TlBr crystals. PbF_2 crystal has a polished surface while the surfaces of the semiconductor crystals are unpolished ([95]).

A recent study done by Ariño-Estrada *et al.* 2021 [96] reports on measuring an average of 1.5 photons for TlBr and 2.8 detected photons per event for TlCl when these materials were coupled to a silicon photomultiplier. The best CTRs for events in TlBr and TlCl they obtained were 329 ± 9 and 316 ± 9 ps, respectively, when events with four photons and more than seven photons per event were selected.

3.4 Lead fluoride (PbF_2)

This work focuses on crystalline lead fluoride (PbF_2), shown in Figure 3.7, one of the best known Cherenkov radiators. PbF_2 is a pure Cherenkov radiator, so it produces no scintillation light. It is very dense ($\rho = 7.8$ g/cm^3) and has one of the highest photofractions (46%), thanks to its high effective atomic number ($Z_{eff} = 77$). Attenuation coefficient and photofraction as a function of energy for PbF_2, BGO, and LSO are shown in Figure 3.8.

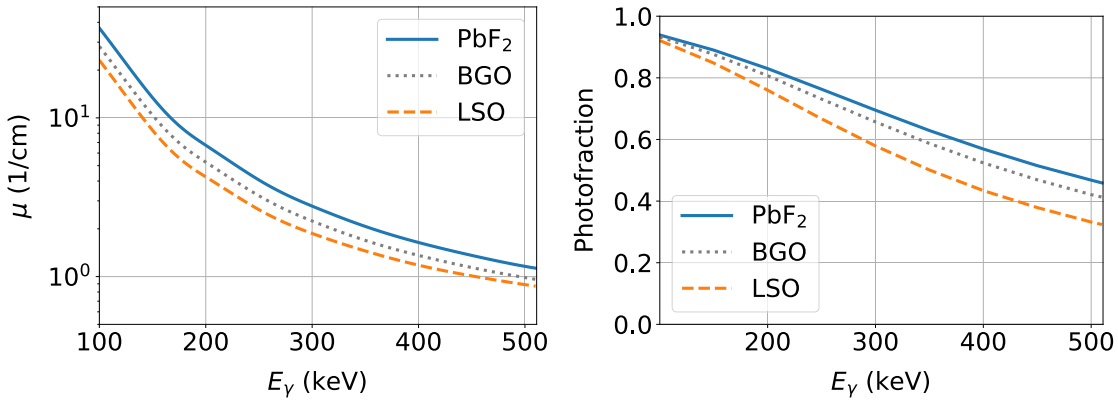

Figure 3.8: Attenuation coefficient (left) and photofraction (right) as a function of photon energy for PbF_2, BGO, and LSO (data obtained from NIST [79]).

Lead fluoride also has good optical properties, its wavelength dependence of optical transmission and refractive index are shown in Figure 3.9. Table 3.1 shows the physical properties of PbF_2 and some other selected Cherenkov radiators and inorganic scintillators.

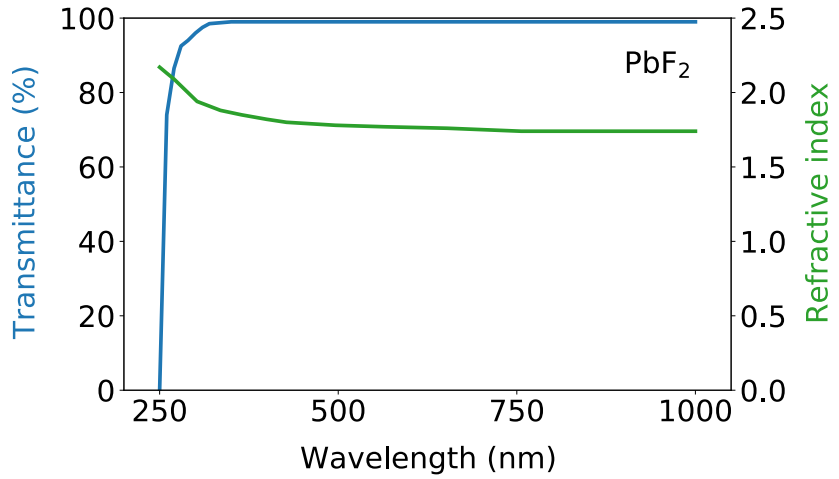

Figure 3.9: Optical transmittance and refractive index of lead fluoride ([97]).

Table 3.1: Physical properties of selected Cherenkov radiators and inorganic scintillators [6, 79, 98, 99]. Attenuation coefficient μ and the photofraction are given for 511 keV photons. Optical transmission cutoff wavelength is defined as the lowest wavelength at which the material is still transparent.

Material	PbF_2	Lu_2SiO_5	$Bi_4Ge_3O_{12}$	TlBr	TlCl	$PbWO_4$
Density (g/cm^3)	7.8	7.4	7.1	7.5	7.0	8.3
Effective atomic number	77	64	71	73	76	74
μ (cm^{-1})	1.13	0.87	0.96	1.0	1.0	1.14
Photofraction	0.46	0.32	0.41	0.42	0.45	0.43
Refractive index at 550 nm	1.77	1.8	2.12	2.47	2.28	2.16
Cutoff wavelength (nm)	250	370	300	440	380	320
Melting point (°C)	824	2050	1050	460	430	1123

Simulations done by Canot *et al.* 2019 [100] showed that the electrons emitted through the photoelectric effect are sufficiently fast to produce about 20 optical photons on average, and these simulated results agree well with the predicted intrinsic Cherenkov photon yield of 16.5 ± 3.3 estimated for PbF_2 from measurements [6].

High ρ and Z_{eff} give PbF_2 excellent gamma stopping power (attenuation length $= 1/\mu = 8.8$ mm). Among the potential PET Cherenkov radiators (or scintillators) found in the literature, only lead tungstate ($PbWO_4$) has a bit higher attenuation coefficient. Unlike PbF_2, $PbWO_4$ also emits scintillation light with an output of about 200 photons/MeV. This light output is not sufficient to give it good energy resolution, and triggering on a signal that is a mixture between a fast Cherenkov and slow scintillation component results in high timestamp fluctuations on an event-by-event basis, observed as "long tails" in time histograms [17, 101].

Furthermore, compared to PbF_2, $PbWO_4$ has a lower photofraction and higher cutoff wavelength. Cutoff wavelength is a very important parameter for Cherenkov radiators, as it strongly impacts the number of produced Chrenkov photons that can be detected due to the $1/\lambda^2$ dependence of Cherenkov emission spectrum (3.3). For example, high cutoff lengths of 440 nm and 380 nm for TlBr and TlCl, respectively, result in a very low number (~ 10) of Cherenkov photons that are produced within the crystal's transparent range and present one of the limitations of these semiconductor Cherenkov radiators [96]. Lead glass has a similar problem with a cutoff wavelength of 370-380 nm, in addition to a low density of 4.0-5.2 g/cm, depending on the percentage of lead content [81].

Comparing the linear attenuation coefficients of 1.13 cm^{-1} for PbF_2 and 0.87 cm^{-1} for LSO, while using the Eq. 2.7 we can estimate that we need about 15 mm of PbF_2 to achieve the same gamma stopping power as 20 mm of LSO. Scanners using PbF_2 crystals instead of LSO crystals thus have the potential to achieve better sensitivity at the same crystal length or the same sensitivity at shorter crystal length, while achieving better spatial resolution due to the reduced DOI effect.

Lastly, low price is also an important and appealing feature of PbF_2. All the major commercial PET vendors use expensive Lu-based crystals, and their cost is one of the dominant components of the PET scanner cost. Crystal cost becomes especially important when considering long-axial total-body PET scanners [4]. BGO and PbF_2 - which is even cheaper (1/3 of BGO [102]) thanks to its low material cost and lower melting point - might enable cost-effective total-body imaging.

3.5 Challenges and limitations

Following a 511 keV interaction in a radiator, the overall number of produced Cherenkov photons is small (a few tens) compared to hundreds or thousands of scintillation photons that are available for detection in scintillation detectors. The number of Cherenkov photons reaching the photo-detector is even smaller as some of the emitted photons can leave the radiator or are absorbed in the reflector coating or the radiator itself. Consequently, high detection efficiency of the photo-detector is essential for a pure Cherenkov PET detector since if none of the produced Cherenkov photons is detected, the event is lost, resulting in reduced detector sensitivity. Furthermore, pure Cherenkov detectors have basically no energy resolution, since we can not infer much information about the energy of the interacting gamma from the few detected Cherenkov photons (Eq. 2.22). Having no energy resolution means we can not discriminate between the scattered and unscattered gammas.

3.5.1 Limitations of fast timing

Once a gamma enters the detector, the detection time depends on the time between the gamma interaction and emission of Cherenkov photon(s), the time for the Cherenkov photon(s) to reach the photo-detector, accounting also for the depth of interaction, and the time resolution of the photo-detector. The distribution of the detection times is, therefore a convolution of the emission distribution function, optical transfer time distribution (OTTD), and the single-photon timing spectrum (SPTS) of the photo-detector

$$t = t_{emission} * t_{OTTD} * t_{SPTS} \tag{3.6}$$

Cherenkov photons are produced promptly and therefore, the contribution of the emission process to the timing resolution can be neglected. The photo-detector has its own intrinsic time resolution, which directly impacts the timing resolution of the whole gamma detector. The FWHM of the single-photon timing spectrum is called the single-photon time resolution (SPTR) or, in the specific case of a vacuum photo-multiplier tube, the transit time spread (TTS). Even with an ideal photo-detector, the detection time will fluctuate due to the variations in path length between the photon production location in the radiator and the photodetector. The FWHM of optical transfer time distribution is usually called the optical transfer time spread (OTTS) and can be seen as a measure of the loss of time information due to the kinetics of optical transfer.

It is important to note here that, while gamma rays travel with the speed of light (c_0) through the radiator, the (optical) Cherenkov photons travel slower, c_0/n, where the value of the refractive index (n) is relatively high, about 1.8 for PbF_2 as can be seen in Figure 3.9. We can obtain a simple estimate of OTTS, by considering two extreme cases, as shown in Figure 3.10.

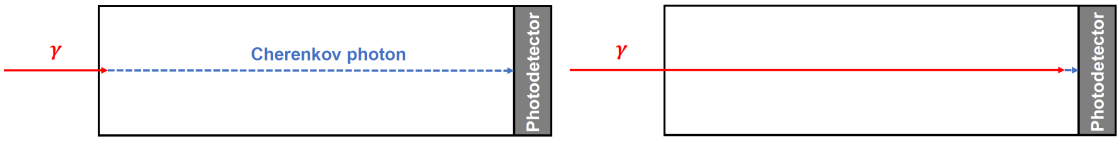

Figure 3.10: The time of arrival of the Cherenkov photons depends on their production position and on the position of the photodetector. Two extreme cases of Cherenkov photon production are shown schematically. *Left*: the 511 keV gamma ray is absorbed at the beginning of the crystal, and the Cherenkov photon has to travel the full thickness of the crystal until it reaches the photodetector. *Right*: The gamma ray is absorbed close to the photodetector, and the Cherenkov photon is detected almost immediately.

In the first case, the annihilation gamma interacts with the radiator as soon as it enters, meaning that the Cherenkov photon, produced by the interaction, needs to travel the whole thickness of the radiator before it reaches the exit surface, coupled to the photodetector. In the second case, the annihilation gamma interacts at the end of the crystal, and the Cherenkov photon exits the crystal almost immediately. Assuming the radiator is PbF_2 with a refractive index n of 1.8 and thickness d of 20 mm, the Cherenkov photon in the first case reaches the end of the crystal at a time t_1:

$$t_1 = \frac{d}{c_0/n} = \frac{20 \text{ mm}}{0.3 \frac{\text{mm}}{\text{ps}}/1.8} = 120 \text{ ps} \tag{3.7}$$

and in the second case at a time t_2:

$$t_2 = \frac{d}{c_0} = \frac{20 \text{ mm}}{0.3 \text{ mm/ps}} = 67 \text{ ps} \tag{3.8}$$

The time difference (Δt) is about 50 ps, even in this simple case, which does not consider, for example, increased path length due to photons traveling at an angle or Cherenkov photons reaching the exit surface after one or more internal reflections.

Neglecting the emission function and assuming the timing contributions are Gaussian shaped and therefore their uncertainties add quadratically, we can express the CTR of two identical detector pair as:

$$CTR^2 = 2 \cdot OTTS^2 + 2 \cdot SPTR^2 \tag{3.9}$$

The factor 2 is because both detectors contribute the same uncertainty to the coincidence timing measurement. It is evident that for the best timing resolution, we want fast photo-detectors and the radiator dimensions need to be small. One possibility to reduce the effect of timing spread without affecting the gamma stopping power is by using a multi-layer configuration with shorter crystals [103], as shown in Figure 3.11.

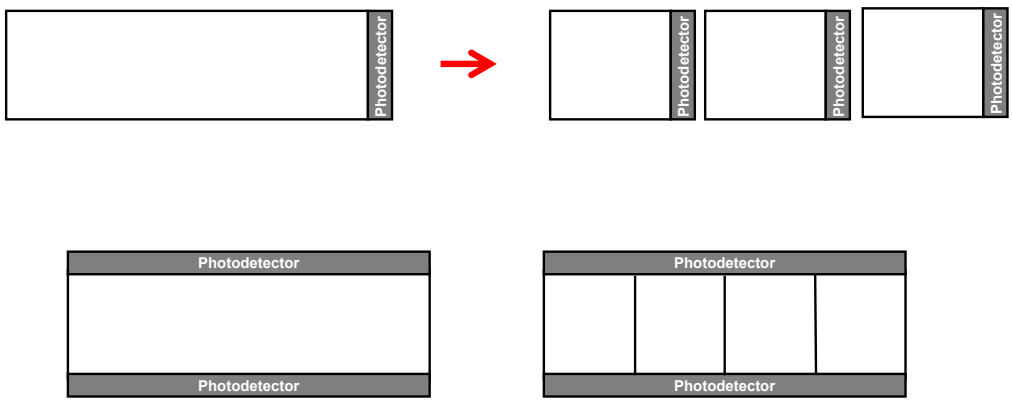

Figure 3.11: The optical transfer time spread of the PET detector can be reduced by segmenting the crystal into the multi-layer configuration, shown schematically in the top images, or by using a lateral side-readout design. A configuration with a 2-sided lateral readout is shown in the bottom images. Segmented crystals can also potentially provide better DOI information than unsegmented ones.

Another possibility is lateral side-readout configuration, where one or more lateral sides of each crystal element are covered with photodetectors, e.g., SiPMs (Figure 3.11). The lateral side-readout results in the improvement of the light collection efficiency and a reduction in the variation in optical transfer time, thus improving the overall timing performance of the PET detector [104, 105].

Both the multi-layer and the lateral side-readout detector configurations can also potentially provide better DOI information, than the standard end-readout. This information can be used to reduce the parallax error, and therefore improve the spatial resolution of the scanner. On the other hand, both of these configurations require a substantially increased number of photosensors and thus suffer from a high readout complexity and manufacturing costs.

4. Methodology

First, a simulation study of different detector designs based on PbF_2 with SiPMs as photosensors was performed. Three of the simulated designs were selected to model whole-body Cherenkov PET systems. The performance of Cherenkov PET scanners was then evaluated and compared to the reference scanner - our model of Siemens Biograph Vision clinical PET scanner. Count rates and image quality of the PET scanners were assessed and compared following the National Electrical Manufacturers Association (NEMA) NU 2-2018 standard[1]. Next, a Derenzo phantom was imaged for a visual inspection of the resolution. Finally, the potential of pure Cherenkov PET detectors for long axial FOV PET scanners was investigated. Monte Carlo simulations were performed on the Slovenian national super-computing network (SLING) using GATE [106] version 8.1, a Geant4 [107] Application for Tomographic Emission: a simulation toolkit for PET and SPECT medical imaging.

4.1 GATE simulation

GATE is an advanced open-source software developed by the international OpenGATE collaboration and dedicated to numerical simulations in medical imaging and radiotherapy. It currently supports simulations of emission tomography (PET and SPECT), computed tomography (CT), optical imaging (bioluminescence and fluorescence), and radiotherapy experiments. GATE merges the benefits of the GEANT4 simulation toolkit, well-validated physics models, sophisticated geometry description, and powerful visualization and 3D rendering tools with original features specific to emission tomography. The heart of the simulation is the Monte Carlo method - a method to search for solutions to a mathematical problem using statistical sampling with random numbers. GATE plays a key role in the design of new medical imaging devices, in the optimization of acquisition protocols, and in the development and assessment of image reconstruction algorithms and correction techniques. It can also be used for dose calculation in radiation therapy, brachytherapy, or any other application.

[1] https://www.nema.org/standards/view/Performance-Measurements-of-Positron-Emission-Tomographs

In the Monte Carlo simulation, the particles are transported step-by-step by taking into account the interactions with materials (and external electromagnetic fields) until the particle loses all off its kinetic energy, disappears in an interaction, or comes to the end of the simulation volume. Accessing the transportation process allows the user to obtain various information such as the time when the particle is going into the sensitive volume (detector), deposited energy inside a volume, etc. In each simulation of medical imaging, the user has to:

- define the scanner geometry
- define the phantom geometry
- set up the physics processes
- initialize the simulation
- set up the detector model
- define the source(s)
- specify the data output format
- start the acquisition

4.1.1 Simulation physics

The *emstandard_opt*4 physics list from Geant4 was used in the simulations. It uses accurate standard and low-energy models of electromagnetic interactions, making it suitable for medical physics applications [108]. The cut (production threshold) in the radiator - for the charged particles producing Cherenkov photons - was set to 10 μm. A maximum of one Cherenkov photon was produced in a step. The cut was verified to be low enough so that further lowering it did not impact the distribution and the number of produced Cherenkov photons. Cherenkov photons were simulated in the range 250-1000 nm, and the simulated spectrum is shown in Figure 4.1.

4.1.2 Materials

The primary method for defining the properties of the materials used in GATE is by a materials database. The density used for the simulation of PbF_2 crystal is specified in Table 3.1. From the material density and elemental composition, Geant4 derives most of the material properties required for the simulation, except for the optical properties of the materials and optical boundaries, which need to be defined by the user. The values of the refractive index and of optical transmittance, used in the simulation to determine the optical absorption lengths of PbF_2, are shown in Figure 3.9. The transmittance is defined as a ratio of the intensity of light that passes through the object (I) and the intensity of incident light (I_0); $\tau = I/I_0$. The absorption length Λ is determined from transmittance by relation

$$\Lambda = \frac{d}{\ln(1/\tau)} \tag{4.1}$$

where d is the thickness of the sample. Figure 4.2 shows the absorption length as a function of wavelength in PbF_2.

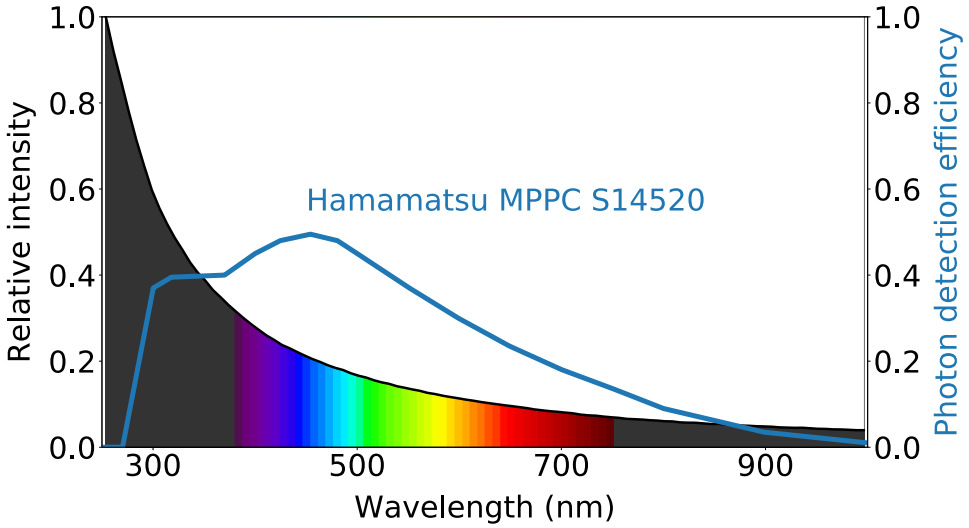

Figure 4.1: The spectrum of Cherenkov photons produced in the simulation and the photon detection efficiency of the light sensor, Hamamatsu MPPC S14520, as used in the simulation. The spectrum agrees well with the $1/\lambda^2$ dependence, theoretically predicted by the Frank-Tamm equation (Eq. 3.3).

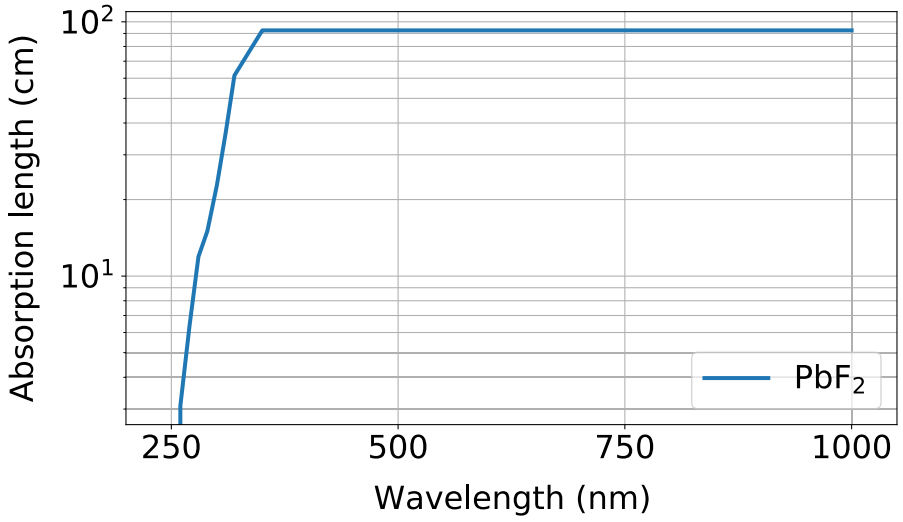

Figure 4.2: The wavelength dependence of the absorption length in PbF_2 used in the simulation. The cutoff wavelength in PbF_2 is at about 250 nm. Absorption lengths were calculated with Equation 4.1, using data from [97].

4.1.3 Optical surfaces

Two different surface treatments of the crystal were considered in the simulations: absorbing (black) and reflective coating (reflector). The Geant4 *unified* model [109] was used to simulate the physical processes at the optical boundary. In the *unified* model, four kinds of surface reflections are possible: specular spike, specular lobe, backscatter, and Lambertian (Figure 4.3).

The black surface was modeled as smooth with a refractive index of 1.5 [110], and the optical photon was stopped if it was refracted and would thus exit the crys-

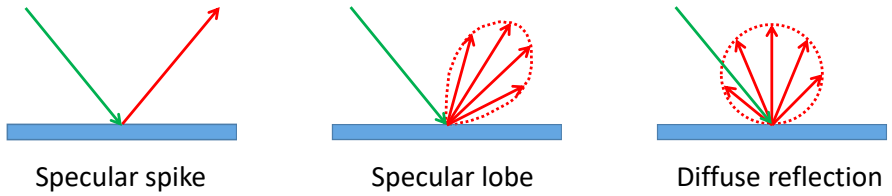

Figure 4.3: Reflection types in the *unified* model. For a specular spike reflection, the angle of reflection is equal to the incidence angle. For a specular lobe reflection, the angle of reflection is calculated with respect to a micro facet normal. For diffuse (Lambertian) reflection an optical photon can be reflected into any direction in the surface's hemisphere.

tal. The reflective surface was modeled as air-coupled (refractive index equal to one) with a Lambertian (diffuse) reflector with 95% reflectivity. The surface roughness was modeled with *sigmaalpha* parameter (Figure 4.4), which describes the angular distribution (Gaussian) of the microfacets that make up the macro-surface, set to 5°. In addition to the already mentioned references, the choice of optical parameters was also informed by Janecek *et al.* 2010 [111], 2012 [112] and Roncali *et al.* 2013 [113], as well as previous experimental work [82, 87] done by the colleagues at our group. Figure 4.5 illustrates the gamma interaction in a PbF_2 crystal that results in a production of Cherenkov photons, and the subsequent optical transport inside a crystal with an absorbing and with a reflective coating.

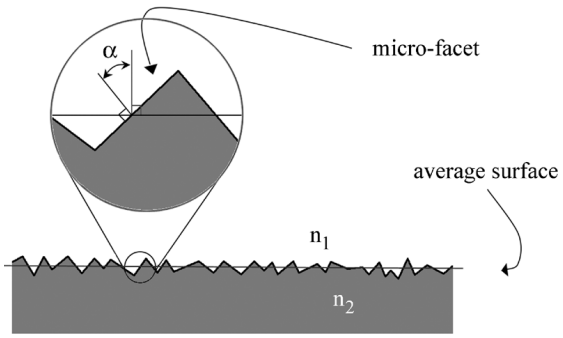

Figure 4.4: For a ground surface in the *unified* model, the parameter *sigmaalpha* defines the standard deviation of the Gaussian distribution of microfacets around the average surface normal [111].

(a) Black surface (b) Reflective coating

Figure 4.5: The behavior of Cherenkov photons (blue) in a crystal with a black surface and a crystal with a reflective coating.

4.1.4 Photo-detector

The photo-detectors were simulated with a photon detection efficiency based on the Hamamatsu MPPC S14520 SiPM with a peak PDE of about 50% at around 450 nm (Figure 4.1). The SiPM used also has good sensitivity in the near-ultraviolet part of the spectrum - important for Cherenkov photons as they are more likely to be produced at lower wavelengths. The Cherenkov emission-weighted photon detection efficiency can be determined by weighting the photo-detector's PDE with the Cherenkov emission spectrum, which gives a value of 22%. The effect of the optical interface between the crystal and the photo-detector's sensitive surface was considered by adding a quartz block - with a refractive index of 1.5 - in between, representing the window of a realistic photo-detector. The window and the photo-detector were modeled to be of negligible size (0.01 mm thick). The trigger in the GATE digitizer was set to one photon, meaning that detecting one or more Cherenkov photons counted as a detection event.

4.2 Detector study

Detectors with single, dual, and all sided crystal readouts were investigated. In the 2-sided readout scheme, three different configurations were considered: dual-ended readout, lateral readout with photo-detectors on opposing sides of the crystal, and a mix-readout with one photo-detector at the end and one on the lateral side. The studied detector designs are shown in Figure 4.6.

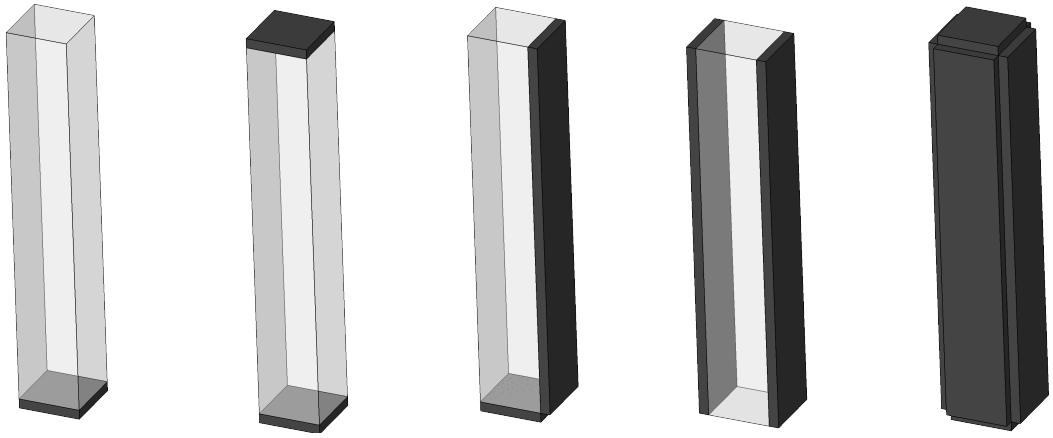

(a) Single-sided (b) Dual-ended (c) End-lateral (d) Dual-lateral (e) All-sided

Figure 4.6: Different readout schemes investigated in the detector study. The colored text indicates the designs considered in the whole-body TOF PET Cherenkov scanner study.

Detectors were based on the $3.2 \times 3.2 \times 20$ mm^3 PbF_2 crystals, corresponding to the size of crystals used by the Siemens Biograph Vision scanner. Two detectors were placed back-to-back, and a point 511 keV gamma source was placed in-between as shown in Figure 4.7. One million back-to-back gamma pairs were simulated for each detector design.

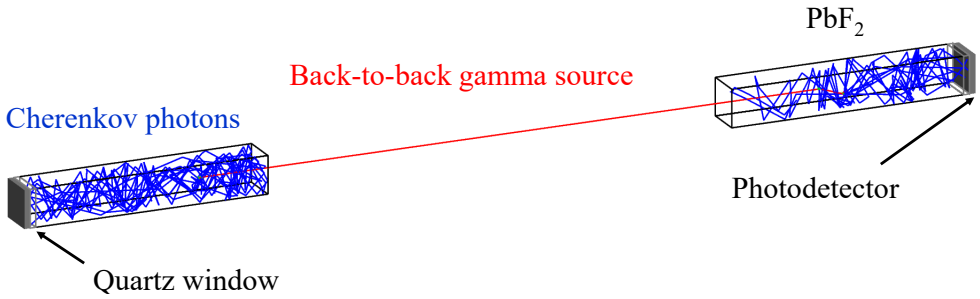

Figure 4.7: Back-to-back detector setup for studying detection efficiency and CTR of different detector designs: different surface treatments and photo-detectors covering one, two, or all crystal faces. The size of the studied PbF_2 crystals was $3.2 \times 3.2 \times 20$ mm^3.

4.2.1 Detector evaluation

The primary parameters of interest were coincidence detection efficiency and CTR, as they are two important detector parameters that directly impact the sensitivity of the scanner. The CTR was studied in an ideal and realistic case by setting the intrinsic single photon time resolution of the photo-detector (SiPM) to 0 ps and 70 ps [53], respectively. In the ideal case, the time spread due to the interaction depth and different path lengths of Cherenkov photons in the PbF_2 crystal was the primary limiting factor of the timing performance of the detector, as Cherenkov photons are produced promptly. To gain insight into the obtained values of detection efficiency and CTR, the light transfer efficiency (LTE) - defined as the ratio of the number of Cherenkov photons reaching the photo-detector and the total number of Cherenkov photons produced - was also determined and compared among the different detector designs. Finally, a figure of merit (FOM) was used to compare and choose detector designs for a whole-body scanner simulation. FOM was defined as the ratio between the coincidence detection efficiency and CTR

$$FOM = \varepsilon^2/CTR \tag{4.2}$$

The FOM corresponds to the equation for the detection efficiency of the scanner (Eq. 2.16) without the geometric efficiency of the system and the parameters related to the imaged object.

4.3 Simulation of a whole-body TOF PET Cherenkov scanner

Three detector designs were selected for a whole-body scanner study:

- 1-sided readout (crystal wrapped with reflector)
- 2-sided lateral readout of the reflector wrapped crystal
- 6-sided crystal readout (all surfaces covered with photo-detectors)

The 1-sided readout represents the standard, used in all the commercially available clinical PET/CT scanners. The 6-sided readout is a theoretical ideal, with the highest optical photon collection efficiency and the lowest optical transfer time spread. The 2-sided readout represents an intermediate option and something that is more likely to be practically feasible than a 6-sided readout, due to fewer electronic channels and the associated complexity and cost. The reference scanner and the Cherenkov scanners were modeled following the design of the Siemens Biograph Vision PET/CT scanner. The performances of Cherenkov PET scanners were compared among themselves as well as to the reference scanner based on the selected standard PET performance measures. To evaluate the goodness of our model, the reference scanner's simulated values were compared with the measured values from Sluis *et al.* 2019 [114] obtained with the clinical Siemens Biograph Vision PET/CT scanner.

4.3.1 Reference scanner - geometry

The reference system was modelled following the design of Siemens Biograph Vision PET/CT scanner [114, 115]. The system has a 78 cm bore and an axial field of view of 26.3 cm. The detector consists of an array of $3.2 \times 3.2 \times 20$ mm^3 LSO crystals packaged in blocks as 20 crystals radially and 10 crystals axially. The detector is further subdivided into mini-blocks (Figure 4.8) of 5×5 crystals optically coupled to a 4×4 array of SiPMs. The 16×16 mm array of SiPMs completely covers the 16×16 mm array of LSO crystals. A detector module contains 16 detectors (two radially by eight axially), and 19 detector modules are arranged in an 82 cm diameter cylinder to form the tomograph (Figure 4.9). Additional characteristics of the system can be seen in Table 4.1

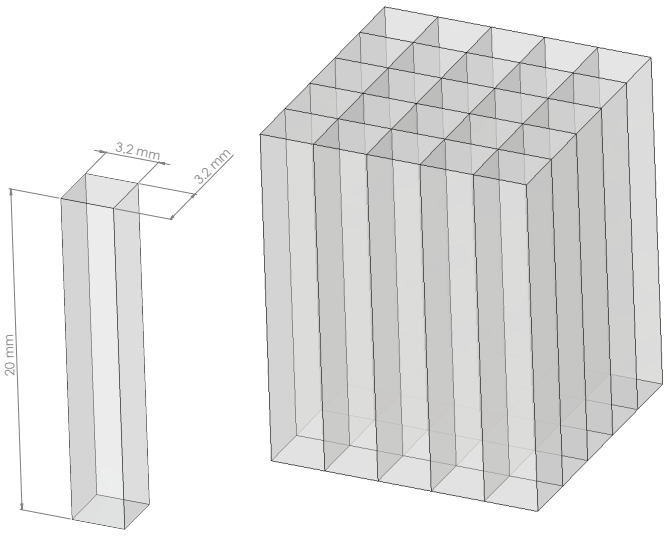

Figure 4.8: The studied PET detectors were based on $3.2 \times 3.2 \times 20$ mm^3 sized crystals. 5×5 crystals were packaged into mini-blocks (right image), which were then further packaged into block detectors (4×2 mini-blocks). Finally, a PET module consisted of 2×8 block detectors.

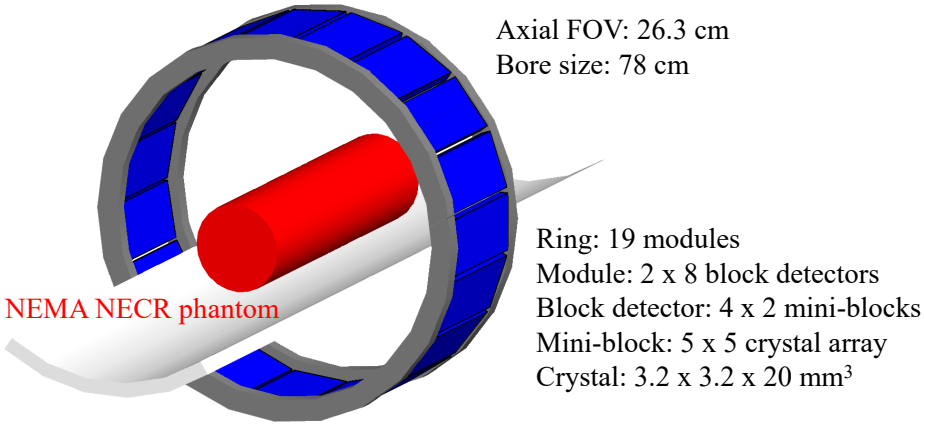

Figure 4.9: Scanner geometry simulated in GATE. In addition to the simulated detector ring, lead shielding, carbon-fiber bed, and cylindrical NEMA NECR phantom can also be seen in the figure.

Table 4.1: Siemens Biograph Vision characteristics.

Scintillator	LSO
Crystal size	$3.2 \times 3.2 \times 20$ mm^3
Crystals per ring	760
Number of crystal rings	80
Detector ring diameter	82 cm
Axial FOV	26.3 cm
Time window	4.7 ns
Energy window	435-585 kev
Energy resolution	10%
CTR	214 ps

4.3.2 Simulation parameters

In the GATE Monte Carlo simulation, the digitizer module was used to simulate the behaviour of the PET detectors and signal processing chain. When simulating the scintillation (reference) detector, the annihilation gammas were tracked through materials, but unlike the Cherenkov photons, the scintillation photons were not simulated and tracked. The digitizer was used to build, from the gamma interaction information, the detector pulses, which correspond to the observed data and contain the information about energy, position, and time of detection. Modeling a detector in such a manner allows us to skip the very time-consuming simulation of scintillation photons, and set the performance of the detector to the measured values. The scintillation process could not be omitted if, for example, the focus of the study was to explore the theoretical limits of the LSO based detectors and search for the ways to improve them.

Through Gaussian blurring of the energy spectrum, the energy resolution of the reference scanner was set to 10%. A 435 - 585 keV energy window was used, and a coincidence time window, used for accepting events, was set to 4.7 ns. The

readout was simulated at the module level (Figure 4.9) - signals inside the module were summed, and if the total deposited energy inside the module was within the specified energy window, the (singles) event was accepted, and its position within the module was determined with energy centroid policy (GATE *TakeEnergyCentroid*). In the case of multiple coincidences, all good coincidence pairs were included (GATE *takeAllGoods* policy).

The reference scanner's CTR was set to 214 ps FWHM. This was realized by simulating 10^7 back-to-back 511 keV gammas from a source placed in the center of the scanner and obtaining the coincidence time distribution from the collected events. The desired CTR of the reference scanner was achieved iteratively by changing the GATE timing of the detectors in the digitizer and observing the resulting CTR. The CTR of 214 ps FWHM was obtained by setting the timing to 148 ps, while setting it to 0 ps resulted in a CTR of 64 ps FWHM (Figure 4.10). In this case, a non-zero CTR was obtained because the simulation software records the time of the first gamma interaction in the detector, and thus, we get a time distribution due to the depth-of-interaction effect.

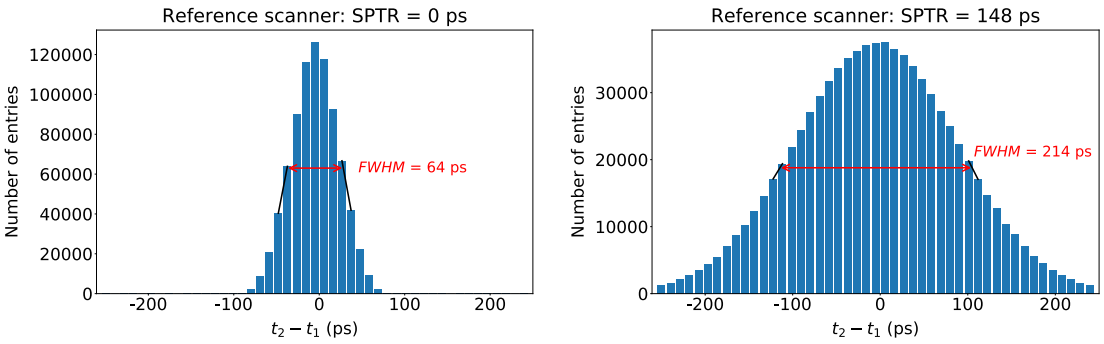

Figure 4.10: Histogram of time differences ($t_2 - t_1$) of events forming the coincidences for the reference scanner. The scanner's CTR of 214 ps FWHM was achieved in the simulations by setting the SPTR of the detectors to 148 ps (right). Recording the time of the first gamma interaction in the detector leads to a depth-of-interaction effect, and a CTR of 64 ps FWHM is obtained even when the SPTR is set to 0 ps (left).

For the Cherenkov scanners, we used the same coincidence time window and coincidence forming and sorting policy as for the reference scanner, except there was no energy window applied - in this case, the detection was based on optical photons instead of gammas, and in the GATE digitizer the *opticaladded* was used instead of *adder*. The SPTR of the photo-detector was set to 70 ps FWHM in the whole-body scanner study.

The intrinsic detector or the acquisition dead-times were not taken into account. This can be justified by the fact that the dead-time of modern PET scanners is very low compared to the traditional PMT-based system due to minimal or no multiplexing. Therefore any differences in count rate performance, at least in the range of activities used for clinical imaging, are primarily determined by the system sensitivity [19].

4.4 Image reconstruction

An iterative 3D OSEM TOF image reconstruction was performed using CASToR - Customizable and Advanced Software for Tomographic Reconstruction [116]. CASToR is an open-source multi-platform project for 4D emission (PET and SPECT) and transmission (CT) tomographic reconstruction. This platform is a scalable software providing both basic image reconstruction features for "standard" users and advanced tools for specialists in the reconstruction field, to develop, incorporate and assess their own methods in image reconstruction (through the implementation of new classes).

Following the reconstruction parameters used in a clinical Siemens Biograph Vision scanner [114], the data was reconstructed using the OSEM algorithm with 8 iterations and 5 subsets, onto a $225 \times 225 \times 225$ matrix with a voxel size of $1.6 \times 1.6 \times 1.6$ mm^3. The data from the simulations was obtained in a list-mode format. An accelerated Siddon projector [117], a ray-tracing algorithm that computes the exact path length of a line through the voxels, was used in reconstructions. The normalization factors were computed by the CASToR software and embedded in the data file used for reconstruction. Based on the geometry of the scanner, CASToR computed the geometric sensitivity of the scanner (Figure 4.11), and used the reciprocal values for normalization.

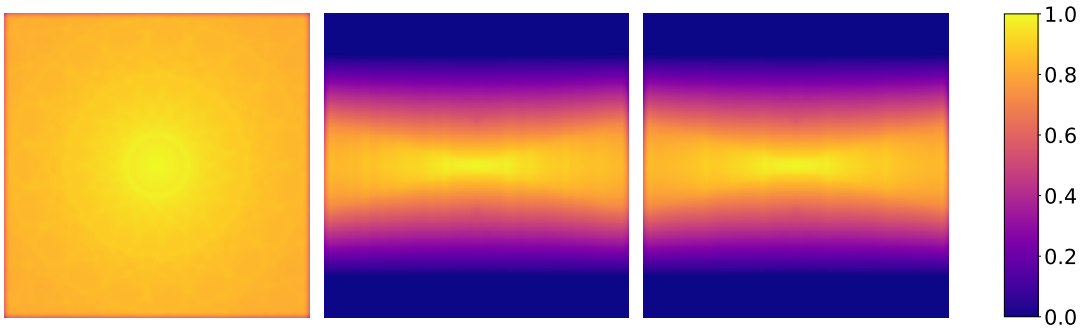

Figure 4.11: The geometrical sensitivity image of the reference scanner, computed by CASToR and used for normalization, is shown in different views (axial, sagittal, coronal). The sensitivity does not vary in the radial direction as much as in the axial direction. In the axial direction, the sensitivity decreases till it reaches zero at the edge of the FOV.

4.4.1 TOF - timing kernels

TOF information was also applied in the image reconstruction. The uncertainty of TOF measurements is usually modeled with a normalized Gaussian function. This single Gaussian TOF kernel was used for the reference scanner, but an additional double Gaussian TOF kernel was considered for the Cherenkov scanners. By imaging a point 511 keV gamma source placed in the center of the scanner, the timing resolution of Cherenkov scanners was obtained from a histogram of differences in the detection times ($t_2 - t_1$) of the coincidence events. The histogram of detection time differences could not be well fitted with a single Gaussian (Figure 4.12), as was also observed by other groups performing timing measurements on PbF_2 [6, 100]

and BGO [90, 93]. The long time differences can be explained with optical travel time spread, as the optical photons can bounce around in the crystal many times before reaching the photo-detector, additionally, the trigger can be set off by the first arriving optical photon or, in the other extreme case, by the last one, if none of the preceding photons were detected. To account for "long tails", the distribution of time differences was modeled with a double Gaussian model:

$$f(x) = a_1 \exp(-\frac{x^2}{2\sigma_1}) + a_2 \exp(-\frac{x^2}{2\sigma_2}) \tag{4.3}$$

Figure 4.12 shows that the time histograms are well fitted with a double Gaussian function, and the mixing ratio a_1/a_2 is also shown. The CASToR code had to be modified in order to implement a double Gaussian TOF kernel used in the image reconstruction.

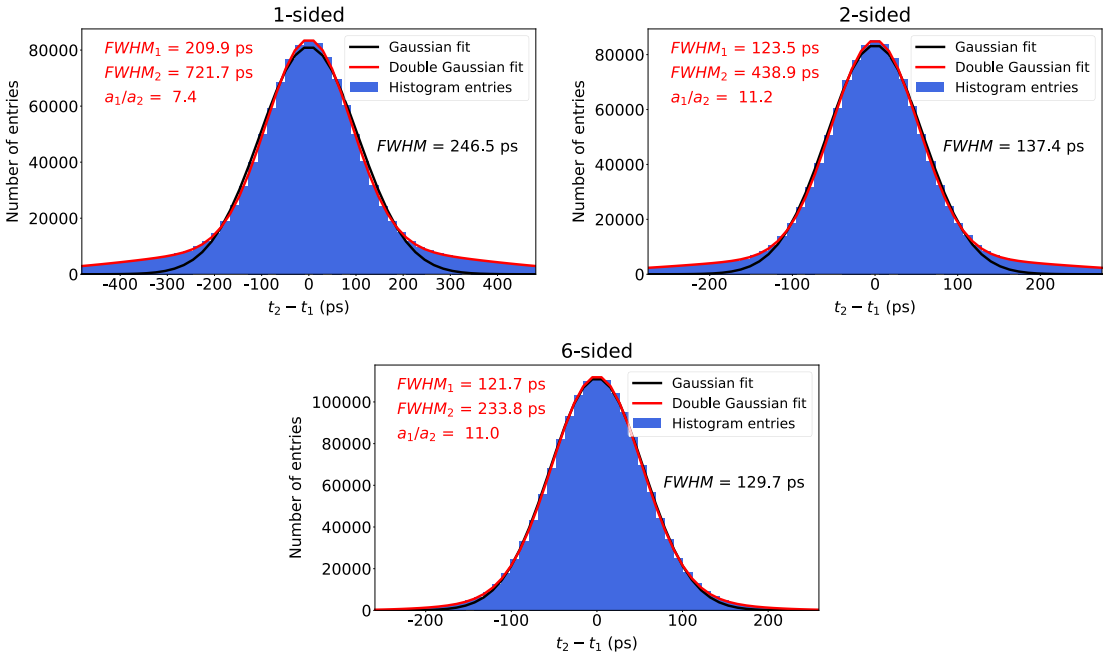

Figure 4.12: Histogram of time differences ($t_2 - t_1$) of events forming the coincidences, obtained by imaging a point 511 keV gamma source placed in the center of the Cherenkov scanner. Due to the long tails in the distribution, a double Gaussian (red) fits the histogram data better than a single Gaussian function (black). The FWHMs and their mixing ratios (a_1/a_2) are also shown for each Cherenkov detector design. The SPTR of the photo-detector was set to 70 ps FWHM.

4.5 Performance Measurements

4.5.1 NECR and Scatter fraction

Variations in designs and implementations cause PET scanners to have different sensitivities to scatter and random radiation. Following the NEMA NU 2-2018 standard, the phantom used to determine the count rate performance of the scanners consisted of a simulated line source of uniform activity inside of the 70 cm long polyethylene cylinder with a diameter of 20 cm (Figure 4.13). Because true, scatter, and random count rates were accurately known from the simulation, the NECR was

determined according to Equation 2.24 with k set to one; $NECR = T^2/(T+S+R)$. The values of true, random, and scatter coincidence count rates can be affected by user-controlled parameters in an actual PET system [118]. In this work, we defined them in the following way: true coincidences were considered those having both their singles initiated from the same annihilation event, scatter coincidences were considered the true coincidences for which one of the two single photons (or both) interacted with the material before reaching the detector, and random coincidences were those for which the coincidence event was formed by two gamma rays from different annihilation events.

For every simulated scanner, approximately $\sim 10^6$ prompt coincidences were collected (at least $5 \cdot 10^5$ prompt counts are suggested by the NEMA standard) at each activity level.

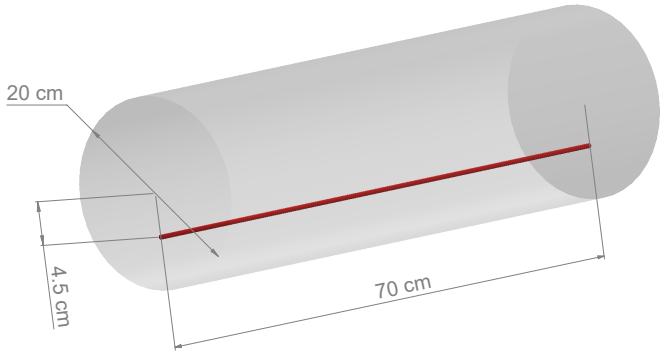

Figure 4.13: The NECR test phantom consisting of a polyethylene cylinder with an inserted linear source (red).

The scatter fraction was determined according to Equation 2.23 Scattered gammas are a potential weak point of Cherenkov scanners as they do not use an energy window (discussed in Section 3.5). To study the impact of scattering in more detail, we expanded the NEMA standard by determining the NECR and SF of phantoms with different diameters. The studied phantoms consisted of water-filled cylinders with diameters from 0.2 cm up to 40 cm and filled with activity 5.3 kBq/mL. This activity concentration coresponds to 370 MBq (10 mCi) per 70 L, a typical injected dose for whole-body FDG studies.

4.5.2 Spatial resolution

The Cherenkov scanners had the same geometrical characteristics as the reference scanner, therefore no difference in the spatial resolution was expected between the scanners, except if the differences in intracrystal scatterings have a notable impact on the spatial resolution. To check this and to characterize the scanner's resolution, a Derenzo phantom with hot rods was imaged. The phantom had 6 groups of 4 cm long rods with a diameter of 4.0 mm, 3.6 mm, 3.2 mm, 2.8 mm, 2.4 mm, 2.0 mm, and the separation between the rods was the same as the rod diameter (Figure 4.14). The specific activity was set to a low value (0.1 Bq/mm^3) to suppress the acquisition of random events, and 10^8 events were collected in the simulation.

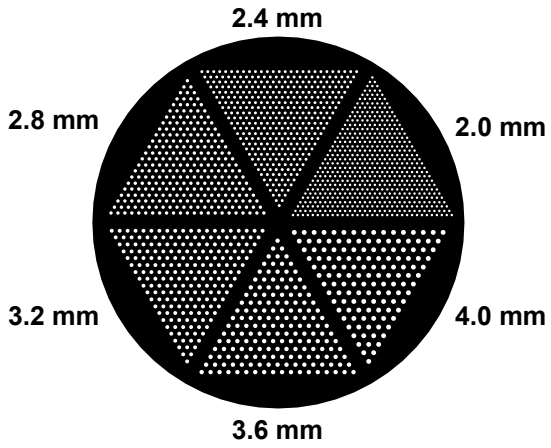

Figure 4.14: A schematic view a Derenzo phantom used in the spatial resolution study.

4.5.3 NEMA Image quality

Because of the complex interplay of different aspects of system performance, it is desirable to be able to compare the image quality of different imaging systems for a standardized imaging situation that simulates a clinical imaging condition. Due to variations in the uptake of radiopharmaceuticals and inpatient sizes and shapes, it is difficult to simulate clinical imaging conditions using a phantom. For these reasons, the results of a single phantom study can only give indications of image quality for that particular imaging situation.

The NEMA standard proposes a measurement which produces images simulating those obtained in a whole-body imaging study with hot spheres. Six spheres of different diameters (37, 28, 22, 17, 13 and 10 mm) are imaged in a thorax-shaped body phantom with non-uniform attenuation (Figure 4.15). Image contrast and background variability ratios for hot spheres are used as measures of image quality. The phantom was positioned in the center of the scanner, and 4 minute scans were simulated. The variance of percent contrast and percent background variability were estimated from 5 independently simulated 4 minute scans.

Analysis

Following the standard in the simulations, the background activity was set to 5.3 kBq/cm^3 (0.14 μCi/cm^3), and the ratio between the hot spheres and the background was 4:1. The transverse slice, one voxel thick and centered on the hot spheres, was used in the analysis. True sphere masks were used as regions of interest (ROIs) for contrast recovery calculations, and partial pixels were also accounted for by expanding the matrix of the reconstructed image by a factor of ten and then including voxels that had their centers within the ROI. ROIs of the same sizes as the ROIs drawn on the hot spheres were drawn in the background of the phantom. Twelve 37 mm diameter ROIs were drawn throughout the background at a distance of at least 15 mm from the edge of the phantom or any of the hot spheres (Figure 4.15). ROIs of smaller sizes were drawn concentric to the 37 mm background ROIs. The ROIs were also drawn on the slices closest to the +2 cm, +1 cm, -1 cm, -2 cm on either side of the central slice. Thus, a total of 60 background ROIs of each size, 12 ROIs on each of five slices, were drawn.

The percent contrast $Q_{H,j}$ for each hot sphere j was calculated as:

$$Q_{H,j} = \frac{(C_{H,j}/C_{B,j}) - 1}{(a_H/a_B) - 1} \tag{4.4}$$

where $C_{H,j}$ is the average number of counts in the ROI for sphere j and $C_{B,j}$ is the average of the background ROI counts for sphere j. a_H and a_B are activity concentration in the hot spheres and in the background, respectively, and thus the ratio a_H/a_B was equal to 4.

The background variability N_j for each sphere j was calculated as:

$$N_j = \frac{SD_j}{C_{B,j}} \tag{4.5}$$

where SD_j is the standard deviation of the background ROI counts for sphere j, calculated as:

$$SD_j = \sqrt{\sum_{k=1}^{K} (C_{B,j,k} - C_{B,j})^2/(K-1)} \tag{4.6}$$

where the sum is taken over the $K = 60$ background ROIs.

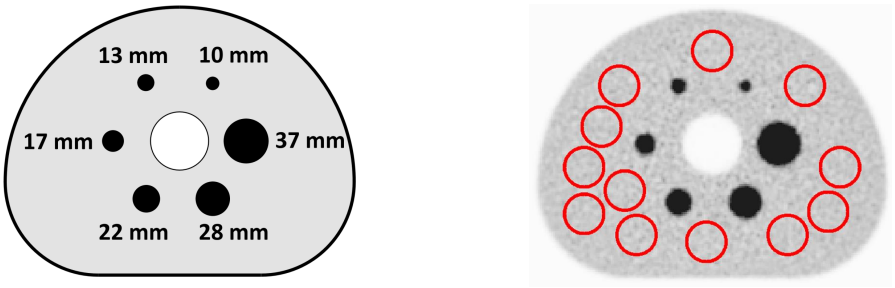

Figure 4.15: Schematic view of an NEMA image quality phantom (left) and an example of 12 background spheres selection from a slice of a reconstructed image (right).

Correction factors

The true attenuation map (Figure 4.16) was used for computing attenuation correction factors following the Equation 2.9. The process of scatter and random correction is illustrated in Figure 4.17. The scatter and random correction method was based on the assumption that the reconstruction method is linear and that different types of coincidences (trues, scatters, randoms) can be reconstructed independently. With this assumption, the scatter and random corrected image was obtained by subtracting from the image where all coincidences in the reconstruction were used, an image reconstructed from only scatter and random coincidences obtained from a separate simulation.

Since OSEM is not a linear algorithm, the introduced error due to the linearity assumption was evaluated. The reconstructed NEMA images using all coincidences were compared with those obtained by separately reconstructing true and scatter&random images and then adding them. The comparison was made both for the reference and the Cherenkov scanner. Although the relative difference on the voxel

level was up to a few percent, the impact on percent contrast for all the hot spheres was below 1%, and the impact on background variability was about 1%, meaning that OSEM algorithm behaves quite linearly, at least in the studied regime - using 8 iterations and 5 subsets.

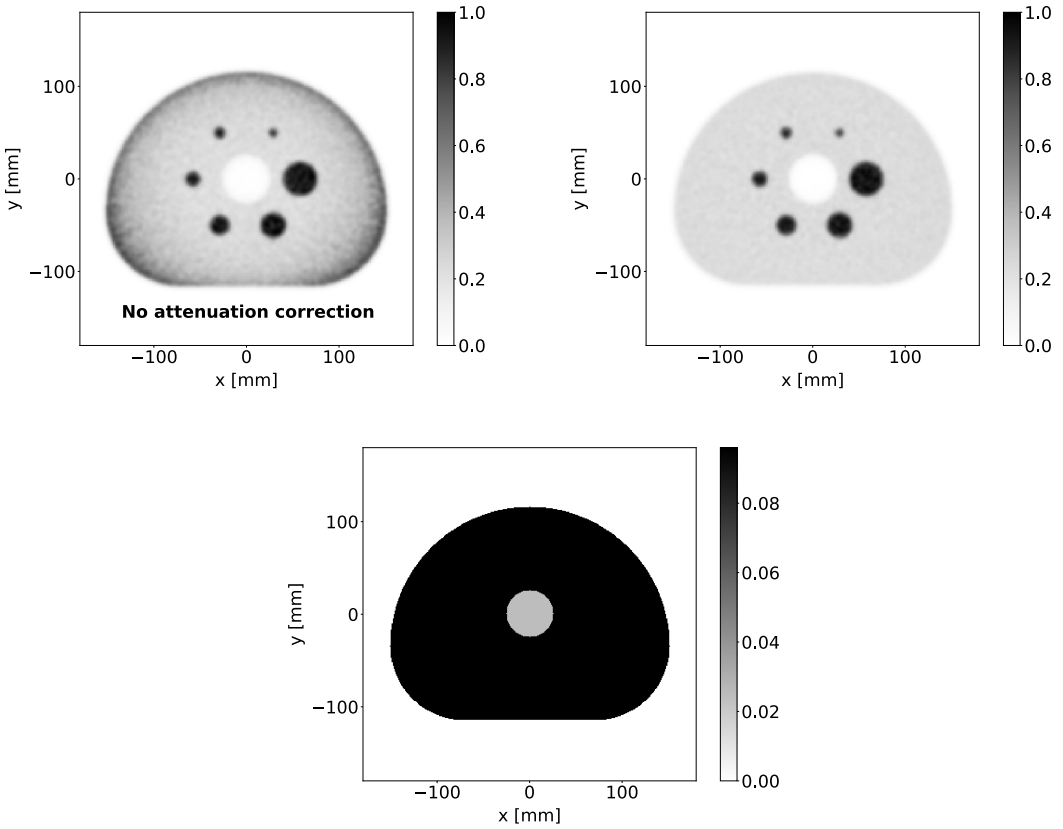

Figure 4.16: *Top:* Reconstructed image of the reference scanner without and with attenuation correction. *Bottom:* Attenuation image used for computing the attenuation correction factors. The attenuation coefficient of water at 511 keV is 0.096 cm^{-1} and 0.025 cm^{-1} for the cylindrical insert (modeling the lung region).

4.6 Long axial field of view Cherenkov PET scanner

To test the scalebility and performance of pure Cherenkov detectors with extended AFOV, the number of detector rings was increased by 4 times. The geometry of the studied PET scanner is shown in Figure 4.18. This increase follows the design of Siemens Biograph Vision Quadra PET/CT system [119] and gives the scanners an AFOV of 106 cm. The 1-sided and 2-sided Cherenkov designs were considered in this study as well as the extended LSO-based reference scanner. In the simulations, the axial length of modules was increased by a factor of four, while the other simulation parameters were kept the same as in the whole-body scanner study.

A four-dimensional (4D) eXtended CArdiac-Torso (XCAT) highly anatomically detailed phantom [120, 121] was used to evaluate the performance of a long axial FOV system. These phantoms were developed to provide accurate computerized models of human anatomy and physiology. The default male voxelized model was used in the study and it was cropped at the thighs so that the whole model was

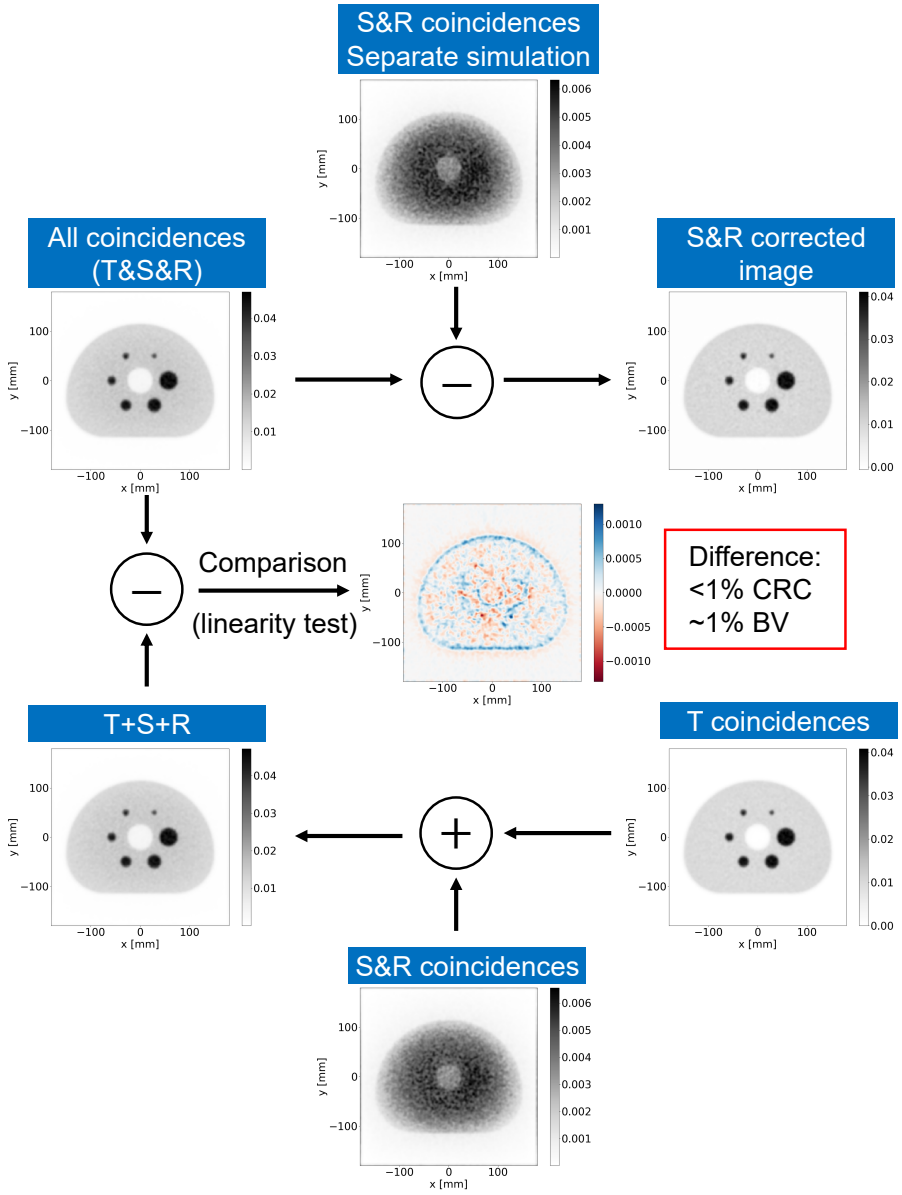

Figure 4.17: Graphical illustration of the method used for scatter and random correction. The used notation is T-true, S-scatter, and R-random coincidences. Because this method assumes that the reconstruction method is linear, a linearity test was performed by comparing the reconstructed NEMA images using all coincidences (T&S&R) with the images T+S+R obtained by separately reconstructing T and S&R images and then adding them. The comparison showed that OSEM is satisfactorily linear - only minor (negligible) differences in percent contrast (CRC - contrast recovery coefficient) and background variability (BV) are observed for all the hot spheres.

approximately 1 m long and fitted whole inside the long AFOV scanner.

The phantom consisted of a $330 \times 200 \times 90$ matrix with $3 \times 3 \times 3$ mm^3 voxel. Figure 4.19 shows the attenuation image, also used for attenuation correction during image reconstruction, and the material map of the phantom, where 18 different materials - defined by the density and elemental composition - were considered in the GATE simulation and are listed in the Appendix A.

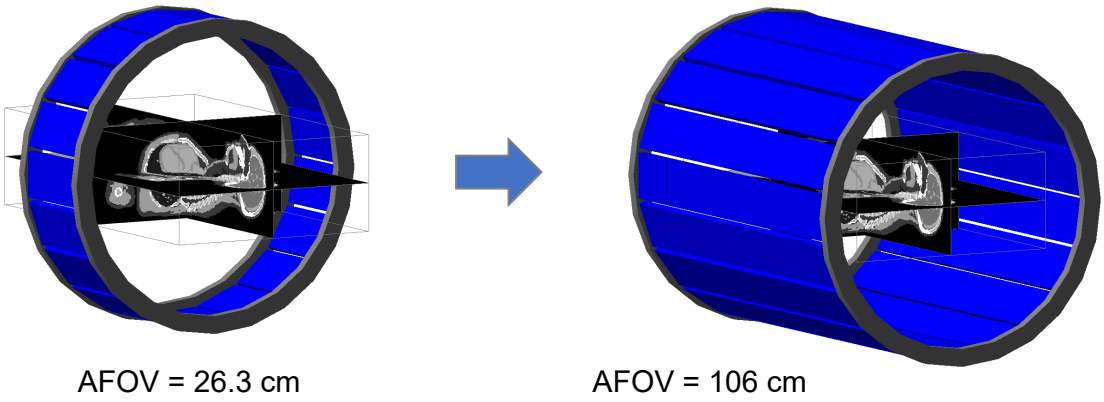

Figure 4.18: A schematic view of a the standard and long axial field of view PET scanner used in the simulations with an inserted XCAT highly anatomically detailed phantom.

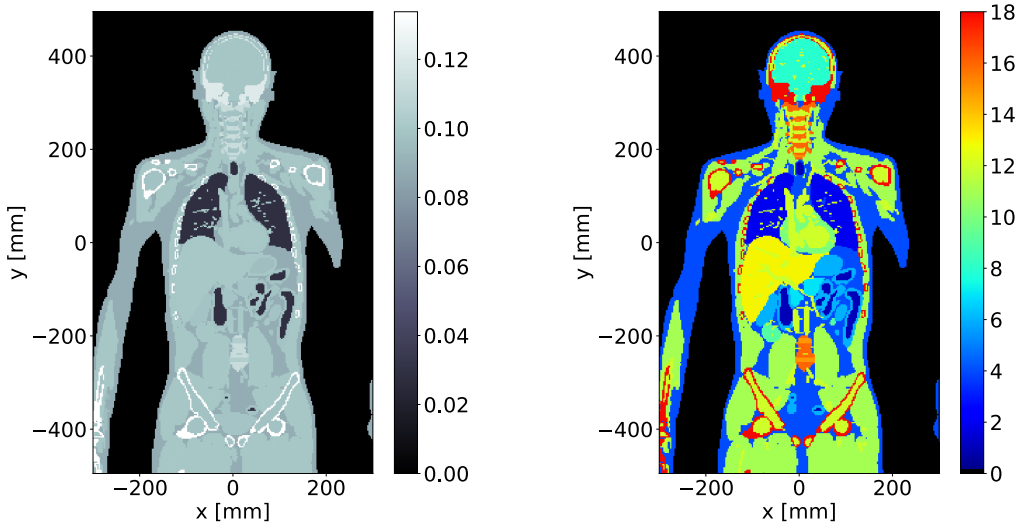

Figure 4.19: *Left:* Attenuation image used for computing the attenuation correction factors. *Right:* The map of 18 different materials defined in the GATE simulation.

The activity ratios between the organs and tissues was set according to the paper by Zincirkeser *et al.* 2007 [122], and following the NEMA standard, the activity of background (tissues with the standardized uptake value of one) was set to 5.3 kBq/cm^3. Two separate 15 second scans were simulated where one was used for scatter and random correction as described in the previous section. TOF-OSEM algorithm with 8 iterations and 5 subsets was used in the reconstruction, and a 5 mm FWHM Gaussian postfilter was applied. The simulated datasets were reconstructed on the matrix with $3 \times 3 \times 3$ mm^3 sized voxels.

Two quantitative measures were used to evaluate the differences between the reference (simulation input) and the reconstructed images: normalized root-mean-square error (NRMSE) and the structural similarity index (SSIM). There are no consistent means of normalization of the root-mean-square error (RMSE). In this study, we used the mean of the measured data:

$$\text{NRMSE} = \frac{1}{\bar{y}}\sqrt{\frac{1}{n}\sum_{i=1}^{n}(y_i - x_i)^2} \tag{4.7}$$

where y_i is the intensity in the i-th voxel of the reconstructed image, $\bar{y} = \frac{1}{n}\sum_{i=1}^{n} y_i$ is the average intensity, and x_i is the intensity in the i-th voxel of the simulation input - ground truth image.

A structure similarity index was used as a quantitative perceptional measure that accounts for patch-wise image statistics

$$\text{SSIM}(x, y) = \frac{(2\mu_x\mu_y + C_1)(2\sigma_{xy} + C_2)}{(\mu_x^2 + \mu_y^2 + C_1)(\sigma_x^2 + \sigma_y^2 + C_2)} \tag{4.8}$$

where mean (μ), variance (σ^2) and covariance (σ_{xy}) represent local statistics in a patch of the reference image - x and reconstructed image - y. C_1 and C_2 are stabilizing terms. Following [123], a sliding window with a side-length of 11 to move voxel-by-voxel over the entire image was used, and each patch had its mean and variance spatially weighted by a normalized Gaussian kernel with a standard deviation of 1.5. An SSIM index map is obtained in this manner. NRMSE and the SSIM were not evaluated on the whole image but only on the phantom region and a mean SSIM (MSSIM) index was used as a single overall quality measure of the reconstructed image.

To better understand the particular values of NRMSE and MSSIM, their behavior was tested under 3 image degradation effects:

- changed contrast (added constant background)
- noise (Gaussian noise added uniformly)
- reduced spatial resolution (image processed with a Gaussian filter)

Figure 4.20 shows the images modified by degrading effects, where the targeted MSSIMs were 0.7, 0.5, and 0.3. MSSIM is not very sensitive to changes in contrast, compared to NRMSE, but it is very sensitive to noise which changes local patterns in the image.

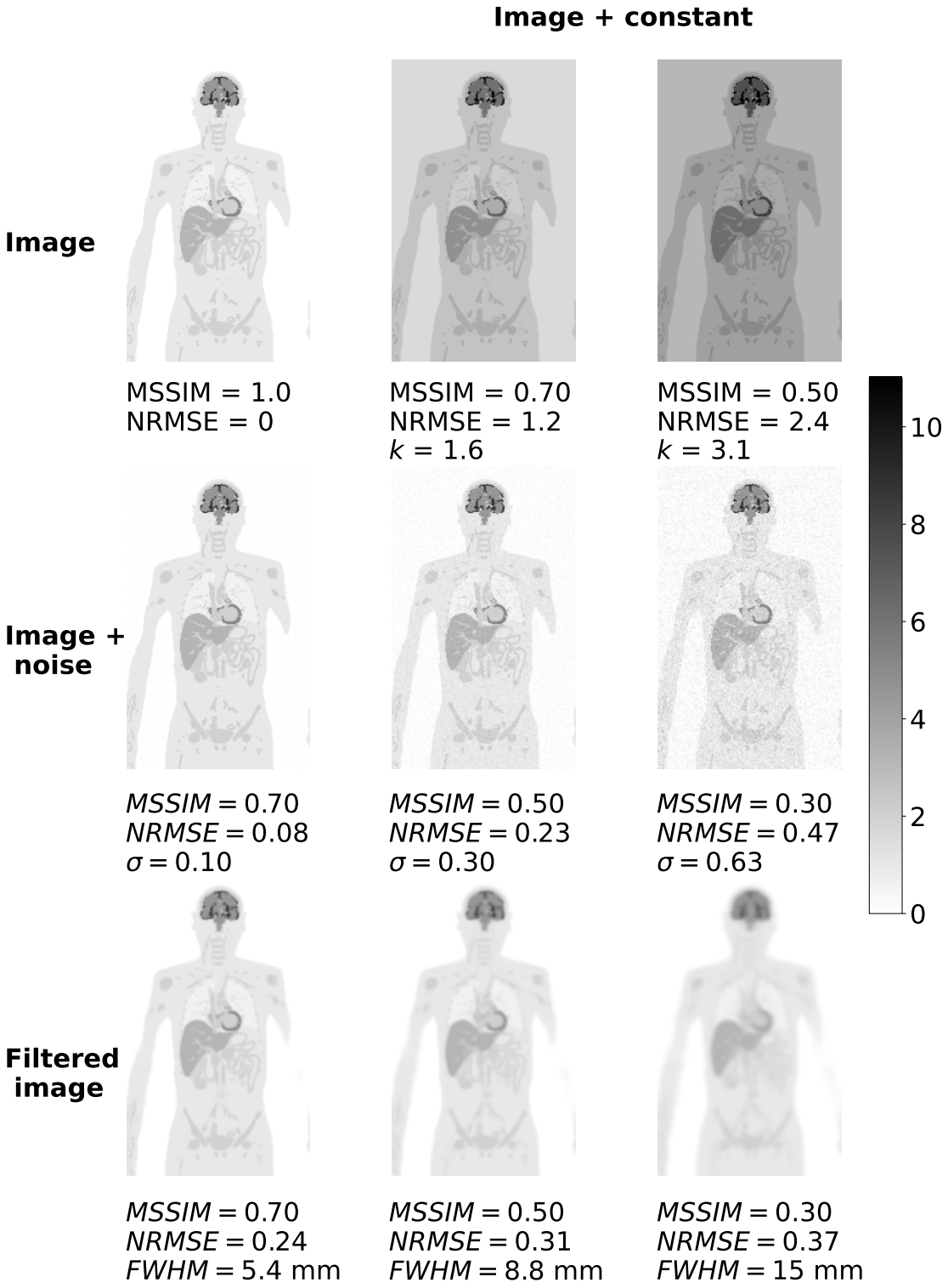

Figure 4.20: Demonstration of image degrading effects on MSSIM and NRMSE metrics. The reference activity distribution (top-left) modified by adding a constant (k), normally distributed noise (σ), or filtering the image with a Gaussian filter ($FWHM$). The k and σ are in the SUV scale.

5. Results

5.1 Detector study

In the detector study, Cherenkov detectors based on the $3.2 \times 3.2 \times 20$ mm^3 PbF_2 crystals with multi-sided crystal readout and with two different surface treatments - black and reflective coating - were investigated. Coincidence detection efficiency, CTR, and FOM were evaluated and compared. The results are shown in Table 5.1.

Table 5.1: Performances of different sensor designs in terms of figure-of-merit (FOM). The FOM is defined as the ratio between the coincidence detection efficiency (ϵ^2) and CTR (Eq. 4.2). Two SPTR values of the photo-detector were considered: 0 ps and 70 ps. The color shadings indicate detector designs used in the whole-body scanner study.

	Cherenkov detector	Surface treatment	Light transfer efficiency (%)	ε^2 (%)	CTR-FWHM (ps)		FOM	
					0 ps SPTR	70 ps SPTR	0 ps SPTR	70 ps SPTR
	Single-sided	Black	17.2	8.6	100.7	145.5	0.85	0.59
		Reflector	51.6	35.3	135.7	184.8	2.60	1.91
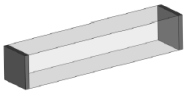	Dual-ended	Black	26.3	17.6	183.4	206.2	0.96	0.85
		Reflector	55.9	35.2	192.7	229.7	1.83	1.53
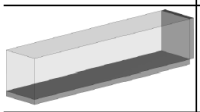	End-lateral	Black	31.9	22.1	67.2	156.1	3.29	1.42
		Reflector	76.0	41.7	80.0	137.8	5.21	3.02
	Dual-lateral	Black	37.5	26.2	47.0	111.1	5.57	2.36
		Reflector	71.1	40.5	48.9	117.8	8.28	3.44
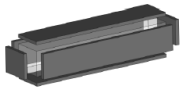	All-sided	/	94.5	44.4	54.1	115.4	8.21	3.85

Black painted crystals achieve better CTRs than crystals wrapped in a reflector. However, their significantly lower coincidence detection efficiency, as a result of lower light transfer efficiency, resulted in lower FOMs. In the single-sided black pained crystals, only about 17% of emitted photons reach the photo-detector and have a chance of being detected. In contrast, this number increases to about 50% when wrapping the crystals with a reflector. Among the detectors with a 2-sided readout, the configuration with lateral readout resulted in the best FOM, mainly thanks to the superior CTR (Figure 5.1; *Dual-lateral* Cherenkov detector), compared to the Dual-ended and End-lateral 2-sided readouts. As expected, the highest LTE of about 95%, and consequently the highest coincidence detection efficiency, was

achieved with the All-sided readout. Interestingly, the FOM of the 2-sided detector design with lateral readout is only about 10% worse than the FOM of the All-sided readout due to the 10% worse coincidence detection efficiency, while it achieves the same CTR, 120 ps, when rounded to two significant digits.

The coincidence time distributions of selected detector designs - obtained by histogramming the difference in detection times of the two detectors in coincidence - are shown in Figure 5.1.

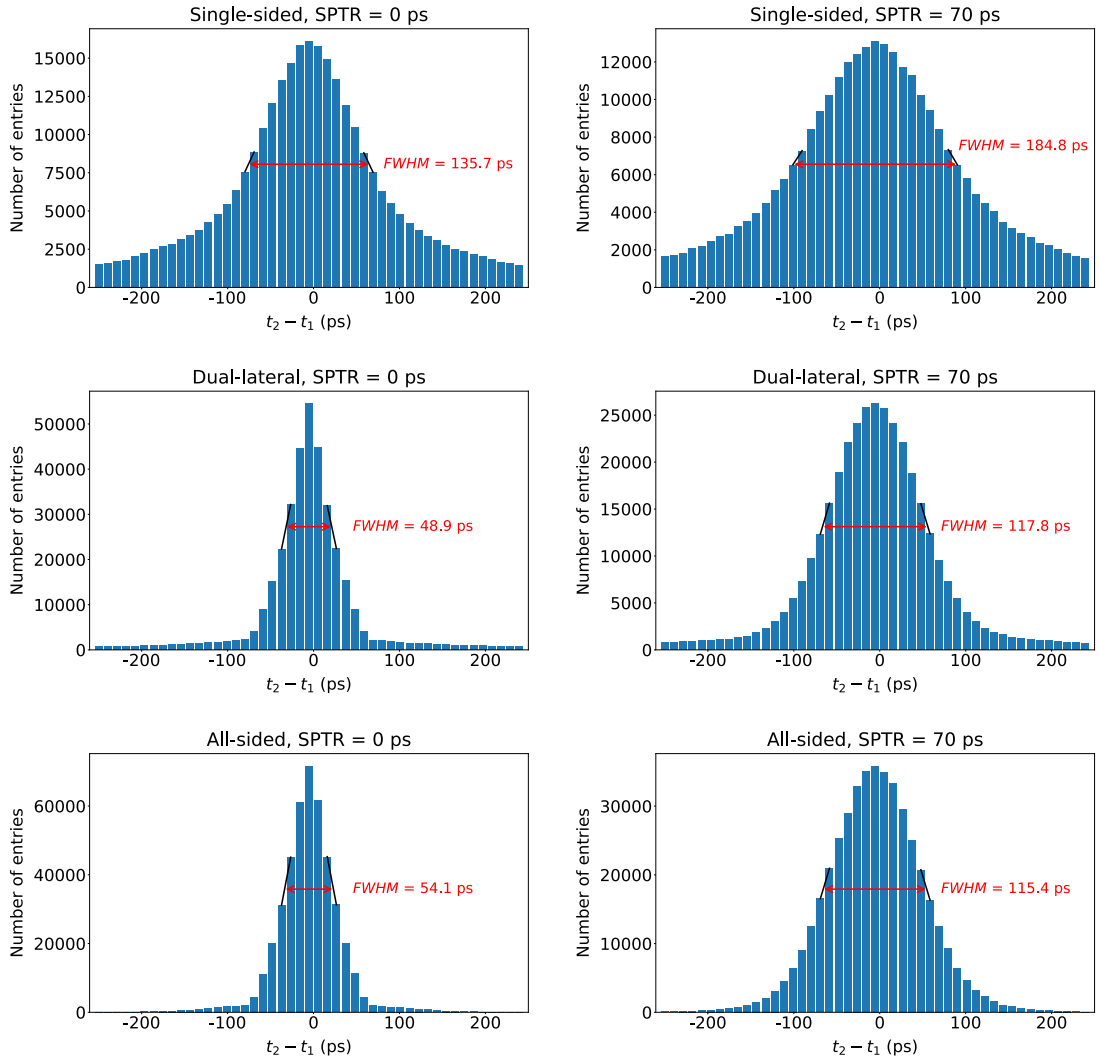

Figure 5.1: The coincidence time distributions of the Cherenkov detector designs used in the whole-body scanner study (top to bottom): Single-sided, Dual-lateral and All-sided readout. The crystals in Single-sided and Dual-lateral design were wrapped with a reflector. The left column are distributions simulated using a photodetector with perfect timing resolution; SPTR = 0 ps, and the right column with realistic timing resolution; SPTR = 70 ps.

Note that the histogram of time differences for a whole-body scanner is slightly different from a single back-to-back detector pair (Figure 4.12), as annihilation gammas can hit the detectors at different angles, changing the mean depth of interaction and the angular distribution of the emitted Cherenkov photons. There is also an impact of intracrystal scattering, where gammas scatter inside and also among

PET modules, potentially forming additional coincidence pairs (due to using GATE *takeAllGoods* policy), and this effect is not present in the single detector pair configuration.

Setting the SPTR of the photo-detector to 0 ps, we get an estimate of the optical travel time spread (OTTS). For a Single-sided readout, the CTR due to OTTS is 136 ps, and by adding the SPTR of 70 ps, the CTR degrades to 185 ps. Using Equation 3.9, we would predict the CTR of 168 ps, but because the optical transfer time spread has long tails (is not Gaussian), Equation 3.9 has limited accuracy in predicting the FWHM of the resulting coincidence time distribution.

For reference, LSO crystals were also simulated in the same back-to-back crystal configuration with 10% energy resolution and a 435-585 keV energy window and obtained a coincidence detection efficiency of 17.6%. However, this value has to be compared to Cherenkov detectors with caution. The described setup does not test scatter-rejection and does not account for intracrystal scatterings that can result in accepted events in a full-sized detector (scanner). Therefore, comparing count rates at the system level between the Cherenkov-based and scintillation-based scanner is more appropriate.

Figure 5.2 shows the distribution of the emitted Cherenkov photons in PbF_2 crystal following a 511 keV gamma interaction. The direct photoelectric effect is followed by an average of 19.4 emitted Cherenkov photons, while any interaction or combination of interactions - that resulted in at least one produced Cherenkov photon - produces, on average, 14.5 Cherenkov photons. These simulated results agree well with the predicted intrinsic Cherenkov photon yield of 16.5±3.3 estimated for PbF_2 from measurements [6].

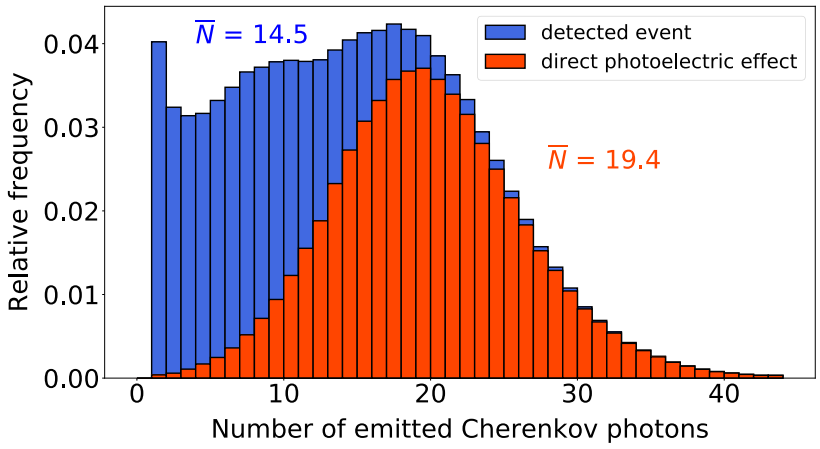

Figure 5.2: Distribution of the emitted Cherenkov photons in PbF_2 following a 511 keV gamma interaction that produced at least one Cherenkov photon. Cherenkov photon(s) can be produced as a result of a single or multiple gamma interaction in the crystal, e.g., multiple scatterings and then photo-absorption.

The events detected through the direct photoelectric effect in Figure 5.2 represent about 57% of all detected events while the photofraction of PbF_2 is 46% (Table 3.1). This difference is because a fraction of the events, where the gamma is scattered first, does not produce Cherenkov photons, and therefore such events are not counted as detected.

The average number of emitted Cherenkov photons in PbF_2 increases with increasing incident gamma energy (Figure 5.3). The threshold for Cherenkov photon production is at about 100 keV, and the gammas with energy below approximately 300 keV are almost exclusively detected through the direct photoelectric effect.

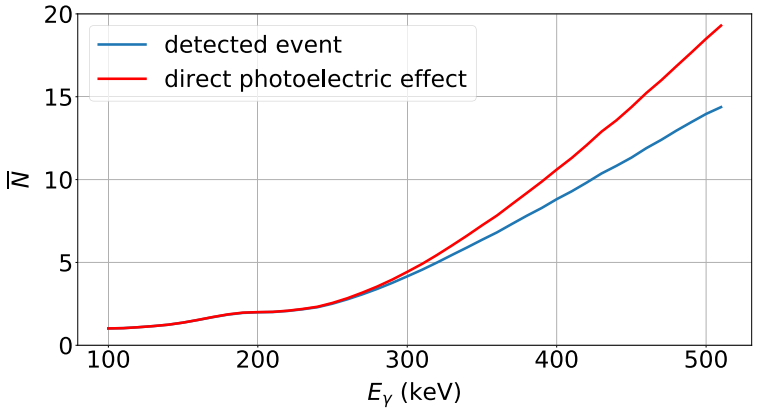

Figure 5.3: Average number of the emitted Cherenkov photons in PbF_2 as a function of energy of the incident gamma ray. The energy scale goes from production threshold ($\sim$ 100 keV) to 511 keV.

As the emitted Cherenkov photons travel through the crystal and interact at the surfaces, some of them are lost. The wavelength distribution of the emitted Cherenkov photons, photons reaching the photo-detector, and the detected photons, in a Single-sided readout crystal wrapped in a reflector, are shown in Figure 5.4. The absorption length in PbF_2 starts rapidly decreasing at wavelengths shorter than about 300 nm and has a cutoff wavelength at about 250 nm (Figure 4.2). Consequently, Cherenkov photons below 300 nm are more likely to be absorbed in the crystal, and the result can be seen in the spectrum of the Cherenkov photons reaching the photo-detector. The detection spectrum is a convolution of the spectrum of Cherenkov photons reaching the photo-detector and the photon detection efficiency (PDE) of the photo-detector (Figure 4.1). The Cherenkov photons start being detected above 270 nm, where the PDE of the photo-detector becomes non-zero.

Figure 5.5 shows the distribution of the number of detected Cherenkov photons in the selected Cherenkov detectors using an idealistic photo-detector and a photo-detector with a realistic quantum efficiency. In the Single-sided detector design, the average number of detected Cherenkov photons is 7.5 in the ideal case. Based on the emission spectrum (Figure 5.2), 14.5 could, in principle, be detected on average, but not all photons reach the photo-detector resulting in an LTE of 51.6% (Table 5.1).

The average number of detected Cherenkov photons drops to 2.8 with a realistic photo-detector, and events that correspond to only one detected Cherenkov photon account for about 27% of detected events, whereas in the ideal case, they corresponded to only about 7%. The average number of detected Cherenkov photons increases by going to the Dual-lateral or All-sided readout. The quantum efficiency of the photo-detector does not only determine the number of detected Cherenkov photons. For an event to count as detected, at least one Cherenkov photon has to be detected. Therefore, the quantum efficiency also directly impacts the gamma detection efficiency.

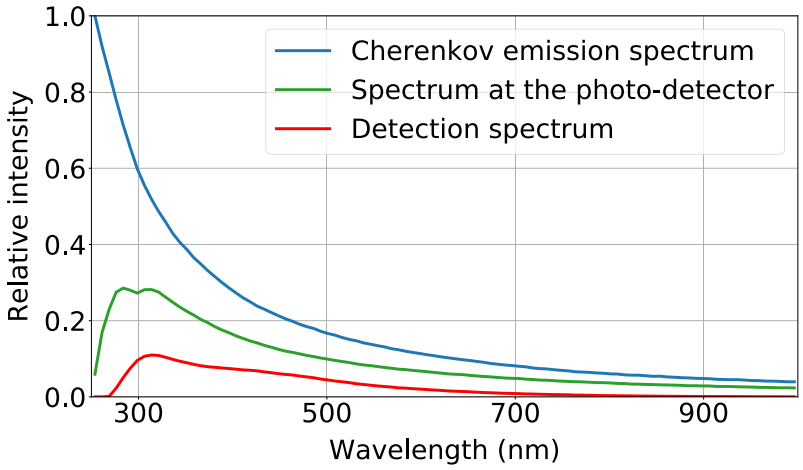

Figure 5.4: Wavelength distribution of the emitted Cherenkov photons, photons reaching the photodetector, and detected photons in a Single-sided readout crystal wrapped in a reflector.

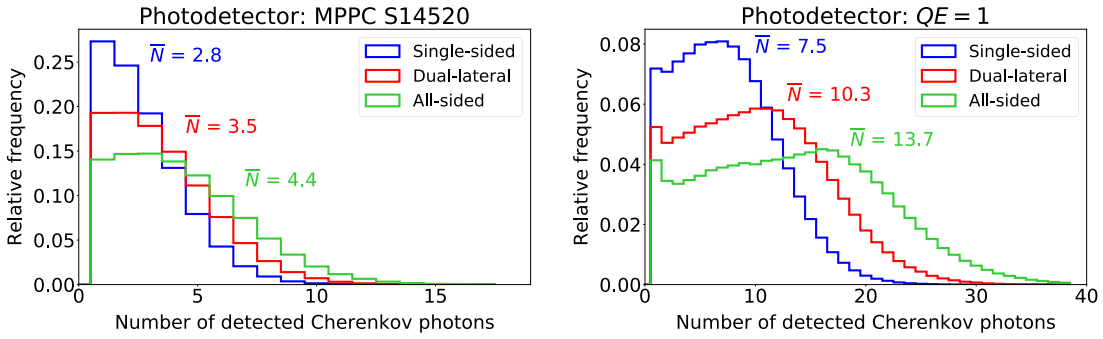

Figure 5.5: Distribution of the detected Cherenkov photons in the Cherenkov detectors designs used in the whole-body scanner study coupled to a realistic (left) and idealistic (right) photo-detector. The average number of detected Cherenkov photons increases with increasing number of readout sides.

The detection efficiency as a function of energy of the incident gamma-ray for the selected Cherenkov detectors is shown in Figure 5.6. As the average number of detected Cherenkov photons increase, so does the detection efficiency when using detectors with multi-sided readout or ideal/better photo-detectors. Gamma rays with lower energies are less likely to be detected, with no detection probability below the threshold of Cherenkov photon production, which in PbF_2 is about 100 keV. This represents a built-in intrinsic mechanism suppressing an important part of events, scattered in the patient's body. Although the number of produced Cherenkov photons increases with deposited gamma energy, which in turn increases the probability of detecting the event in a Cherenkov detector, the attenuation coefficient and photofraction decrease with gamma energy (Figure 3.8), meaning the higher energy gamma is less likely to interact in the detector and also is more likely to deposit only a fraction of its energy due to scattering, resulting in a plateau or even a decrease in detection efficiency at higher gamma energies (Figure 5.6).

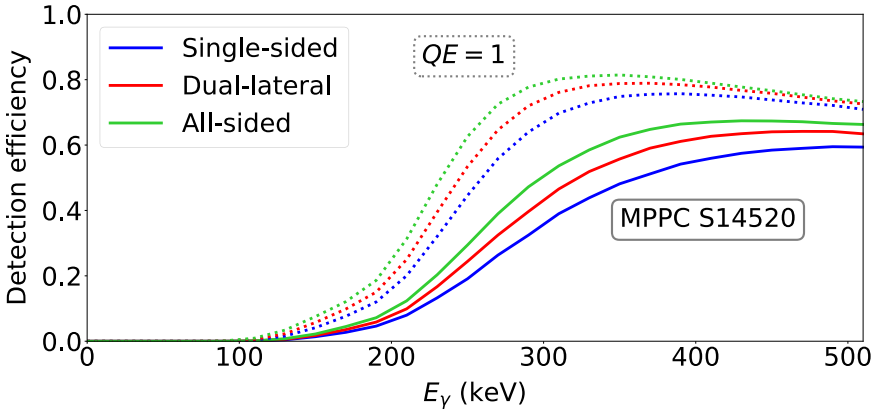

Figure 5.6: The detection efficiency of Cherenkov detector as a function of energy of the incident gamma ray. The doted line shows performances of detectors coupled to an ideal photo-detector, while the solid line is for detectors coupled to a realistic photo-detector (MPPC S14520).

5.2 Simulation of a whole-body TOF PET Cherenkov scanner

Single-sided, Dual-lateral, and All-sided detector designs were selected for a whole-body scanner study. The naming of the selected detector designs is now shortened to:

- Single-sided → 1-sided
- Dual-lateral → 2-sided
- All-sided → 6-sided

5.2.1 NECR and Scatter fraction

First, a NECR and SF comparison between the Cherenkov scanner and the reference Siemens Biograph Vision scanner was performed (Figure 5.7). The NECR curve of the Cherenkov scanner with a 1-sided readout is very similar to that of the reference scanner, even though it has a notably higher SF - 47.3%, compared to the reference scanner's 32.5%. The best NECR is achieved by the 6-sided Cherenkov scanner, while the 2-sided design lies in-between, with its NECR closer to the 6-sided design than the 1-sided Cherenkov scanner. The SF of just below 50% are observed for all the Cherenkov scanners. The increased detection of scatter coincidences in the Cherenkov scanners is compensated by a higher detection efficiency of true coincidences leading to the same or better NECR values.

There is a good agreement between the simulated NECR values for the reference scanner and the values measured on the Siemens Biograph Vision scanner at lower (clinically relevant FDG) activities, but a little less so at higher activities, which was expected due to the omission of the detector's dead-time in the simulation. Focusing only on the count rates, the NECR values were not modified with TOF information (effective NECR), which would benefit Cherenkov scanners the most.

The impact of the diameter of the cylindrical phantom on the NECR (Figure 5.8) and scatter fraction (Figure 5.9) was also investigated. As expected, the scatter

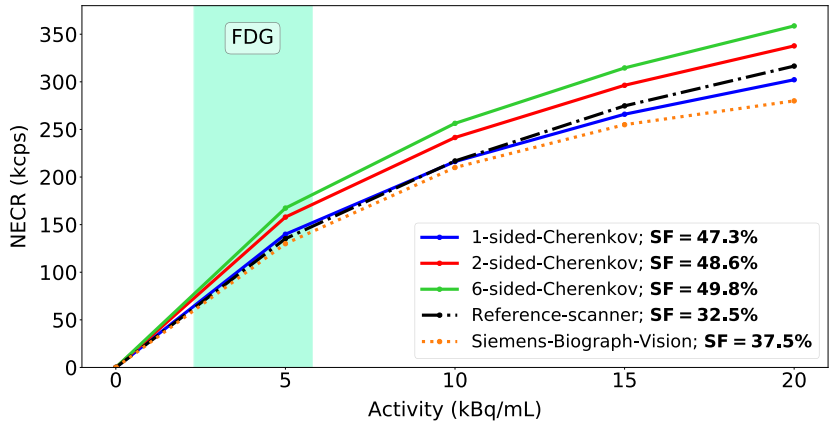

Figure 5.7: NECR values as a function of the activity: a comparison between the Cherenkov scanners, the simulated reference scanner, and measurements performed on Siemens Biograph Vision [114]. The scatter fractions of different scanners are shown in the legend. The shaded rectangle shows the typical range of activities used at the start of clinical FDG whole-body scans.

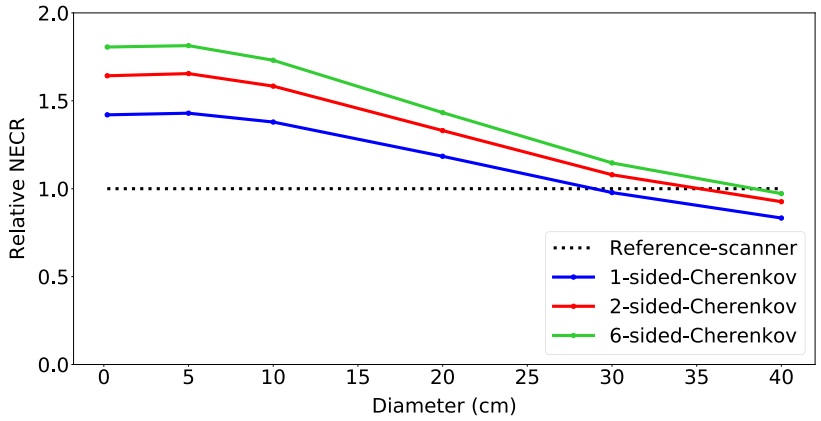

Figure 5.8: Relative NECR values of the Cherenkov scanners, compared to the reference scanner, as a function of the diameter of the cylindrical phantom.

fraction increases for all scanners with the diameter of the phantom and is higher for the Cherenkov scanners for all phantom diameters. Compared to the NEMA standards 20 cm diameter cylindrical phantom with a line source, the scatter fraction is lower when using a 20 cm diameter phantom with homogeneously distributed activity ($\sim 40\%$ vs $\sim 50\%$ for Cherenkov scanners), as the mean path through the phantom of the annihilation gammas is shorter, resulting in the reduced probability for scattering (Appendix B). This example also illustrates the importance of activity distribution, not only the distribution of scatter material, on the NECR and scatter fraction of any scanner.

The higher gamma detection efficiency of the Cherenkov detectors results in a proportionally better NECR compared to the reference scanner when there is almost no scatter material (just a line source). In this case, the NECR of the 1-sided Cherenkov scanner is almost 50% higher than that of the reference scanner. However, the negative impact of scatter coincidences on NECR with the increasing diameter of the phantom is higher for the Cherenkov scanners, resulting in a falling of

relative NECR. The NECR of the Cherenkov scanner with 1-sided readout becomes equivalent to that of the reference scanner at about 30 cm, and for the 2-sided and 6-sided readout at around 35 cm and 40 cm, respectively.

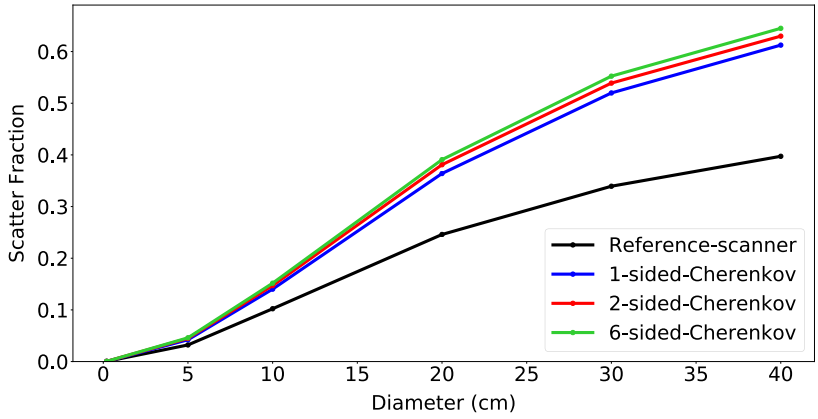

Figure 5.9: Scatter fraction of the studied scanners as a function of the diameter of the cylindrical phantom.

5.2.2 Spatial resolution

Figure 5.10 shows transverse views of the reconstructed images of the Derenzo phantom for the studied scanner designs. Based on visual inspection of the images, the spatial resolution of the scanners seems the same, and we can estimate it to be around 2.8 mm. Activity line profiles through the selected hot rods for the 1-sided Cherenkov scanner, are shown in Figure 5.11. Comparing the line profiles between the scanners (Figure 5.12), we can observe a slightly higher difference between the peaks and the valleys, meaning higher resolution (sharper) images of 2-sided and 6-sided Cherenkov scanners compared to the 1-sided Cherenkov and reference scanner. This difference can be explained by a faster convergence of the iterative (OSEM) algorithm due to better TOF information. The difference between the peaks and the valleys is also getting smaller from the center of the FOV towards the edge (from right to left on the profiles in Figure 5.12). This shows (expected) degradation of spatial resolution due to the depth-of-interaction effect.

5.2.3 Image quality

The thorax-shaped phantom with hot spheres was imaged, and firstly, the impact of the timing kernel - used during image reconstruction - on the image quality was investigated. Figure 5.13 shows transverse images of the NEMA image quality phantom, where a single Gaussian and a double Gaussian TOF kernels were used to reconstruct the coincidence events simulated for the Cherenkov scanner with 1-sided readout. Using a double Gaussian TOF kernel with Cherenkov scanners resulted in the improved percent contrast (Figure 5.14). At the same time, there was no difference in the background variability within the estimated uncertainty.

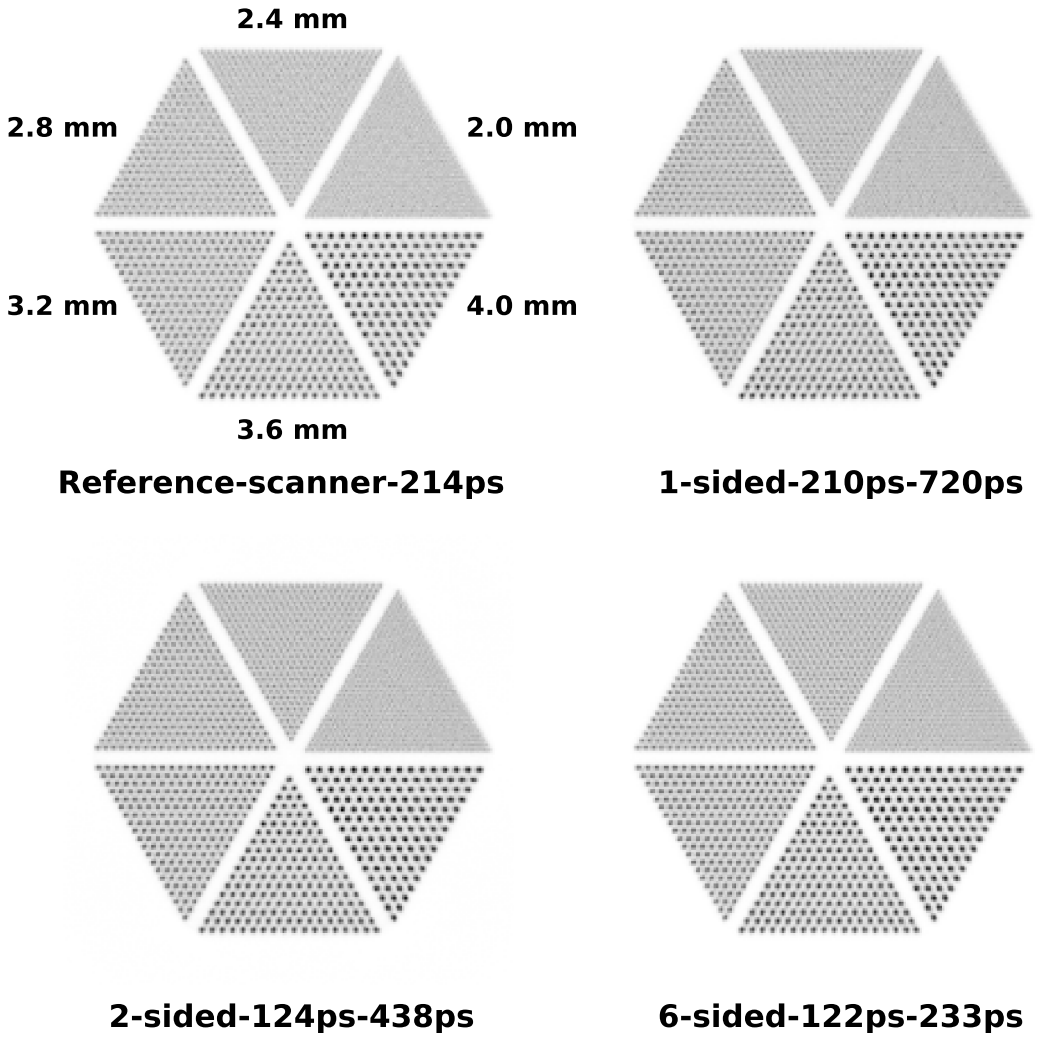

Figure 5.10: Transverse views of the reconstructed images of the Derenzo phantom for the reference scanner and the studied Cherenkov scanners. The OSEM reconstruction with 8 iterations and 5 subsets was done on a $225 \times 225 \times 225$ matrix with $1.6 \times 1.6 \times 1.6$ mm^3 sized voxels (equivalent reconstruction parameters as used in the image quality study).

Additionally, using a standard single Gaussian TOF kernel, which did not fit well the time differences forming the coincidence events (Figure 4.12), resulted in more residual counts in the cylindrical (lung) insert of the NEMA phantom. This effect can be seen in a profile through the selected reconstructed images in Figure 5.15.

Figure 5.16 shows transverse images of the reconstructed phantom for different scanner designs, where a double Gaussian TOF kernel was used in the image reconstruction for Cherenkov scanners with parameters as shown in Figure 4.12 and indicated in the figures. A Gaussian filter of 5 mm, which is clinically often used, was applied to the reconstructed images [114]. The relations between percent contrast and background variability for the studied scanners are shown in Figure 5.17. The relations were calculated from a series of images filtered by a Gaussian post-filter of different widths (FWHM from 0 to 15 mm in steps of 1 mm).

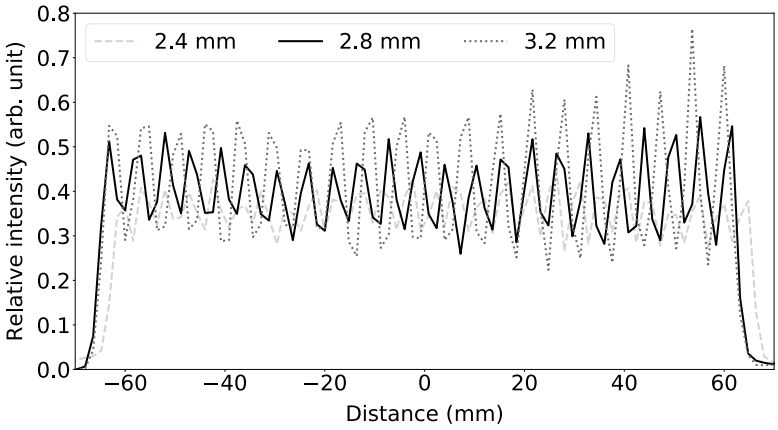

Figure 5.11: 1-sided Chrenkov scanner: activity line profiles through the 2.4 mm, 2.8 mm, and 3.2 mm hot rods obtained from the Derenzo phantom image.

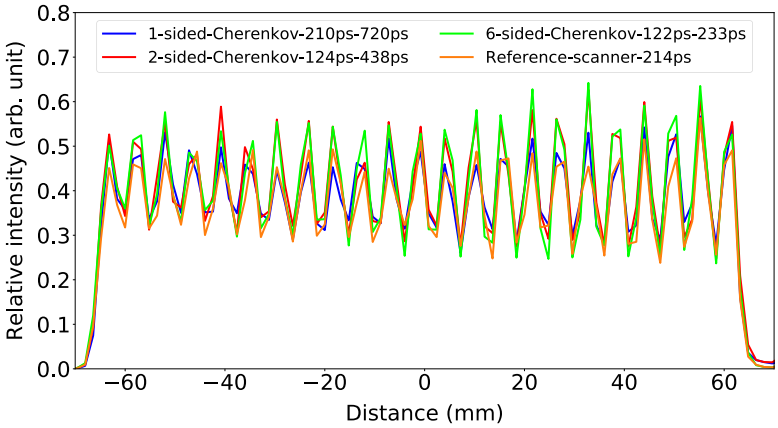

Figure 5.12: Activity line profiles of the 2.8 mm hot rods for different scanner designs.

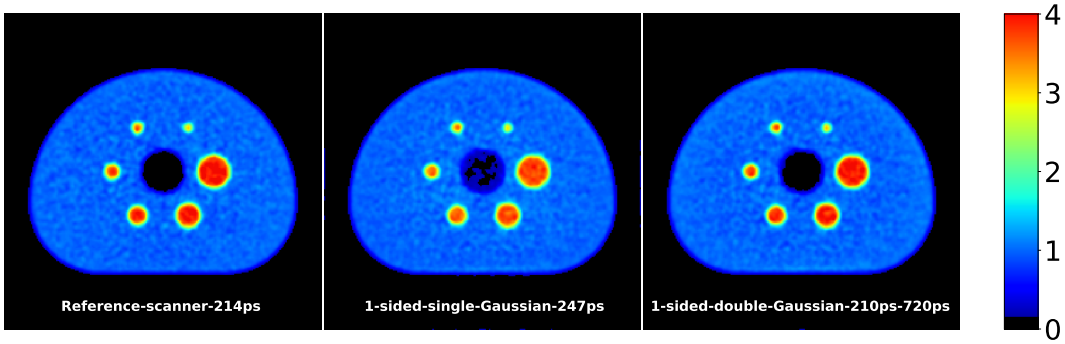

Figure 5.13: Transverse views of the reconstructed images of the NEMA image quality phantom, where two different TOF kernels are compared for the Cherenkov scanners with 1-sided crystal readout. The colormap is chosen in a way to make the residual counts in the cylindrical insert more visible.

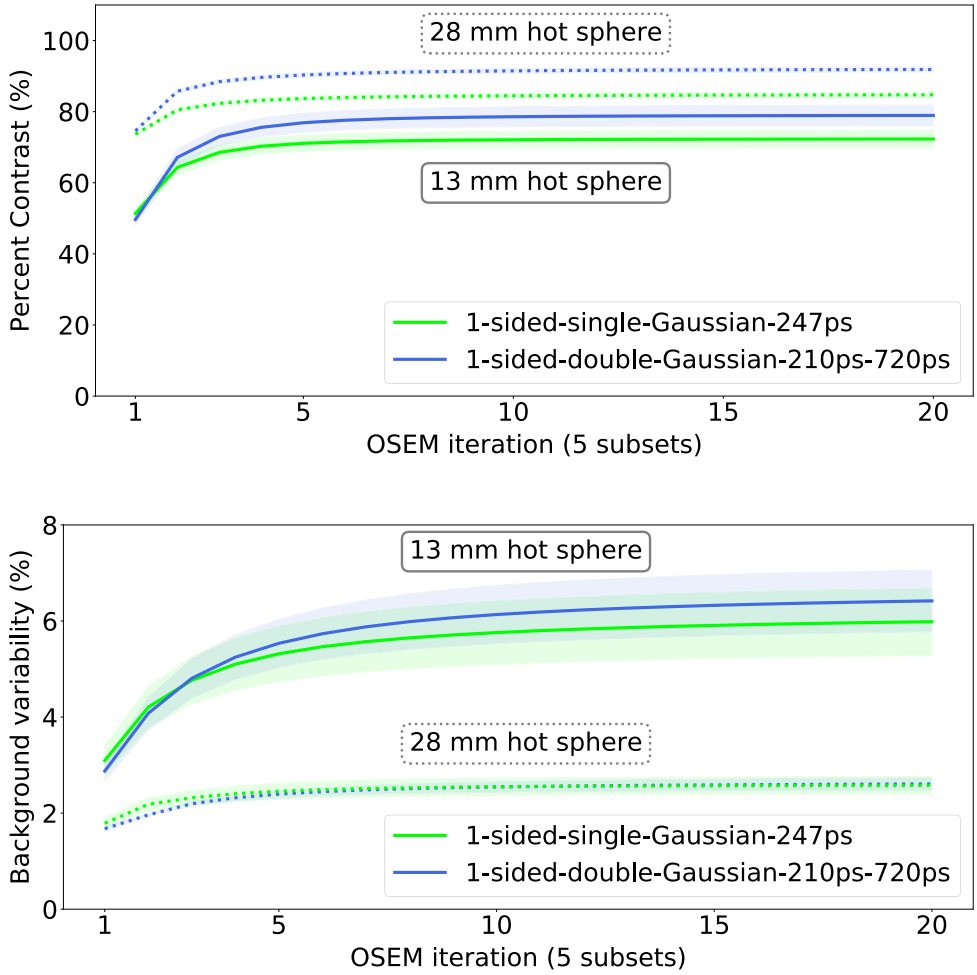

Figure 5.14: Percent contrast (top) and background variability (bottom) for reconstruction with two different TOF kernels as a function of OSEM iteration number, where 5 subsets were used.

Cherenkov scanner with 1-sided readout achieved very similar image quality as the reference scanner, while the 2-sided and the 6-sided designs performed better and can achieve a given percent contrast at lower values of background variability. Note that the percent contrasts of different scanners converge to a similar value, which can be attributed to the similar spatial resolution the scanners achieve. With all the scanners, the background variability converges to about 1%. Using very broad filters, one might expect the background variability to converge to zero, but this would only be the case, if the normalization was perfect and the background spheres were placed at equal distances from the edges dividing different activity levels, which could only be achieved in a phantom with cylindrically symmetric distribution of material and activity.

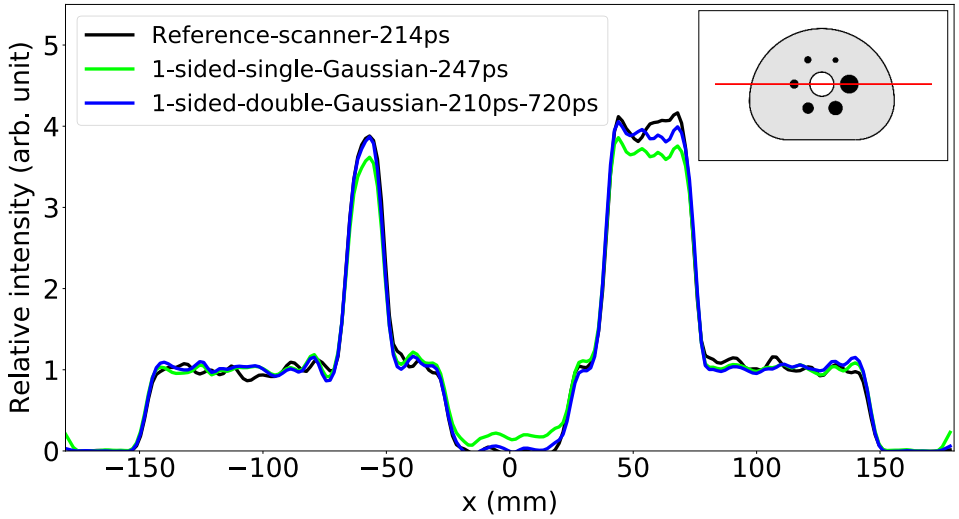

Figure 5.15: A line profile with a cross-section of a single voxel, obtained from reconstructed images of the NEMA image quality phantom. Profiles of the Cherenkov scanners with 1-sided crystal readout are compared, where two different TOF kernels were used during image reconstruction - a single Gaussian (green) and a double Gaussian (blue). A Gaussian post-filter with 5 mm FWHM was used on the images. The profile passes through the 17 mm and 37 mm diameter hot spheres, and shows an improved contrast when using a double Gaussian TOF kerenel.

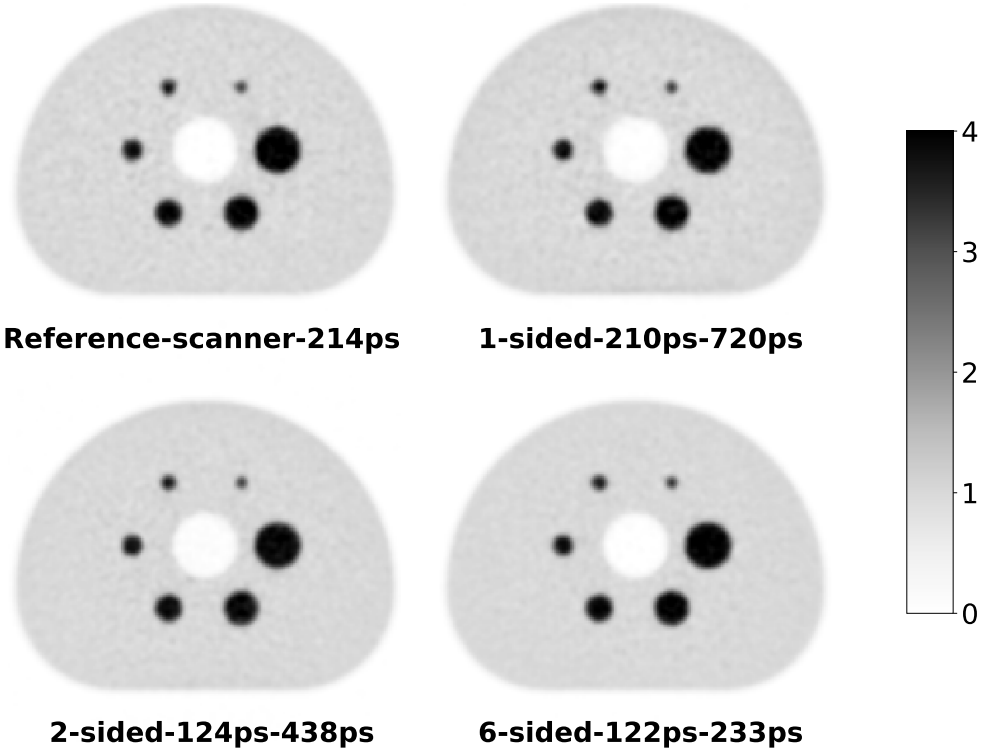

Figure 5.16: Transverse views of the reconstructed images of the NEMA image quality phantom for different scanners. A Gaussian post-filter with 5 mm FWHM was applied on all images.

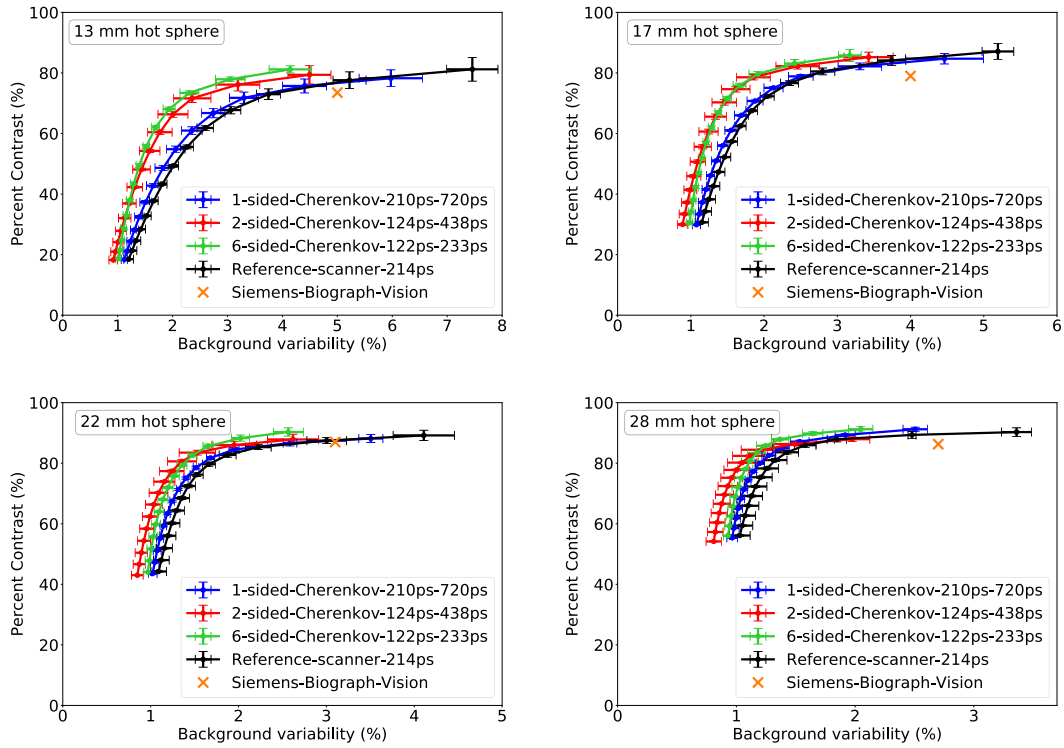

Figure 5.17: Percent contrast vs background variability for a 13 mm, 17 mm, 22 mm and 28 mm diameter hot spheres. Gaussian post-filters with different widths were used to vary the background variability. The measured value of the Siemens Biograph Vision scanner is added for reference [114].

5.3 Long axial field of view Cherenkov PET scanner

Figure 5.18 shows images of the reconstructed XCAT phantom for the scanners with the extended axial field of view. With a visual inspection, one can observe very similar image quality between the extended reference scanner and the extended Cherenkov scanners. This observation is supported by very similar MSSIM and NRMSE values. The extended reference and 2-sided Cherenkov scanners achieve $MSSIM = 0.34$. To make better sense of this number, such a number can be achieved by applying a 13.4 mm FWHM Gaussian filter to the reference distribution or by adding normally distributed noise (with a non-negativity constraint) with a sigma of 0.60 in the SUV scale 4.20.

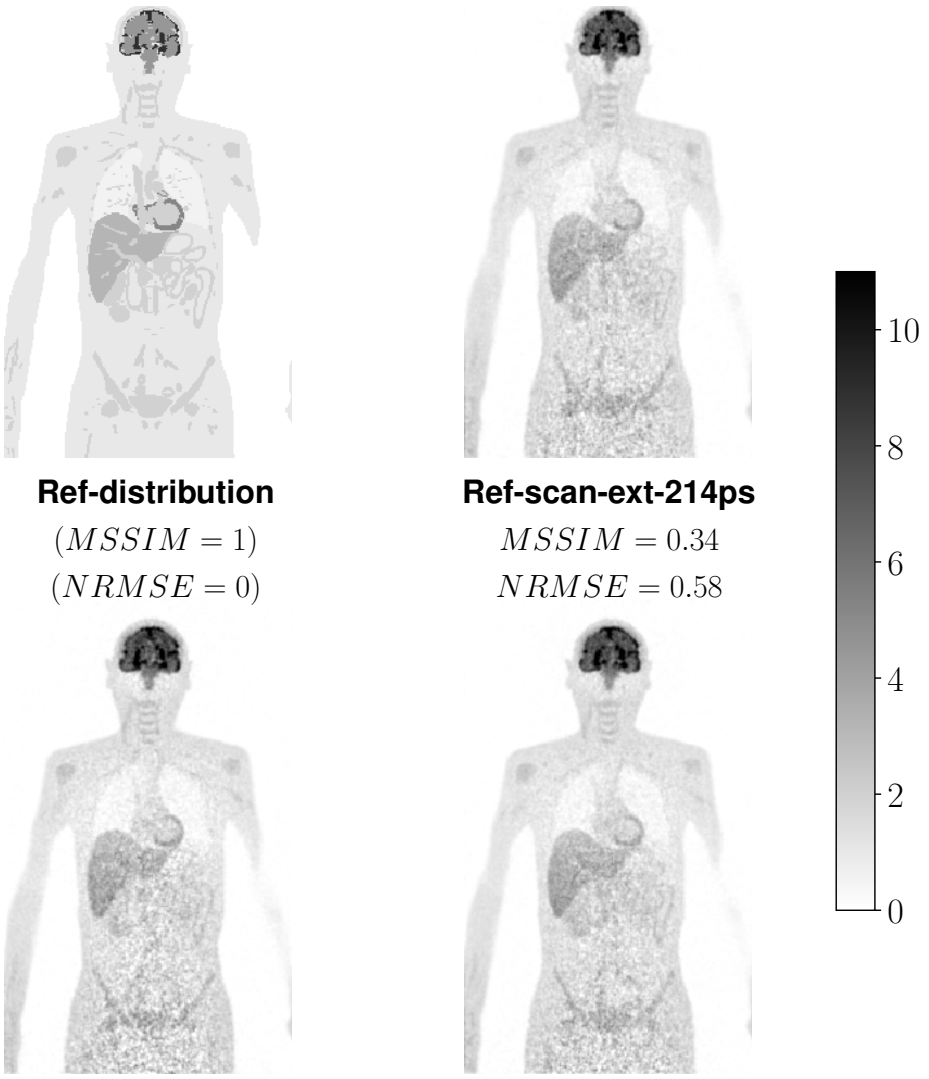

Figure 5.18: Frontal (coronal) plane of the reference distribution and the images reconstructed with the extended reference and Cherenkov scanners.

6. Discussion

6.1 Detector design

The performance and potential of pure Cherenkov detectors and TOF PET scanners based on them were explored using Monte Carlo simulation. In the detector study, crystals with black surface treatments achieve better coincidence time resolutions, but this does not outweigh, based on the figure-of-merit, the decreased coincidence detection efficiency compared to the crystals wrapped with a reflector (Table 5.1). This is true for both the ideal and the realistic timing resolution of the photo-detector. In consequence, most studies in this work focused on detectors using reflective wrappings.

Among the studied 2-sided crystal readouts, the design with photo-detectors placed at the lateral sides of the crystal (Dual-lateral) achieved the best combination of detection efficiency and CTR. The results for a Dual-lateral detector design are comparable to that of the All-sided crystal readout, which served as an idealized reference that probably has limited practical application due to its increased cost, dimensions, and complexity. The detection trigger was set to the first arriving Cherenkov photon, and no time-corrections on the trigger times were used, which could improve CTRs of multi-sided readouts [124].

As discussed in Section 3.5.1, the detection time depends, among other things, on the optical transfer time distribution, and this distribution is also affected by the placement of the photo-detector. Therefore, with multi-sided readout, the time differences of coincidence-forming events can also depend on the relative position of the photo-detectors which detected the first Cherenkov photon. For example, in the Double-ended configuration, the detection time distribution of events where the back-end placed photo-detectors are triggered is different from the distribution where a front-end placed photo-detector triggered for one event and a back-end placed photo-detector triggered for the other event forming the coincidence event. The difference comes from the broken circular symmetry as photo-detectors forming the coincidence event are placed at different lengths from the scanner's axis. This effect does not apply for Dual-lateral readout if the photo-detector at each lateral side is considered (electronically read) as one. However, the effect would become relevant and could be exploited to improve the CTR if the photo-detector was segmented along the main axis of the crystal. The segmentation of the lateral readout could also be combined with the segmentation of the crystal and thus potentially also provide (better) depth-of-interaction information than with an unsegmented crystal (Figure 3.11).

A simple trigger correction method with dual-ended scintillation detectors takes the average of the trigger times of both photo-detectors [125, 126]. In general, the trigger times of both photo-detectors have different variances because of a different

fraction of received optical photons. Thus, a simple average is not the best statistical estimator of the trigger time. An example of a better method is to weigh the corrected trigger times estimated from each photo-detector by the inverse of their variances [127]. In a pure Cherenkov detector, both photo-detectors might not be triggered in a substantial number of events, thus making the previously discussed trigger correction methods less applicable to Cherenkov detectors. A good option, likely worth pursuing, would be to combine experimental data and possibly also Monte Carlo simulation data with deep (convolutional) neural networks [128] to better estimate the time-of-flight from signals obtained by Cherenkov detectors with two or more sided readouts.

In short, there is still much room for improvement of the detectors with multi-sided readouts in terms of CTR and getting depth-of-interaction information.

6.2 Scanner performance

The geometry of the reference scanner and Cherenkov scanners was based on the Siemens Biograph Vision. Consequently, as expected, there was no significant difference in the spatial resolution between the reference and the Cherenkov scanners. In the NECR study, the 1-sided Cherenkov scanner had a similar count rate performance to the reference scanner (Figure 5.7). This was despite a notably higher scatter fraction of 47.3%, compared to the reference scanner's 32.5%. The 6-sided readout achieved the best NECR values, while the 2-sided design (Dual-lateral) was in-between, with its values closer to the 6-sided design than the 1-sided one.

The order of performance of the studied scanners predicted by the NECR analysis was repeated in the NEMA image quality study (Figure 5.17). Cherenkov scanner with 1-sided readout had comparable TOF performance and achieved very similar image quality as the reference scanner. These results thus indicate that there are no theoretical barriers and Cherenkov PET can achieve image quality competitive to the current state-of-the-art despite having no energy resolution to be used for scatter suppression. The similarity in performance between the 1-sided Cherenkov and the reference scanner can also be attribute to the fact that PET scanners using scintillation detectors have a relatively poor energy resolution to begin with and tend to accept a high number of scatter coincidences (SF $>$ 30%, Figure 5.7). By using multi-sided detector designs, even better image quality was achieved.

Although the scatter coincidences are not a show stopper for pure Cherenkov PET, they do impact the Cherenkov scanners more than a scintillation-based scanner, as shown in Figure 5.8. Still, in terms of image quality, the Cherenkov scanners can have a significant edge over scintillation-based scanners, especially for imaging objects of smaller diameters ($<$ 20 cm), such as brain imaging, breast imaging, and also preclinical imaging.

6.3 Geometrical coverage

Cherenkov detectors were also investigated in the long axial field of view PET. Reconstruction and analysis of an anatomically detailed phantom showed that Cherenkov detectors are just as suited for long AFOV imaging as the scintillation detectors. The advantage of Cherenkov detectors lies in their potentially significantly lower cost, which is an important parameter to consider. As discussed in Section 2.11.1, one of the major hurdles of disseminating long AFOV PET scanners to clinics is their larger price which scales approximately linearly with the length of the AFOV [64].

In this study, the photo-detectors were modeled to be of negligible size, meaning that the detector with readouts at the sides (Dual-lateral, All-sided) had basically the same size compared to the detector with the readout at the back of the crystal. Although this is an ideal case, practically, the SiPM can be made very thin, and the detectors with side readouts could be implemented in sparse designs, where not all axial rings are filled with detectors. A feasibility study was done by Zhang *et al.* 2019 [129], showing that removing 50% of detectors in the transverse or the axial direction did not have a major impact on the standard uptake values (SUVs) for a Philips Vereos scanner. A recent Monte Carlo study of the Siemens Biograph Vision PET with extended axial field-of-view (AFOV) using sparse detector module rings configuration [130] reports that sparse design allows extending the current limited AFOV of conventional PET systems by more than 100% at no additional detector material costs and without significantly affecting NEMA contrast recovery, system sensitivity, and transaxial spatial resolution. The concept of sparse design is therefore also viewed as an option for creating total-body PET systems with reduced cost [64], and would be especially suited for the Dual-lateral Cherenkov detector studied here.

6.4 Noise - SiPM dark counts

The main limitation of this study is not including the noise in the simulation - especially the dark count events of the SiPMs - which could notably affect the image quality when the trigger is set to only a single triggered SiPM micro-cell, as it was in this simulation study. The noise of the photo-detectors would increase the number of random events, which would decrease the NECR of the scanner, resulting in more noisy reconstructed images. Noise could also impact image quality by degrading the CTR or the spatial resolution, especially in detector designs that involve multiplexing of signals across many SiPMs. The dark count rate (primary noise) can be greatly reduced by cooling the SiPMs, although a remaining question would be the impact of correlated noise (afterpulsing and optical crosstalk [131]).

To get an estimate of the impact of SiPM's dark count rate (DCR) on image quality, the Poisson noise was simulated at the module level for the 1-sided Cherenkov scanner. The energy distribution of the noise was flat and corresponded to the detection of a single optical photon. Thus, a single noise event was sufficient to go into the coincidence sorter and potentially form a random coincidence event(s). The noise description in GATE uses the distribution of the time intervals between consecutive events. If the probability of detecting k events in a time interval of t is distributed according to the Poisson law $P_1(k,t) = \frac{(\lambda t)^k}{k!}e^{-\lambda t}$, then the probability density of having a time interval in the range $[t; t+dt]$ between two consecutive events is given by $dP_2(t) = \lambda e^{-\lambda t}dt$. Accordingly, a single exponential distribution was defined in the simulations where λ defined the average DCR per PET module. The impact of noise was quantified with the NEMA NECR performance test at the 5 kBq/mL activity level (in the range of typical injected activities for whole-body FDG studies).

Figure 6.1 shows the number of random coincidences and their fraction compared to all the registered coincidences as a function of DCR. The impact of DCR on the NECR is shown in Figure 6.2. The results show that the DCR starts to have a notable effect on the scanner's performance at 10 cps/mm^2, which corresponds to a module count rate of about $3 \cdot 10^5$ cps. At a few 100 cps/mm^2, dark count

coincidences start to dominate all other coincidence types, and the NECR starts falling rapidly. The results suggest that a 1-sided Cherenkov scanner with a trigger set to one optical photon could be usefully operated to about 100 cps/mm^2 DCR, preferably at 10 cps/mm^2 or lower. When considering multi-sided readout, with an increased surface area of SiPMs per crystal, the above DCR values would have to be reduced by approximately the same factor to not degrade the image quality due to additional dark count coincidences.

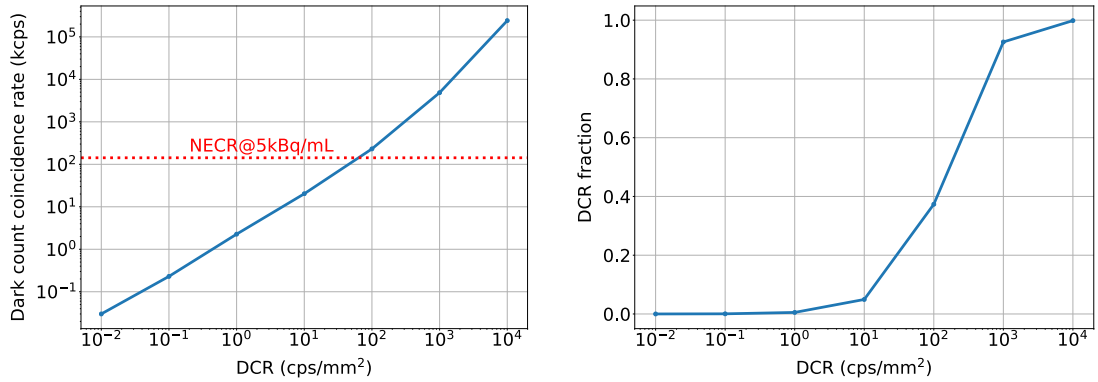

Figure 6.1: The impact of SiPM's DCR on the 1-sided Cherenkov scanner. *Left:* Dark count coincidence rate, representing a fraction of random coincidence rate, as a function of the DCR. The red dotted line shows the NECR at a clinical activity level, when the SiPMs are noise-less. *Right:* The fraction of dark count coincidences, compared to all coincidences, as a function of DCR.

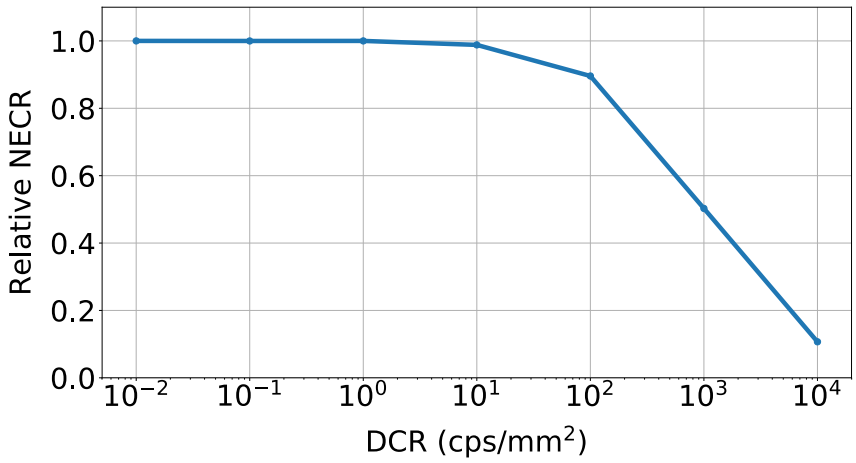

Figure 6.2: Relative NECR of a 1-sided Cherenkov scanner as a function of SiPM's DCR, where the noise-less SiPM serves as reference.

Silicon photomultipliers have very high DCR, typically on the order of 100 kcps/mm^2 at room temperature. However, these can be mitigated by operating the devices at a lower temperature since the rate decreases with the temperature. Figure 6.3 shows the DCR as a function of temperature for several SiPMs available on the market. The first thing to note is the exponential decrease of DCR with temperature, and from the selected SiPMs we can infer that DCR of 100 cps/mm^2 can be achieved

approximately in the temperature range from -40°C to -60°C, while 10 cps/mm^2 in the range from -70°C to -90°C. The second thing to note is the excellent progress that has been made in the last decade in reducing the DCR. If similar technological improvements will be continued in the future, the SiPM cooling requirements could be even further relaxed.

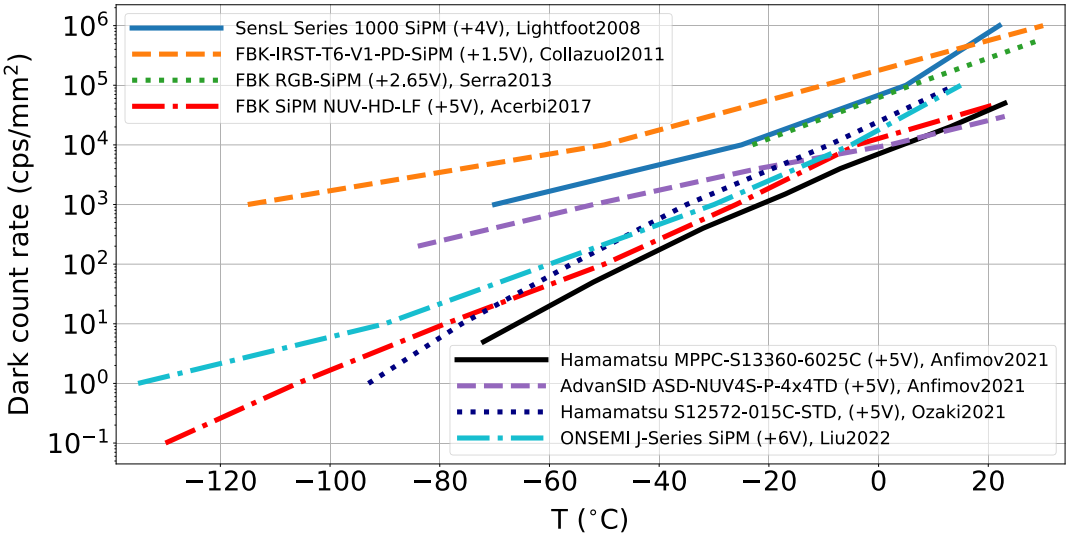

Figure 6.3: DCR as a function of temperature for the selected SiPMs. The values were recreated from the selected articles; [132, 133, 134, 135, 136, 137, 138]. The SiPM overvoltage at the measurement, which impacts the DCR, is shown in the brackets.

Besides cooling, the noise could also be tackled by raising the trigger level to, e.g., two or three photons. However, the impact of higher trigger levels on the detection efficiency would have to be evaluated, and it would most notably affect the detector with a lower number of detected Cherenkov photons on average (Figure 5.2). With two or more-sided readout, there is also an option to suppress noise by leaving the trigger level at the single optical photon but demand the triggering of two separate SiPMs attached to the Cherenkov radiator.

6.5 Photon detection efficiency

Potential exists to further improve the photon detection efficiency, which would also reduce the issue of raising the trigger levels. One way to achieve this is by using existing photo-detectors in multi-sided readout detectors, as demonstrated here (Figure 5.2). In the last decade, the SiPMs have improved greatly in terms of photodetection efficiency, noise and cross-talk reduction, timing performance, etc. [139]. However, there is still plenty of room for further development [17].

The crystal surfaces play a major role in determining the performance of the detector. Not only the surface type, e.g., black or reflector but also the surface roughness impacts the light transfer efficiency and consequently the PDE and CTR [140]. The optical parameters in the simulations were based on the values obtained from the literature. However, to get an idea of the impact of the surface roughness, Single-sided and Double-lateral readout Cherenkov detectors with reflective coating

were studied in the back-to-back configuration. The impact of surface roughness on the coincidence detection efficiency and CTR is shown in Figure 6.4 and Figure 6.5, respectively.

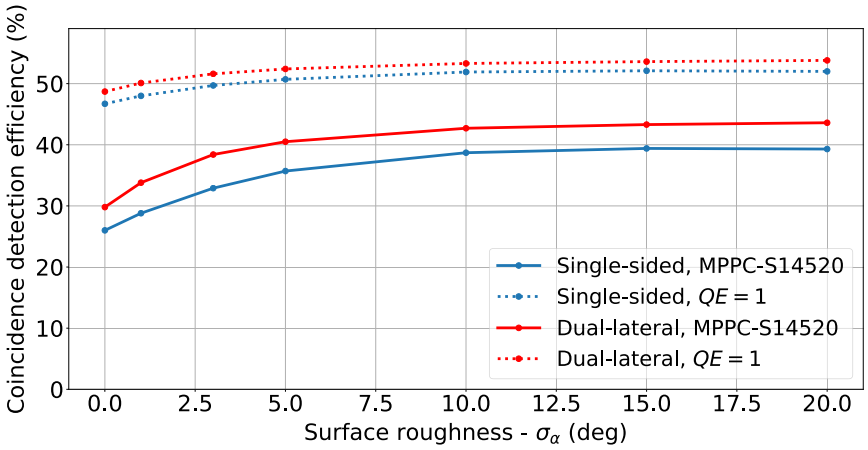

Figure 6.4: Coincidence detection efficiency of a pair of back-to-back Cherenkov detectors as a function of surface roughness modeled in the simulations with the *sigmalpha* parameter. The results are shown for a photo-detector with a perfect quantum efficiency ($QE = 1$) and a realistic quantum efficiency (Hamamatsu MPPC S14520 SiPM).

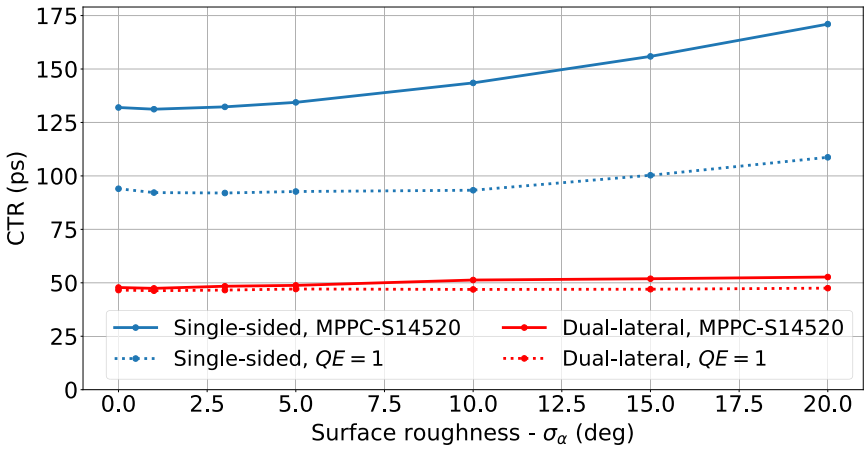

Figure 6.5: CTR of a pair of back-to-back Cherenkov detectors as a function of surface roughness.

The detection efficiency increases with surface roughness in the beginning and then reaches a plateau at the *sigmaalpha* parameter at about 10°. On the other hand, surface roughness has a minor impact on the CTR for Dual-lateral design, while it has a notable effect in a Single-sided design, especially at higher surface roughness. Both the coincidence detection efficiency and CTR are more impacted at lower quantum efficiency of the photo-detector. The results suggest that there is an optimal surface roughness. Similarly, for example, an optimal surface roughness exists to

provide a dual-ended scintillation detector with the best DOI capability [141]. However, due to its limitations, caution is in order when trying to predict the optimal surface roughness with the *unified* model. The *unified* model is fairly accurate when predicting the light transport for polished surfaces (corresponding to *sigmaalpha* of a few degrees), but gets less accurate at higher roughness ($sigmaalpha > 10°$), due to the fact that the surface is described only by the orientation of micro-facets, height is not included, and also the model assumes that the reflectance properties of the surface are independent of the incidence angle, which does not agree with experiments [111, 113].

The optimal surface roughness could be determined experimentally or with an improved optical model. The optical model can be improved, for example, by using the reflectance measurements and saving them in a look-up table [142]. Unfortunately, such a table, requiring surface measurements using, e.g., atomic force microscopy, does not yet exist for PbF_2, as it does for certain other scintillators (e.g., LSO). Therefore, a look-up table could not be tested in this work.

Detection efficiency and CTR would also be improved if the optical coupling between the crystal and the photo-detector is improved. Optical boundaries exist between the radiator and the photo-detector, and a mismatch in the refractive index can lead to light loss - reduced light transfer efficiency - due to the internal trapping inside the crystal. This is also why surface roughness can increase the photon detection efficiency, as it changes the distribution of incident angles of Cherenkov photons on the window of the photo-detector and can therefore make a photon refract at the window and reach the photo-detector instead of reflecting.

Different methods to improve LTE were demonstrated. In Ota *et al.* 2019 [84], they improved Cherenkov photon transmission to the photocathode by removing the optical boundaries - using Cherenkov-radiator-integrated micro-channel plate photomultiplier tube. In Pots *et al.* 2020 [143], they improved LTE from an inorganic BaF_2 scintillator by coupling the crystal, with UV-transparent optical grease, to the photo-detector. Photonic crystals are another possible solution that was proposed and is being investigated to improve the LTE through photonic nano-structuring of the different surfaces of the crystal [76]. Using nanoimprinted photonic crystals, an enhancement of 50% in scintillation light extraction, and 20% in the energy resolution, compared to the standard grease coupling, was experimentally demonstrated [144].

6.6 Image reconstruction

For the best image quality, a double Gaussian TOF kernel - as opposed to the conventional single Gaussian - had to be used because the time difference of the detected events in the Cherenkov detectors has long tails (Figure 5.15). A recent study has also successfully implemented a double Gaussian TOF kernel for BGO detectors while also exploring Gaussian mixture models, where different kernels account for a different number of detected Cherenkov photons that impact the pulse rise time, alongside the normal BGO scintillation light [101].

Another potential improvement could be weighted reconstruction on an event-by-event basis. Both unwanted types of events - scattered gammas and DCR - have on average a lower number of triggered SiPM SPADs compared to the true 511 keV gamma interaction. A weighted reconstruction could be an option to improve image quality, where events with a high number of triggered SPADs are given more weight

in the reconstruction process. This can also mitigate the problem with the trade-off between a clean signal where a high threshold is used and high statistics where a low threshold is used [6].

The scatter correction in this work was based on Monte Carlo simulation which is recognized as one of the most (if not the most) accurate method for this task. However, the major disadvantage of Monte Carlo simulations is the long computation time which made it unfeasible for the clinical environment. One way to tackle this problem is to use graphics processing units (GPUs) to accelerate the simulations [145]. In clinics, single scatter simulation is the most widely used method for scatter correction, but due to the assumption that all scattered events are single scatter, this method breaks down for scanners with poor energy resolution, and therefore it is most likely not the best option for scatter correction in pure Cherenkov PET.

Deep learning is now having a widespread impact on many and diverse fields, including PET imaging [146]. Deep learning algorithms are promising candidates to be used for fast and accurate scatter correction [147] and other types of corrections, such as attenuation correction [148]. They also show potential as the default framework for the whole process of PET image reconstruction [149, 150].

6.7 Scalability

A pure Cherenkov detector based on PbF_2 can achieve excellent CTR, as seen and discussed throughout this work. However, in experimental settings, the best (sub 100 ps) timing resolutions have been achieved with high-power electronics that cannot be easily scaled to large devices. Having said that, the very recent work done by Krake *et al.* 2022 [151] demonstrates that it is possible to find low-power front-end solutions for the highest timing performance in TOF-PET, with a minimum power consumption of 17 mW per channel. The recently developed FastIC chip [152] is another example of high channel density, low power consumption electronics with potential for fast readout in Cherenkov PET scanners. In summary, there appear to be no theoretical or practical barriers that would make pure Cherenkov PET unfeasible. On the contrary, with its many options for improvement, Cherenkov PET is likely to attract more attention in the future.

7. Conclusion and Prospect

In this work, pure Cherenkov PET detectors and the performance of scanners based on them have been investigated. Cherenkov detectors are commonly viewed as fast detectors that can achieve excellent CTR but are not feasible for clinical PET detectors due to the low number of Cherenkov photons produced and the consequent fact that they provide very little energy information. Results from Monte Carlo simulations presented in this work show that Cherenkov scanners can achieve image quality comparable if not better to that of the current state-of-the-art PET scanners - even though they have a larger scatter fraction - due to improved efficiency and CTR attainable with PbF_2. A more general message that can be drawn from this work is that a PET detector's reduced or absent energy resolution can be compensated by its gamma detection efficiency and/or CTR. Nonetheless, the scatter coincidences do impact the Cherenkov scanners more than a scintillation-based scanner. Still, in low scatter environments such as brain, breast, and preclinical imaging, the Cherenkov scanners can have a significant edge over scintillation-based scanners in terms of performance. The detection efficiency and CTR of Cherenkov detectors is improved even further by considering multi-sided crystal readout. The simulation results show a similar performance of detectors with a 2-sided readout (Double-lateral) to theoretically ideal detectors with a 6-sided readout. A detector with side readouts could practically be realized in sparse scanner designs. The low-cost Cherenkov detectors could also become especially interesting for total-body scanners as their current high cost is limiting their dissemination in hospitals and research clinics. With expected further improvements in photo-detector and dedicated Cherenkov PET technologies, pure Cherenkov detectors would be a promising path to ultra-fast, low-cost next-generation PET.

8. Bibliography

[1] T. Jones and D. Townsend, *History and future technical innovation in positron emission tomography*, J. Nucl. Med. **4**, 011013 (2017), https://doi.org/10.1117/1.JMI.4.1.011013.

[2] J. J. Vaquero and P. Kinahan, *Positron Emission Tomography: Current Challenges and Opportunities for Technological Advances in Clinical and Preclinical Imaging Systems*, Annu. Rev. Biomed. Eng. **17**, 385 (2015), https://doi.org/10.1146/annurev-bioeng-071114-040723.

[3] E. Berg and S. R. Cherry, *Innovations in Instrumentation for Positron Emission Tomography*, Semin. Nucl. Med. **48**, 311 (2018), https://doi.org/10.1053/j.semnuclmed.2018.02.006.

[4] S. R. Cherry *et al.*, *Total-Body PET: Maximizing Sensitivity to Create New Opportunities for Clinical Research and Patient Care*, J. Nucl. Med. **59**, 3 (2018), https://doi.org/10.2967/jnumed.116.184028.

[5] C. L. Melcher, *Scintillation Crystals for PET*, J. Nucl. Med. **41**, 1051 (2000), https://pubmed.ncbi.nlm.nih.gov/10855634/.

[6] N. Kratochwil, S. Gundacker and E. Auffray, *A roadmap for sole Cherenkov radiators with SiPMs in TOF-PET*, Phys. Med. Biol. **66**, 195001 (2021), https://doi.org/10.1088/1361-6560/ac212a.

[7] M. Dahlbom, *Physics of PET and SPECT Imaging*, 1st ed. (CRC Press, 2017) https://www.routledge.com/Physics-of-PET-and-SPECT-Imaging/Dahlbom/p/book/9780367782368.

[8] M. Khalil, *Basic Science of PET Imaging*, 1st ed. (Springer, 2017) https://link.springer.com/book/10.1007/978-3-319-40070-9.

[9] A. D. Guerra, *Ionizing Radiation Detectors for Medical Imaging* (World Scientific Pub., 2004) https://www.worldscientific.com/worldscibooks/10.1142/5408#t=aboutBook.

[10] A. Sanchez-Crespo, *Comparison of Gallium-68 and Fluorine-18 imaging characteristics in positron emission tomography*, Appl Radiat Isot **76**, 55 (2013), https://doi.org/10.1016/j.apradiso.2012.06.034.

[11] D. L. Bailey *et al.*, *Positron Emission Tomography Basic Sciences*, 1st ed. (Springer, 2005) https://link.springer.com/book/10.1007/b136169.

[12] J. V. Jelly, *Cerenkov radiation and its applications*, Br. J. Appl. Phys. **6**, 227 (1955), https://doi.org/10.1088/0508-3443/6/7/301.

[13] S. R. Cherry, J. A. Sorenson and M. E. Phelps, *Physics in Nuclear Medicine*, 4th ed. (W.B. Saunder, 2012) https://www.sciencedirect.com/book/9781416051985/physics-in-nuclear-medicine.

[14] N. Tsoulfanidis and S. Landsberger, *Measurement and Detection of Radiation*, 4th ed. (CRC Press, Taylor & Francis Group, 2015) https://www.worldcat.org/title/measurement-and-detection-of-radiation/oclc/908080143.

[15] F. Sauli, *Gaseous Radiation Detectors: Fundamentals and Applications* (Cambridge University Press, 2014) https://www.cambridge.org/core/books/gaseous-radiation-detectors/742D8E89DC5EFE1BE285978833E5A860.

[16] V. Nadig *et al.*, *Hybrid total-body pet scanners—current status and future perspectives*, Eur. J. Nucl. Med. **49**, 445 (2022), https://doi.org/10.1007/s00259-021-05536-4.

[17] S. Gundacker and A. Heering, *The silicon photomultiplier: fundamentals and applicationsof a modern solid-state photon detector*, Phys. Med. Biol. **65** (2020), https://doi.org/10.1088/1361-6560/ab7b2d.

[18] S. Gundacker *et al.*, *On the comparison of analog and digital SiPM readout in terms of expected timing performance*, Nucl. Instrum. Methods **787**, 6 (2015), https://doi.org/10.1016/j.nima.2014.10.020.

[19] S. Surti and J. S. Karp, *Update on latest advances in time-of-flight PET*, Phys. Med. **80**, 251 (2020), https://doi.org/10.1016/j.ejmp.2020.10.031.

[20] A. D. Guerra, N. Belcari and M. Giuseppina, *Positron Emission Tomography: Its 65 years*, Riv. del Nuovo Cim. **39**, 155 (2016), https://doi.org/10.1393/ncr/i2016-10122-6.

[21] D. Bharkhada *et al.*, *Listmode Reconstruction for Biograph Vision PET/CT Scanner*, J. Nucl. Med. **61**, 1463 (2020), https://doi.org/10.1109/NSS/MIC42101.2019.9059953.

[22] M. Conti, *Why is TOF PET reconstruction a more robust method in the presence of inconsistent data?*, Phys. Med. Biol. **56**, 155–168 (2011), https://doi.org/10.1088/0031-9155/56/1/010.

[23] E. J. Hoffman *et al.*, *PET system calibrations and corrections for quantitative and spatially accurate images*, IEEE Trans. Nucl. Sci. **36**, 1108 (1989), https://doi.org/10.1109/23.34613.

[24] R. D. Badawi and P. K. Marsden, *Developments in component-based normalization for 3D PET*, Phys. Med. Biol. **44**, 571 (1999), https://doi.org/10.1088/0031-9155/44/2/020.

[25] M. E. Casey and E. J. Hoffman, *Quantitation in positron emission computed-tomography. 7. A technique to reduce noise in accidental coincidence measurements and coincidence efficiency calibration*, J. Comput. Assist. Tomogr **10**, 845 (1986), https://pubmed.ncbi.nlm.nih.gov/3489018/.

[26] D. L. Bailey and S. R. Meikle, *A convolution-subtraction scatter correction method for 3D PET*, Phys. Med. Biol. **39**, 411 (1994), https://doi.org/10.1088/0031-9155/39/3/009.

[27] M. Bentourkia *et al.*, *Assessment of scatter components in high-resolution PET: correction by nonstationary convolution subtraction*, J. Nucl. Med. **36**, 121 (1995), https://pubmed.ncbi.nlm.nih.gov/7799064/.

[28] C. S. Levin, M. Dahlbom and E. J. Hoffman, *A Monte Carlo correction for the effect of Compton scattering in 3-D PET brain imaging*, IEEE Trans. Nucl. Sci. **42**, 1181 (1995), https://doi.org/10.1109/23.467880.

[29] S. Grootoonk *et al.*, *Correction for scatter in 3D brain PET using a dual energy window method*, Phys. Med. Biol. **41**, 2757 (1996), https://doi.org/10.1088/0031-9155/41/12/013.

[30] L. Shao, R. Freifelder and J. S. Karp, *Triple energy window scatter correction technique in PET*, IEEE Trans. Med. Imag. **13**, 641 (1994), https://doi.org/10.1109/42.363104.

[31] J. M. Ollinger, *Model-based scatter correction for fully 3D PET*, Phys. Med. Biol. **41**, 153 (1996), https://doi.org/10.1088/0031-9155/41/1/012.

[32] C. C. Watson, *New, faster, image-based scatter correction for 3D PET*, IEEE Trans. Nucl. Sci. **47**, 1587 (2000), https://doi.org/10.1109/23.873020.

[33] R. Accorsi *et al.*, *Optimization of a fully 3D single scatter simulation algorithm for 3D PET*, Phys. Med. Biol. **49**, 2577–2598 (2004), https://doi.org/10.1088/0031-9155/49/12/008.

[34] C. C. Watson, *Extension of Single Scatter Simulation to Scatter Correction of Time-of-Flight PET*, IEEE Trans. Nucl. Sci. **54**, 1679 (2007), https://doi.org/10.1109/NSSMIC.2005.1596846.

[35] C. H. Holdsworth *et al.*, *Investigation of accelerated Monte Carlo techniques for PET simulation and 3D PET scatter correction*, IEEE Trans. Nucl. Sci. **48**, 74 (2001), https://doi.org/10.1109/23.910835.

[36] C. H. Holdsworth *et al.*, *Performance analysis of an improved 3-D PET Monte Carlo simulation and scatter correction*, IEEE Transactions on Nuclear Science **49**, 83 (2002), https://doi.org/10.1109/TNS.2002.998686.

[37] R. E. Carson, M. E. Daube-Witherspoon and M. V. Green., *A Method for Postinjection PET Transmission Measurements with a Rotating Source*, J. Nucl. Med. **29**, 1558 (1988), https://pubmed.ncbi.nlm.nih.gov/3261786/.

[38] J. S. Karp *et al.*, *Singles transmission in volume-imaging PET with a* ^{137}*Cs source*, Phys. Med. Biol. **40**, 929 (1995), https://doi.org/10.1088/0031-9155/40/5/014.

[39] P. E. Kinahan, B. H. Hasegawa and T. Beyer, *X-ray-based attenuation correction for positron emission tomography/computed tomography scanners*, Semin. Nucl. Med. **33**, 166 (2003), https://doi.org/10.1053/snuc.2003.127307.

[40] S. Vandenberghe and P. K. Marsden, *PET-MRI: a review of challenges and solutions in the development of integrated multimodality imaging*, Phys. Med. Biol. **60**, R115 (2015), https://doi.org/10.1088/0031-9155/60/4/R115.

[41] S. H. Keller *et al.*, *Image artifacts from MR-based attenuation correction in clinical, whole-body PET/MRI*, Magn. Reson. Mater. Phys., Biol. Med. **26**, 173 (2013), https://doi.org/10.1007/s10334-012-0345-4.

[42] Y. Berker and Y. Li, *Attenuation correction in emission tomography using the emission data - A review*, Med. Phys. **43**, 807 (2016), https://doi.org/10.1118/1.4938264.

[43] W. H. Wong and H. Li, *A scintillation detector signal processing technique with active pileup prevention for extending scintillation count rates*, IEEE Trans. Nucl. Sci. **45**, 838 (1998), https://doi.org/10.1109/23.682647.

[44] S. Surti, *Update on time-of-flight PET imaging*, J. Nucl. Med. **56**, 98 (2015), https://doi.org/10.2967/jnumed.114.145029.

[45] S. Vandenberghe *et al.*, *Recent developments in time-of-flight PET*, EJNMMI Phys. **3** (2016), https://doi.org/10.1186/s40658-016-0138-3.

[46] T. F. Budinger, *Time-of-Flight Positron Emission Tomography: Status Relative to Conventional PET*, J. Nucl. Med. **24**, 73 (1983), https://pubmed.ncbi.nlm.nih.gov/6336778/.

[47] M. Conti, *State of the art and challenges of time-of-flight PET*, Phys Med. **25**, 1 (2009), https://doi.org/10.1016/j.ejmp.2008.10.001.

[48] V. Westerwoudt, M. Conti and L. Eriksson, *Advantages of Improved Time Resolution for TOF PET at Very Low Statistics*, IEEE Trans. Nucl. Sci. **61**, 126 (2014), https://doi.org/10.1109/TNS.2013.2287175.

[49] A. R. M Defrise and J. Nuyts, *Time-of-flight PET data determine the attenuation sinogram up to a constant*, Phys. Med. Biol. **57**, 885–899 (2012), https://doi.org/10.1088/0031-9155/57/4/885.

[50] G. Razdevšek *et al.*, *Multi-panel limited angle PET system with 50 ps FWHM coincidence time resolution: a simulation study*, IEEE trans. radiat. plasma med. sci. **6**, 721 (2022), https://doi.org/10.1109/TRPMS.2021.3115704.

[51] D. Kersting *et al.*, *Silicon-photomultiplier-based PET/CT reduces the minimum detectable activity of iodine-124*, Sci Rep. **1**, 11 (2021), https://doi.org/10.1038/s41598-021-95719-8.

[52] B. Kunnen *et al.*, *Comparison of the Biograph Vision and Biograph mCT for quantitative ^{90}Y PET/CT imaging for radioembolisation*, EJNMMI Phys. **7** (2020), https://doi.org/10.1186/s40658-020-0283-6.

[53] S. Gundacker *et al.*, *High-frequency SiPM readout advances measured coincidence time resolution limits in TOF-PET*, Phys. Med. Biol. **64** (2019), https://doi.org/10.1088/1361-6560/aafd52.

[54] W. W. Moses, *Fundamental limits of spatial resolution in PET*, Nucl Instrum Methods Phys Res A **648**, S236–40 (2011), https://doi.org/10.1016/j.nima.2010.11.092.

[55] P. Colombino, B. Fiscella and L. Trossi, *Study of positronium in water and ice from 22 to -144 °C by annihilation quanta measurements*, Nuovo Cimento **38**, 707 (1965), https://doi.org/10.1007/BF02748591.

[56] M. Dahlbom *et al.*, *Comparison of noise equivalent count rates and image noise*, IEEE Trans. Nucl. Sci. **52**, 1386 (2005), https://doi.org/10.1109/NSSMIC.2004.1466671.

[57] A. P. Dempster, N. M. Laird and D. B. Rubin, *Maximum likelihood from incomplete data via the EM algorithm*, J R Stat Soc Ser B Methodol. **39**, 1 (1977), https://www.jstor.org/stable/2984875.

[58] L. A. Shepp and Y. Vardi, *Maximum Likelihood Reconstruction for Emission Tomography*, IEEE Trans. Med. Imaging. **1**, 113 (1982), https://doi.org/10.1109/TMI.1982.4307558.

[59] S. Tong, A. M. Alessio and P. E. Kinahan, *Image reconstruction for PET/CT scanners: past achievements and future challenges*, Imaging Med. **2**, 529 (2010), https://www.ncbi.nlm.nih.gov/pmc/articles/PMC3039307/.

[60] H. M. Hudson and R. S. Larkin, *Accelerated image reconstruction using ordered subsets of projection data*, IEEE Trans. Med. Imaging. **13**, 601 (1994), https://doi.org/10.1109/42.363108.

[61] A. Sangtae and J. A. Fessler, *Globally convergent image reconstruction for emission tomography using relaxed ordered subsets algorithms*, IEEE Trans. Med. Imag. **22**, 613 (2003), https://doi.org/10.1109/TMI.2003.812251.

[62] G. Muehllehner and J. S. Karp, *Positron emission tomography*, Phys. Med. Biol. **51**, R117 (2006), https://doi.org/10.1088/0031-9155/51/13/R08.

[63] E. Roncali and S. R. Cherry, *Application of silicon photomultipliers to positron emission tomographys*, Ann. Biomed. Eng. **39**, 1358 (2011), https://doi.org/10.1007/s10439-011-0266-9.

[64] S. Vandenberghe, P. Moskal and J. S. Karp, *State of the art in total body PET*, EJNMMI Phys. **7** (2020), https://doi.org/10.1186/s40658-020-00290-2.

[65] B. A. Spencer *et al.*, *Performance evaluation of the uEXPLORER Total-body PET/CT scanner based on NEMA NU 2-2018 with additional tests to characterize long axial field-of-view PET scanners*, J. Nucl. Med. **62**, 861 (2020), https://doi.org/10.2967/jnumed.120.250597.

[66] S. R. Cherry *et al.*, *Total-body imaging: Transforming the role of positron emission tomography*, Sci. Transl. Med. **9**, eaaf6169 (2017), https://doi.org/10.1126/scitranslmed.aaf6169.

[67] R. D. Badawi *et al.*, *First Human Imaging Studies with the EXPLORER Total-Body PET Scanner*, J. Nucl. Med. **60**, 299 (2019), https://doi.org/10.2967/jnumed.119.226498.

[68] Q. K.-T. Ng *et al.*, *Total-body PET/CT - First Clinical Experiences and Future Perspectives*, Semin. Nucl. Med. **52**, 330 (2022), https://doi.org/10.1053/j.semnuclmed.2022.01.002.

[69] P. A. Cherenkov, *Visible light from clear liquids under the action of gamma radiation*, C. R. Dokl. Akad. Nauk SSSR **2**, 451 (1934), https://ufn.ru/ru/articles/1967/10/n/.

[70] P. A. Cherenkov, *Visible Radiation Produced by Electrons Moving in a Medium with Velocities Exceeding that of Light*, Phys. Rev. **52**, 378 (1937), https://journals.aps.org/pr/abstract/10.1103/PhysRev.52.378.

[71] T. M. Shaffer, E. C. Pratt and J. Grimm, *Utilizing the power of Cerenkov light with nanotechnology*, Nat. Nanotechnol **12**, 106 (2017), https://doi.org/10.1038/nnano.2016.301.

[72] J. V. Jelly, *Cherenkov radiation, and its applications* (Pergamon Press, New York, 1958) https://archive.org/details/cerenkovradiatio030980mbp/page/n7/mode/2up.

[73] E. Ciarrocchi and N. Belcari, *Cerenkov luminescence imaging: physics principles and potential applications in biomedical sciences*, EJNMMI Phys. **4** (2017), https://doi.org/10.1186/s40658-017-0181-8.

[74] M. Conti *et al.*, *Comparison of Fast Scintillators With TOF PET Potential*, IEEE Trans. Nucl. Sci. **56**, 926 (2009), https://doi.org/10.1109/TNS.2008.2009446.

[75] D. N. ter Weele, D. R. Schaart and P. Dorenbos, *Intrinsic scintillation pulse shape measurements by means of picosecond x-ray excitation for fast timing applications*, Nucl. Instrum. Methods Phys. Res., Sect. A **767**, 206 (2014), https://doi.org/10.1016/j.nima.2014.08.019.

[76] P. Lecoq, *Pushing the Limits in Time-of-Flight PET Imaging*, IEEE Trans. Radiat. Plasma Med. Sci. **1**, 473 (2017), https://doi.org/10.1109/TRPMS.2017.2756674.

[77] P. Lecoq *et al.*, *Roadmap toward the 10 ps time-of-flight PET challenge*, Phys. Med. Biol. (2020), https://doi.org/10.1088/1361-6560/ab9500.

[78] G. Knoll, *Radiation Detection and Measurement (4th ed.)*, 4th ed. (John Wiley, 2010) https://www.wiley.com/en-us/Radiation+Detection+and+Measurement%2C+4th+Edition-p-9780470131480.

[79] *https://physics.nist.gov/cgi-bin/Xcom/xcom2*, (Accessed: 13/07/2022).

[80] T. Ooba *et al.*, *Proposal of Cherenkov TOFPET with silica aerogel*, IEEE Nucl. Sci. Symp. Conf. Rec. **6**, 3781 (2004), https://doi.org/10.1109/NSSMIC.2004.1466703.

[81] M. Miyata *et al.*, *Development of TOF-PET using Cherenkov radiation*, J. Nucl. Sci. Technol. **43**, 339 (2006), https://doi.org/10.1080/18811248.2006.9711101.

[82] S. Korpar *et al.*, *Study of TOF PET using Cherenkov light*, Nucl. Instrum. Methods Phys. Res., Sect. A **654**, 532 (2011), https://doi.org/10.1016/j.nima.2011.06.035.

[83] R. Ota *et al.*, *Timing-performance evaluation of Cherenkov-based radiation detectors*, Nucl. Instrum. Methods Phys. Res., Sect. A **923**, 1 (2019), https://doi.org/10.1016/j.nima.2019.01.034.

[84] R. Ota *et al.*, *Coincidence time resolution of 30 ps FWHM using a pair of Cherenkov-radiator-integrated MCP-PMTs*, Phys. Med. Biol. **64**, 07LT01 (2019), https://doi.org/10.1088/1361-6560/ab0fce.

[85] S. I. Kwon *et al.*, *Ultrafast timing enables reconstruction-free positron emission imaging*, Nature Photonics **15**, 914 (2021), https://doi.org/10.1038/s41566-021-00871-2.

[86] S. Gundacker *et al.*, *Experimental time resolution limits of modern SiPMs and TOF-PET detectors exploring different scintillators and Cherenkov emission*, Phys. Med. Biol. **65** (2020), https://doi.org/10.1088/1361-6560/ab63b4.

[87] R. Dolenec *et al.*, *The Performance of Silicon Photomultipliers in Cherenkov TOF PET*, IEEE Trans. Nucl. Sci. **63**, 2478 (2016), https://doi.org/10.1109/TNS.2015.2512564.

[88] D. Consuegra *et al.*, *Improving the Cherenkov Based PET Performance Using Multi-Layer Detectors*, in *IEEE Symp. on Nuclear Science (NSS/MIC)* (2019) pp. 1–5, https://doi.org/10.1109/NSS/MIC42101.2019.9059871.

[89] M. Alokhina *et al.*, *Simulation and optimization of the Cherenkov TOF whole-body PET scanner*, Nucl. Instrum. Methods Phys. Res., Sect. A **912**, 378 (2018), https://doi.org/10.1016/j.nima.2018.01.027.

[90] S. I. Kwon *et al.*, *Bismuth germanate coupled to near ultraviolet silicon photomultipliers for time-of-flight PET*, Phys. Med. Biol. **61**, L38 (2016), https://doi.org/10.1088/0031-9155/61/18/l38.

[91] S. E. Brunner and D. R. Schaart, *BGO as a hybrid scintillator / Cherenkov radiator for cost-effective time-of-flight PET*, Phys. Med. Biol. **62**, 4421 (2017), https://doi.org/10.1088/1361-6560/aa6a49.

[92] T. Szczęśniak *et al.*, *MPPC Arrays in PET Detectors With LSO and BGO Scintillators*, IEEE Trans. Nucl. Sci. **60**, 1533 (2013), https://doi.org/10.1109/TNS.2013.2251002.

[93] N. Kratochwil *et al.*, *Pushing Cherenkov PET with BGO via coincidence time resolution classification and correction*, Phys. Med. Biol. **65**, 115004 (2020), https://doi.org/10.1088/1361-6560/ab87f9.

[94] G. Ariño-Estrada *et al.*, *Towards time-of-flight PET with a semiconductor detector*, Phys. Med. Biol. **63**, 04LT01 (2018), https://doi.org/10.1088/1361-6560/aaaa4e.

[95] G. Terragni *et al.*, *Time Resolution Studies of Thallium Based Cherenkov Semiconductors*, Front. Phys. **10** (2022), https://doi.org/10.3389/fphy.2022.785627.

[96] G Ariño-Estrada *et al.*, *Study of Cerenkov Light Emission in the Semiconductors TlBr and TlCl for TOF-PET*, IEEE Trans. Radiat. Plasma Med. Sci. **5**, 630 (2021), https://doi.org/10.1109/TRPMS.2020.3024032.

[97] P. Achenbach *et al.*, *Radiation resistance and optical properties of lead fluoride Cherenkov crystals*, Nucl. Instrum. Methods Phys. Res., Sect. A **416**, 357 (1998), https://doi.org/10.1016/S0168-9002(98)00748-7.

[98] T. K. Lewellen, *Recent developments in PET detector technology*, Phys. Med. Biol. **53**, R287 (2008), https://doi.org/10.1088/0031-9155/53/17/R01.

[99] D. F. Anderson *et al.*, *Lead fluoride: An ultra-compact Cherenkov radiator for em calorimetry*, Nucl. Instrum. Methods Phys. Res., Sect. A **290**, 385 (1990), https://doi.org/10.1016/0168-9002(90)90553-I.

[100] C. Canot and other, *Fast and efficient detection of 511 keV photons using Cherenkov light in PbF2 crystal, coupled to a MCP-PMT and SAMPIC digitization module*, J. Instrum. **14**, P12001 (2019), https://doi.org/10.1088/1748-0221/14/12/P12001.

[101] N. Efthimiou *et al.*, *TOF-PET Image Reconstruction With Multiple Timing Kernels Applied on Cherenkov Radiation in BGO*, IEEE Trans. Radiat. Plasma Med. Sci. **5**, 703 (2021), https://doi.org/10.1109/TRPMS.2020.3048642.

[102] R. Mao, L. Zhang and R. Zhu, *A Search for Scintillation in Doped Cubic Lead Fluoride Crystals*, IEEE Trans. Nucl. Sci. **57**, 3841 (2010), https://doi.org/10.1109/TNS.2010.2076372.

[103] D. Consuegra *et al.*, *Simulation study to improve the performance of a whole-body PbF_2 Cherenkov TOF-PET scanner*, Phys. Med. Biol. **65**, 055013 (2020), https://doi.org/10.1088/1361-6560/ab6f97.

[104] J. W. Cates and C. S. Levin, *Evaluation of a clinical TOF-PET detector design that achieves $\leq$100 ps coincidence time resolution*, Phys. Med. Biol. **63**, 115011 (2018), https://doi.org/10.1088/1361-6560/aac504.

[105] M. S. Lee *et al.*, *High-resolution time-of-flight PET detector with 100 ps coincidence time resolution using a side-coupled phoswich configuration*, Phys. Med. Biol. **66**, 125007 (2021), https://doi.org/10.1088/1361-6560/ac01b5.

[106] S. Jan *et al.*, *GATE: a simulation toolkit for PET and SPECT*, Phys. Med. Biol. **49**, 4543 (2004), https://doi.org/10.1088/0031-9155/49/19/007.

[107] S. Agostinelli *et al.*, *Geant4 - a simulation toolkit*, Nucl. Instrum. Methods Phys. Res., Sect. A **506**, 250 (2003), https://doi.org/10.1016/S0168-9002(03)01368-8.

[108] J. Allison *et al.*, *Recent developments in Geant4*, Nucl. Instrum. Methods Phys. Res., Sect. A **835**, 186 (2016), https://doi.org/10.1016/j.nima.2016.06.125.

[109] A. Levin and C. Moisan, *A more physical approach to model the surface treatment of scintillation counters and its implementation into DETECT*, Proc. IEEE Nucl. Sci. Symp. **2**, 702 (1996), https://doi.org/10.1109/NSSMIC.1996.591410.

[110] R. Levinson, P. Berdahl and H. Akbari, *Solar spectral optical properties of pigments - Part II: Survey of common colorants*, Sol. Energy Mater. Sol. Cells **89**, 351 (2004), https://doi.org/10.1016/j.solmat.2004.11.013.

[111] M. Janecek and W. W. Moses, *Simulating Scintillator Light Collection Using Measured Optical Reflectance*, IEEE Trans. Nucl. Sci. **57**, 964 (2010), https://doi.org/10.1109/TNS.2010.2042731.

[112] M. Janecek, *Reflectivity Spectra for Commonly Used Reflectors*, IEEE Trans. Nucl. Sci. **59**, 490 (2012), https://doi.org/10.1109/TNS.2012.2183385.

[113] E. Roncali and S. R. Cherry, *Simulation of light transport in scintillators based on 3D characterization of crystal surfaces*, Phys. Med. Biol. **58**, 2185 (2013), https://doi.org/10.1088/0031-9155/58/7/2185.

[114] J. van Sluis *et al.*, *Performance Characteristics of the Digital Biograph Vision PET/CT System*, J. Nucl. Med. **60**, 1031 (2019), https://doi.org/10.2967/jnumed.118.215418.

[115] J. Zhang and M. V. Knopp, *Advances in PET*, 1st ed. (Springer, 2020) https://link.springer.com/book/10.1007/978-3-030-43040-5.

[116] T. Merlin *et al.*, *CASToR: a generic data organization and processing code framework for multi-modal and multi-dimensional tomographic reconstruction*, Phys. Med. Biol. **63** (2018), https://doi.org/10.1088/1361-6560/aadac1.

[117] F. Jacobs *et al.*, *A Fast Algorithm to Calculate the Exact Radiological Path through a Pixel or Voxel Space*, Journal of Computing and Information Technology **6**, 89 (1998), http://hdl.handle.net/1854/LU-281913.

[118] D. Nikolopoulos *et al.*, *GATE Simulation of the Biograph 2 PET/CT Scanner*, J. Nucl. Med. Radiat. Ther. **6**, 1 (2014), https://doi.org/10.4172/2155-9619.1000201.

[119] G. A. Prenosil *et al.*, *Performance Characteristics of the Biograph Vision Quadra PET/CT system with long axial field of view using the NEMA NU 2-2018 Standard*, J. Nucl. Med. (2021), https://doi.org/10.2967/jnumed.121.261972.

[120] W. P. Segars *et al.*, *4D XCAT phantom for multimodality imaging research*, Med. Phys. **37**, 4902 (2010), https://doi.org/10.1118/1.3480985.

[121] W. P. Segars *et al.*, *Application of the 4D XCAT Phantoms in Biomedical Imaging and Beyond*, IEEE Trans. Med. Imag. **PP**, 1 (2017), https://doi.org/10.1109/TMI.2017.2738448.

[122] S. Zincirkeser *et al.*, *Standardized Uptake Values of Normal Organs on 18F-Fluorodeoxyglucose Positron Emission Tomography and Computed Tomography Imaging*, J. Int. Med. Res. **35**, 231 (2007), https://doi.org/10.1177/147323000703500207.

[123] Z. Wang *et al.*, *Image quality assessment: from error visibility to structural similarity*, IEEE Trans. Image Process. **13**, 600 (2004), https://doi.org/10.1109/TIP.2003.819861.

[124] L. Guo *et al.*, *Improving timing performance of double-ended readout in TOF-PET detectors*, J. Instrum. **15**, P01003 (2020), https://doi.org/10.1088/1748-0221/15/01/P01003.

[125] S. Seifert and D. R. Schaart, *Improving the Time Resolution of TOF-PET Detectors by Double-Sided Readout*, IEEE Trans. Nucl. Sci. **62**, 3 (2015), https://doi.org/10.1109/TNS.2014.2368932.

[126] H. G. Kang *et al.*, *A Dual-Ended Readout Detector Using a Meantime Method for SiPM TOF-DOI PET*, IEEE Trans. Nucl. Sci. **62**, 1935 (2015), https://doi.org/10.1109/TNS.2015.2449891.

[127] S. Derenzo *et al.*, *Monte Carlo calculations of PET coincidence timing: Single and double-ended readout*, Phys. Med. Biol. **60**, 7309 (2015), https://doi.org/10.1088/0031-9155/60/18/7309.

[128] E. Berg and S. Cherry, *Using convolutional neural networks to estimate time-of-flight from PET detector waveforms*, Phys. Med. Biol. **63** (2017), https://doi.org/10.1088/1361-6560/aa9dc5.

[129] J. Zhang, M. I. Knopp and M. V. Knopp, *Sparse Detector Configuration in SiPM Digital Photon Counting PET: a Feasibility Study*, Mol. Imaging Biol. **21**, 447–453 (2019), https://doi.org/10.1007/s11307-018-1250-7.

[130] S. Zein *et al.*, *Monte Carlo Simulation of the Siemens Biograph Vision PET With Extended Axial Field of View Using Sparse Detector Module Rings Configuration*, IEEE Trans. Radiat. Plasma Med. Sci. **5**, 331 (2021), https://doi.org/10.1109/TRPMS.2020.3034676.

[131] R. Dolenec *et al.*, *Efficiency of a Cherenkov based PET module with an array of SiPMs*, Nucl. Instrum. Methods Phys. Res., Sect. A **952**, 162327 (2020), https://doi.org/10.1016/j.nima.2019.06.068.

[132] P. K. Lightfoot *et al.*, *Characterisation of a silicon photomultiplier device for applications in liquid argon based neutrino physics and dark matter searches*, J. Instrum. **3**, P10001 (2008), https://doi.org/10.1088/1748-0221/3/10/P10001.

[133] G. Collazuol *et al.*, *Studies of silicon photomultipliers at cryogenic temperatures*, Nucl. Instrum. Methods Phys. Res., Sect. A **628**, 389 (2011), https://doi.org/10.1016/j.nima.2010.07.008.

[134] N. Serra *et al.*, *Characterization of new FBK SiPM technology for visible light detection*, J. Instrum. **8**, P03019 (2013), https://doi.org/10.1088/1748-0221/8/03/P03019.

[135] C. E. Aalseth *et al.*, *Cryogenic Characterization of FBK RGB-HD SiPMs*, J. Instrum. **12**, P09030 (2017), https://doi.org/10.1088/1748-0221/12/09/P09030.

[136] N. Anfimov *et al.*, *Study of silicon photomultiplier performance at different temperatures*, Nucl. Instrum. Methods Phys. Res., Sect. A **997**, 165162 (2021), https://doi.org/10.1016/j.nima.2021.165162.

[137] K. Ozaki *et al.*, *Characterization of new silicon photomultipliers with low dark noise at low temperature*, J. Instrum. **16**, P03014 (2021), https://doi.org/10.1088/1748-0221/16/03/P03014.

[138] F. Liu *et al.*, *Characterization of a Mass-Produced SiPM at Liquid Nitrogen Temperature for CsI Neutrino Coherent Detectors*, Sensors **22** (2022), https://doi.org/10.3390/s22031099.

[139] P. Lecoq and S. Gundacker, *SiPM applications in positron emission tomography: toward ultimate PET time-of-flight resolution*, Eur. Phys. J. Plus **136** (2021), https://doi.org/10.1140/epjp/s13360-021-01183-8.

[140] E. Berg, E. Roncali and S. R. Cherry, *Optimizing light transport in scintillation crystals for time-of-flight PET: an experimental and optical Monte Carlo simulation study.*, Biomed. Opt. Express **6**, 2220 (2015), https://doi.org/10.1364/BOE.6.002220.

[141] A. Choghadi *et al.*, *Evaluation of dual-ended readout GAGG-based DOI-PET detectors with different surface treatments*, Med. Phys. **48**, 3470 (2021), https://doi.org/10.1002/mp.14874.

[142] E. Roncali *et al.*, *An integrated model of scintillator-reflector properties for advanced simulations of optical transport*, Phys. Med. Biol. **62**, 4811 (2017), https://doi.org/10.1088/1361-6560/aa6ca5.

[143] R. H. Pots, E. Auffray and S. Gundacker, *Exploiting Cross-Luminescence in BaF2 for Ultrafast Timing Applications Using Deep-Ultraviolet Sensitive HPK Silicon Photomultipliers*, Front. Phys. **8** (2020), https://doi.org/10.3389/fphy.2020.592875.

[144] B. Singh *et al.*, *Enhanced Scintillation Light Extraction Using Nanoimprinted Photonic Crystals*, IEEE Trans. Nucl. Sci. **65**, 1059 (2018), https://doi.org/10.1109/TNS.2018.2811646.

[145] B. Ma *et al.*, *Scatter Correction based on GPU-accelerated Full Monte Carlo Simulation for Brain PET/MRI*, IEEE Trans. Med. Imag. **39**, 140 (2019), https://doi.org/10.1109/TMI.2019.2921872.

[146] H. Arabi *et al.*, *The promise of artificial intelligence and deep learning in PET and SPECT imaging*, Phys. Med. **83**, 122 (2021), https://doi.org/10.1016/j.ejmp.2021.03.008.

[147] S. Mostafapour *et al.*, *Feasibility of Deep Learning-Guided Attenuation and Scatter Correction of Whole-Body 68Ga-PSMA PET Studies in the Image Domain*, Clin. Nucl. Med. **46**, 609 (2021), https://doi.org/10.1097/RLU.0000000000003585.

[148] R. Guo *et al.*, *Using domain knowledge for robust and generalizable deep learning-based CT-free PET attenuation and scatter correction*, Nat. Commun. **13**, 5882 (2022), https://doi.org/10.1038/s41467-022-33562-9.

[149] A. J. Reader *et al.*, *Deep Learning for PET Image Reconstruction*, IEEE trans. radiat. plasma med. sci. **5**, 1 (2021), https://doi.org/10.1109/TRPMS.2020.3014786.

[150] Z. Liu *et al.*, *Deep-Learning-Based Framework for PET Image Reconstruction from Sinogram Domain*, Appl. Sci. **12**, 8118 (2022), https://doi.org/10.3390/app12168118.

[151] M. Krake *et al.*, *Power-efficient high-frequency readout concepts of SiPMs for TOF-PET and HEP*, Nucl. Instrum. Methods Phys. Res., Sect. A **1039**, 167032 (2022), https://doi.org/10.1016/j.nima.2022.167032.

[152] S. Gomez *et al.*, *FastIC: a fast integrated circuit for the readout of high performance detectors*, JINST **17** (2022), https://doi.org/10.1088/1748-0221/17/05/C05027.

Appendix A
GATE materials - XCAT phantom

```
Air: d=1.29 mg/cm3 ; n=4 ; state=gas
     +el: name=Nitrogen   ; f=0.755268
     +el: name=Oxygen     ; f=0.231781
     +el: name=Argon      ; f=0.012827
     +el: name=Carbon     ; f=0.000124

Lung:  d=0.26 g/cm3 ; n=9
       +el: name=Hydrogen   ; f=0.103
       +el: name=Carbon     ; f=0.105
       +el: name=Nitrogen   ; f=0.031
       +el: name=Oxygen     ; f=0.749
       +el: name=Sodium     ; f=0.002
       +el: name=Phosphor   ; f=0.002
       +el: name=Sulfur     ; f=0.003
       +el: name=Chlorine   ; f=0.003
       +el: name=Potassium  ; f=0.002

Adipose: d=0.92 g/cm3 ; n=11
        +el: name=Hydrogen   ; f=0.120
        +el: name=Carbon     ; f=0.640
        +el: name=Nitrogen   ; f=0.008
        +el: name=Oxygen     ; f=0.229
        +el: name=Phosphor   ; f=0.002
        +el: name=Calcium    ; f=0.001
        +el: name=Scandium   ; f=0.0
        +el: name=Titanium   ; f=0.0
        +el: name=Vandium    ; f=0.0
        +el: name=Chromium   ; f=0.0
        +el: name=Manganese  ; f=0.0

Body:   d=1.00 g/cm3 ; n=2
        +el: name=Hydrogen   ; f=0.112
        +el: name=Oxygen     ; f=0.888

Lymph:  d=1.03 g/cm3 ; n=11
        +el: name=Hydrogen   ; f=0.108
        +el: name=Carbon     ; f=0.041
        +el: name=Nitrogen   ; f=0.011
        +el: name=Oxygen     ; f=0.832
        +el: name=Sodium     ; f=0.003
        +el: name=Sulfur     ; f=0.001
        +el: name=Chlorine   ; f=0.004
        +el: name=Argon      ; f=0.0
        +el: name=Potassium  ; f=0.0
        +el: name=Calcium    ; f=0.0
        +el: name=Scandium   ; f=0.0

Intestine: d=1.03 g/cm3 ; n=11
        +el: name=Hydrogen   ; f=0.106
        +el: name=Carbon     ; f=0.115
        +el: name=Nitrogen   ; f=0.022
        +el: name=Oxygen     ; f=0.751
        +el: name=Sodium     ; f=0.001
        +el: name=Phosphor   ; f=0.001
        +el: name=Sulfur     ; f=0.001
        +el: name=Chlorine   ; f=0.002
        +el: name=Potassium  ; f=0.001
        +el: name=Calcium    ; f=0.0
        +el: name=Scandium   ; f=0.0

Pancreas: d=1.04 g/cm3 ; n=11
        +el: name=Hydrogen   ; f=0.106
        +el: name=Carbon     ; f=0.169
        +el: name=Nitrogen   ; f=0.022
        +el: name=Oxygen     ; f=0.694
        +el: name=Sodium     ; f=0.002
        +el: name=Phosphor   ; f=0.002
        +el: name=Sulfur     ; f=0.001
        +el: name=Chlorine   ; f=0.002
        +el: name=Potassium  ; f=0.002
        +el: name=Calcium    ; f=0.0
        +el: name=Scandium   ; f=0.0

Brain:  d=1.04 g/cm3 ; n=11
        +el: name=Hydrogen   ; f=0.107
        +el: name=Carbon     ; f=0.145
        +el: name=Nitrogen   ; f=0.022
        +el: name=Oxygen     ; f=0.712
        +el: name=Sodium     ; f=0.002
        +el: name=Phosphor   ; f=0.004
        +el: name=Sulfur     ; f=0.002
        +el: name=Chlorine   ; f=0.003
        +el: name=Potassium  ; f=0.003
        +el: name=Calcium    ; f=0.0
        +el: name=Scandium   ; f=0.0

Kidney: d=1.05 g/cm3 ; n=11
        +el: name=Hydrogen   ; f=0.103
        +el: name=Carbon     ; f=0.132
        +el: name=Nitrogen   ; f=0.03
        +el: name=Oxygen     ; f=0.724
        +el: name=Sodium     ; f=0.002
        +el: name=Phosphor   ; f=0.002
        +el: name=Sulfur     ; f=0.002
        +el: name=Chlorine   ; f=0.002
        +el: name=Potassium  ; f=0.002
        +el: name=Calcium    ; f=0.001
        +el: name=Scandium   ; f=0.0

Heart:  d=1.05 g/cm3 ; n=11
        +el: name=Hydrogen   ; f=0.104
        +el: name=Carbon     ; f=0.139
        +el: name=Nitrogen   ; f=0.029
        +el: name=Oxygen     ; f=0.718
        +el: name=Sodium     ; f=0.001
        +el: name=Phosphor   ; f=0.002
        +el: name=Sulfur     ; f=0.002
        +el: name=Chlorine   ; f=0.002
        +el: name=Potassium  ; f=0.003
        +el: name=Calcium    ; f=0.
        +el: name=Scandium   ; f=0.0

Muscle: d=1.05 g/cm3 ; n=11
        +el: name=Hydrogen   ; f=0.102
        +el: name=Carbon     ; f=0.143
        +el: name=Nitrogen   ; f=0.034
        +el: name=Oxygen     ; f=0.71
        +el: name=Sodium     ; f=0.001
        +el: name=Phosphor   ; f=0.002
        +el: name=Sulfur     ; f=0.003
        +el: name=Chlorine   ; f=0.001
        +el: name=Potassium  ; f=0.004
        +el: name=Calcium    ; f=0.0
        +el: name=Scandium   ; f=0.0

Blood:  d=1.06 g/cm3 ; n=11
        +el: name=Hydrogen   ; f=0.102
        +el: name=Carbon     ; f=0.11
        +el: name=Nitrogen   ; f=0.033
        +el: name=Oxygen     ; f=0.745
        +el: name=Sodium     ; f=0.001
        +el: name=Phosphor   ; f=0.001
        +el: name=Sulfur     ; f=0.002
        +el: name=Chlorine   ; f=0.003
        +el: name=Potassium  ; f=0.002
        +el: name=Iron       ; f=0.001
        +el: name=Cobalt     ; f=0.0

Liver:  d=1.06 g/cm3 ; n=11
        +el: name=Hydrogen   ; f=0.102
        +el: name=Carbon     ; f=0.139
        +el: name=Nitrogen   ; f=0.03
        +el: name=Oxygen     ; f=0.716
        +el: name=Sodium     ; f=0.002
        +el: name=Phosphor   ; f=0.003
        +el: name=Sulfur     ; f=0.003
        +el: name=Chlorine   ; f=0.002
        +el: name=Potassium  ; f=0.003
        +el: name=Calcium    ; f=0.0
        +el: name=Scandium   ; f=0.0

Spleen: d=1.06 g/cm3 ; n=11
        +el: name=Hydrogen   ; f=0.103
        +el: name=Carbon     ; f=0.113
        +el: name=Nitrogen   ; f=0.032
        +el: name=Oxygen     ; f=0.741
        +el: name=Sodium     ; f=0.001
        +el: name=Phosphor   ; f=0.003
        +el: name=Sulfur     ; f=0.002
        +el: name=Chlorine   ; f=0.002
        +el: name=Potassium  ; f=0.003
        +el: name=Calcium    ; f=0.0
        +el: name=Scandium   ; f=0.0

Cartilage: d=1.10 g/cm3 ; n=11
        +el: name=Hydrogen   ; f=0.096
        +el: name=Carbon     ; f=0.099
        +el: name=Nitrogen   ; f=0.022
        +el: name=Oxygen     ; f=0.744
        +el: name=Sodium     ; f=0.005
        +el: name=Phosphor   ; f=0.022
        +el: name=Sulfur     ; f=0.009
        +el: name=Chlorine   ; f=0.003
        +el: name=Argon      ; f=0.0
        +el: name=Potassium  ; f=0.0
        +el: name=Calcium    ; f=0.0

SpineBone: d=1.42 g/cm3 ; n=11
        +el: name=Hydrogen   ; f=0.063
        +el: name=Carbon     ; f=0.261
        +el: name=Nitrogen   ; f=0.039
        +el: name=Oxygen     ; f=0.436
        +el: name=Sodium     ; f=0.001
        +el: name=Magnesium  ; f=0.001
        +el: name=Phosphor   ; f=0.061
        +el: name=Sulfur     ; f=0.003
        +el: name=Chlorine   ; f=0.001
        +el: name=Potassium  ; f=0.001
        +el: name=Calcium    ; f=0.133

Skull:  d=1.61 g/cm3 ; n=11
        +el: name=Hydrogen   ; f=0.05
        +el: name=Carbon     ; f=0.212
        +el: name=Nitrogen   ; f=0.04
        +el: name=Oxygen     ; f=0.435
        +el: name=Sodium     ; f=0.001
        +el: name=Magnesium  ; f=0.002
        +el: name=Phosphor   ; f=0.081
        +el: name=Sulfur     ; f=0.003
        +el: name=Calcium    ; f=0.176
        +el: name=Scandium   ; f=0.0
        +el: name=Titanium   ; f=0.0

RibBone: d=1.92 g/cm3 ; n=11
        +el: name=Hydrogen   ; f=0.034
        +el: name=Carbon     ; f=0.155
        +el: name=Nitrogen   ; f=0.042
        +el: name=Oxygen     ; f=0.435
        +el: name=Sodium     ; f=0.001
        +el: name=Magnesium  ; f=0.002
        +el: name=Phosphor   ; f=0.103
        +el: name=Sulfur     ; f=0.003
        +el: name=Calcium    ; f=0.225
        +el: name=Scandium   ; f=0.0
        +el: name=Titanium   ; f=0.0
```

Appendix B

Photon path lengths in a cylindrical phantom

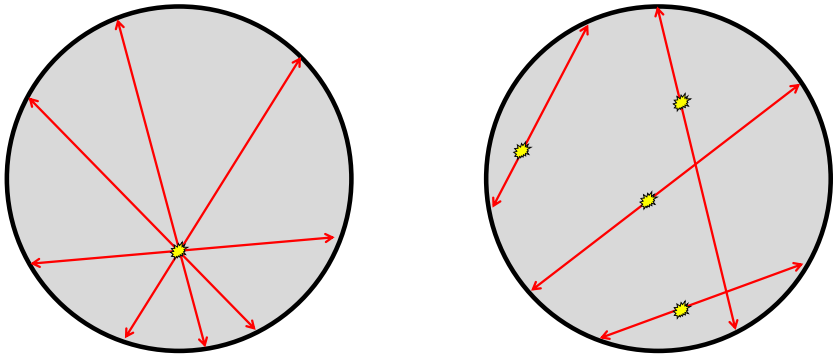

Figure B.1: Schematic representation of path lengths in the 20 cm diameter cylindrical phantom with a line sorce placed 4.5 cm bellow the center (NEMA standard) and with a homogeneously distributed activity within the volume. Considering the 2D case with a circle, the mean path length of the annihilation gammas is ~ 18.9 cm in the phantom with a line source (Monte Carlo method used to approximate the mean line segment length, number of simulated segments $= 10^6$), compared to the ~ 17.0 cm length in the phantom with homogeneously distributed activity, resulting in a higher probability of attenuation in the phantom, and a higher scatter fraction when imaging such a phantom.

Razširjeni povzetek v slovenskem jeziku

Uvod

Med vsemi tomografskimi molekularnimi slikovnimi modalitetami, ki so na voljo za neinvazivno študijo fiziologije, metabolizma in molekularnih poti pri ljudeh, je pozitronska emisijska tomografija (PET) splošno priznana kot najbolj občutljiva in specifična [1]. Pri PET preiskavi se v telo pacienta vbrizga radiofarmak, ki razpade z oddajanjem pozitronov. Tehnika PET slikanja temelji na zaznavanju dveh koincidenčnih, nasprotno potujočih visokoenergijskih (511 keV) fotonov, ki nastaneta pri anihilaciji pozitrona z elektroni v telesu. Fizika emisije in zaznavanja koincidenčnih fotonov daje PET slikanju zmožnost doseganja visoke občutljivost in natančnega določanja koncentracije vbrizganega radiofarmaka v različnih delih telesa. PET slikanje je široko sprejeto kot pomembna klinična preiskava predvsem na področju onkologije, kardiologije in nevrologije [2].

Kljub desetletjem razvoja še vedno obstajajo znatne priložnosti za izboljšanje delovanja PET sistemov za različne klinične in raziskovalne preiskave [3]. Vse študije nuklearne medicine pri ljudeh so omejene s kompromisom med številom zaznanih dogodkov, časom slikanja in prejeto dozo sevanja. Razmerje med signalom in šumom (angl. signal-to-noise ratio; SNR) je ena ključnih mer kakovosti slike, in v PET slikanju je to razmerje, v prvem približku, določeno s številom zaznanih dogodkov. Nizek SNR je verjetno največja tehnična omejitev pri današnjem PET slikanju, saj igra ključno vlogo tudi pri nekaterih drugih omejitvah PET slikanja, kot so nizka prostorska ločljivost, dolg čas slikanja in relativno visoka sevalna obremenitev [4].

Detektorji imajo glavno vlogo pri določanju zmogljivosti PET skenerja. Zato ni presenetljivo, da se veliko inovacij v PET instrumentaciji osredotoča na razvoj boljših ali novih detektorskih tehnologij. To delo raziskuje možnost izboljšanja PET skenerjev z uporabo detektorjev na osnovi zaznave Čerenkove namesto scintilacijske svetlobe. Dva pomembna vidika detektorja, ki neposredno vplivata na SNR skenerja sta učinkovitost zaznave žarkov gama in časovna ločljivost. Z meritvijo časa preleta (angl. time-of-flight; TOF) žarkov gama lahko zmanjšamo šum na rekonstruirani PET sliki. PbF_2 je potencialno odličen material za zaustavljanje in zaznavanje žarkov gama zaradi visoke gostote in visokega efektivnega atomskega števila, kar vodi v višji atenuacijski koeficient in višji delež fotoefekta, kot sta pri najbolj razširjenem scintilatorju v PET; L(Y)SO. Poleg tega so fotoni Čerenkova promptni; izsevajo se v nekaj pikosekundah. Ta lastnost naredi Čerenkovovo sevanje zelo privlačno za uporabo v aplikacijah hitrega časovnega merjenja, saj je prispevek procesa izsevanja fotonov, k skupni časovni ločljivosti detektorja, skoraj ničen.

Vendar pa, ker je skupno število proizvedenih fotonov Čerenkova majhno (nekaj deset), to predstavlja izziv za učinkovitost zaznave žarkov gama in energijsko ločljivost čistega Čerenkovega detektorja. V splošnem se želi detektor s čim večjo energijsko ločljivostjo, da se lahko ločujejo sipani fotoni od primarnih. Poleg tega je visok izkoristek fotodetektorja ključnega pomena za čisti Čerenkov PET detektor, saj če se noben od proizvedenih fotonov Čerenkova ne zazna, se dogodek izgubi, kar vodi v zmanjšano občutljivost detektorja. Silicijeve fotopomnoževalke (SiPM) so postali prva izbira fotodetektorjev za klinične/scintilacijske PET detektorje in so tudi zelo obetavni fotodetektorji za branje čistih Čerenkovih sevalcev. Z uporabo novih SiPM z dobro učinkovitostjo zaznave fotonov (tudi v UV območju) so v delu Kratochwil et al. 2021 [6] iz meritev ocenili zelo obetavno 74% verjetnost zaznave koincidenčnega dogodka z uporabo kristalov PbF_2 dolžine 20 mm.

To delo raziskuje kakovost slike pri Čerenkovi pozitronski tomografiji, z uporabo Monte Carlo simulacij. Simulacije so bile zasnovane v programu GATE in izvedene na slovenskem nacionalnem superračunalniškem omrežju (SLING). Glavno raziskovalno vprašanje, ki ga to delo poskuša odgovoriti, je: Ali lahko skener, ki temelji na čistem Čerenkovem sevalcu PbF_2 in praktično nima energijske ločljivosti, zagotavlja konkurenčno kakovost slike v primerjavi s trenutnimi najnovejšimi kliničnimi PET skenerji? Negativni vpliv sipanih dogodkov na kakovost slike, lahko kompenziramo z detektiranjem večjega števila pravih dogodkov, zato so bile preučene tudi različne konfiguracije Čerenkovih detektorjev s potencialno višjo učinkovitostjo zaznave žarkov gama.

Čisti Čerenkovi detektorji PET pa nimajo potenciala samo za visoko zmogljivost, ampak so lahko potencialno tudi dosti cenejši od trenutnih detektorjev, zahvaljujoč nižji ceni materiala in manjšega vložka energije, potrebnega za proizvodnjo kristalov. Uporaba Čerenkovih detektorjev v visoko zmogljivih, a trenutno zelo dragih dolgih skenerjih celotnega človeškega telesa (angl. total-body PET scanner), bi lahko te skenerje naredila bolj dostopne in bolj razširjene.

Uporaba Čerenkove svetlobe v PET

Uporaba svetlobe Čerenkova za zaznavanje žarkov gama v PETu je bila prvič razpravljana v Ooba et al. 2004 [80], kjer je bilo predlagano izboljšanje časovne ločljivost detektorja z uporabo svetlobe Čerenkova, ki jo proizvede silikatni aerogel z lomnim količnikom 1.2. Ampak silikatni aerogel kot sevalec ne bi imel zelo visoke učinkovitosti zaznave žarkov gama zaradi nizke gostote (~ 5 kg/m^3) in nizkega svetlobnega pridelka, zaradi nizkega lomnega količnika.

Zelo dobre časovne ločljivosti koincidenc (angl. coincidence time resolution; CTR) so bile dosežene z uporabo čistih Čerenkovih sevalcev, združenih z mikrokanlnimi fotopomnoževalkami (MCP-PMT) kot senzorji svetlobe. Na primer, Miyata et al. 2006 [81] so opravili meritve z uporabo svinčevega stekla (PbG) in poročali o CTR 170 ps.

Svinčev fluorid (PbF_2) je bil prvič eksperimentalno raziskan v Korpar et al. 2011 [82], kjer so izmerili CTR 95 ps FWHM za kristale dolžine 15 mm. Nedavno so Ota et al. 2019 [83] z uporabo PbF_2 kristalov dolžine 5 mm, poročali o CTR 47 ps FWHM, kar ustreza krajevni ločljivosti 7.0 mm vzdolž črte odziva. Ta skupina je preizkusila tudi integriran detektor Čerenkovega sevalca in mikrokanalne fotopomnoževalke (CRI-MCP-PMT), kjer ni bilo optičnih meja med sevalcem in fotokatodo. Dosegli so izjemni CTR okoli 30 ps FWHM [84], in demonstrirali so tudi neposredno

(brez rekonstrukcije) PET slikanje z uporabo teh hitrih detektorjev [85]. Vendar pa so bili za dosego takšne časovne ločljivosti uporabljeni skrbno izbrani signali, ki predstavljajo le majhno število vseh zaznanih dogodkov. Avtorji priznavajo, da ti detektorji v takšnem načinu delovanja, ne dosegajo učinkovitosti zaznave žarkov gama, ki je potrebna za klinične PET detektorje. Čeprav imajo MCP-PMT odličen časovni odziv, imajo tudi nekaj pomanjkljivosti, kot so visoka cena, velikost in nizek izkoristek zaznavanja opičnih fotonov.

Silicijeve fotopomnoževalke so obetavni fotodetektorji za uporabo s čistimi sevalci svetlobe Čerenkova. Imajo višji izkoristek zaznave fotonov kot MCP-PMT, so kompaktne, cenovno dostopne in lahko zaznavajo optične fotone s časovno ločljivostjo zaznave posameznega fotona (SPTR) pod 100 ps [86]. Uporaba SiPM s kristali PbF_2 je bila najprej raziskana s strani Dolenec et al. 2016 [87], kjer je bil najboljši CTR 297 ps FWHM. Ta vrednost se je izboljšala na 197 ps FWHM za kristale dolžine 15 mm, ko so bili uporabljeni le dogodki s samo eno sproženo mikrocelico, vendar se je pri tem zmanjšala učinkovitost zaznave žarkov gama [88]. Z uporabo drugačne verige detekcije (SiPM + elektronika + digitalizacija) se je nedavno dosegla časovna ločljivost 215 ps FWHM (142 ps FWHM) za kristale PbF_2 velikosti $2 \times 2 \times 20$ mm^3 ($2 \times 2 \times 3$ mm^3) [6]. Omenjene študije Čerenkov PET detektorjev so pokazale tudi, da ima obdelava površine kristalov pomemben vpliv tako na učinkovitost zaznave kot tudi na časovno ločljivost detektorja.

Efektivno hitrost štetja z ekvivalentnim šumom (angl. noise equivalent count rate; NECR) in prostorsko ločljivost celotnega PbF_2 Čerenkov TOF-PET skenerja so preučevali Alokhina et al. 2018 [89] z uporabo simulacij GATE/Geant4. Med študiranimi konstrukcijami detektorja so dosegli najboljši efektivni NECR z 10 mm dolgimi kristali z difuznim belim premazom, s katerimi je bila dosežena TOF ločljivost 180 ps.

Fotoni Čerenkova se proizvajajo tudi v scintilatorjih in se lahko potencialno uporabijo za izboljšanje časovne ločljivosti. Obstaja ponovno zanimanje za BGO kot hibridni scintilator in sevalec svetlobe Čerenkova, ki bi se uporabljal kot cenovno učinkovita rešitev za TOF PET [90, 91]. Natančneje, BGO je približno za tretjino cenejši od scintilatorjev, ki temeljijo na luteciju [19].

Iz meritev se ocenjuje, da se v povprečju proizvede 17 ± 3 fotonov Čerenkova ob interakciji 511 keV fotona v BGO [17]. BGO je bil prva izbira scintilatorja za uporabo v PET skenerjih od začetka 1980-ih do sredine 2000-ih zahvaljujoč visokemu atenuacijskemu koeficientu in deležu fotoefekta (višji od L(Y)SO). Vendar zaradi nizkega pridelka svetlobe in počasnega scintilacijskega signala, ni bil primeren za TOF PET (najboljši CTR približno 1.5 ns FWHM izmerjen za 20 mm dolge kristale [92]). Toda pred kratkim je bilo demonstrirano, da je možno TOF slikanje z uporabo promptnih fotonov Čerenkova. CTR približno 260 ps je bil izmerjen za 20 mm dolge BGO kristale [93].

Polprevodniški materiali z visoko prepustnostjo vidne svetlobe, visokim lomnim količnikom in visoko absorpcijo žarkov gama, kot sta talijev bromid (TlBr) in talijev klorid (TlCl), so bili predlagani kot detektorji sevanja, ki lahko združujejo odlično energijsko ločljivost preko zbranega naboja ter časovno ločljivostjo doseženo preko detekcije svetlobe Čerenkova [94]. Nedavna študija, ki so jo opravili Ariño-Estrada et al. 2021 [96], poroča, da so zaznali povprečno 1.5 fotona za TlBr in 2.8 fotona na dogodek za TlCl, ko so bili ti materiali brani s silicijevo fotopomnoževalko. Najboljši izmerjen CTR pri TlBr je bil 329 ± 9 ter 316 ± 9 ps pri TlCl.

To delo se osredotoča na svinčev fluorid, ki je eden izmed najboljših znanih Čerenkovih sevalcev. PbF_2 je čisti Čerenkov sevalec, kar pomeni, da ne proizvaja scintilacijske svetlobe. Je zelo gost ($\rho = 7.8$ g/cm^3) in ima eno najvišjih fotofrakcij (46%), zahvaljujoč njegovemu visokemu atomskemu številku ($Zeff = 77$). V Tabeli 8.1 so prikazane fizikalne lastnosti PbF_2 in nekaterih drugih Čerenkovih sevalcev ter anorganskih scintilatorjev.

Tabela 8.1: Fizične lastnosti izbranih Čerenkovih sevalcev in anorganskih scintilatorjev citeLSO2008, PbF2-1990, Kratochwil2021, nist. Atenuacijski koeficient μ in delež fotoefekta (fotofrakcija) so podani za 511 keV fotone.

Material	PbF_2	Lu_2SiO_5	$Bi_4Ge_3O_{12}$	TlBr	TlCl	$PbWO_4$
Gostota (g/cm^3)	7.8	7.4	7.1	7.5	7.0	8.3
Efektivno atomsko število	77	64	71	73	76	74
μ (cm^{-1})	1.13	0.87	0.96	1.0	1.0	1.14
Fotofrakcija	0.46	0.32	0.41	0.42	0.45	0.43
Lomni količnik pri 550 nm	1.77	1.8	2.12	2.47	2.28	2.16
Mejna valovna dolžina(nm)	250	370	300	440	380	320
Tališče (°C)	824	2050	1050	460	430	1123

Simulacije, ki so jih opravili Canot et al. 2019 [100], so pokazale, da so elektroni, ki so bili izbiti preko fotoelektričnega pojava v Pb_2, dovolj hitri, da proizvedejo približno 20 optičnih fotonov na začetku. Ti rezultati simulacij se dobro ujemajo s predvidenim nastankom 16.5 ± 3.3 fotonov Čerenkova, ki je bil ocenjen za PbF_2 iz meritev [6].

Visoki ρ in Z_{eff} dajejo PbF_2 odlično moč ustavljanja anihilacijskih žarkov gama (atenuacijska dolžina $= 1/\mu = 8.8$ mm). Med potencialnimi scintilatorji in Čerenkovimi sevalci za PET, ki jih najdemo v literaturi, ima le svinčev volframat ($PbWO_4$) nekoliko višji atenuacijski koeficient. V nasprotju s PbF_2, $PbWO_4$ tudi scintilira z okoli 200 fotoni/MeV. Teh scintilacijskih fotonov ni dovolj, da bi $PbWO_4$ imel dobro energijsko ločljivost, poleg tega pa proženje na signalu, ki je mešanica med hitro Čerenkovo in počasno scintilacijsko komponento, rezultira v poslabšani časovni ločljivosti [17, 101].

Poleg tega ima $PbWO_4$, v primerjavi s PbF_2, nižji delež fotoefekta in višjo mejno valovno dolžino. Mejna valovna dolžina je določena kot najnižja valovna dolžina, pri kateri je snov še vedno prosojna in je zelo pomemben parameter za Čerenkove sevalce, saj močno vpliva na število proizvedenih fotonov Čerenkova, ki jih lahko zaznamo zaradi odvisnosti $1/\lambda^2$ spektra Čerenkove emisije. Na primer, visoke mejne dolžine 440 nm in 380 nm za TlBr in TlCl, rezultirajo v zelo nizkem številu (približno 10) fotonov Čerenkova, ki so proizvedeni v prosojnem območju kristala in predstavljajo eno od omejitev teh polprevodniških Čerenkovih sevalcev [96]. Svinčevo steklo ima podoben problem z mejno valovno dolžino 370-380 nm, poleg tega pa ima tudi nizko gostoto 4.0-5.2 g/cm^3, ki je odvisna od vsebnosti svinca [81].

S primerjavo atenuacijskih koeficientov 1.13 cm^{-1} za PbF_2 in 0.87 cm^{-1} za LSO, lahko ocenimo, da potrebujemo približno 15 mm PbF_2, da dosežemo enako moč ustavljanja žarkov gama kot 20 mm LSO. Skenerji, ki uporabljajo kristale PbF_2 namesto kristalov LSO, imajo tako potencial za boljši izkoristek detekcije pri enaki dolžini kristalov ali enak izkoristek pri krajši dolžini kristala, hkrati pa bi na ta način dosegli boljšo prostorsko ločljivost zaradi zmanjšanega učinka globine interakcije.

Nizka cena je tudi pomembna in privlačna lastnost PbF_2. Komercialni proizvajalci PET uporabljajo drage kristale na osnovi lutecija, in njihova cena je ena od dominantnih komponent cene skenerja PET. Cena kristalov postane še posebej pomembna, ko razmišljamo o podaljšanih PET skenerjih za slikanje celotnega telesa [4]. BGO in PbF_2, ki je še cenejši (1/3 BGO [102]) zahvaljujoč nizki ceni surovin in nižji točki taljenja, lahko omogočita cenovno učinkovito PET slikanje celotnega telesa.

Metodologija

Najprej je bila izvedena simulacijska študija različnih konfiguracij detektorjev s silicijevimi fotopomnoževalkami kot fotodetektorji. Nato je bilo izbranih nekaj teh konfiguracij za modeliranje celotnih Čerenkovih PET skenerjev. Zmogljivost Čerenkovih PET skenerjev je bila ocenjena in primerjana z referenčnim skenerjem; modelom kliničnega PET skenerja Siemens Biograph Vision. Ocenjena in primerjana je bila hitrost zbiranja dogodkov in kakovost slike skenerjev PET po NEMA NU 2-2018[1] standardu. Simulacije Monte Carlo so bile izvedene na slovenskem nacionalnem superračunalniškem omrežju z uporabo programa GATE [106] različice 8.1.

Študija detektorskih konfiguracij

Preučevani so bil detektorji z 1, 2 in 6-stranskim branjem kristala. Detektorji so temeljili na $3.2 \times 3.2 \times 20$ mm^3 velikih PbF_2 kristalih, kar ustreza velikosti kristalov, ki jih uporablja skener Siemens Biograph Vision. Dva detektorja sta bila postavljena nasproti eden drugemu, vmes pa je bil postavljen točkasti izvor žarkov gama energije 511 keV, kot je prikazano na sliki 8.2. Za vsako konfiguracijo detektorja je bilo simuliranih en milijon parov žarkov gama.

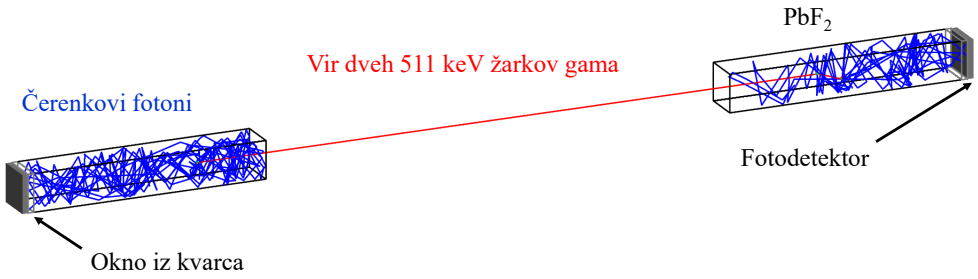

Slika 8.2: Postavitev detektorjev za preučevanje izkoristka in CTR različnih konfiguracij detektorjev; različne površinske obdelave in fotodetektorji, ki pokrivajo eno, dve ali vse ploskve kristala.

[1]https://www.nema.org/standards/view/Performance-Measurements-of- Pozitronski emisijski tomografi

Za simuliranje fizikalnih procesov je bil uporabljen model *emstandard_opt4* programa Geant4, ki uporablja natančne standardne in nizkoenergijske modele elektromagnetnih interakcij, zaradi česar je primeren za uporabo v medicinski fiziki [108]. Prag v sevalcu, za nabite delce, ki proizvajajo fotone Čerenkova, je bil nastavljen na 10 μm, v posameznem koraku pa je bil proizveden največ en foton Čerenkova. Fotoni Čerenkova so bili simulirani v območju 250-1000 nm, simulirani spekter pa je prikazan na sliki 8.3.

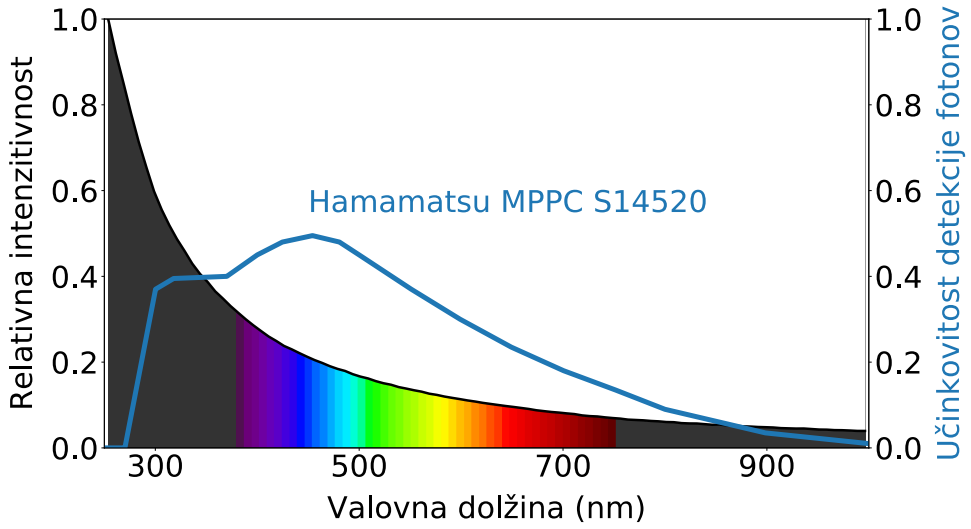

Slika 8.3: Spekter fotonov Čerenkova, proizvedenih v simulaciji, in učinkovitost zaznavanja fotonov fotodetektorja Hamamatsu MPPC S14520, ki je bil uporabljen v simulacijah.

V simulacijah sta bili uporabljeni dve različni površinski obdelavi kristala: absorpcijska (črna) površina in odbojna prevleka (reflektor). Za simulacijo fizikalnih procesov na optični meji je bil uporabljen model Geant4 UNIFIED [109]. Črna površina je bila modelirana kot gladka z lomnim količnikom 1.5 [110], optični foton pa je bil ustavljen, če je zapustil kristal. Odbojna površina je bila modelirana kot rahlo groba in preko zračne reže (lomni količnik - 1) sklopljena z difuznim reflektorjem s 95% odbojnostjo. Grobost površine je bila modelirana s parametrom *sigmaalpha*, ki opisuje kotno porazdelitev mikropovršin, ki sestavljajo makropovršino, nastavljeno na 5°. Poleg že omenjenih referenc so na izbiro optičnih parametrov vplivala tudi dela Janecek *et al.* 2010 [111], 2012 [112] in Roncali *et al.* 2013 [113], kot tudi eksperimentalno delo opravljeno znotraj odseka F9 Instituta Jožef Stefan [82, 87].

Fotodetektorji so bili simulirani z učinkovitostjo zaznavanja fotonov (angl. photon detection efficiency; PDE), ki je temeljila na silicijevi fotopomnoževalki Hamamatsu MPPC S14520 SiPM z vrhom PDE približno 50% pri okoli 450 nm (slika 8.3). Uporabljeni SiPM ima tudi dobro občutljivost v bližnjem ultravijoličnem delu spektra, kar je pomembno za fotone Čerenkova, saj je večja verjetnost, da bodo ti nastali pri krajših valovnih dolžinah. Učinek optične sklopitve med kristalom in fotodetektorjem je bil upoštevan tako, da je bil vmes dodan kvarčni blok, z lomnim količnikom 1.5, ki predstavlja okno realističnega fotodetektorja. Okno in fotodetektor sta bila modelirana tako, da sta imela zanemarljive velikosti (debelina 0.01 mm). Dogodek

je bil sprejet, če je bil zaznan najmanj en foton Čerenkova. Šum SiPM na tej točki ni bil simuliran, saj je bil glavni poudarek tega dela na škodljivih učinkih sipanja žarkov gama.

Učinkovitost zaznavanja koincidenc in CTR sta bila določena za par detektorjev. CTR je bil preučen za idealni in realistični primer tako, da je bila intrinzična enofotonska časovna ločljivost (SPTR) fotodetektorja (SiPM) nastavljena na 0 ps oziroma 70 ps [53]. V idealnem primeru je bila časovna variacija, zaradi globine interakcije in različnih dolžin poti fotonov Čerenkova v kristalu PbF_2, glavni omejevalni dejavnik časovne ločljivosti detektorja, saj so fotoni Čerenkova proizvedeni promptno. Nazadnje smo uporabili mero uspešnosti (angl. figure of merit; FOM) za primerjavo in izbiro konfiguracij detektorjev za simulacijo PET skenerja. FOM je bil definiran kot razmerje med učinkovitostjo zaznavanja koincidenc in CTR, to sta parametra detektorja, ki neposredno vplivata na občutljivost skenerja in posledično na kakovost PET slike [3].

Študija Čerenkovega PET skenerja

Za študijo PET skenerja so bile izbrane tri konfiguracije detektorjev:

- 1-stransko branje (kristal ovit z reflektorjem)
- 2-stransko branje s fotodetektorji ob bokih kristala, ovitega z reflektorjem
- 6-stransko branje (vse površine prekrite s fotodetektorji)

1-stransko branje predstavlja standard, 6-stransko branje je teoretični ideal, 2-stransko branje pa je nekaj, kar se smatra, kot še vedno praktično izvedljivo. Referenčni skener in Čerenkovi skenerji so bili oblikovani po konfiguraciji skenerja Siemens Biograph Vision PET/CT [114]. Podrobnosti o geometriji so prikazane na sliki 8.4. Zmogljivost Čerenkovih PET skenerjev se je primerjalo med seboj, kot tudi s simuliranimi rezultati referenčnega skenerja na podlagi izbranih mer iz standarda NEMA. Za verifikacijo simulacije, pa so se simulirane vrednosti referenčnega skenerja prav tako primerjale z izmerjenimi vrednostmi skenerja Siemens Biograph Vision PET/CT [114].

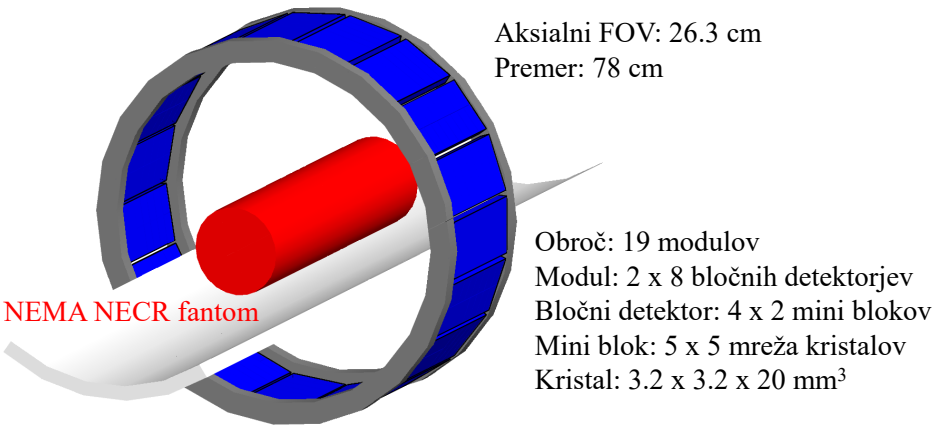

Slika 8.4: Geometrija skenerja, simulirana v GATE. Poleg simuliranega detektorskega obroča je na sliki mogoče videti tudi svinčen ščit, posteljo iz ogljikovih vlaken in cilindrični NEMA NECR fantom.

GATE simulacija

Referenčni skener je bil modeliran po skenerju Siemens Biograph Vision [114, 115]. V GATE Monte Carlo simulaciji je bil CTR referenčnega skenerja nastavljen na 214 ps FWHM, za sprejemanje dogodkov pa je bilo uporabljeno koincidenčno časovno okno 4.7 ns. Energijska ločljivost je bila nastavljena na 10%, in uporabljeno je bilo energijsko okno 435–585 keV. Branje je bil simulirano na ravni modula (slika 8.4). Signali znotraj modula so bili sešteti in če je bila skupna deponirana energija znotraj modula v okvirih energijskega okna, je bil dogodek sprejet in njegov položaj znotraj modula je bil določen po načelu energijskega središča (GATE *TakeEnergyCentroid*). V primeru večkratnih naključnih koincidenc so bili sprejeti vsi dobri pari (GATE načelo *takeAllGoods*).

Za Čerenkove skenerje je bilo uporabljeno isto časovno okno ter enaka strategija tvorjenja in razvrščanja koincidenc kot za referenčni skener, le da ni bilo uporabljenega energijskega okna (v tem primeru je zaznavanje temeljilo na optičnih fotonih namesto na žarkih gamah; GATE *opticaladded* namesto *adder*). SPTR fotodetektorja je bil v študiji PET skenerja nastavljen na 70 ps FWHM. Mrtvi čas detektorja ni bil upoštevan pri simulacijah. To je mogoče upravičiti z dejstvom, da je mrtvi čas sodobnih PET skenerjev zelo nizek v primerjavi s tradicionalnimi sistemi, ki temeljijo na fotopomnoževalkah. Zato so vse razlike v zmogljivosti hitrosti štetja, vsaj pri aktivnostih, ki se uporabljajo za klinično slikanje, v prvi vrsti določene z občutljivostjo sistema [19].

NECR in delež sipanja

NECR je pogosta mera, ki se uporablja za primerjavo delovanja PET sistemov. Karakterizira globalni SNR in deluje kot pokazatelj kakovosti slike na ravni sistema. Po standardu NEMA NU 2-2018 je bil fantom, uporabljen za to študijo, sestavljen iz simuliranega linijskega vira enakomerne aktivnosti znotraj 70 cm dolgega polietilenskega valja s premerom 20 cm. Ker so bile prave (T), sipane (S) in naključne (R) hitrosti štetja koincidenc natančno znane iz simulacije, je bil NECR določen kot

$$\mathrm{NECR} = \frac{T^2}{T + S + R} \tag{1}$$

V tem delu so bile hitrost štetja definirane na naslednji način: prave koincidence so bile posledica zaznanih anihilacijskih fotonov iz istega izvora (anihilacijskega dogodka), za sipane koincidence je veljal enako, le da je eden od obeh fotonov (ali oba) interagiral s snovjo (fantomom), preden je dosegel detektor. Naključne koincidence pa so tvorili signali dveh žarkov gama, ki sta prišla iz dveh različnih anihilacijskih dogodkov. Za vsak skener je bilo zbranih približno $\sim 10^6$ koincidenc (vsaj $5 \cdot 10^5$ dogodkov predlaga standard NEMA) za vsako stopnjo aktivnosti. Delež sipanja (SF) je bil določen kot

$$\mathrm{SF} = \frac{S}{T + S} \tag{2}$$

Kakovost slike

Za določitev odstotnega kontrasta in odstotne variabilnosti ozadja je bil uporabljen fantom v obliki prsnega koša z vročimi kroglicami iz standarda NEMA. Aktivnost ozadja je bila nastavljena na 5.3 kBq/cm^3 (0,14 μCi/cm^3), razmerje med aktivnostjo vročih kroglic in ozadjem pa je bilo 4:1. Uporabljene so bile točne maske kroglic kot

preučevano območje (angl. region of interest; ROI) za izračune odstotnega kontrasta in pri izračunih je bil upoštevan popravek delnih pikslov. Fantom je bil postavljen na sredino skenerja in simulirana so bila 4-minutna slikanja. Variacija odstotnega kontrasta in odstotne variabilnosti kontrasta je bila ocejena iz 5 neodvisno simuliranih 4-minutnih slikanj.

Rekonstrukcija slike

Za rekonstrukcijo slik je bil uporabljen odprtokodni program CASToR [116]. Rekonstrukcijski parametri so bili osnovani na parametrih uporabljenih v kliničnem skenerju Siemens Biograph Vision [114]. Zbrani podatki so bili rekonstruirani z uporabo 3D-iterativnega algoritma OSEM (ordered subset expectation maximization) z 8 iteracijami in 5 podmnožicami na 225 $\times 225 \times 225$ veliko matriko z velikostjo vokslov $1.6 \times 1.6 \times 1.6$ mm^3. Korekcijski faktorji za normalizacijo so bili izračunani s pomočjo programa CASToR. Za izračun korekcijskih faktorjev atenuacije je bila uporabljena prava atenuacijska slika fantoma.

Postopek korekcije naključnih in sipanih koincidenc je prikazan na sliki 8.5. Korekcijska metoda temelji na predpostavki, da je rekonstrukcija linearna in da lahko ločeno rekonstruiramo različne vrste koincidenc (prave, sipane in naključne). Ob upoštevanju te predpostavke je bila popravljena slika dobljena tako, da se je od slike, kjer so bile pri rekonstrukciji uporabljene vse koincidence, odštela slika, rekonstruirana samo iz sipanih in naključnih koincidenc, dobljenih iz ločene simulacije. Ker OSEM ni linearen algoritem, je bila ovrednotena vnesena napaka zaradi predpostavke o linearnosti. Rekonstruirana slika NEMA fantoma z uporabo vseh koincidenc ja bila primerjana s sliko, pridobljeno z združitvijo slik ločeno rekonstruiranih pravih ter sipanih in naključnih koincidenc. Primerjava je bila narejena tako za referenčni kot za Čerenkov skener. Čeprav je bila relativna razlika na ravni vokslov do nekaj odstotkov, je bil vpliv na odstotek kontrasta za vse vroče kroglice pod 1%, vpliv na variabilnost ozadja pa približno 1%, kar pomeni, da se algoritem OSEM obnaša precej linearno, vsaj v proučevanem režimu; pri uporabi 8 iteracij in 5 podmnožic.

Pri rekonstrukciji slike je bila uporabljena tudi informacija TOF. S slikanjem točkastega vira gama 511 keV, postavljenega v sredino skenerja, je bila, iz histograma razlik v časih zaznavanja ($t_2 - t_1$) koincidenčnih dogodkov, pridobljena časovna ločljivost Čerenkovih skenerjev. Histograma časovnih razlik zaznavanja ni bilo mogoče dobro prilagoditi z eno samo Gaussovo funkcijo, kar so opazile tudi druge skupine, ki so izvajale meritve časa na PbF_2 [6, 100] in BGO [90, 93]. Za upoštevanje presežnih dogodkov pri daljših časovnih zamikih je bila porazdelitev časovnih razlik modelirana z dvojno Gaussovo funkcijo

$$f(x) = a_1 \exp(-\frac{x^2}{2\sigma_1}) + a_2 \exp(-\frac{x^2}{2\sigma_2}) \tag{3}$$

Slika 8.6 prikazuje, da so časovni histogrami dobro prilagojeni z dvojno Gaussovo funkcijo, prikazano pa je tudi mešalno razmerje a_1/a_2.

Negotovost meritev TOF je običajno modelirana z normalizirano Gaussovo funkcijo. Za implementacijo dvojnega Gaussovega jedra TOF, uporabljenega pri rekonstrukciji slike, je bilo potrebno dopolniti CASToR kodo. Dobljene slike so bile primerjane s slikami, pridobljenimi s standardnim enojnim Gaussovim jedrom TOF, in rezultati so pokazali boljšo primernost dvojnega Gaussovega jedra TOF.

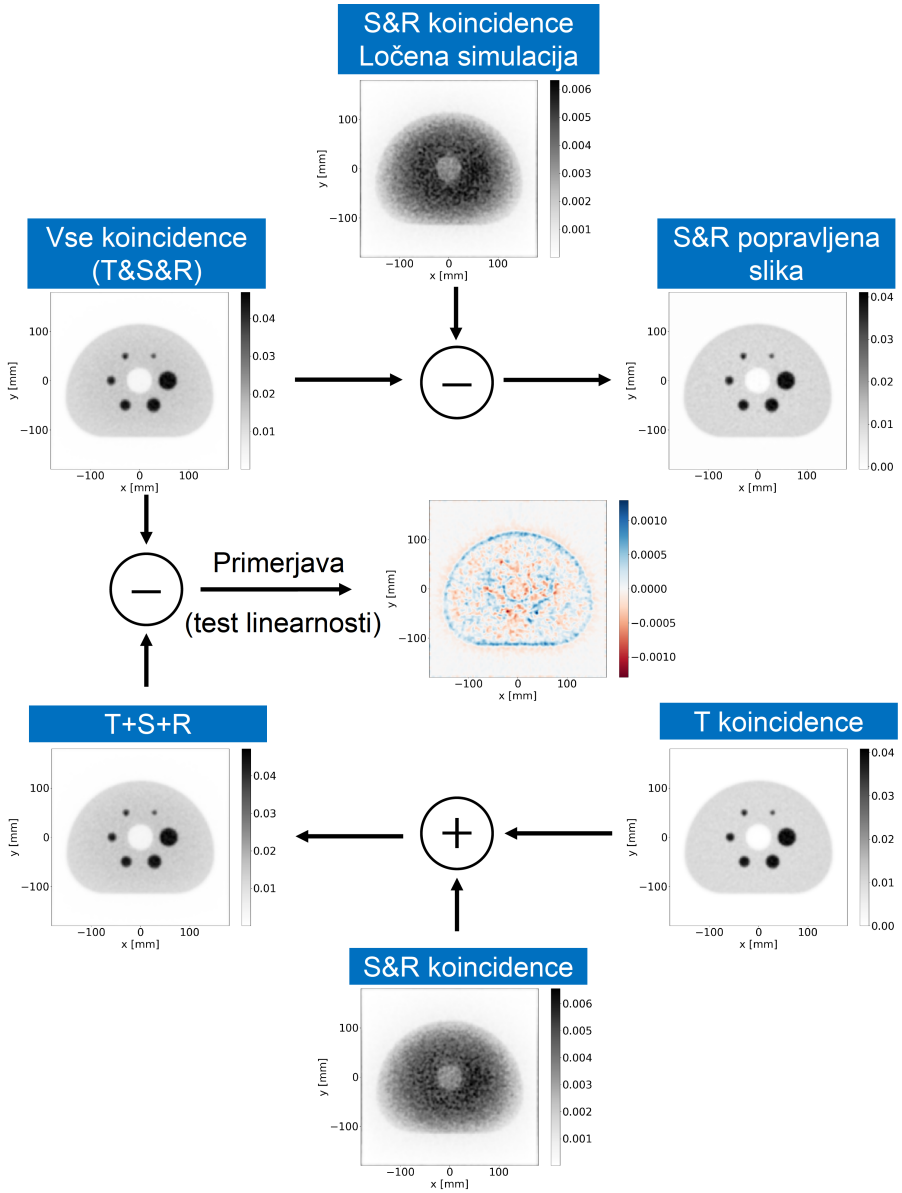

Slika 8.5: Grafična ponazoritev metode, uporabljene za korekcijo sipanih in naključnih koincidenc. Uporabljena notacija je T-prave (true), S-sipane (scatter) in R-naključne (random) koincidence. Ker ta metoda predpostavlja, da je OSEM rekonstrukcija linearna, je bil izveden test linearnosti s primerjavo rekonstruiranih slik NEMA z uporabo vseh koincidenc (T&S&R) s slikami T+S+R, dobljenimi z ločeno rekonstrukcijo slik T in S&R, ki so bile potem seštete. Primerjava je pokazala, da je OSEM zadovoljivo linearen; za vse vroče krogle so opažene le manjše (zanemarljive) razlike v odstotku kontrasta (CRC) in variabilnosti ozadja (BV).

Rezultati

Študija detektorskih konfiguracij

V študiji detektorjev so bili raziskani Čerenkovi detektorji na osnovi $3.2 \times 3.2 \times 20$ mm^3 velikih PbF_2 kristalov z različnim branjem kristalov in z dvema različnima obdelavama površin; črno in odsevno prevleko. Ocenjeni in primerjani so bili učinkovitost zaznavanja koincidenc, CTR in FOM. Rezultati so prikazani v

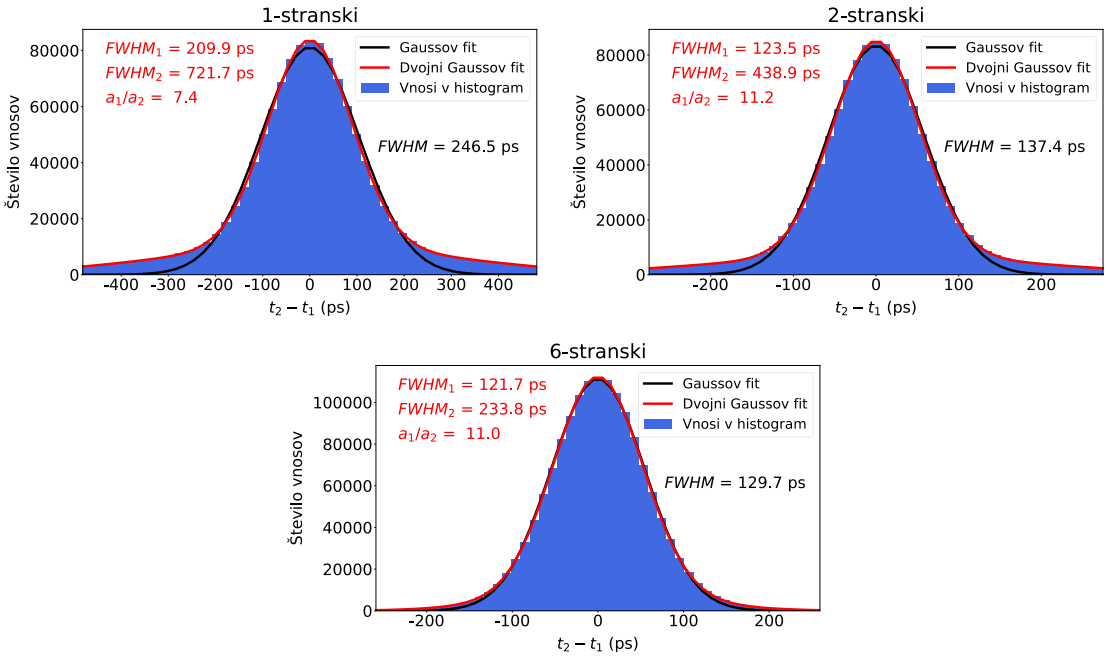

Slika 8.6: Histogram časovnih razlik $(t_2 - t_1)$ dogodkov, ki tvorijo koincidence, dobljen s slikanjem točkastega vira gama 511 keV, postavljenega v središče Čerenkovega skenerja. Zaradi dolgih repov v porazdelitvi se dvojna Gaussova funkcija (rdeča) bolje prilega podatkom histograma kot enojna Gaussova funkcija (črna). FWHM in njihova mešalna razmerja (a_1/a_2) so prav tako prikazani za vsako konfiguracijo Čerenkovega detektorja. SPTR fotodetektorja je bil nastavljen na 70 ps FWHM.

tabeli 5.1. Črno pobarvani kristali dosegajo boljše CTR kot kristali, oviti v reflektor. Vendar pa je njihova znatno nižja učinkovitost zaznavanja koincidenc, zaradi nižje učinkovitosti prenosa svetlobe (angl. light transfer efficiency; LTE), vodi v nižji FOM. Med detektorji z 2-stranskim branjem je konfiguracija s fotodetektorji ob bokih (slika 8.2: *2-stranski-boka*) dosegla najboljšo kombinacijo CTR in učinkovitosti zaznavanja. Zanimivo je, da je FOM 2-stranskega detektorja z bočnim branjem le približno 10% slabši, od FOM detektorja s 6-stranskim branjem zaradi 10% slabše učinkovitosti zaznavanja koincidenc, medtem ko dosega enak CTR, 120 ps (pri zaokrožitvi na dve signifikantni mesti).

S simulacijo kristalov LSO v enaki postavitvi, z 10% energijsko ločljivostjo in energijskim oknom 435-585 keV je bila dobljena 17.6% učinkovitost zaznavanja koincidenc. Vendar je potrebno to vrednost previdno primerjati s Čerenkovimi detektorji. Opisana študija ne preizkuša zavrnitve sipanih koincidenc in ne upošteva sipanj znotraj kristala, ki lahko povzročijo sprejete dogodke v detektorju polne velikosti.

Slika 8.7 prikazuje števila izsevanih fotonov Čerenkova v kristalu PbF_2 po interakciji gama z energijo 511 keV. Neposrednemu fotoelektričnemu pojavu (fotoefektu) sledi v povprečju 19.4 oddanih fotonov Čerenkova, medtem ko vsaka interakcija ali kombinacija interakcij, v kateri nastane vsaj en foton Čerenkova, proizvede v povprečju 14.5 fotonov. Ti simulirani rezultati se dobro ujemajo s predvidenim številom izsevanih fotonov Čerenkova 16.5 ±3.3, ocenjenim za PbF_2 iz meritev [6].

Dogodki, zaznani z neposrednim fotoelektričnim pojavom na sliki 8.7, predstavljajo približno 57% vseh zaznanih dogodkov, medtem ko je delež fotoefekta v PbF_2

Tabela 8.2: Zmogljivosti različnih konfiguracij detektorjev glede na FOM, ki je definiran kot razmerje med učinkovitostjo zaznavanja koincidenc (ϵ^2) in CTR. Preučeni sta bili dve vrednosti SPTR fotodetektorja; 0 ps in 70 ps. Barvno ozadje označuje konfiguracije detektorjev, uporabljenih v študiji PET skenerja.

	Čerenkov detektor	Površina	LTE (%)	ε^2 (%)	CTR-FWHM (ps)		FOM	
					0 ps SPTR	70 ps SPTR	0 ps SPTR	70 ps SPTR
	1-stranski	Črna	17.2	8.6	100.7	145.5	0.85	0.59
		Odbojna	51.6	35.3	135.7	184.8	2.60	1.91
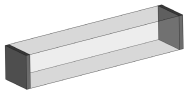	2-stranski-konca	Črna	26.3	17.6	183.4	206.2	0.96	0.85
		Odbojna	55.9	35.2	192.7	229.7	1.83	1.53
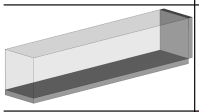	2-stranski-konec-bok	Črna	31.9	22.1	67.2	156.1	3.29	1.42
		Odbojna	76.0	41.7	80.0	137.8	5.21	3.02
	2-stranski-boka	Črna	37.5	26.2	47.0	111.1	5.57	2.36
		Odbojna	71.1	40.5	48.9	117.8	8.28	3.44
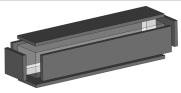	6-stranski	/	94.5	44.4	54.1	115.4	8.21	3.85

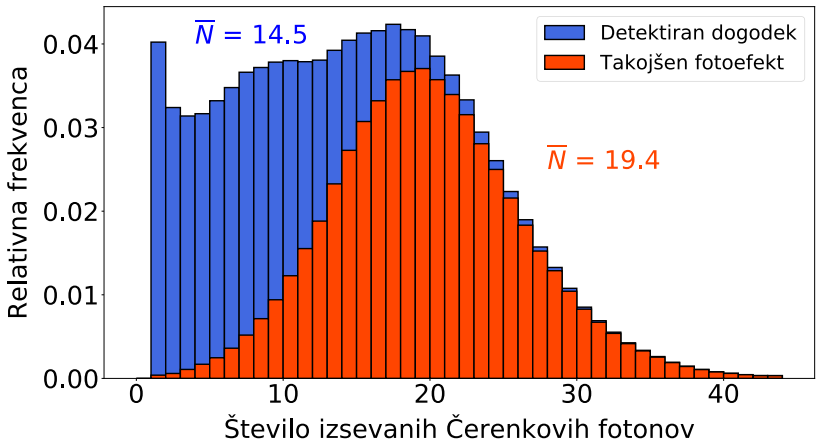

Slika 8.7: Porazdelitev izsevanih fotonov Čerenkova v PbF_2 po interakciji anihilacijskega fotona, v kateri nastane vsaj en foton Čerenkova. Fotoni Čerenkova lahko nastanejo kot posledica ene same ali večkratne interakcije žarka gama v kristalu, npr. večkratnega sipanja in nato fotoefekta.

46% (Tabela 8.1). Ta razlika je posledica dejstva, da del dogodkov, pri katerih se najprej sipa žarek gama, ne proizvede fotonov Čerenkova, zato se takšni dogodki ne štejejo kot zaznani.

Slika 8.8 prikazuje porazdelitev števila zaznanih fotonov Čerenkova v izbranih Čerenkovih detektorjih z uporabo idealističnega fotodetektorja in fotodetektorja z realnim kvantnim izkoristkom. Pri detektorju z 1-stranskim branjem je povprečno število zaznanih fotonov Čerenkova v idealnem primeru 7.5. Glede na emisijski

spekter (slika 8.7) bi lahko načeloma v povprečju zaznali 14.5 fotonov, vendar vsi fotoni ne dosežejo fotodetektorja in posledično je LTE 51,6% (tabela 8.2).

Povprečno število zaznanih fotonov Čerenkova pade na 2.8 z realističnim fotodetektorjem in dogodki, ki ustrezajo samo enemu zaznanemu fotonu Čerenkova, predstavljajo približno 27% zaznanih dogodkov. Medtem pa v idealnem primeru, ti dogodki ustrezajo le približno 7% zaznanih dogodkov. Povprečno število zaznanih fotonov Čerenkova se poveča s prehodom na 2-stransko ali 6-stransko branje. Kvantni izkoristek fotodetektorja pa ne določa le števila zaznanih fotonov Čerenkova. Da se dogodek šteje kot zaznan, mora biti zaznan vsaj en foton Čerenkova. Zato kvantni izkoristek neposredno vpliva tudi na učinkovitost zaznavanja žarkov gama.

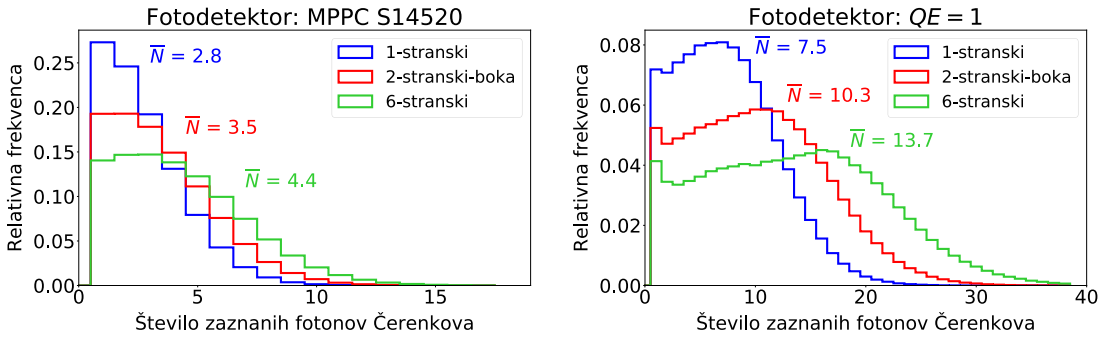

Slika 8.8: Porazdelitev zaznanih fotonov Čerenkova v konfiguracijah Čerenkovih detektorjev, uporabljenih v študiji PET skenerja, povezanim z realističnim (levo) in idealističnim (desno) fotodetektorjem. Povprečno število zaznanih fotonov Čerenkova narašča z naraščajočim številom strani branja kristala.

Učinkovitost detekcije, kot funkcija energije vpadnega žarka gama za izbrane Čerenkove detektorje, je prikazana na sliki 8.9. Tako kot povprečno število zaznanih fotonov Čerenkova, se tudi učinkovitost detekcije poveča z uporabo detektorjev z večstranskim odčitavanjem ali z uporabo idealnih/boljših fotodetektorjev. Za žarke gama z nižjimi energijami je manjša verjetnost detekcije, pri čemer verjetnost pade na nič pod pragom proizvodnje fotonov Čerenkova, ki je v PbF_2 pri približno 100 keV. Na ta način imajo Čerenkovi detektorji vgrajen mehanizem, ki zavrne precejšen del žarkov gama, ki so se sipali v pacientovem telesu. Čeprav se število proizvedenih fotonov Čerenkova povečuje z deponirano energijo žarka gama, kar posledično poveča verjetnost zaznave dogodka v Čerenkovem detektorju, se atenuacijski koeficient in delež fotoefekta zmanjšujeta z energijo, kar pomeni, da je manj verjetno, da bo žarek gama z višjo energijo interagiral v detektorju, poleg tega pa je bolj verjetno, da bo odložil le del svoje energije zaradi sipanja, kar povzroči plato ali celo zmanjšanje učinkovitosti zaznavanja pri višjih energijah gam (slika 8.9).

Študija Čerenkovega PET skenerja

Za študijo skenerja so bili izbrani 1-stranski, 2-stranski z branjem ob bokih in 6-stranski detektor. Izraz 2-stranki detektor se v tem poglavju nanaša na detektor z 2-stranskim branjem iz bokov kristala.

NECR in delež sipanja

Najprej je bila izvedena primerjava NECR krivulj in deleža sipanja med Čerenkovimi skenerji in referenčnim skenerjem Siemens Biograph Vision (slika 8.10). Krivulja

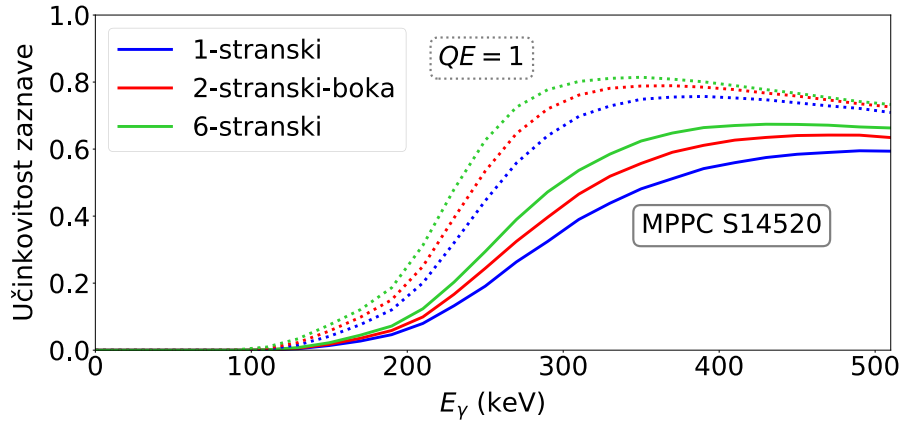

Slika 8.9: Učinkovitost detekcije Čerenkovega detektorja v odvisnosti od energije vpadnega žarka gama. Prekinjena črta prikazuje delovanje detektorjev, ki uporabljajo idealni fotodetektor, polna črta pa je za detektorje z realističnim fotodetektorjem (MPPC S14520).

NECR Čerenkovega skenerja z 1-stranskim branjem je zelo podobna krivulji referenčnega skenerja, čeprav ima znatno višji delež sipanja, 47,3%, v primerjavi z 32,5% pri referenčnem skenerju. Najboljši NECR doseže 6-stranski Čerenkov skener, medtem ko je 2-stranski dizajn vmes, pri čemer je njegov NECR bližje 6-stranskemu kot 1-stranskemu Čerenkovemu skenerju. Vsi Čerenkovih skenerjih imajo delež sipanja tik pod 50% . Povečano zaznavanje sipanih koincidenc v Čerenkovih skenerjih se kompenzira z večjo učinkovitostjo zaznavanja pravih koincidenc, kar vodi do enakih ali boljših vrednosti NECR.

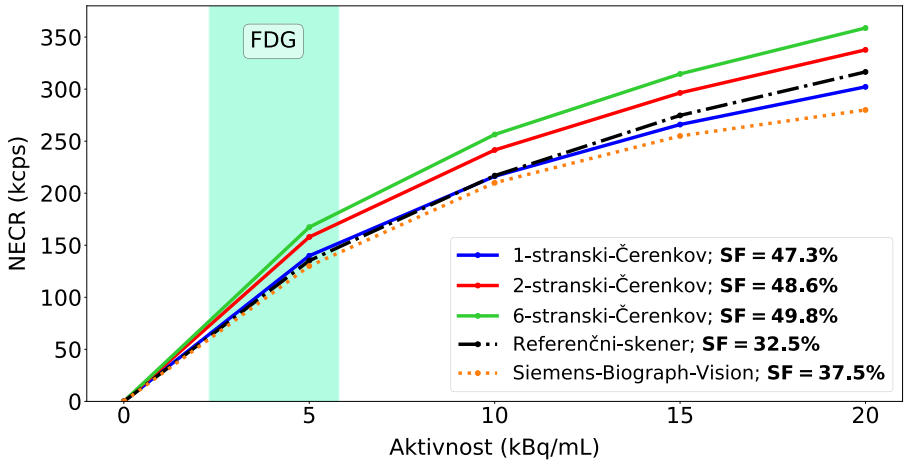

Slika 8.10: Vrednosti NECR kot funkcija aktivnosti: primerjava med Čerenkovimi skenerji, simuliranim referenčnim skenerjem in meritvami, izvedenimi na Siemens Biograph Vision [114]. Deleži sipanja (SF) različnih skenerjev so prikazani v legendi. Zasenčen pravokotnik prikazuje tipičen obseg aktivnost, ki se uporabljajo na začetku kliničnega slikanja telesa s FDG.

Med simuliranimi vrednostmi NECR za referenčni skener in vrednostmi, izmerjenimi na skenerju Siemens Biograph Vision je dobro ujemanje pri nižjih (klinično pomembnih) aktivnostih, nekoliko manj pa pri višjih aktivnostih, kar je bilo pričako-

vano, saj mrtvi čas detektorja ni bil simuliran. Navedene vrednosti NECR niso bile modificirane z informacijo TOF (efektivni NECR), kar bi sicer bolj koristilo skenerjem Čerenkova.

Kakovost slike

Slika 8.11 prikazuje slike rekonstruiranega fantoma kakovosti slike NEMA za različne konfiguracije skenerjev, kjer je bilo pri rekonstrukciji slike za Čerenkove skenerje uporabljeno dvojno Gaussovo jedro TOF. Uporaba standardnega enojnega Gaussovega jedra TOF je pri Čerenkovih skenerjih povzročila slabši odstotni kontrast in več ostanka aktivnosti v vložku fantoma, ki je sicer brez aktivnosti. Ta učinek je viden v profilu skozi izbrane rekonstruirane slike na sliki 8.12. Razmerja med odstotnim kontrastm in variabilnostjo ozadja za proučevane skenerje so prikazana na sliki 8.13. Relacija je bila izračunana iz serije slik, filtriranih z Gaussovim postfiltrom različnih širin (FWHM od 0 do 15 mm v korakih po 1 mm).

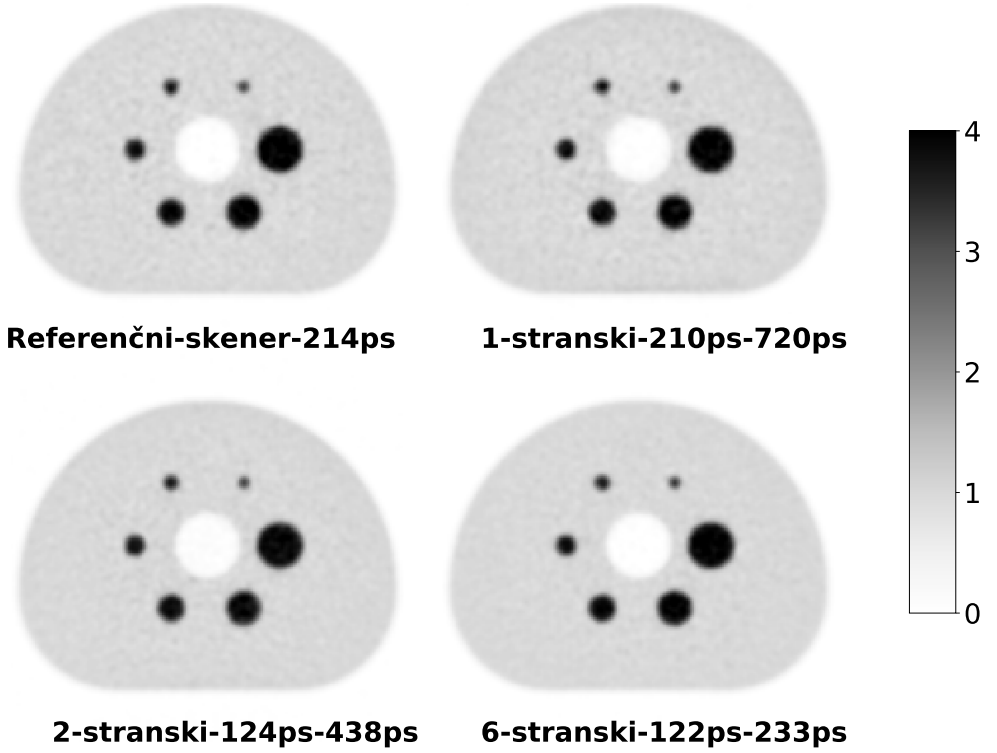

Slika 8.11: Prečni pogledi na rekonstruirane slike fantoma kakovosti slike NEMA za različne skenerje. Na vseh slikah je bil uporabljen Gaussov filter s 5 mm FWHM.

Diskusija

Učinkovitost in potencial čistih Čerenkovih detektorjev in na njih temelječih skenerjih TOF PET so bili raziskani s simulacijami Monte Carlo. V študiji detektorjev so kristali s črno površino dosegli boljše časovne ločljivosti koincidenc, vendar to, glede na FOM, ne odtehta zmanjšane učinkovitosti zaznavanja koincidenc v primerjavi s kristali, ovitimi z reflektorjem (tabela 8.2). To velja tako za idealno kot za realistično časovno ločljivost fotodetektorja. Posledično se je večina študij v tem delu osredotočila na detektorje, ki uporabljajo odsevne površine kristalov.

Med proučevanimi 2-stranskimi detektorji je konfiguracij s fotodetektorji, nameščenimi ob bokih kristala, dosegla najboljšo kombinacijo učinkovitosti zaznavanja koin-

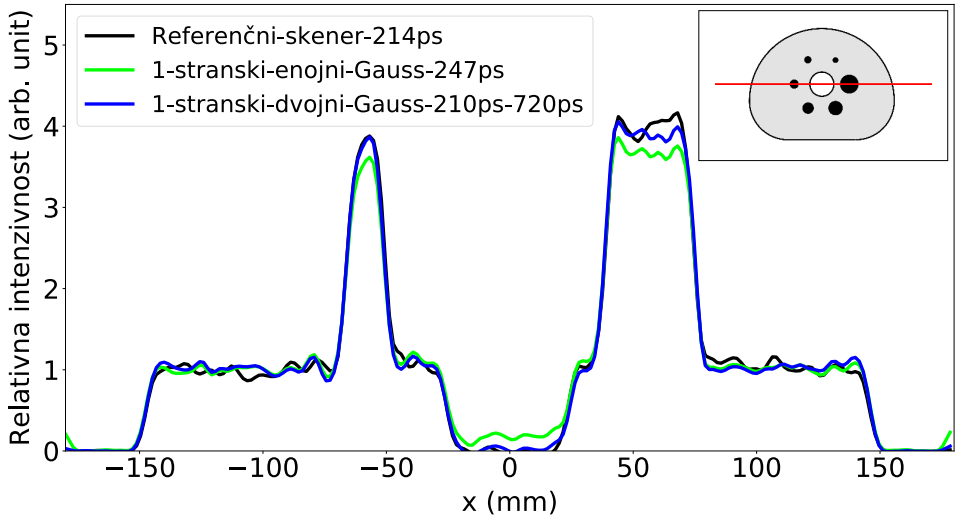

Slika 8.12: Profil s prečnim prerezom enega voksla, pridobljen iz rekonstruiranih slik fantoma kakovosti slike NEMA. Primerjana sta profili Čerenkovega skenerjev z 1-stranskim branjem, kjer sta bili med rekonstrukcijo slike uporabljeni dve različni jedri TOF; enojno Gaussovo (zelena črta) in dvojno Gaussovo (modra črta). Na rekonstruiranih slikah je bil uporabljen Gaussov filter s 5 mm FWHM. Profil prehaja skozi vroči kroglici s premerom 17 mm in 37 mm in kaže izboljšan kontrast pri uporabi dvojnega Gaussovega jedra TOF.

cidenc in CTR. Rezultati za 2-stranski detektor z branjem ob bokih so primerljivi z rezultati 6-stranskega detektorja, ki je služil kot idealizirana referenca, ki ima verjetno omejeno praktično uporabo zaradi povečanih dimenzij, stroškov in kompleksnosti. Čas dogodka je določil prvi prispel foton Čerenkova in uporabljeni niso bili nobeni popravki na teh časih, kar bi lahko izboljšalo CTR detektorjev z večstranskim branjem [124].

Čas detekcije je med drugim odvisen od porazdelitve časa potovanja optičnih fotonov od mesta nastanka do fotodetektorja, na to porazdelitev pa vpliva tudi postavitev fotodetektorja. Zato so lahko pri večstranskem odčitavanju časovne razlike dogodkov, ki tvorijo koincidence, odvisne tudi od relativnega položaja fotodetektorjev, ki so zaznali prvi foton Čerenkova. Na primer, v 2-stranski konfiguraciji s fotodetektorji na koncih se časovna porazdelitev zaznanih dogodkov, pri katerih se sprožita fotodetektorja nameščena na koncih kristala, razlikuje od porazdelitve, pri katerem se za en dogodek, ki tvori koincidenco, sproži prednji ter za drug dogodek zadaj postavljeni fotodetektor. Razlika izhaja iz porušene krožne simetrije, saj so fotodetektorji, ki tvorijo koincidenčen dogodek, nameščeni na različnih razdaljah od osi skenerja. Ta učinek ne velja za 2-stransko bočno odčitavanje, vendar pa bi lahko postal pomemben in bi lahko bil izkoriščen za izboljšanje CTR, če bi bil fotodetektor segmentiran vzdolž glavne osi kristala. Segmentacijo bočnega branja bi lahko kombinirali tudi s segmentacijo kristala in tako potencialno tudi zagotovili (boljšo) informacijo o globini interakcije kot pri nesegmentiranem kristalu.

Preprosta metoda korekcije detekcijskega časa s scintilacijskimi 2-stranskimi detektorji s fotodetektorji na koncih, vzame povprečje časov proženja obeh fotodetektorjev [125, 126]. Na splošno imajo časi proženja obeh fotodetektorjev različne variance zaradi različnega deleža prejetih optičnih fotonov. Tako enostavno povprečje

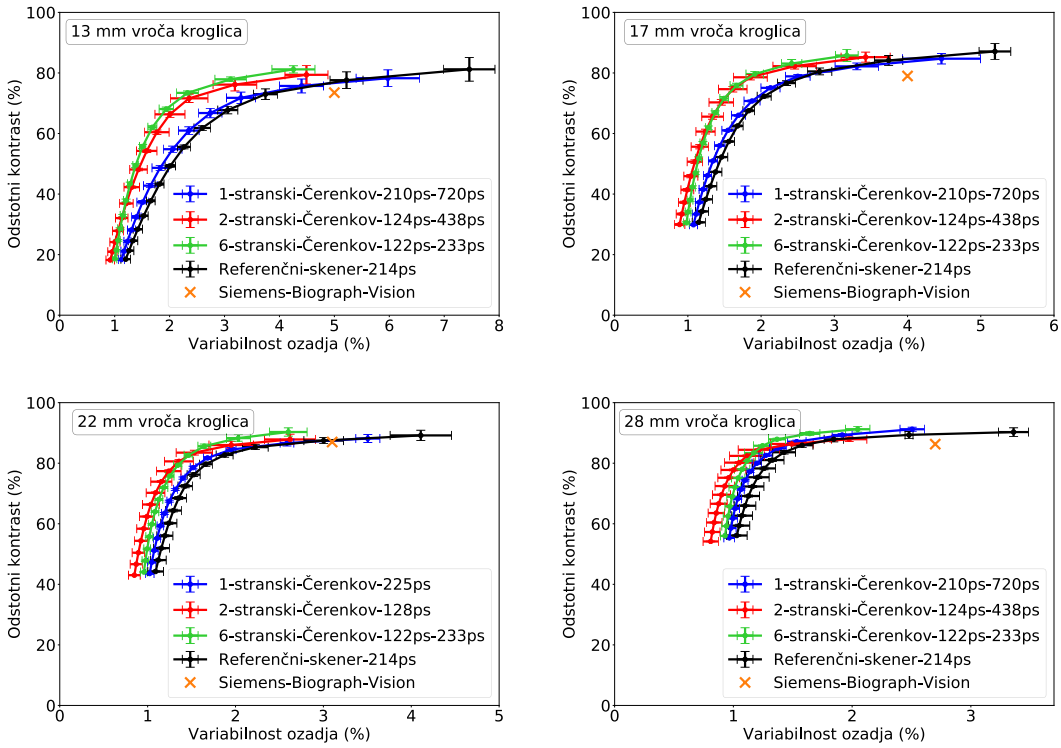

Slika 8.13: Odstotni kontrast glede na variabilnost ozadja za vroče kroglice s premerom 13 mm, 17 mm, 22 mm in 28 mm. Gaussovi filtri različnih širin so bili uporabljeni za spreminjanje variabilnosti ozadja. Izmerjene vrednosti na skenerju Siemens Biograph Vision so dodane za referenco [114].

ni najboljša statistična cenilka časa proženja. Primer boljše metode je uteževanje časov proženja, ocenjenih iz vsakega fotodetektorja, z inverzno vrednostjo njihovih varianc [127]. V čistem Čerenkovem detektorju, se oba fotodetektorja morda ne bosta prožila v znatnem številu dogodkov, zaradi česar so prej obravnavane korekcijske metode proženja časa manj uporabne za Čerenkove detektorje. Dobra možnost za nadaljnje raziskave bi bila uporaba eksperimentalnih podatkov in po možnosti tudi podatkov iz Monte Carlo simulacije z globokimi (konvolucijskimi) nevronskimi mrežami [128] za boljšo oceno časa TOF, pridobljenih z detektorji Čerenkova z večstranskim branjem.

Geometrija referenčnega skenerja in Čerenkovih skenerjev je temeljila na geometriji kliničnega skenerja Siemens Biograph Vision. V študiji NECR je imel 1-stranski Čerenkov skener podobno hitrost štetja kot referenčni skener (slika 8.10). To je bilo kljub občutno višjemu deležu sipanj, 47.3%, v primerjavi z referenčnim skenerjem, ki znaša 32.5%. 6-stranski skener je dosegel najboljše vrednosti NECR, medtem ko je bil 2-stranski dizajn vmes, s svojimi vrednostmi bližje 6-stranskemu kot 1-stranskemu.

Vrstni red zmogljivosti proučevanih skenerjev, predviden z analizo NECR, je bil ponovljen v študiji kakovosti slike NEMA (slika 8.13). Čerenkov skener z 1-stranskim branjem je imel primerljiv CTR in je dosegel zelo podobno kakovost slike kot referenčni skener. Ti rezultati kažejo, da ni nobenih teoretičnih ovir in da lahko čisti Čerenkov PET skener doseže kakovost slike, ki je konkurenčna trenutnim najboljšim kliničnim skenerjem, kljub temu, da nima energetske ločljivosti, ki bi

se uporabljala za zavračanje sipanih koincidenc. Podobnost v zmogljivosti med 1-stranskim Čerenovim in referenčnim skenerjem je mogoče pripisati tudi dejstvu, da je energijska ločljivost scintilacijskih PET skenerjev daleč od idealne in posledično tudi sami sprejemajo veliko število sipanih koincidenc (SF $>$ 30 %, Slika 8.10). Z uporabo večstranskih konfiguracij detektorjev je bila dosežena še boljša kakovost slike.

V tej študiji so bili fotodetektorji modelirani z zanemarljivo velikostjo, kar pomeni, da so bili detektorji z večstranskim branjem ob bokih enako veliki kot 1-stranski detektor. Čeprav je to idealen primer, je praktično mogoče narediti silicijeve fotopomnoževalke zelo tanke, detektorje z bočnim odčitavanjem pa je mogoče realizirati v skenerjih z redkejšimi detektorji, kjer niso vsi obroči v aksialni smeri napolnjeni z detektorji. Študijo izvedljivosti so opravili Zhang *et al.* 2019 [129], ki je pokazala, da odstranitev 50% detektorjev v prečni ali aksialni smeri ni imela večjega vpliva na standardne vrednosti prevzema (SUV) za skener Philips Vereos. Nedavna Monte Carlo študija skenerja Siemens Biograph Vision PET z razširjenim aksialnim vidnim poljem (AFOV) ter z uporabo razredčene konfiguracije obročev detektorskih modulov [130] poroča, da razredčena konfiguracija omogoča razširitev trenutno omejenega AFOV običajnih sistemov PET za več kot 100% brez dodatnih stroškov in brez pomembnega vpliva na delež kontrasta, občutljivost sistema in transaksialno prostorsko ločljivost. Koncept razredčene zasnove se zato obravnava tudi kot možnost za ustvarjanje sistemov PET za hkratno slikanje celotnega telesa z nižjimi stroški [64] in bi bil posebej primeren za 2-stranski Čerenkov detektor.

Glavna omejitev te študije je, da v simulacijo ni bil vključen šum, zlasti temni šum silicijevih fotopomnoževalk, ki bi lahko opazno vplival na kakovost slike, ko je dogodek zaznan s samo eno sproženo SiPM mikrocelico, kot je bil v tej simulacijski študiji. Šum fotodetektorjev bi povečal število naključnih dogodkov, kar bi zmanjšalo NECR skenerja in povzročilo več šuma tudi v rekonstruiranih slikah. Šum lahko vpliva tudi na kakovost slike z znižanjem CTR ali prostorske ločljivosti, zlasti pri konfiguraciji detektorjev, ki vključujejo zdrževanje signalov. Temni šum silicijevih fotopomnoževalk je mogoče močno zmanjšati s hlajenjem.

Poleg hlajenja, bi šum lahko poskusili zmanjšati tudi z zahtevo, da se meritev sproži šele pri več kot enem zaznanem fotonu, na primer, pri dveh ali treh fotonih. Vendar bi bilo potrebno ovrednotiti vpliv višjih ravni proženja na učinkovitost zaznavanja in te bi najbolj vplivale na detektorje z nižjim povprečnim številom zaznanih fotonov Čerenkova (slika 5.2). Pri večstranskem odčitavanju je na voljo tudi možnost zmanjšanja šuma tako, da se raven proženja pusti pri enem optičnem fotonu, vendar se zahteva proženje dveh ločenih silicijevih fotopomnoževalk.

V zadnjem desetletju so se silicijeve fotopomnoževalke močno izboljšale v smislu učinkovitosti fotodetekcije, zmanjšanja šuma, časovne zmogljivosti, itd. [139]. Vendar pa je še vedno veliko prostora za nadaljnji razvoj [17]. Nadaljnje izboljšanje učinkovitosti zaznavanja fotonov bi dvigovanje ravni proženja naredilo manj problematično.

Učinkovitost zaznavanja in CTR bi se prav tako izboljšala, če bi izboljšali optično sklopitev med kristalom in fotodetektorjem. Med sevalcem in fotodetektorjem so optične meje in razlika v lomnih količnikih zmanjša učinkovitost prenosa svetlobe, saj lahko postanejo fotoni ujeti v kristalu preko odbojev. Grobost površine lahko poveča učinkovitost detekcije fotonov, saj spremeni porazdelitev vpadnih kotov fotonov Čerenkova na okno fotodetektorja in tako lahko povzroči, da se foton

lomi na oknu in doseže fotodetektor, namesto da se odbije.

Predstavljene so bile različne metode za izboljšanje LTE. V Ota *et al.* 2019 [84] so izboljšali prenos fotonov Čerenkova na fotokatodo z integracijo mikrokanalne fotopomnoževalke in sevalca brez optične optične meje med njima. Tako imenovani fotonski kristali so še ena možna rešitev, ki je bila predlagana in se raziskuje za izboljšanje LTE s fotonskim nanostrukturiranjem različnih površin kristala [76]. Z uporabo nanovtisnjenih fotonskih kristalov je bilo eksperimentalno dokazana povečana ekstrakcije scintilacijske svetlobe za 50% in za 20% izboljšanje energijske ločljivosti, v primerjavi s standardno sklopitvijo [144].

Za najboljšo kakovost slike je bilo potrebno pri rekonstrukciji uporabiti dvojno Gaussovo jedro TOF, v nasprotju s konvencionalnim enojnim Gaussovim, saj ima časovna razlika zaznanih dogodkov v Čerenkovih detektorjih dolge repe (slika 8.12). Nedavna študija je prav tako uspešno implementirala dvojno Gaussovo jedro TOF za BGO detektorje, obenem pa raziskala mešan Gaussov model, kjer je uporabljeno različno jedro TOF za različno število zaznanih fotonov Čerenkova [101].

Utežena rekonstrukcija je še ena možnost izboljšave, pri čemer je utež odvisna od dogodka. Obe neželeni vrsti dogodkov, sipani žarki gama in temni šum, v povprečju sprožijo manjše število SiPM mikrocelic v primerjavi s pravo koincidenco. V uteženi rekonstrukciji bi se tako lahko dogodki, ki sprožijo več mikrocelic, močneje utežili in bi se na ta način izboljšala kakovost rekonstruirane slike. Utežen način rekonstrukcije lahko tudi ublaži težavo z iskanjem kompromisa med čistim signalom, kjer je uporabljen visok prag, in visoko statistiko, kjer je uporabljen nizek prag proženja [6].

Popravek sipanja v tem delu je temeljil na simulaciji Monte Carlo, ki je priznana kot ena najbolj natančnih metod za to nalogo. Vendar pa je glavna pomanjkljivost Monte Carlo simulacij dolg računski čas, zaradi česar do sedaj še niso bile na široko implementirane v klinično okolje. Eden od načinov za reševanje te težave je uporaba grafičnih procesnih enot za pospešitev simulacij [145]. V klinikah je metoda s simulacijo enojnega sipanja najpogosteje uporabljena korekcijska metoda sipanja, vendar zaradi predpostavke, da so vsi sipani dogodki enkrat sipani, ta metoda izgubi natančnost pri skenerjih s slabo energijsko ločljivostjo. Posledično ta metoda ni najboljša izbira za korekcijo sipanja pri čistem Čerenkov PET.

Globoko učenje ima širok vpliv na številih in raznolikih področjih, vključno s slikanjem PET [146]. Algoritmi globokega učenja so obetavni kandidati za hitro in natančno korekcijo sipanja [147] in druge vrste popravkov, kot je korekcija atenuacije [148]. Kažejo tudi potencial kot privzeti okvir za celoten proces rekonstrukcije slike PET [149, 150].

Čisti Čerenkovi detektor, ki temelji na PbF_2, lahko doseže odličen CTR, kot je razvidno in obravnavano v tem delu. V dosedanjih eksperimentih so bile najboljše časovne ločljivosti (pod 100 ps) dosežene z visoko zmogljivo elektroniko, ki je ni mogoče zlahka in ekonomično uporabiti v velikih napravah. Vendar pa nedavno delo, ki so ga opravili Krake *et al.* 2022 [151], dokazuje, da je mogoče najti elektronske rešitve z nizko porabo energije in hkrati primerne za vrhunsko časovno ločljivost. Nedavno razviti čip FastIC [152] je še en primer elektronike z visoko gostoto kanalov in nizko porabo energije ter s potencialom za hitro branje v Čerenkovih PET skenerjih. Če povzamemo, zdi se, da ni nobenih teoretičnih ali praktičnih ovir, zaradi katerih bi bil čisti Čerenkov PET skenerji neizvedljivi. Nasprotno, s svojimi številnimi možnostmi za izboljšave bo Čerenkov PET v prihodnosti verjetno pritegnil še več pozornosti.

Zaključek

V tem delu so bili raziskani čisti Čerenkovi PET detektorji in zmogljivost skenerjev, ki temeljijo na njih. Čerenkovi detektorji so znani kot hitri detektorji, ki lahko dosežejo odlično časovno ločljivost, vendar se do sedaj niso smatrali kot primerni za klinične PET detektorje zaradi majhnega števila nastalih fotonov Čerenkova in posledično slabe energijske ločljivosti. Rezultati simulacij, predstavljeni v tem delu, kažejo, da lahko Čerenkovi skenerji dosežejo kakovost slike, ki je primerljiva, če ne celo boljša, kot pri trenutnih najsodobnejših PET skenerjih. To je kljub večjemu deležu sipanja možno, zahvaljujoč izboljšani učinkovitosti detekcije žarkov gama in časovni ločljivosti detektorja, ki temelji na PbF_2. Bolj splošno sporočilo, ki sledi iz tega dela, je, da je zmanjšano ali neobstoječo energijsko ločljivost PET detektorja mogoče kompenzirati z njegovo učinkovitostjo zaznavanja žarkov gama in/ali CTR. Kakovost slike lahko izboljšamo z uporabo večstranskega branja kristalov in rezultati simulacije kažejo podobno delovanje detektorjev z 2-stranskim bočnim branjem kot teoretično idealni detektorji s 6-stranskim branjem. Detektor z bočnim branjem je praktično mogoče realizirati v skenerjih z razredčeno zasnovo detektorjev. Cenejši Čerenkovi detektorji bi lahko postali še posebej zanimivi za skenerje celotnega telesa, saj trenutno visoka cena takšnih skenerjev omejuje njihovo širjenje v bolnišnicah in raziskovalnih klinikah. S pričakovanimi nadaljnjimi izboljšavami fotodetektorjev in namenskih tehnologij za Čerenkov PET, so lahko čisti Čerenkovi detektorji obetavna pot do ultra hitrih in dostopnih PET skenerjev naslednje generacije.

List of publications related to this doctoral thesis

1. Gašper Razdevšek, Rok Pestotnik, Peter Križan, Samo Korpar, Dania Consuegra, Andrej Seljak, Andrej Studen and Rok Dolenec *Exploring the Potential of a Cherenkov TOF PET Scanner: A Simulation Study*, IEEE trans. radiat. plasma med. sci.. **7**, 52 (2023), https://doi.org/10.1109/TRPMS.2022.3202138.

2. Gašper Razdevšek, Rok Dolenec, Peter Križan, Stan Majewski, Andrej Studen, Samo Korpar, Georges El Fakhri, and Rok Pestotnik, *Multipanel Limited Angle PET System With 50 ps FWHM Coincidence Time Resolution: A Simulation Study*, IEEE trans. radiat. plasma med. sci.. **6**, 721 (2022), https://doi.org/10.1109/TRPMS.2021.3115704.

3. Dania Consuegra, Samo Korpar, Peter Križan, Rok Pestotnik, Gašper Razdevšek, and Rok Dolenec, *Simulation study to improve the performance of a whole-body PbF_2 Cherenkov TOF-PET scanner*, Phys. Med. Biol.. **65**, 055013 (2020), https://doi.org/10.1088/1361-6560/ab6f97.